Universidade de Aveiro Departamento de Eletrónica, Telecomunicações e Informática
2013

Nuno Alexandre Peixoto Silva

Criptografia Quântica em Fibras Óticas

Quantum Criptography in Optical Fibers

Universidade de Aveiro
2013
Departamento de Eletrónica, Telecomunicações e Informática

Nuno Alexandre Peixoto Silva

Criptografia Quântica em Fibras Óticas

Quantum Criptography in Optical Fibers

Tese apresentada à Universidade de Aveiro para cumprimento dos requisitos necessários à obtenção do grau de Doutor em Engenharia Eletrotécnica, realizada sob a orientação científica do Doutor Armando Humberto Moreira Nolasco Pinto, Professor Associado do Departamento de Eletrónica, Telecomunicações e Informática da Universidade de Aveiro.

Apoio financeiro da Fundação para a Ciência e a Tecnologia - FCT através da bolsa de investigação com a referência: SFRH / BD / 63958 / 2009, comparticipada pelo Fundo Social Europeu - FSE no âmbito do Programa Operacional Potencial Humano - POPH do QREN, e por fundos nacionais do Ministério da Educação e Ciência - MEC.

o júri / the jury

presidente / president

Doutor Luís António Ferreira Martins Dias Carlos
Professor Catedrático do Departamento de Física da Universidade de Aveiro

vogais / examiners committee

Doutor Paulo Sérgio de Brito André
Professor Associado do Departamento de Engenharia Eletrotécnica e de Computadores do Instituto Superior Técnico da Universidade de Lisboa

Doutor Hélder Manuel Paiva Rebelo Cerejo Crespo
Professor Auxiliar do Departamento de Física da Faculdade de Ciências da Universidade do Porto

Doutor Manfred Niehus
Professor Adjunto da Área Departamental de Física do Instituto Superior de Engenharia de Lisboa

Doutor Armando Humberto Moreira Nolasco Pinto
Professor Associado do Departamento de Eletrónica, Telecomunicações e Informática da Universidade de Aveiro (Orientador)

agradecimentos / acknowledgements

O trabalho apresentado nesta tese teve o contributo de várias pessoas e entidades a quem gostaria de agradecer. Gostaria de agradecer ao Professor Armando Humberto Moreira Nolasco Pinto o facto de ter aceitado orientar-me cientificamente neste Doutoramento. Agradeço ainda o apoio dado na elaboração desta tese, assim como na análise, discussão e interpretação dos vários resultados obtidos ao longo deste Doutoramento. Gostaria de agradecer a todos os meus colegas e amigos do grupo de comunicações óticas do Instituto de Telecomunicações. Nomeadamente, aos meus colegas e amigos Nelson Muga, Álvaro Almeida, Gil Fernandes, Steven Carneiro e Luís Martins agradeço as suas importantes contribuições para o trabalho aqui apresentado, particularmente as suas colaborações laboratoriais, assim como as inúmeras discussões científicas que mantivemos e que se revelaram de grande relevância.

Gostaria ainda de agradecer às seguintes instituições: Universidade de Aveiro e Instituto de Telecomunicações, onde dispus das condições necessárias para a realização do trabalho apresentado nesta tese. Agradeço também à Fundação para a Ciência e a Tecnologia pelo fundamental suporte financeiro através da bolsa de Doutoramento SFRH/BD/63958/2009, e ainda aos projetos de investigação QuantPriveTel, referência: PTDC/EEA-TEL/103402/2008, e P-Quantum, referência: PEst-OE/EEI/LA0008/2011.

Finalmente, mas não por último, gostaria de agradecer à Joana Patrícia pela paciência e apoio, e ainda à Mariana pelas noites acordado, oferecendo-me assim a possibilidade de trabalhar mais horas.

Aos meus Pais e Irmão.

À Joana e Mariana.

palavras-chave

Fibra ótica, absorção, ótica não linear, mistura de quatro ondas, espalhamento de Raman, criptografia quântica, geração de fotões únicos e entrelaçados, estatística de fontes de fotões únicos.

resumo

As comunicações quânticas aplicam as leis fundamentais da física quântica para codificar, transmitir, guardar e processar informação. A mais importante e bem-sucedida aplicação é a distribuição de chaves quânticas (QKD). Os sistemas de QKD são suportados por tecnologias capazes de processar fotões únicos. Nesta tese analisamos a geração, transmissão e deteção de fotões únicos e entrelaçados em fibras óticas. É proposta uma fonte de fotões única baseada no processo clássico de mistura de quatro ondas (FWM) em fibras óticas num regime de baixas potências. Implementamos essa fonte no laboratório, e desenvolvemos um modelo teórico capaz de descrever corretamente o processo de geração de fotões únicos. O modelo teórico considera o papel das não-linearidades da fibra e os efeitos da polarização na geração de fotões através do processo de FWM.

Analisamos a estatística da fonte de fotões baseada no processo clássico de FWM em fibras óticas. Derivamos um modelo teórico capaz de descrever a estatística dessa fonte de fotões. Mostramos que a estatística da fonte de fotões evolui de térmica num regime de baixas potências óticas, para Poissoniana num regime de potências óticas moderadas. Validamos experimentalmente o modelo teórico, através do uso de fotodetetores de avalanche, do método estimativo da máxima verossimilhança e do algoritmo de maximização de expectativa.

Estudamos o processo espontâneo de FWM como uma fonte condicional de fotões únicos. Analisamos a estatística dessa fonte em termos da função condicional de coerência de segunda ordem, considerando o espalhamento de Raman na geração de pares de fotões, e a perda durante a propagação de fotões numa fibra ótica padrão. Identificamos regimes apropriados onde a fonte é quase ideal. Fontes de pares de fotões implementadas em fibras óticas fornecem uma solução prática ao problema de acoplamento que surge quando os pares de fotões são gerados fora da fibra. Exploramos a geração de pares de fotões através do processo espontâneo de FWM no interior de guias de onda com suceptibilidade elétrica de terceira ordem. Descrevemos a geração de pares de fotões em meios com elevado coeficiente de absorção, e identificamos regimes ótimos para o rácio contagens coincidentes/acidentais (CAR) e para a desigualdade de Clauser, Horne, Shimony, and Holt (CHSH), para o qual o compromisso entre perda do guia de onda e não-linearidades maximiza esses parâmetros.

keywords

Optical fiber, absorption, nonlinear optics, four-wave mixing, Raman scattering, quantum cryptography, generation of single and entangled photons, statistics of single photon sources.

abstract

The quantum communications apply fundamental laws of quantum physics to encode, transmit, store and process information. The most successful and important application is the quantum key distribution (QKD). The QKD systems are supported by technologies capable of processing single photons. In this thesis we analyze the generation, transmission and detection of single and entangled photons in optical fibers.

We propose a single photon source based on the classical four-wave mixing (FWM) process in optical fibers in a low power regime. We implement that source in the laboratory, and we develop a theoretical model able to correctly describe the process of generation of single photons. That theoretical model takes into account the role of fiber nonlinearities and polarization effects on the generation of the photons through the FWM process.

We analyze the statistics of the photon source based on the classical FWM process in optical fibers. We derive a theoretical model capable of describe the statistics of that photon source. We show that the photon source statistics goes from a thermal one in a low power regime to a Poissonian in a moderate power regime. We validate experimentally the theoretical results, using avalanche photo-detectors, the maximum-likelihood estimation method and the expectation-maximization algorithm.

We study the spontaneous FWM process as a source of heralded single photons. We analyze the source statistics in terms of the conditional second-order coherence function, considering the impact of Raman scattering on the generation of the photon-pairs, and the loss during the evolution of the photon through a standard single mode fiber (SSMF). We identify appropriate regimes where that source is almost ideal. Optical fiber-based sources of photon-pairs provide a practical solution to the coupling problem that arises when the photon-pairs are obtained outside of the fiber. We explore the generation of photon-pairs through spontaneous FWM inside of waveguides with third-order electrical susceptibility. We describe the generation of the photon-pairs in a medium with non-negligible linear absorption coefficient, and we identified appropriates regimes for the coincidence-to-accidental ratio (CAR) and the CHSH inequality, for which the trade-off between waveguide losses and nonlinearities maximizes that parameters.

Contents

List of Acronyms

APD Avalanche Photo Diode

ASE Amplified Spontaneous Emission

AWG Arrayed Waveguide Grating

BS Beam Splitter

CAR Coincidence-to-Accidental Ratio

CHSH Clauser, Horne, Shimony, and Holt

CV Continuous Variable

CVQKD Continuous Variable Quantum Key Distribution

CW Continuous Wave

DFB Distributed Feedback

DGD Differential Group Delay

DSF Dispersion-Shifted Fiber

ECL External Cavity Laser

EDFA Erbium Doped Fiber Amplifier

EPC Electronic Polarization Controller

EPR Einstein, Podolsky and Rosen

FWHM Full Width at Half Maximum

FWM Four-Wave Mixing

GNLSE Generalized NonLinear Schrödinger Equation

HiBi High Birefringent

HNLF Highly NonLinear Fiber

HWP Half Wave Plate

LP Linear Polarizer

Mod Modulator

MUX Multiplexer

NEQ Noise Equivalent Power

NSE NonLinear Schrödinger Equation

PBS Polarization Beam Splitter

PC Polarization Controller

PCF Photonic Crystal Fiber

PMD Polarization Mode Dispersion

PNR Photon Number Resolving

PSP Principal States of Polarisation

QBER Quantum Bit Error Rate

QKD Quantum Key Distribution

RLP Rotatable Linear Polarizer

RSA Ron Rivest, Adi Shamir, and Leonard Adleman

SPDC Spontaneous Parametric Down Conversion

SPDM Single Photon Detector Module

SPM Self-Phase Modulation

SOP State of Polarization

SRS Stimulated Raman Scattering

SSMF Standard Single Mode Fiber

SVEA Slowly Varying Envelop Approximation

TDM Time Domain Multiplexing

TLS Tunable Laser Source

TTM Time Tag Module

VOA Variable Optical Attenuator

WDM Wavelength-Division Multiplexing

XPM Cross-Phase Modulation

List of Figures

List of Tables

Chapter 1

Introduction

THE amount of Internet traffic transmitted over optical networks suffered a huge increase during the last decade. This increase seems to continue considering the nowadays demand for network services and faster download rates. In particular, services as businesses employing Internet-based networks for banking, home banking, cloud computing and other related Internet services are nowadays commonly used. This has made the security one of the most important issues on the optical telecommunication networks. However, nowadays the security of the network traffic is based on the limited computational power available [1]. Nevertheless, the continuous increase of the number of interconnected computers around the world and the advances in grid computing can, in principle, provide the necessary computational power needed to decipher the protection schemes that we use everyday in Internet. Despite that, there exist a communication protocol that is completely secure, the one-time pad protocol proposed in 1917 by Verman. In that protocol, a plain-text is combined with a random key that is as long as the original plain-text and used only once [1]. In 1949, Shannon proved mathematically that the Verman protocol provides perfect secrecy [2]. However, that protocol has serious drawbacks regarding its practical implementation, namely requires a perfect random key, and the key must be used only once and then must be discarded [1].

To solve the key distribution problem most of modern cryptographic systems adopt public key cryptographic protocols, such as the Ron Rivest, Adi Shamir, and Leonard Adleman (RSA) scheme. The RSA uses two different cryptographic keys: one public and one private [3]. The public key is generated by the receiver (Bob) and sent to the message sender (Alice). Alice encrypt the message with the public key and send it to Bob, over an insecure public channel. The RSA scheme was made in a such way that the encrypt message sent by Alice can only be decrypt with the private key. However, there is no mathematical prove that this protection scheme is

completely unbreakable. For instance, the RSA-155 with 155 decimal digit's was already factorized in 1999 [4]. Nowadays, 16 of the 54 RSA numbers were factorized, becoming obsolete that algorithms. In 2009, it was announced the factorization of the RSA-768 number that contains 232 digit's [5]. Since then, the recommendations for security have steadily grown from a few hundred bits to 2048 bits length [6, 7], or even close to 15 kbits for certain operations that require a high level of security [7, 8]. Nevertheless, the continuous increase of the computational power and the number of networked computers will factorize bigger RSA numbers and in a shorter time period.

In this context, the quantum cryptography, mainly the quantum key distribution (QKD), appears as a natural solution to the key distribution problem. Based on physics laws, QKD provides a secure way to distribute random keys through insecure channels. Those keys can be applied in encryption algorithms, such as the RSA, to enhance information security. In this case, the QKD system allows the continuous refresh of the key used during the communication procedure. At limit the QKD system can be seen as the Verman protocol, where each plain-text is combined with a random key obtained from a QKD system and used only once. Moreover, QKD allows the users to verify if there is an eavesdropper in the communication channel.

1.1 Quantum Key Distribution

Quantum information is a scientific area that exploits the quantum physics proprieties for coding, transmit, store and processing information. Recently, this area has attracted enormous interest due to the potential applications, such as quantum computation and cryptography. The first idea of using the quantum physical fundamentals in cryptography was proposed by Stephen Wiesner in the early 70's [9]. That work was latter extended by C. Bennett and G. Brassard, and applied to the key distribution problem [10]. In 1984 C. Bennett and G. Brassard published the first quantum protocol, the BB84, for application on QKD systems [10]. In 1989, the same authors report the first experimental results regarding the implementation of the BB84 quantum protocol [11]. A complete description of the BB84 protocol and the experimental apparatus used in [10] was latter presented in [12]. In that work, [12], authors also study the impact of an eavesdropper on the generation of the quantum key. Nowadays, several companies have brought QKD into the commercial market. There devices are based in the "plug & play" configurations, mainly commercialized by Id Quantique in Switzerland, MagiQ in USA, SecureNet in France, and QuintessenceLabs in Australia.

The security of the BB84 protocol is based in theorems and principles that the quantum

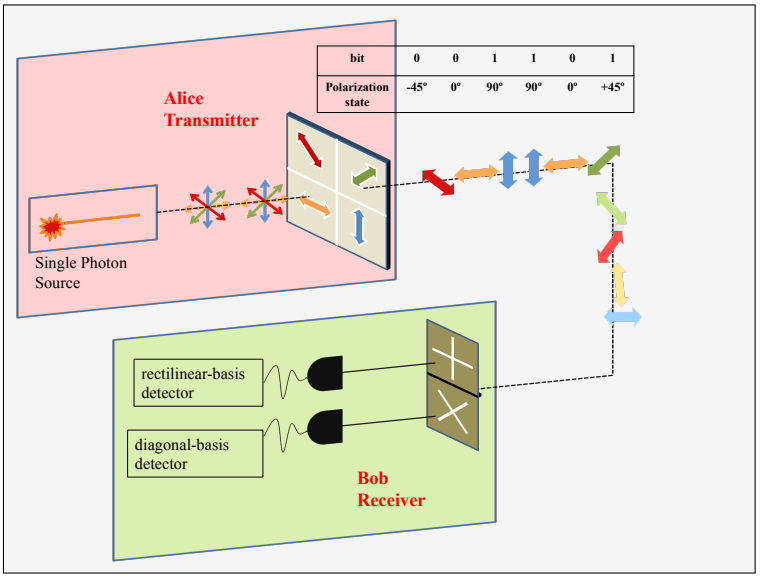

Figure 1.1: Schematic representation of the BB84 quantum protocol.

physics establish, such the no-cloning theorem and the Heisenberg uncertain principle [1]. The no-cloning theorem states that we can not duplicate an unknown quantum state, whereas the Heisenberg uncertain principle states that we can not simultaneously measure the polarization of a photon in the vertical-horizontal basis and simultaneously in the diagonal basis [13]. This means that we can't measure a quantum system without disturbing it. From the quantum information point of view, this means that we can verify if there was an eavesdropper in the quantum channel during the key exchange process from the measurement results [1, 13]. In this scenario the eavesdropper will perturb the physical system that carries the key, and there will be no agreement between the data used by the key sender and the measurements obtained by the receiver. In that sense, the security of the BB84 can be proved mathematically [1, 13].

The BB84 protocol enables two legitimate users, typically known as Alice and Bob, to produce and share a secret key, see Fig. 1.1. In this protocol, Alice and Bob must be connect by a quantum and a classical public channel. Usually the quantum channel is an optical fiber or a free-space link. It is assumed that the quantum channel can be insecure, and the classical channel is authenticated (a channel where the eavesdropper can listen but cannot interfere). In Fig. 1.1 it is presented a schematic representation of that protocol with photon polarization states. In 1992, C. Bennett noticed that in principle only two nonorthogonal states are need to implement a QKD system. That new protocol is known as B92 [14]. In the B92 protocol, instead of Alice using four polarization states, she uses only two. From an experimental point of view, the B92 quantum protocol is more simpler to implement than the BB84. The drawback of this protocol is

the fact that in a real scenario the quantum channel has some optical losses, and an eavesdropper can make use of that to break the security of the protocol. In that case, Alice and Bob would have to monitor the attenuation of the quantum channel [13]. Although only two nonorthogonal states are enough for QKD purposes, in 1998 a six states protocol was proposed [15]. The six state protocol uses three basis which leads to an increases on the security of the key exchanging process, due to the fact that an eavesdropper will introduce an error of 33% in the quantum system. However, the probability that both Alice and Bob choose the same basis is only $1/3$ [13].

Motivated by the work performed by C. Bennett and G. Brassard in the BB84 protocol, other variations of that protocol were suggested. A special variation includes the possibility of implement a QKD system using entangled qubits pairs. This idea is due to A. Ekert that proposed a protocol based on Einstein, Podolsky and Rosen (EPR) pairs, the Ekert91 [16]. In that protocol, a source produces polarization entangled photon-pairs and sent one for Alice and another for Bob. Alice and Bob perform a set of measurement of the incoming photons by randomly and independently choosing the polarization basis among a set of angles [16, 17]. After that, they announce the polarization basis that they have used to perform the measurement, and derive a key from the measurements. The security of this protocol is obtained by testing the Bell's inequalities, which guarantees that the photons where not measured before [13, 16, 17]. A simpler version of the Ekert91 protocol that avoids the Bell's theorem was proposed in [18], the BBM92 quantum protocol. In that protocol, Alice and Bob receive one photon from a polarization entangled source and randomly select one of two conjugates basis, rectilinear or diagonal, to measure their incoming photons. When they use the same basis they will obtain the same result, and when their choice is different they obtain different results [13, 17]. Due to the quantum correlation of the photon-pairs, empty pulses are removed in this protocol [17].

1.2 Experimental Implementations of QKD Systems

In a quantum cryptographic system, the information that we want to transmit is encoded in one of the degrees of freedom of the single or entangled photons, such as polarization or phase. Polarization encoding appears as a natural way of encoding the information since it is easy to be controlled, analyzed, and requires only passive optical components. However, in optical fibers due to the random evolution of the polarization state inside the fiber, usually phase encoding is much simpler to implement in a real scenario. In that case, Mach-Zehnder interferometers are used to generate different phase shifts between the two arms of the interferometer.

1.2.1 Few-Photon Emitters and Receivers for QKD Systems

Most of the QKD protocols demand single or few-photon sources. However, true single photon sources (typically known as on-demand sources or photon guns) are very complex to realize since must of them demands cryogenic temperatures or be operated in vacuum. Examples of true single photon sources are implemented based on quantum dots and quantum wells, single atoms or molecules, single ions and color centers [19]. Typically, those single photon sources use an external control systems, such as a laser, to put the quantum system in an excited state, that will emit a single photon during the relaxation process [19]. Although this kind of source allows to obtain true single photon sources, they also demand the manipulation of quantum systems. Due to that, they are difficult to implement and not easily integrable with other components of the communication system. A different approach to obtain a single photon source is based on the generation of quantum correlated photon-pairs in a nonlinear material. In this case, one photon of the pair heralds the presence of the other photon [20]. This kind of sources are known as heralded single photon sources, and uses a laser and a $\chi^{(2)}$ or $\chi^{(3)}$ material to obtain photon-pairs [20]. Nevertheless, due to the probabilist nature of the nonlinear process that give rises to the photon-pairs, this source is not on-demand source. However, they are much simple to implement when compared with true single photon sources. Although some applications on the field of quantum information demand true single photon sources, there are other applications which requires only weak coherent light fields, such as QKD [13, 21]. Those kind of sources are very simple to obtain and implement in real world applications. A simple example is a highly attenuated laser source [13]. Moreover, that probabilistic single photon source is fully integrable with nowadays communication technologies, and could operate at very high repetition rate.

A different class of quantum protocols demands entangled photon sources. The firsts sources of entangled photons were based on atomic cascades of calcium or mercury atoms [22]. However, that pioneer method to obtain entangled photon pairs is very complex to manipulate, and collect the emitted pairs is very difficult, since the photons are emitted randomly to a whole solid angle [22]. A different approach to obtain entangled photon pairs uses a laser source and a nonlinear crystal. In a $\chi^{(2)}$ nonlinear crystal the photon pairs are obtained through the spontaneous parametric down conversion (SPDC) process [22]. In that nonlinear process a photon from a laser source is annihilated and two new photons are created (typically known as signal and idler photons), such that the energy and phase matching conditions are fulfilled [23]. Higher-order nonlinear processes are also applicable to obtaining entangled photon pairs. In that sense, materials with $\chi^{(3)}$ nonlinearities can also be used to generated entangled photons through

the spontaneous four-wave mixing (FWM) process [24]. In that nonlinear process, two photons from a laser source are annihilated and two new photons are created [25]. In this case, the entangled photons pairs can be generated inside of an optical fiber, since the strong spatial-temporal confinement of the light in those waveguides, and the presence of a zero-dispersion frequency enhance the efficiency of the spontaneous FWM process [22, 25].

Encoding information in pulses with single or few-photons brings another challenge, the detection of those pulses. The difficulty arises from the fact that the photon energy is of the order of 10^{-19} J, and the detector after receiving a photon typically convert that energy in a macroscopic current [19]. The single photon detectors are typically divided in two main categories, depending if they are capable (or not) to discriminate the number of photons that arrives to the detector. Nowadays, there are commercial available non-photon resolving detectors, mainly for QKD applications. There are several approaches to obtain that kind of detector, such as photomultiplier tubes, quantum dots with field effect transistors, superconducting nanowires, up-conversion processes, and avalanche photo-diodes [19]. The most common for QKD applications at telecom wavelengths is the single photon avalanche photo-diodes working in the Geiger mode. This kind of detector works at temperatures of 210 K to 250 K, with a detection efficiency of 75% in the visible spectral region and 10% in the infrared one [19, 26]. The outcome of this detector is a click, independently if one or more photon reaches the detector.

Although, non-resolving single photon detectors can be used in some applications of quantum information science, others applications demand photon number resolving (PNR) detectors, such as quantum computation. The most common PNR detectors are based on superconducting tunnel junctions, quantum dots with field effect transistors, parallel superconducting nanowires, superconducting transition edge sensors, visible light photon counters, and time-multiplexed or arrays of avalanche photo-diodes [19]. A different approach uses only a single avalanche photo-diode in conjugation with a self-differencing circuit, which allows to measure small currents at the beginning of avalanche process [27]. More recently, authors divided electrically the area of the single avalanche photo-diode into smaller zones, maintaining the self-differencing circuit. With that, they were able to discriminate until four photons in a single pulse [28]. Since detectors based on avalanche photo-diodes are nowadays a mature technology, this approach for PNR detectors is promising for practical implementations.

1.2.2 Polarization Encoded QKD

The first QKD system implemented experimentally was reported in [11], over a 30 cm free-space link. Since them, many progresses were made in this research field. Typically in the BB84 protocol, Alice's system consists of four strongly attenuated lasers polarized at 0°, 90°, 45°, and -45°, that emits a very low average number of photons per pulse, of the order of 0.1 [13, 29]. It is essential that the photons polarization be the same at quantum channel input/output, for Bob be able to extract the information encoded by Alice. Bob randomly selects the polarization basis with a symmetric optical coupler, and analyze the photons in rectilinear or diagonal basis with the use of polarization beam splitters (PBSs) [13, 29]. Nevertheless, implementations of polarization encoding QKD systems in optical fibers faces mainly two difficulties: (1) the polarization mode dispersion (PMD); (2) the fiber intrinsic birefringence [30]. The first difficulty, PMD, is due to the fact that in the fiber the fundamental mode has two orthogonal polarizations with different group velocities. This phenomenons tends to depolarize the light, since PMD leads to a spread or overlap of the light between the two orthogonal polarization modes [30, 31]. The second difficulty, the fiber intrinsic birefringence, arises from the random change of the fiber birefringence along the fiber length. This result in a random coupling between the polarization axis, which produces an instability of the state of polarization of the light at the output of the fiber [30, 31]. This difficulties can be overcome with the use of manual or electronic polarization controllers (PCs) [32]. Nevertheless, for both high speed and long transmission systems the compensation of the polarization rotations inside the fiber can only be obtained with an active real time polarization control scheme based on electronic polarization controllers (EPCs) with a feedback system [33].

After the pioneer work [11], subsequent studies have been mainly focused on solutions for the development of long-distance fiber optics QKD systems, and for the increase of the generation rate of quantum keys. In the early 1990s, the 30 cm of free space link used in [11] was replaced by an optical fiber with length of 1 km [34]. After successful implementations in laboratory, QKD systems have evolve to real word implementations. The first real world scenario was reported in [35] over 23 km of optical fiber installed under Lake Geneva, Swiss. In that work, the receiver measured a quantum bit error rate (QBER) of 3-4% [35]. The random polarization rotations that occurs inside the fiber were compensated using a manual PC at the fiber output [34]. The generation rate of quantum keys also suffered a high increase, from a few kbits/s [34] until some Mbits/s [36, 37]. Moreover, the clock frequency that Alice transmit bits to Bob can be nowadays of the order of 2 GHz, maintaining the QBER below 10% [37–39]. Nevertheless,

due to the random polarization rotations of the photons inside the fiber the transmission distance were kept below the 10 km. In order to overcome that difficulty, two active polarization control schemes were proposed using in both cases a feedback polarization control scheme based on EPCs: (1) a time domain multiplexing (TDM) technique; (2) a wavelength-division multiplexing (WDM) compensation method. In the TDM technique the quantum communication between Alice and Bob is interrupted in order to Alice sent to Bob two nonorthogonal reference signals for polarization control and analysis. The optical intensity of the reference pulses will gave to Bob the variation of the state of polarization (SOP) imposed by the optical fiber. With that information Bob can compensate that transformations using an EPC. Using the TDM compensation scheme it was possible implement the BB84 protocol over distances of 75 km [40]. In the WDM compensation method, besides the quantum channel, it is sent to the optical fiber two wavelength distinct nonorthogonal reference signals [41]. The remain procedure is the same that used for TDM. Although the WDM method avoids interruption of the quantum communication system, which allow a high generation rate of the quantum key, the polarization correlation between the quantum and classical signals at different wavelengths is lost after few kilometers [33]. Nevertheless, with this two polarization control schemes it is possible to implement polarization based QKD systems within a long-term operation. Recently, in [42] was described a different approach to compensate the random polarization rotations in the fiber. In that work, the measured QBER value is used to adjust the EPC at optical fiber output. In this case, no reference optical signals are needed since this method applies a feedback software based control scheme [42].

1.2.3 Phase Encoding QKD Scheme

In this scheme, Alice and Bob sides are composed by two an unbalanced interferometers, and they apply different phase shifts between the two arms of the interferometer. The use of unbalanced interferometer by Alice allows to encode the quantum key in the phase of single photons [13]. When photons choose the combination short path in Alice side and long arm on Bob interferometer (or vice versa) the photons will produce interference, and then Alice and Bob can exchange the key using the phase of the photons. Alice can apply one of four phase shifts in its interferometer 0, $\pi/2$, π, $3\pi/2$. Bob performs the basis choice by randomly applying a phase shift of 0 or $\pi/2$. When the phase difference is 0 or π, Alice and Bob have used compatible basis, and they obtain deterministic results. When the phase difference is $\pi/2$ or $3\pi/2$ the basis are incompatible and the photon in the Bob side randomly chooses one of the two coupler ports [13].

The first systems based on phase encoding were proposed in [43, 44]. Both prototypes were implement over 10 km of optical fiber. Subsequent studies extend the distance over which it is possible to distribute quantum keys. In [45] a distance of 30 km was reported with a QBER smaller than 4% [45]. Nevertheless, due to thermal drifts the unbalanced interferometers at Alice and Bob sides tend to misaligned every few seconds [45]. However, in [46] was presented a QKD system using phase encoding photons over 23 km of installed optical fiber with an interferometer that does not need alignment or polarization control. In that work [46], authors used an interferometric system with Faraday mirrors. With that, the phase coding setup at Alice side does not need alignment of the interferometer. A QKD system that does not need any adjustment in the interferometers used by Alice and Bob is known as "plug & play" [47]. The "plug & play" configuration was described in [47]. An improved version of the QKD system in [47], where the reflections on the interferometer were removed was described in [48]. Both prototypes [47, 48] were tested over 23 km of optical fiber. After, the phase encoding QKD system was tested in a WDM scenario where the quantum signal shares the same fiber with classical data signals [49]. In that work, a 1300 nm quantum signal was added to a classical data optical signal at 1550 nm over 28 km of optical fiber. Results showed no significant degradation on the QBER of the quantum signal [49]. Nevertheless, the minimum value of the loss in standard single mode fibers (SSMFs) is in the third telecom window around 1550 nm, and this translates into a possible of 50% increase in transmission distance of the QKD system, when compared with the 1300 nm window [25, 50]. In [50] it was reported the implementation of an interferometric quantum cryptographic system for a transmission distance up to 40 km, with a QBER of the order of 9%. After, in this new telecom window for QKD, a distance exceeding 100 km was reported in [51]. This achievement required a careful optimization of the interferometers and the single photon detector module (SPDM) [51]. Nowadays, distances longer than 200 km were already achieved [52, 53].

A real world experiment was performed in [54] over 67 km of installed optical fiber between two Swiss cities, Geneva and Lausanne, using the 1550 nm telecom window. In that work, authors develop a QKD prototype that fits into two 19 inch boxes (48.3 cm), one for Alice and one for Bob. The QBER measured in that work was about 6% [54]. More recently, the coexistence between quantum and classical signals all at 1550 telecom window was studied [55, 56]. Although the fiber nonlinear impairments tends to degrade the QBER of the quantum system, mainly for long transmission lengths, results have shown that even for fiber lengths of 90 km it is possible to obtain a QBER smaller than 8% [55]. This can allow to bring the QKD system to the classical optical network, instead of the need for a dedicated dark optical fiber exclusively

reserved for the quantum channel [56].

1.2.4 Entanglement Based QKD

Motivated by the work performed by A. Ekert [16], three research groups independently demonstrated quantum cryptography with entangled photons [57–59]. For implementations of QKD systems with entangled photon-pairs the information can be encoded in one the of degrees of freedom of the pairs such that polarization [57, 58], energy and time [59], orbital angular momentum [60], or time-bin entanglement which is a special case of energy-time entanglement [61].

The first implementations of cryptographic systems with entangled photons were reported in [57–59]. In these works, the entangled photon pairs were obtained through the SPDC process in a nonlinear crystal, where both photons of the pair have the same frequency. In [57] the photons were distributed over 500 m of optical fiber with Alice and Bob are separated by 360 m. The quantum cryptography system was based on the polarization of the photon pairs [57]. In [58], the cryptographic system was implemented over a short free space link, and Alice and Bob were separated by few meters. In that work [58], authors also use polarization entangled photon pairs from SPDC in order to encode the quantum key, and they continuous cheeked the presence of an eavesdropper by measuring Bell's inequalities. Finally, in [59] was reported a quantum cryptography system based on energy-time entangled photon pairs, in a back-to-back configuration. In that configuration the QBER measure was smaller than 4%. Moreover, introducing a 6 dB of loss, equivalent approximately to 20 km of optical fiber, the QBER increased only 1% [59]. Immediately after, a detailed analysis of quantum key distribution employing energy-time entangled states was reported in [62]. The quantum key was distributed over 8.5 km of optical fiber with a QBER of the order of 8.6%. After these first experimental demonstrations, it was presented a complete QKD system using energy-time entangled photon pairs over a 30 km of SSMF [63]. The obtained QBER was smaller than 11%. In [64] was tested the fidelity of a QKD system based on polarization entangled photon-pairs in a WDM link. The quantum signals and the synchronization classical signal gating the single photon detector were multiplexed in the same optical fiber with 27 km of length [64]. Moreover, in [65] was demonstrated the possibility of distributing entangled photon-pairs over 100 km of fiber length. Recently, was reported an entanglement-based QKD experiment over 100 km of optical fiber [66]. In that work, authors measure a QBER of 9.1% with a key rate of 0.15 bit/s. Nowadays, the distance over which the entangled photon-pairs can be distributed is higher than 200 km [67, 68].

In 2004, was performed a pioneer experience using polarization entangled photon-pairs [69].

In that work, they implement a QKD system based on photon-pairs in a real world scenario. In Vienna, a secret key was distributed over 1.45 km long installed fiber, between a bank and the City Hall.

1.2.5 Continuous Variables QKD Systems

Most of the QKD protocols encode the key information in one of the degrees of freedom of individual photons. In that sense, the quantum information used in that protocols is discrete, i.e. described by qubits [13]. Recently, an alternative approach to discrete QKD has been suggested, which is based on continuous variables (CVs) [70]. An example of continuous variables (CVs) is the quantized harmonic oscillator (position and momentum), or the different degrees of freedom of the electromagnetic field, such as phase and amplitude [71, 72]. This new approach to QKD has been suggested in order to replace the single photon detectors (with low quantum efficiency) with standard telecom detectors, which are faster and more efficient [73, 74]. Moreover, continuous variable quantum key distribution (CVQKD) protocols can be implemented with weak coherent light fields, which are easy to generate and to practically implement [21]. CVQKD protocols can encode the key information on both quadratures or in the Stokes parameters of a light pulse. Nevertheless, CVQKD protocols demands homodyne or heterodyne detection schemes instead of direct detection used in most of discrete QKD systems [13, 71]. In CVQKD systems the security of the key generation process is ensured by the non-cloning theorem and the Heisenberg uncertain principle [71, 74]. Due to that, it isn't possible to measure simultaneous the exact value of both quadratures or a pair of Stokes parameters of a light field, since they are non-orthogonal states, so their commutator is a non-zero value [72, 75]. In that case, an eavesdropper can't determine the prepared non-orthogonal state. When compared with the discrete QKD scheme, detecting different quadratures or Stokes parameters in CVQKD corresponds to measuring single photon states in two distinct non-orthogonal basis [13, 72, 73]

The first CVQKD protocols were proposed by Ralph [70], Reid [76], and Hillery [77]. Those protocols were based on discrete modulation of Gaussian states, since a CV encodes a discrete key [78]. In [70] was considered two variations of this protocol: (1) an implementation with a bright coherent state; (2) an entanglement based scheme. In [76] and [77] authors focus on the use of squeezed states rather than in coherent states. Subsequent studies were enable to present a continuous Gaussian modulation based protocol [78]. In that protocol both the key and the carrier are continuous. In 2002, Grosshans and Grangier [21] proposed a protocol based on Gaussian modulated coherent states. The security of the protocol is based on the fact that coherent states

are non-orthogonal. Since coherent states are much simply to generate in comparison with entangled states, the protocol proposed in [21] opened the door to experimental implementation of CVQKD systems based on coherent states, in both laboratory and real field tests.

Recently, the coherent state protocol [21] was implemented experimentally using homodyne detection and reverse reconciliation [79]. This protocol starts with Alice generating random two-dimensional Gaussian distribution with variance V_A. After, Alice send to Bob the coherent state, and he chooses randomly the quadrature to be measured with a homodyne detector. Later, Bob informs Alice (over a public channel) about which quadrature he perform the measurement. After repeat these steps many times, both Alice and Bob share two correlated Gaussian variables, that they can use to obtain a key. In this practical implementation [79] was used reverse reconciliation instead of direct due to the fact that, reverse reconciliation allows to both users Alice and Bob distribute security keys beyond the 3 dB channel loss limit of the direct reconciliation protocol [79, 80]. Subsequent studies demonstrated the feasibility of CVQKD over optical fibers [81–85]. Moreover, it was already presented a prototype that implement a CVQKD system over optical fibers [86]. That prototype was tested in the network developed by SECOQC [86, 87]. Recently, was implemented a point-to-point communication link between the cities of Massy and Palaiseau, France [88]. The quantum keys were generated through the implementation of a CVQKD system, and was operational during six months over a fiber link of 17.7 km. The quantum keys were used to refresh a classical symmetric encryption system. A different strategy to beating the 3 dB loss limit of the quantum channel was proposed in [89]. In the post-processing stage of the CVQKD system, instead of using reverse reconciliation authors proposed the use of post-selection protocol [90]. Using this post-selection protocol, it was implemented a CVQKD system using the Stokes parameters as encoding variables [75]. This avoids the use of a local oscillator to perform homodyne detection [75]. Recently, was reported the implementation of a CVQKD system over 80 km of optical fiber [91].

The fact that Bob uses homodyne detection in all of the previous protocols, implies that half of the data generated by Alice is discarded. In order to overcome that drawback was proposed a protocol, known as non-switching protocol, that uses heterodyne detection instead of homodyne [92]. In that case, Bob measures the two conjugate bases simultaneously. This provides higher secret key rates and bandwidths compared with protocols based on homodyne detection schemes [92]. The non-switching protocol was implemented in [93], using post-selection strategy for key distillation. Nevertheless, since heterodyne detection typically uses a beam splitter at detection stage, the simultaneously quadrature measurements are more noisier than the single

result of the homodyne strategy.

1.3 Thesis Objectives and Outline

This thesis is intended to provide a comprehensive study of the physical layer of a QKD system. In that context, the main goal of this thesis is to study the generation and transmission of single and entangled photons in optical fibers for QKD applications. As such, the work was carried out targeting the following objectives:

1. Study of new processes that can lead to the development of novel few-photon sources for QKD applications. We also intend to develop new theoretical models capable of describe the generation rate of photons. Finally, we intend to access to the photon number distribution of the photon source.

2. Study the robustness of a quantum channel in a multi-wavelength lightwave system. We intend to access the robustness of the quantum channel in a real world scenario, where the quantum channel share the optical fiber with others classical signals. With this study we expect to contribute for the insertion of the quantum channels in the optical networks that are implemented nowadays, employing only C-band WDM technology.

3. Quantify the limitations on the propagation and generation of quantum correlated photon-pairs in optical fibers. We intend to develop a theoretical model that will describe the impact of fiber loss on the propagation of single photons in optical fibers. We also intend to study the role of absorption on the generation of entangled photon-pairs. With this work we expect to find solutions that overcomes the limitations imposed by the fiber absorption coefficient.

The thesis is divided into nine Chapters, organized as follows:

- Chapter 2 provides a mathematical derivation of the general formalism used throughout this thesis. The classical and quantum version of the generalized nonlinear Schrödinger equation (GNLSE) is presented. The two formalisms are used to describe the propagation of optical fields inside a $\chi^{(3)}$ optical waveguide.

- Chapter 3 considers the generation of few-photons through the stimulated FWM process in optical fibers, with the focus on the role of the nonlinear contribution to the phase matching condition, and the polarization effects. The photon source is modeled theoretically, and is

experimentally validated through the implementation of the stimulated FWM process in a low power regime inside a dispersion-shifted fiber (DSF). The average number of photons per pulse generated inside the DSF is measured using an avalanche photo-detector.

- Chapter 4 analyses the impact of the stimulated Raman scattering (SRS) on classical process of FWM in high birefringent (HiBi) optical fibers. The influence of the SRS on FWM is analyzed considering the single- and dual-pump configurations, for several different pump polarization schemes. After, the theoretical model for the dual-pump configuration is extended in order to consider the generation of two idler waves inside a HiBi optical fiber through three FWM processes.

- Chapter 5 deals with photon statistics of the few-photon source based on the classical process of FWM. The statistics of the source is quantified using the second-order coherence function. After obtaining a theoretical model for the source statistics, are presented results considering two case: (1) the idler wave is fully generated inside the fiber; (2) there exist a low power optical field at fiber input, and idler photons are generated at that field. The theoretical model is validated experimentally using avalanche photo-detectors assisted by the maximum-likelihood estimation method and the expectation-maximization algorithm.

- Chapter 6 analyses the spontaneous FWM process as a heralded single photon source. After modeling the spontaneous FWM in optical fibers, the quality of the source is studied using the conditional second-order coherence function. Two scenarios are analyzed: (1) a back-to-back configuration; (2) there exist a SSMF between the heralded single photon source and the detection stage.

- Chapter 7 considers the generation of quantum-correlated photon pairs through spontaneous FWM in $\chi^{(3)}$ waveguides, with non-negligible loss parameter. The impact of linear loss on the generation of signal and idler photon pairs is analyzed in terms of the Cauchy-Schwarz inequality, and in terms of the Clauser, Horne, Shimony, and Holt (CHSH) inequality.

- Chapter 8 considers the generation of polarization entangled photon pairs through spontaneous FWM in $\chi^{(3)}$ waveguides, with high nonlinear coefficient and non-negligible loss parameter. The trade-off between waveguide losses and nonlinearities is analyzed in terms of the CHSH inequality.

- Chapter 9 summarizes the main results obtained in this thesis, and presents suggestions for future work.

Besides that nine Chapters, this thesis also comprises a List of Acronyms, a List of Figures, and a List of Tables. A global List of Symbols is not included due to the large number of symbols present in the thesis. The symbols used in the equations are defined in each Chapter.

1.4 Main Contributions

In the author opinion, the main achievements reported in this thesis are the following:

- Proposal of a new few-photon source based on the classical process of FWM. The source was implemented experimentally [94, 95], and theoretically modeled considering linear and nonlinear processes that occur simultaneously with the FWM inside the fiber [96, 97]. The photon source was used to transmit polarization encoded photons through a 20 km of SSMF [98, 99]. After the transmission we decode correctly the information at receiver stage using two single photon detector modules (SPDMs) [98, 99]. We describe the photon statistics of the single photon source [100–102], and we model the impact of the FWM process in a co-propagating quantum channel [100, 102].

- Detailed characterization of a heralded single photon source based on the spontaneous FWM process. We analyze the statistics of the source in terms of the conditional second-order coherence function. We identify regimes for the pump power and frequency that minimizes the conditional second-order coherence function, which allow us to obtain an almost perfect single photon source [103]. Moreover, we consider the presence of noise photons from the Raman scattering process and from a room temperature absorption reservoir [103].

- Modeling the impact of the fiber absorption and nonlinearities on the generation of quantum correlated photon pairs in optical fibers [104, 105]. It is shown that a strong violation of the CHSH inequality happens for moderate values of nonlinear fiber parameter and for high values of loss coefficient. This result can help to guide the implementation of on-chip quantum technologies. We use the spontaneous FWM process and implement a source of polarization entangled photon pairs. We test the CHSH parameter in optical fibers, and we observe a violation of the CHSH inequality for a fiber with length 150 m and a nonlinear parameter of 10 $\mathrm{W}^{-1}\mathrm{km}^{-1}$ [106, 107].

1.5 List of Publications

1.5.1 Journal Articles

- **N. A. Silva**, and A. N. Pinto, "Comprehensive characterization of a heralded single photon source based on four-wave mixing in optical fibers," 2013, submitted to: *Optics Communications, Special Issue on Nonlinear Quantum Photonics*.

- A. N. Pinto, **N. A. Silva**, Á. J. Almeida, and N. J. Muga, "Using quantum technologies to improve fiber-optic communication systems," *IEEE Communications Magazine*, vol. 51, pp. 42-48 , 2013.

- **N. A. Silva**, and A. N. Pinto, "Effects of losses and nonlinearities on the generation of polarization entangled photons," *IEEE/OSA Journal of Lightwave Technology*, vol. 31, pp. 1309-1317, 2013.

- **N. A. Silva**, and A. N. Pinto, "Role of absorption on the generation of quantum-correlated photon pairs through FWM," *IEEE Journal of Quantum Electronics*, vol. 48, pp. 1380-1388, 2012.

- Á. J. Almeida, **N. A. Silva**, P. S. André, and A. N. Pinto, "Four-wave mixing: Photon statistics and the impact on a co-propagating quantum signal," *Optics Communications*, vol. 285, pp. 2956-2960, 2012.

- **N. A. Silva**, Á. J. Almeida, and A. N. Pinto, "Interference in a quantum channel due to classical four-wave mixing in optical fibers," *IEEE Journal of Quantum Electronics*, vol. 48, pp. 472-479, 2012.

- **N. A. Silva**, N. J. Muga, and A. N. Pinto, "Evolution of first-order sidebands from multiple FWM processes in HiBi optical fibers," *Optics Communications*, vol. 284, pp. 3408-3415, 2011.

- N. J. Muga, **N. A. Silva**, M. F. Ferreira, and A. N. Pinto, "Evolution of the degree of copolarization in high-birefringence fibers," *Optics Communications*, vol. 283, pp. 2125-2132, 2010.

- **N. A. Silva**, N. J. Muga, and A. N. Pinto, "Effective nonlinear parameter measurement using FWM in optical fibers in a low power regime," *IEEE Journal of Quantum Electronics*, vol. 46, pp. 285-291, 2010.

- **N. A. Silva**, N. J. Muga, and A. N. Pinto, "Influence of the stimulated Raman scattering on the four-wave mixing process in birefringent fibers," *IEEE/OSA Journal of Lightwave Technology*, vol. 27, pp. 4979-4988, 2009.

1.5.2 Conference Presentations

- **N. A. Silva**, and A. N. Pinto, "Photon-Pair Generation in Chalcogenide Glass: Role of Waveguide Linear Absorption," in *PHOTOPTICS 2014*, January 2014.

- **N. A. Silva**, and A. N. Pinto, "Characterization of a fiber based heralded single photon source at telecom wavelength," in *RIAO/OPTILAS 2013*, vol. 8785, July 2013, pp. 8785F0-1 - 8785F0-5.

- Á. J. Almeida, D. J. Macedo, **N. A. Silva**, N. J. Muga, P. André, and A. N. Pinto, "Quantum communication using polarization-encoded photons in optical fibers," in *Conf. on Telecommunications - ConfTele*, vol. 1, May 2013, pp. 205 - 208.

- Á. J. Almeida, **N. A. Silva**, P. André, and A. N. Pinto, "Four-wave mixing: Photon statistics and the impact on a co-propagating quantum signal," in *Conf. on Quantum Cryptography - QCRYPT*, vol. 1, September 2012, pp. 1 - 3.

- Á. J. Almeida, **N. A. Silva**, P. André, and A. N. Pinto, "Impact of FWM process on the statistics of a co-propagating quantum signal in a WDM lightwave system," in *International Conf. on Transparent Optical Networks - ICTON*, vol. 1, July 2012, pp. Tu.P.6-1 - Tu.P.6-4.

- Á. J. Almeida, **N. A. Silva**, P. André, and A. N. Pinto, "Experimental characterization of the photon statistics of four-wave mixing photon source," in *European Conf. on Networks and Optical Communications and Conf. on Optical Cabling and Infrastructure - NOC/OC*, vol. 1, June 2012, pp. 142 - 147.

- Á. J. Almeida, N. J. Muga, **N. A. Silva**, P. André, and A. N. Pinto, "Long-term time evolution measurements of polarization drift in optical fibers," in *Symp. on Enabling Optical Networks and Sensors - SEONS*, vol. 1, June 2012, pp. 1 - 4.

- A. N. Pinto, Á. J. Almeida, **N. A. Silva**, N. J. Muga, and L. M. Pinto, "Engineering quantum communication systems," in *SPIE Photonics Europe*, vol. 8440, April 2012, pp. 84400B-1 - 84400B-13.

- Á. J. Almeida, L. M. Pinto, **N. A. Silva**, N. J. Muga, and A. N. Pinto, "Correlated photon-pair generation in a highly nonlinear fiber using spontaneous FWM," in *Symp. on Enabling Optical Networks - SEON*, vol. 1, July 2011, pp. 1 - 4.

- A. N. Pinto, Á. J. Almeida, **N. A. Silva**, N. J. Muga, and L. M. Pinto, "Optical quantum communications: An experimental approach," in *International Conf. on Applications of Optics and Photonics - AOP2011*, vol. 8001, May 2011, pp. 80011M-1 - 80011M-8.

- Á. J. Almeida, **N. A. Silva**, N. J. Muga, and A. N. Pinto, "Single-photon source using stimulated FWM in optical fibers for quantum communication," in *International Conf. on Applications of Optics and Photonics - AOP2011*, vol. 8001, May 2011, pp. 80013W-1 - 80013W-7.

- Á. J. Almeida, S. R. Carneiro, **N. A. Silva**, N. J. Muga, and A. N. Pinto, "Polarization-entangled photon pairs using spontaneous four-wave mixing in a fiber loop," in *EUROCON and CONFTELE*, vol. 1, April 2011, pp. 1 - 4.

- **N. A. Silva**, Á. J. Almeida, and A. N. Pinto, "Statistical characterization of a single-photon source based on stimulated FWM in optical fibers," in *Conf. on Telecommunications - ConfTele*, vol. 1, April 2011, pp. 1 - 4.

- Á. J. Almeida, **N. A. Silva**, N. J. Muga, and A. N. Pinto, "Fiber-optical communication system using polarization-encoding photons," in *European Conf. on Networks and Optical Communications and Conf. on Optical Cabling and Infrastructure - NOC/OC*, vol. 1, June 2010, pp. 127 - 132.

- N. J. Muga, **N. A. Silva**, M. Ferreira, and A. N. Pinto, "Generalized analysis of the polarization evolution in high-birefringence fibers," in *International Conf. on Transparent Networks ICTON*, vol. 1, June 2010, pp. MoP2.

- **N. A. Silva**, N. J. Muga, and A. N. Pinto, "Measurement of the effective nonlinear parameter using FWM in random polarization optical fibers," in *European Conf. on Networks and Optical Communications - NOC*, vol. 1, June 2010, pp. 185 - 190.

- N. J. Muga, **N. A. Silva**, M. Ferreira, and A. N. Pinto, "Relative state-of-polarization in high-birefringence fibers," in *European Conf. on Networks and Optical Communications - NOC*, vol. 1, June 2010, pp. 121 - 126.

- Á. J. Almeida, S. R. Carneiro, **N. A. Silva**, N. J. Muga, and A. N. Pinto, "Time coincidence of entangled photon pairs using spontaneous four-wave mixing in a fiber loop," in *Symp. on Enabling Optical Networks - SEON*, vol. 1, June 2010, pp. 1 - 2.

References

[1] A. V. Sergienko, *Quantum Communications and Cryptography*. Florida,USA: Crc Press, 2006.

[2] C. E. Shannon, "Communication theory of secrecy systems," *Bell Systems Technical Journal*, vol. 28, pp. 656–715, 1949.

[3] R. Rivest, A. Shamir, and L. Adleman, "A method for obtaining digital signatures and public-key cryptosystems," *Communications of the ACM*, vol. 21, pp. 120–126, 1978.

[4] "RSA laboratories," http://www.rsa.com/rsalabs/node.asp?id=2098.

[5] "RSA laboratories," http://www.rsa.com/rsalabs/node.asp?id=3723.

[6] B. Kaliski, "RSA Laboratories, TWIRL and RSA Key Size," http://www.rsa.com/rsalabs/node.asp?id=2004.

[7] D. Elkouss, J. Martinez-Mateo, A. Ciurana, and V. Martin, "Secure optical networks based on quantum key distribution and weakly trusted repeaters," *J. Opt. Commun. Netw.*, vol. 5, pp. 316–328, 2013.

[8] E. Barker, W. Barker, W. Burr, W. Polk, and M. Smid, "Recommendation for key management - part 1: General (revised)," NIST Special Publication, 2006.

[9] S. Wiesner, "Conjugate coding," *SIGACT News*, vol. 15, pp. 78–88, 1983.

[10] C. H. Bennett and G. Brassard, *Quantum cryptography: Public key distribution and coin tossing*. Bangalore, India, Dec. 1984: IEEE, 1984, vol. 175, pp. 175–179.

[11] C. H. Bennett and G. Brassard, "The dawn of a new era for quantum cryptography: the experimental prototype is working!" *SIGACT News*, vol. 20, pp. 78–80, 1989.

[12] C. H. Bennett, F. Bessette, G. Brassard, L. Salvail, and J. A. Smolin, "Experimental quantum cryptography," *J. Cryptology*, vol. 5, pp. 3–28, 1992.

[13] N. Gisin, G. Ribordy, W. Tittel, and H. Zbinden, "Quantum cryptography," *Rev. Mod. Phys.*, vol. 74, pp. 145–195, 2002.

[14] C. H. Bennett, "Quantum cryptography using any two nonorthogonal states," *Phys. Rev. Lett.*, vol. 68, pp. 3121–3124, 1992.

[15] D. Bruß, "Optimal eavesdropping in quantum cryptography with six states," *Phys. Rev. Lett.*, vol. 81, pp. 3018–3021, 1998.

[16] A. K. Ekert, "Quantum cryptography based on Bell's theorem," *Phys. Rev. Lett.*, vol. 67, pp. 661–663, 1991.

[17] Z.-S. Yuan, X.-H. Bao, C.-Y. Lu, J. Zhang, C.-Z. Peng, and J.-W. Pan, "Entangled photons and quantum communication," *Physics Reports*, vol. 497, pp. 1 – 40, 2010.

[18] C. H. Bennett, G. Brassard, and N. D. Mermin, "Quantum cryptography without Bell's theorem," *Phys. Rev. Lett.*, vol. 68, pp. 557–559, 1992.

[19] M. D. Eisaman, J. Fan, A. Migdall, and S. V. Polyakov, "Invited review article: Single-photon sources and detectors," *Review of Scientific Instruments*, vol. 82, p. 071101, 2011.

[20] S. A. Castelletto and R. E. Scholten, "Heralded single photon sources: a route towards quantum communication technology and photon standards," *The European Physical Journal Applied Physics*, vol. 41, pp. 181–194, 2008.

[21] F. Grosshans and P. Grangier, "Continuous variable quantum cryptography using coherent states," *Phys. Rev. Lett.*, vol. 88, p. 057902, 2002.

[22] K. Edamatsu, "Entangled photons: Generation, observation, and characterization," *Japanese Journal of Applied Physics*, vol. 46, pp. 7175–7187, 2007.

[23] D. C. Burnham and D. L. Weinberg, "Observation of simultaneity in parametric production of optical photon pairs," *Phys. Rev. Lett.*, vol. 25, pp. 84–87, 1970.

[24] M. Fiorentino, P. Voss, J. Sharping, and P. Kumar, "All-fiber photon-pair source for quantum communications," *IEEE Photonics Technology Letters*, vol. 14, pp. 983–985, 2002.

[25] G. Agrawal, *Nonlinear Fiber Optics*, 3rd ed. Academic Press, 2001.

[26] S. Cova, M. Ghioni, A. Lotito, I. Rech, and F. Zappa, "Evolution and prospects for single-photon avalanche diodes and quenching circuits," *Journal of Modern Optics*, vol. 51, pp. 1267–1288, 2004.

[27] B. E. Kardynal, Z. L. Yuan, and A. J. Shields, "An avalanche-photodiode-based photon-number-resolving detector," *Nature Photonics*, vol. 2, pp. 425–428, Jun. 2008.

[28] O. Thomas, Z. L. Yuan, and A. J. Shields, "Practical photon number detection with electric field-modulated silicon avalanche photodiodes," *Nature Communications*, vol. 3, p. 644, Jan. 2012.

[29] H. Zbinden, H. Bechmann-Pasquinucci, N. Gisin, and G. Ribordy, "Quantum cryptography," *Applied Physics B: Lasers and Optics*, vol. 67, pp. 743–748, 1998.

[30] J. Breguet, A. Muller, and N. Gisin, "Quantum cryptography with polarized photons in optical fibres – Experiment and practical limits," *Journal of Modern Optics*, vol. 41, pp. 2405–2414, 1994.

[31] J. Gordon and H. Kogelnik, "PMD fundamentals: polarization mode dispersion in optical fibers." *PNAS*, vol. 97, pp. 4541–50, 2000.

[32] N. J. Muga, A. N. Pinto, M. F. S. Ferreira, and J. R. F. da Rocha, "Uniform polarization scattering with fiber-coil-based polarization controllers," *IEEE/OSA Journal of Lightwave Technology*, vol. 24, pp. 3932–3943, 2006.

[33] N. J. Muga, M. F. S. Ferreira, and A. N. Pinto, "QBER estimation in QKD systems with polarization encoding," *IEEE/OSA Journal of Lightwave Technology*, vol. 29, pp. 355–361, 2011.

[34] A. Muller, J. Breguet, and N. Gisin, "Experimental demonstration of quantum cryptography using polarized photons in optical fibre over more than 1 km," *EPL (Europhysics Letters)*, vol. 23, p. 383, 1993.

[35] A. Muller, H. Zbinden, and N. Gisin, "Quantum cryptography over 23 km in installed under-lake telecom fibre," *EPL (Europhysics Letters)*, vol. 33, p. 335, 1996.

[36] P. Townsend, "Experimental investigation of the performance limits for first telecommunications-window quantum cryptography systems," *IEEE Photonics Technology Letters*, vol. 10, pp. 1048 –1050, 1998.

[37] X. Tang, L. Ma, A. Mink, A. Nakassis, H. Xu, B. Hershman, J. C. Bienfang, D. Su, R. F. Boisvert, C. W. Clark, and C. J. Williams, "Experimental study of high speed polarization-coding quantum key distribution with sifted-key rates over Mbit/s," *Opt. Express*, vol. 14, pp. 2062–2070, 2006.

[38] K. Gordon, V. Fernandez, P. Townsend, and G. Buller, "A short wavelength gigahertz clocked fiber-optic quantum key distribution system," *IEEE Journal of Quantum Electronics*, vol. 40, pp. 900 – 908, 2004.

[39] K. Gordon, V. Fernandez, G. Buller, I. Rech, S. Cova, and P. Townsend, "Quantum key distribution system clocked at 2 GHz," *Opt. Express*, vol. 13, pp. 3015–3020, 2005.

[40] J. Chen, G. Wu, Y. Li, E. Wu, and H. Zeng, "Active polarization stabilization in optical fibers suitable for quantum keydistribution," *Opt. Express*, vol. 15, pp. 17 928–17 936, 2007.

[41] G. V. de Faria, J. Ferreira, G. Xavier, G. Temporao, and J. von der Weid, "Polarisation control schemes for fibre-optics quantum communications using polarisation encoding," *Electronics Letters*, vol. 44, pp. 228–229, 2008.

[42] Á. J. Almeida, N. J. Muga, N. A. Silva, J. M. Prata, P. S. André, and A. N. Pinto, "QBER-based control of polarization rotation in quantum communications," 2013, to be submitted to: IEEE/OSA Journal of Lightwave Technology.

[43] P. Townsend, J. Rarity, and P. Tapster, "Enhanced single photon fringe visibility in a 10 km-long prototype quantum cryptography channel," *Electronics Letters*, vol. 29, pp. 1291 –1293, 1993.

[44] P. Townsend, J. Rarity, and P. Tapster, "Single photon interference in 10 km long optical fibre interferometer," *Electronics Letters*, vol. 29, pp. 634–635, 1993.

[45] C. Marand and P. D. Townsend, "Quantum key distribution over distances as long as 30 km," *Opt. Lett.*, vol. 20, pp. 1695–1697, 1995.

[46] H. Zbinden, J. Gautier, N. Gisin, B. Huttner, A. Muller, and W. Tittel, "Interferometry with faraday mirrors for quantum cryptography," *Electronics Letters*, vol. 33, pp. 586 –588, 1997.

[47] A. Muller, T. Herzog, B. Huttner, W. Tittel, H. Zbinden, and N. Gisin, "Plug and play systems for quantum cryptography," *Applied Physics Letters*, vol. 70, pp. 793–795, 1997.

[48] G. Ribordy, J.-D. Gautier, N. Gisin, O. Guinnard, and H. Zbinden, "Automated plug and play quantum key distribution," *Electronics Letters*, vol. 34, pp. 2116 –2117, 1998.

[49] P. Townsend, "Simultaneous quantum cryptographic key distribution and conventional data transmission over installed fibre using wavelength-division multiplexing," *Electronics Letters*, vol. 33, pp. 188 –190, 1997.

[50] M. Bourennane, F. Gibson, A. Karlsson, A. Hening, P. Jonsson, T. Tsegaye, D. Ljunggren, and E. Sundberg, "Experiments on long wavelength (1550 nm) plug and play quantum cryptography systems," *Opt. Express*, vol. 4, pp. 383–387, 1999.

[51] C. Gobby, Z. L. Yuan, and A. J. Shields, "Quantum key distribution over 122 km of standard telecom fiber," *Applied Physics Letters*, vol. 84, pp. 3762–3764, 2004.

[52] D. Stucki, N. Walenta, F. Vannel, R. T. Thew, N. Gisin, H. Zbinden, S. Gray, C. R. Towery, and S. Ten, "High rate, long-distance quantum key distribution over 250 km of ultra low loss fibres," *New Journal of Physics*, vol. 11, p. 075003, 2009.

[53] S. Wang, W. Chen, J.-F. Guo, Z.-Q. Yin, H.-W. Li, Z. Zhou, G.-C. Guo, and Z.-F. Han, "2 GHz clock quantum key distribution over 260 km of standard telecom fiber," *Opt. Lett.*, vol. 37, pp. 1008–1010, 2012.

[54] D. Stucki, N. Gisin, O. Guinnard, G. Ribordy, and H. Zbinden, "Quantum key distribution over 67 km with a plug & play system," *New Journal of Physics*, vol. 4, p. 41, 2002.

[55] K. A. Patel, J. F. Dynes, I. Choi, A. W. Sharpe, A. R. Dixon, Z. L. Yuan, R. V. Penty, and A. J. Shields, "Coexistence of high-bit-rate quantum key distribution and data on optical fiber," *Phys. Rev. X*, vol. 2, p. 041010, 2012.

[56] P. Eraerds, N. Walenta, M. Legré, N. Gisin, and H. Zbinden, "Quantum key distribution and 1 Gbps data encryption over a single fibre," *New Journal of Physics*, vol. 12, p. 063027, 2010.

[57] T. Jennewein, C. Simon, G. Weihs, H. Weinfurter, and A. Zeilinger, "Quantum cryptography with entangled photons," *Phys. Rev. Lett.*, vol. 84, pp. 4729–4732, 2000.

[58] D. S. Naik, C. G. Peterson, A. G. White, A. J. Berglund, and P. G. Kwiat, "Entangled state quantum cryptography: Eavesdropping on the Ekert protocol," *Phys. Rev. Lett.*, vol. 84, pp. 4733–4736, 2000.

[59] W. Tittel, J. Brendel, H. Zbinden, and N. Gisin, "Quantum cryptography using entangled photons in energy-time Bell states," *Phys. Rev. Lett.*, vol. 84, pp. 4737–4740, 2000.

[60] A. Mair, A. Vaziri, G. Weihs, and A. Zeilinger, "Entanglement of orbital angular momentum states of photons," *NATURE*, vol. 412, p. 3123, 2001.

[61] I. Marcikic, H. de Riedmatten, W. Tittel, V. Scarani, H. Zbinden, and N. Gisin, "Time-bin entangled qubits for quantum communication created by femtosecond pulses," *Phys. Rev. A*, vol. 66, p. 062308, 2002.

[62] G. Ribordy, J. Brendel, J.-D. Gautier, N. Gisin, and H. Zbinden, "Long-distance entanglement-based quantum key distribution," *Phys. Rev. A*, vol. 63, p. 012309, 2000.

[63] S. Fasel, N. Gisin, G. Ribordy, and H. Zbinden, "Quantum key distribution over 30 km of standard fiber using energy-time entangled photon pairs: a comparison of two chromatic dispersion reduction methods," *The European Physical Journal D - Atomic, Molecular, Optical and Plasma Physics*, vol. 30, pp. 143–148, 2004.

[64] S. Sauge, M. Swillo, S. Albert-Seifried, G. B. Xavier, J. Waldebäck, M. Tengner, D. Ljunggren, and A. Karlsson, "Narrowband polarization-entangled photon pairs distributed over a WDM link for qubit networks," *Opt. Express*, vol. 15, pp. 6926–6933, 2007.

[65] H. Hübel, M. R. Vanner, T. Lederer, B. Blauensteiner, T. Lorünser, A. Poppe, and A. Zeilinger, "High-fidelity transmission of polarization encoded qubits from an entangled source over 100 km of fiber," *Opt. Express*, vol. 15, pp. 7853–7862, 2007.

[66] H. Takesue, K. ichi Harada, K. Tamaki, H. Fukuda, T. Tsuchizawa, T. Watanabe, K. Yamada, and S. ichi Itabashi, "Long-distance entanglement-based quantum key distribution experiment using practical detectors," *Opt. Express*, vol. 18, pp. 16 777–16 787, 2010.

[67] J. F. Dynes, H. Takesue, Z. L. Yuan, A. W. Sharpe, K. Harada, T. Honjo, H. Kamada, O. Tadanaga, Y. Nishida, M. Asobe, and A. J. Shields, "Efficient entanglement distribution over 200 kilometers," *Opt. Express*, vol. 17, pp. 11 440–11 449, 2009.

[68] T. Inagaki, N. Matsuda, O. Tadanaga, M. Asobe, and H. Takesue, "Entanglement distribution over 300 km of fiber," *Opt. Express*, vol. 21, pp. 23 241–23 249, 2013.

[69] A. Poppe, A. Fedrizzi, R. Ursin, H. Böhm, T. Lörunser, O. Maurhardt, M. Peev, M. Suda, C. Kurtsiefer, H. Weinfurter, T. Jennewein, and A. Zeilinger, "Practical quantum key distribution with polarization entangled photons," *Opt. Express*, vol. 12, pp. 3865–3871, 2004.

[70] T. C. Ralph, "Continuous variable quantum cryptography," *Phys. Rev. A*, vol. 61, p. 010303, 1999.

[71] C. Weedbrook, S. Pirandola, R. García-Patrón, N. J. Cerf, T. C. Ralph, J. H. Shapiro, and S. Lloyd, "Gaussian quantum information," *Rev. Mod. Phys.*, vol. 84, pp. 621–669, 2012.

[72] S. L. Braunstein and P. van Loock, "Quantum information with continuous variables," *Rev. Mod. Phys.*, vol. 77, pp. 513–577, 2005.

[73] U. Andersen, G. Leuchs, and C. Silberhorn, "Continuous-variable quantum information processing," *Laser & Photonics Reviews*, vol. 4, pp. 337–354, 2010.

[74] V. Scarani, H. Bechmann-Pasquinucci, N. J. Cerf, M. Dušek, N. Lütkenhaus, and M. Peev, "The security of practical quantum key distribution," *Rev. Mod. Phys.*, vol. 81, pp. 1301–1350, 2009.

[75] S. Lorenz, N. Korolkova, and G. Leuchs, "Continuous-variable quantum key distribution using polarization encoding and post selection," *Applied Physics B*, vol. 79, pp. 273–277, 2004.

[76] M. D. Reid, "Quantum cryptography with a predetermined key, using continuous-variable Einstein-Podolsky-Rosen correlations," *Phys. Rev. A*, vol. 62, p. 062308, 2000.

[77] M. Hillery, "Quantum cryptography with squeezed states," *Phys. Rev. A*, vol. 61, p. 022309, 2000.

[78] N. J. Cerf, M. Lévy, and G. V. Assche, "Quantum distribution of gaussian keys using squeezed states," *Phys. Rev. A*, vol. 63, p. 052311, 2001.

[79] F. Grosshans, G. Van Assche, J. Wenger, R. Brouri, N. J. Cerf, and P. Grangier, "Quantum key distribution using gaussian-modulated coherent states," *Nature*, vol. 421, pp. 238–241, 2003.

[80] F. Grosshans and P. Grangier, "Reverse reconciliation protocols for quantum cryptography with continuous variables," *eprint arXiv:quant-ph/0204127*, 2002.

[81] M. Legre, H. Zbinden, and N. Gisin, "Implementation of continuous variable quantum cryptography in optical fibres using a go-&-return configuration," *Quantum Info. Comput.*, vol. 6, pp. 326–335, 2006.

[82] J. Lodewyck, T. Debuisschert, R. Tualle-Brouri, and P. Grangier, "Controlling excess noise in fiber-optics continuous-variable quantum key distribution," *Phys. Rev. A*, vol. 72, p. 050303, 2005.

[83] B. Qi, L.-L. Huang, L. Qian, and H.-K. Lo, "Experimental study on the gaussian-modulated coherent-state quantum key distribution over standard telecommunication fibers," *Phys. Rev. A*, vol. 76, p. 052323, 2007.

[84] J. Lodewyck, M. Bloch, R. García-Patrón, S. Fossier, E. Karpov, E. Diamanti, T. Debuisschert, N. J. Cerf, R. Tualle-Brouri, S. W. McLaughlin, and P. Grangier, "Quantum key distribution over 25 km with an all-fiber continuous-variable system," *Phys. Rev. A*, vol. 76, p. 042305, 2007.

[85] J. Lodewyck, M. Bloch, R. García-Patrón, S. Fossier, E. Karpov, E. Diamanti, T. Debuisschert, N. J. Cerf, R. Tualle-Brouri, S. W. McLaughlin, and P. Grangier, "Quantum key distribution device with coherent states," *Proc. SPIE*, vol. 6780, pp. 67 800Z–67 800Z–14, 2007.

[86] S. Fossier, E. Diamanti, T. Debuisschert, A. Villing, R. Tualle-Brouri, and P. Grangier, "Field test of a continuous-variable quantum key distribution prototype," *New Journal of Physics*, vol. 11, p. 045023, 2009.

[87] "SECOQC-Project," http://www.secoqc.net.

[88] P. Jouguet, S. Kunz-Jacques, T. Debuisschert, S. Fossier, E. Diamanti, R. Alléaume, R. Tualle-Brouri, P. Grangier, A. Leverrier, P. Pache, and P. Painchault, "Field test of classical symmetric encryption with continuous variables quantum key distribution," *Opt. Express*, vol. 20, pp. 14 030–14 041, 2012.

[89] C. Silberhorn, T. C. Ralph, N. Lütkenhaus, and G. Leuchs, "Continuous variable quantum cryptography: Beating the 3 dB loss limit," *Phys. Rev. Lett.*, vol. 89, p. 167901, 2002.

[90] J. Lodewyck, T. Debuisschert, R. Tualle-Brouri, and P. Grangier, "Controlling excess noise in fiber-optics continuous-variable quantum key distribution," *Phys. Rev. A*, vol. 72, p. 050303, 2005.

[91] P. Jouguet, S. Kunz-Jacques, A. Leverrier, P. Grangier, and E. Diamanti, "Experimental demonstration of long-distance continuous-variable quantum key distribution," *Nature Photonics*, vol. 7, pp. 378–381, 2013.

[92] C. Weedbrook, A. M. Lance, W. P. Bowen, T. Symul, T. C. Ralph, and P. K. Lam, "Quantum cryptography without switching," *Phys. Rev. Lett.*, vol. 93, p. 170504, 2004.

[93] A. M. Lance, T. Symul, V. Sharma, C. Weedbrook, T. C. Ralph, and P. K. Lam, "No-switching quantum key distribution using broadband modulated coherent light," *Phys. Rev. Lett.*, vol. 95, p. 180503, 2005.

[94] N. A. Silva, N. J. Muga, and A. N. Pinto, "Effective nonlinear parameter measurement using FWM in optical fibers in a low power regime," *IEEE Journal of Quantum Electronics*, vol. 46, pp. 285–291, 2010.

[95] N. A. Silva, N. J. Muga, and A. N. Pinto, "Measurement of the effective nonlinear parameter using FWM in random polarization optical fibers," in *European Conf. on Networks and Optical Communications - NOC*, vol. 1, June 2010, pp. 185–190.

[96] N. A. Silva, N. J. Muga, and A. N. Pinto, "Influence of the stimulated Raman scattering on the four-wave mixing process in birefringent fibers," *IEEE/OSA Journal of Lightwave Technology*, vol. 27, pp. 4979–4988, 2009.

[97] N. A. Silva, N. J. Muga, and A. N. Pinto, "Evolution of first-order sidebands from multiple FWM processes in HiBi optical fibers," *Optics Communications*, vol. 284, pp. 3408 – 3415, 2011.

[98] A. J. Almeida, N. A. Silva, N. J. Muga, and A. N. Pinto, "Fiber-optical communication system using polarization-encoding photons," in *European Conf. on Networks and Optical Communications and Conf. on Optical Cabling and Infrastructure - NOC/OC*, vol. 1, June 2010, pp. 127–132.

[99] A. J. Almeida, N. A. Silva, N. J. Muga, and A. N. Pinto, "Single-photon source using stimulated FWM in optical fibers for quantum communication," in *International Conf. on Applications of Optics and Photonics - AOP2011*, vol. 8001, May 2011, pp. 80 013W–1 – 80 013W–7.

[100] N. A. Silva, A. J. Almeida, and A. N. Pinto, "Interference in a quantum channel due to classical four-wave mixing in optical fibers," *IEEE Journal of Quantum Electronics*, vol. 48, pp. 472 –479, 2012.

[101] N. A. Silva, A. J. Almeida, and A. N. Pinto, "Statistical characterization of a single-photon source based on stimulated FWM in optical fibers," in *Conf. on Telecommunications - ConfTele*, vol. 1, April 2011, pp. 1–4.

[102] Á. J. Almeida, N. A. Silva, P. S. André, and A. N. Pinto, "Four-wave mixing: Photon statistics and the impact on a co-propagating quantum signal," *Optics Communications*, vol. 285, pp. 2956 – 2960, 2012.

[103] N. A. Silva and A. N. Pinto, "Comprehensive characterization of a heralded single photon source based on four-wave mixing in optical fibers," 2013, submitted to: Optics Communications.

[104] N. A. Silva and A. N. Pinto, "Effects of losses and nonlinearities on the generation of polarization entangled photons," *IEEE/OSA Journal of Lightwave Technology*, vol. 31, pp. 1309–1317, 2013.

[105] N. A. Silva and A. N. Pinto, "Role of absorption on the generation of quantum-correlated photon pairs through FWM," *IEEE Journal of Quantum Electronics*, vol. 48, pp. 1380 –1388, 2012.

[106] A. J. Almeida, S. R. Carneiro, N. A. Silva, N. J. Muga, and A. N. Pinto, "Polarization-entangled photon pairs using spontaneous four-wave mixing in a fiber loop," in *EUROCON and CONFTELE 2011*, vol. 1, April 2011, pp. 1–4.

[107] A. N. Pinto, A. J. Almeida, N. A. Silva, N. J. Muga, and L. M. Pinto, "Engineering quantum communication systems," in *SPIE Photonics Europe*, vol. 8440, April 2012, pp. 84 400B–1 – 84 400B–13.

Chapter 2

Low-Power Signal Propagation in $\chi^{(3)}$ Optical Waveguides

THE propagation of low-power signals in optical fibers requires a detailed analysis of the generalized nonlinear Schrödinger equation (GNLSE) in its classical and quantum versions. In this Chapter, we derive the classical GNLSE which describes the evolution of optical fields inside a fiber. Besides that, to deal with low-power optical signals we introduce the quantum version of the GNLSE, that considers the particle nature of the photons, as well the background noise reservoirs. This Chapter provides a general theoretical formalism which underlies all the topics covered in this thesis.

This Chapter is organized as follows: In section 2.1 we derive the classical GNLSE, and we discuss the linear and nonlinear parts of the induced polarization in the dielectric medium. Section 2.2 considers the theory of pulse propagation in a quantum regime, where the optical signal contains only few-photons. We also discuss the fundamental noise properties associated with the propagation of low-power optical fields in optical fibers.

2.1 General Nonlinear Wave Propagation Equation

The propagation of optical fields in fibers is governed by the Maxwell's equations. For a non-magnetic medium without free charges or currents, such as an optical fiber, the equation that describes the propagation of the electric field in the fiber, known as the wave equation, is given by [1, 2]

$$\nabla^2\mathbf{E} - \frac{1}{c^2}\frac{\partial^2\mathbf{E}}{\partial t^2} = \mu_0\frac{\partial^2\mathbf{P}}{\partial t^2}\,, \tag{2.1}$$

where $\mathbf{E}$ is the electric field vector, $c = (\varepsilon_0\mu_0)^{-1/2}$ is the speed of light in vacuum, μ_0 represents the vacuum permeability, ε_0 is the vacuum permittivity, and t is the time. In (2.1), $\mathbf{P}$ is the induced electric polarization, and considers the material response due to the presence of an electromagnetic field.

We assume that the optical field is quasi-monochromatic. This assumption, also known as the slowly varying envelop approximation (SVEA), is valid whenever the spectral spread $\Delta\omega$ of the field is much smaller than its central frequency, ω_0. With that assumption, the electric field can be written as [1, 2]

$$\mathbf{E}(r,t) = \frac{1}{2}\left[\hat{x}E_x(r,t) + \hat{y}E_y(r,t)\right]e^{-i\omega_0 t} + c.c.\,, \tag{2.2}$$

where $\hat{x}$ and $\hat{y}$ are the polarization unit vectors, $c.c.$ denotes the complex conjugate, $E_x(r,t)$ and $E_y(r,t)$ are the two polarization components of the slowly varying envelope in the linear basis, and r represents the space coordinates. The optical field is propagating along the z axis with an unchanging transverse profile [1, 2].

The induced polarization $\mathbf{P}$ is typically a complicated function of the electric field. Nevertheless, such dependence can be studied by expanding the induced polarization in a Taylor series as a function of the electric field strength [1, 2]

$$\mathbf{P}(r,t) = \mathbf{P}^{(1)}(r,t) + \mathbf{P}^{(2)}(r,t) + \mathbf{P}^{(3)}(r,t) + \ldots = \mathbf{P}_{\mathrm{L}}(r,t) + \mathbf{P}_{\mathrm{NL}}(r,t)\,, \tag{2.3}$$

where $\mathbf{P}^{(1)}(r,t)$ represents the linear contribution, $\mathbf{P}_{\mathrm{L}}(r,t)$, and the other terms account for the second, third, and higher order nonlinear effects, represented by $\mathbf{P}_{\mathrm{NL}}(r,t)$ in (2.3). The material response of the fiber can also be separated into its slowly varying envelope and its rapidly oscillating carrier frequency [1, 2]

$$\mathbf{P}(r,t) = \frac{1}{2}\left\{\hat{x}\left[P_x^{(1)}(r,t) + P_{\mathrm{NL},x}(r,t)\right] + \hat{y}\left[P_y^{(1)}(r,t) + P_{\mathrm{NL},y}(r,t)\right]\right\}e^{-i\omega_0 t} + c.c.\,. \tag{2.4}$$

2.1.1 First-Order Linear Polarization

The linear contribution for the total induced polarization, assuming that the electric-dipole approximation is valid and the material response is local, can be written as [2]

$$P_i^{(1)}(r,t) = \varepsilon_0 \int_{-\infty}^{+\infty} \sum_j R_{ij}^{(1)}(t-\tau)E_j(r,\tau)e^{i\omega_0(t-\tau)}d\tau\,, \tag{2.5}$$

where $R_{ij}^{(1)}(t-\tau)$ is the linear response function of the fiber, with $\{i,j=x,y\}$. We have assumed that $R_{ij}^{(1)}(t-\tau)$ obeys the causality condition $R_{ij}^{(1)}(t-\tau)=0$ for $t<\tau$. Equation (2.5) can be transformed into the frequency domain by introducing the Fourier transforms

$$E_j(r,t)=\frac{1}{2\pi}\int_{-\infty}^{+\infty}\tilde{E}_j(r,\omega-\omega_0)e^{-i(\omega-\omega_0)t}d\omega\,, \tag{2.6}$$

$$\tilde{E}_j(r,\omega-\omega_0)=\int_{-\infty}^{+\infty}E_j(r,t)e^{i(\omega-\omega_0)t}dt\,, \tag{2.7}$$

where ω represents the optical frequency. In that case, the linear induced polarization can be written as

$$P_i^{(1)}(r,t)=\frac{\varepsilon_0}{2\pi}\int_{-\infty}^{+\infty}\sum_j\tilde{\chi}_{ij}^{(1)}(\omega)\tilde{E}_j(r,\omega-\omega_0)e^{-i(\omega-\omega_0)t}d\omega\,, \tag{2.8}$$

where we have introduced an explicit expression for the linear susceptibility given by [2]

$$\tilde{\chi}_{ij}^{(1)}(\omega)=\int_{-\infty}^{+\infty}R_{ij}^{(1)}(\tau)e^{i\omega\tau}d\tau\,. \tag{2.9}$$

Equation (2.8) gives the time-varying polarization in terms of the frequency components of the applied field and the frequency dependent linear response function. The linear polarization can be obtained in frequency domain by applying the Fourier transform to (2.8)

$$\tilde{P}_i^{(1)}(r,\omega-\omega_0)=\varepsilon_0\sum_j\tilde{\chi}_{ij}^{(1)}(\omega)\tilde{E}_j(r,\omega-\omega_0). \tag{2.10}$$

The linear susceptibility, $\tilde{\chi}_{ij}^{(1)}(\omega)$, is in general a complex function and its real and imaginary parts can be related to the refractive index $n(\omega)$ and the absorption coefficient $\alpha(\omega)$ by the relations [1, 2]

$$n_i(\omega)=1+\frac{1}{2}\mathrm{Re}\left[\tilde{\chi}_{ii}^{(1)}(\omega)\right] \tag{2.11}$$

$$\alpha_i(\omega)=\frac{\omega}{nc}\mathrm{Im}\left[\tilde{\chi}_{ii}^{(1)}(\omega)\right]\,, \tag{2.12}$$

where Re and Im stand for the real and imaginary parts, respectively.

2.1.2 Nonlinear Properties of $\chi^{(3)}$ Waveguides

The nonlinear part of the of the induced polarization in (2.3), $\mathbf{P}_{\mathrm{NL}}(r,t)$, is given by

$$\mathbf{P}_{\mathrm{NL}}(r,t) = \mathbf{P}^{(2)}(r,t) + \mathbf{P}^{(3)}(r,t) + \dots \ . \tag{2.13}$$

In silica based waveguides, such as optical fibers, all the even-order nonlinear polarization terms vanish, $\mathbf{P}^{(2n)}(r,t) \approx 0$ with $n = 1,2,\dots$, due to the fact that fused silica exhibits an inversion symmetry [1, 2]. In that case, the lowest-order nonlinear effect is of third order. Assuming that the electric-dipole approximation is valid and the material response is local, the third-order nonlinear polarization in a medium such as silica glass can be written as [3, 4]

$$P_i^{(3)}(r,t) = \varepsilon_0 \chi_0 \sum_{j,k,l} E_j(r,t) \int_{-\infty}^{+\infty} R_{ijkl}^{(3)}(t-\tau) E_k^*(r,\tau) E_l(r,\tau) d\tau, \tag{2.14}$$

where χ_0 is the magnitude of third-order susceptibility, $i,j,k,l = x,y$, and $R_{ijkl}^{(3)}(t-\tau)$ is the third-order response function of the waveguide. Note that, the nonlinear response function obeys the causality condition with $R_{ijkl}^{(3)}(t-\tau) = 0$ for $t < \tau$. The nonlinear response function in (2.14) governs the nonlinear process that occurs inside the waveguide, such as four-wave mixing (FWM), Raman scattering, self-phase modulation (SPM) and cross-phase modulation (XPM) [1]. In time domain, the nonlinear response function can be written as [4, 5]

$$R_{ijkl}^{(3)}(\tau) = \frac{1-f_R}{3}\delta(\tau)(\delta_{ij}\delta_{kl} + \delta_{ik}\delta_{jl} + \delta_{il}\delta_{jk}) + f_R R_a(\tau)\delta_{ij}\delta_{kl} + \frac{f_R}{2} R_b(\tau)(\delta_{ik}\delta_{jl} + \delta_{il}\delta_{jk}), \tag{2.15}$$

where δ_{ij} represents the Kronecker delta function, $R_a(\tau)$ and $R_b(\tau)$ are normalized isotropic and anisotropic Raman response, and f_R represents their fractional contribution to the nonlinear refractive index. The form of $R_a(\tau)$ and $R_b(\tau)$ is set by vibrations of silica molecules induced by the optical field [1, 2, 4, 5]. The first term in right side of (2.15) accounts for the instantaneous electronic response of the waveguide, whereas the remain terms govern the delayed Raman response. Applying the Fourier transform to (2.14) we obtain the time-varying nonlinear polarization in terms of the frequency components of the applied field and the frequency dependent nonlinear response function

$$P_i^{(3)}(r,t) = \frac{\varepsilon_0 \chi_0}{(2\pi)^3} \iiint_{-\infty}^{+\infty} d\omega\, d\omega_1\, d\omega_2 \sum_{j,k,l} \tilde{R}_{ijkl}^{(3)}(\omega_1 - \omega) \tilde{E}_k^*(r, \omega - \omega_0) \tilde{E}_l(r, \omega_1 - \omega_0) \times \tilde{E}_j(r, \omega_2 - \omega_0) e^{-i(\omega_2 + \omega_1 - \omega - \omega_0)t}, \tag{2.16}$$

where $\tilde{R}^{(3)}_{ijkl}(\Omega)$ is the Fourier transform of $R^{(3)}_{ijkl}(\tau)$, and is given by

$$\tilde{R}^{(3)}_{ijkl}(\Omega) = \frac{1-f_R}{3}\left(\delta_{ij}\delta_{kl}+\delta_{ik}\delta_{jl}+\delta_{il}\delta_{jk}\right) + f_R\tilde{R}_a(\Omega)\delta_{ij}\delta_{kl} + \frac{f_R}{2}\tilde{R}_b(\Omega)\left(\delta_{ik}\delta_{jl}+\delta_{il}\delta_{jk}\right), \tag{2.17}$$

where Ω is the Stokes ($\Omega<0$) or anti-Stokes ($\Omega>0$) frequency shift. In frequency domain the third-order nonlinear induced polarization can be written as

$$\tilde{P}^{(3)}_i(r,\omega-\omega_0) = \frac{\varepsilon_0\chi_0}{(2\pi)^2}\iint_{-\infty}^{+\infty} d\omega_1 d\omega_2 \sum_{j,k,l}\tilde{R}^{(3)}_{ijkl}(\omega_2-\omega_1)\tilde{E}^*_k(r,\omega_1-\omega_0)\tilde{E}_l(r,\omega_2-\omega_0) \times \tilde{E}_j(r,\omega+\omega_1-\omega_2-\omega_0). \tag{2.18}$$

2.1.3 The GNLSE in $\chi^{(3)}$ Optical Waveguides

The lowest-order nonlinear effects in optical fibers are originate from the third-order susceptibility $\chi^{(3)}$, which is responsible for phenomena such as nonlinear refraction, a phenomenon referring to the intensity dependence of the refractive index [1]. The propagation of optical waves inside silica fibers is described by a dynamic equation called generalized nonlinear Schrödinger equation (GNLSE). We start the derivation of the GNLSE from the wave equation (2.1). Transferring (2.1) into frequency we obtain [1, 2]

$$\nabla^2\tilde{\mathbf{E}}(r,\omega-\omega_0) + \frac{\omega^2}{c^2}\overleftrightarrow{\varepsilon}(\omega)\cdot\tilde{\mathbf{E}}(r,\omega-\omega_0) = -\mu_0\omega^2\tilde{\mathbf{P}}_{\mathrm{NL}}(r,\omega-\omega_0), \tag{2.19}$$

where $\overleftrightarrow{\varepsilon}(\omega)$ is the dielectric tensor and accounts for the linear dispersive and material birefringent properties of the medium [1, 2]. Equation (2.19) can be solved using the method of separation of variables [1, 6]

$$\tilde{E}_i(r,\omega-\omega_0) = F_i(x,y,\omega)\tilde{A}_i(z,\omega-\omega_0), \tag{2.20}$$

where $F_i(x,y,\omega)$ is the spatial distribution of the fiber mode in which the jth field propagates inside the fiber, perpendicular to the direction of propagation, and $\tilde{A}_i(z,\omega-\omega_0)$ is the amplitude envelope of the electric field that is a slowly varying function of z [1, 2, 6]. Substituting (2.20) in (2.19), multiplying by $F^*_i(x,y,\omega)$ and integrating over the transverse plane, x and y, we obtain

$$\frac{\partial^2\tilde{A}_i(z,\omega-\omega_0)}{\partial z^2} + \frac{\omega^2}{c^2}\sum_j \overleftrightarrow{\varepsilon}_{ij}(\omega)\frac{\iint dxdyF^*_i(x,y,\omega)F_j(x,y,\omega)}{\iint dxdy|F_i(x,y,\omega)|^2}\tilde{A}_j(z,\omega-\omega_0) + \frac{\iint F^*_i(x,y,\omega)\nabla^2_T F_i(x,y,\omega)dxdy}{\iint dxdy|F_i(x,y,\omega)|^2}\tilde{A}_i(z,\omega-\omega_0) = -\mu_0\omega^2\frac{\iint dxdyF^*_i(x,y,\omega)\tilde{P}^{(3)}_i(z,\omega-\omega_0)}{\iint dxdy|F_i(x,y,\omega)|^2}, \tag{2.21}$$

where $\tilde{P}_i^{(3)}(z,\omega-\omega_0)$ is given by (2.18) in conjugation with (2.20), and ∇_T^2 denotes derivation operation over the transverse coordinates x and y. We assume that the transverse profile of the field distribution exhibits only a slight dependence on the frequency for the two fundamental polarization modes [1, 6]. In that case, we obtain

$$\sum_j \left[\frac{\omega^2}{c^2}\overleftrightarrow{\varepsilon}_{ij}(\omega)\frac{\iint dxdyF_i^*(x,y,\omega)F_j(x,y,\omega)}{\iint dxdy|F_i(x,y,\omega)|^2}+\frac{\iint F_i^*(x,y,\omega)\nabla_T^2F_i(x,y,\omega)dxdy}{\iint dxdy|F_i(x,y,\omega)|^2}\overleftrightarrow{I}_{ij}\right]\tilde{A}_j(z,\omega-\omega_0)$$
$$+\frac{\partial^2\tilde{A}_i(z,\omega-\omega_0)}{\partial z^2}=$$
$$-\frac{\chi_0}{c^2}\omega^2\frac{\iint dxdyF_i^*(x,y,\omega)F_k^*(x,y,\omega)F_l(x,y,\omega)F_j(x,y,\omega)}{\iint dxdy|F_i(x,y,\omega)|^2}\tilde{P}_i^{NL}(z,\omega-\omega_0), \quad (2.22)$$

where $\overleftrightarrow{\mathbf{I}}$ is the second order unit tensor, and

$$\tilde{P}_i^{NL}(z,\omega-\omega_0)=\frac{1}{(2\pi)^2}\iint_{-\infty}^{+\infty}d\omega_1d\omega_2\sum_{j,k,l}\tilde{R}_{ijkl}^{(3)}(\omega_2-\omega_1)\tilde{A}_k^*(z,\omega_1-\omega_0)\tilde{A}_l(z,\omega_2-\omega_0)$$
$$\times\tilde{A}_j(z,\omega+\omega_1-\omega_2-\omega_0), \quad (2.23)$$

In optical fibers, the modal index difference between the two polarization modes are at least three orders of magnitude smaller than the modal indices themselves [1, 7, 8]. In that case [7, 8]

$$\left[\frac{\omega^2}{c^2}\overleftrightarrow{\varepsilon}_{ij}(\omega)\frac{\iint dxdyF_i^*(x,y,\omega)F_j(x,y,\omega)}{\iint dxdy|F_i(x,y,\omega)|^2}+\frac{\iint F_i^*(x,y,\omega)\nabla_T^2F_i(x,y,\omega)dxdy}{\iint dxdy|F_i(x,y,\omega)|^2}\overleftrightarrow{I}_{ij}\right]=$$
$$\beta^2(\omega)\overleftrightarrow{\mathbf{I}}-\beta(\omega)\omega\overleftrightarrow{\mathbf{B}}, \quad (2.24)$$

where $\beta(\omega)=\omega n(\omega)/c$ is the propagation constant with $n(\omega)$ representing the modal index, and $\overleftrightarrow{\mathbf{B}}$ represents the birefringence properties of the waveguide [7]. We assume that $F_i(x,y,\omega)$ is the same for both polarization modes, $F_x(x,y,\omega)\approx F_y(x,y,\omega)=F(x,y,\omega)$, since the anisotropic contribution to the dielectric tensor is typically much smaller compared to the isotropic part [8, 9]. As result, equation (2.22) can be written as

$$\frac{\partial^2\tilde{A}_i(z,\omega-\omega_0)}{\partial z^2}+\sum_j\left[\beta^2(\omega)\overleftrightarrow{I}_{ij}-\beta(\omega)\omega\overleftrightarrow{B}_{ij}\right]\tilde{A}_j(z,\omega-\omega_0)=$$
$$-\frac{\chi_0}{c^2}\omega^2\frac{\iint dxdy|F(x,y,\omega)|^4}{\iint dxdy|F(x,y,\omega)|^2}\tilde{P}_i^{NL}(z,\omega-\omega_0), \quad (2.25)$$

Using the SVEA as follows [1, 8]

$$\frac{\partial^2\tilde{A}_i(z,\omega-\omega_0)}{\partial z^2}+\beta^2(\omega)\tilde{A}_i(z,\omega-\omega_0)\approx 2i\beta(\omega)\left[\frac{\partial\tilde{A}_i(z,\omega-\omega_0)}{\partial z}-i\beta(\omega)\tilde{A}_i(z,\omega-\omega_0)\right], \quad (2.26)$$

the wave equation (2.25) can be written as

$$\frac{\partial \tilde{A}_i(z,\omega-\omega_0)}{\partial z} = i\beta(\omega)\tilde{A}_i(z,\omega-\omega_0) - \frac{i}{2}\omega\sum_j \overleftrightarrow{B}_{ij}\tilde{A}_j(z,\omega-\omega_0) + \frac{i}{2}\frac{\chi_0}{\beta(\omega)}\frac{\omega^2}{c^2}\frac{\iint dxdy|F(x,y,\omega)|^4}{\iint dxdy|F(x,y,\omega)|^2}\tilde{P}_i^{NL}(z,\omega-\omega_0)\,. \quad (2.27)$$

Normalizing the field amplitude such that $|A_i(z,t)|^2$ represents the optical power [10, 11]

$$A_i(z,t) \to \frac{A_i(z,t)}{N_c}\,, \quad (2.28)$$

where N_c is the normalization constant given by [10, 11]

$$N_c = \left[\frac{1}{2}\varepsilon_0 n(\omega_0)c\iint |F(x,y,\omega)|^2 dxdy\right]^{\frac{1}{2}}\,, \quad (2.29)$$

we obtain the GNLSE in frequency domain

$$\frac{\partial \tilde{A}_i(z,\omega-\omega_0)}{\partial z} = i\beta(\omega)\tilde{A}_i(z,\omega-\omega_0) - \frac{i}{2}\omega\sum_j \overleftrightarrow{B}_{ij}\tilde{A}_j(z,\omega-\omega_0) + i\gamma[1+(\omega-\omega_0)\eta]\,\tilde{P}_i^{NL}(z,\omega-\omega_0), \quad (2.30)$$

where γ is the fiber nonlinear parameter, given by [1]

$$\gamma = \frac{\omega_0 n_2(\omega_0)}{cA_{\text{eff}}(\omega_0)}\,, \quad (2.31)$$

and $n_2(\omega_0) = \chi_0/(\varepsilon_0 c n^2(\omega_0))$ is the nonlinear index coefficient [1], and $A_{\text{eff}}(\omega_0)$ is effective mode area defined as [1]

$$A_{\text{eff}}(\omega_0) = \frac{\left[\iint dxdy|F(x,y,\omega_0]|^2\right]^2}{\iint dxdy|F(x,y,\omega_0)|^4}\,. \quad (2.32)$$

In (2.30), η is related to the dispersion in the magnitude of fiber nonlinearity and is given by [1]

$$\eta = \frac{1}{\omega_0} - \frac{1}{n(\omega_0)}\frac{\partial n(\omega)}{\partial\omega}\bigg|_{\omega=\omega_0} - \frac{1}{A_{\text{eff}}(\omega_0)}\frac{\partial A_{\text{eff}}(\omega)}{\partial\omega}\bigg|_{\omega=\omega_0} + \cdots\,. \quad (2.33)$$

Equation (2.30) can also include the waveguide linear loss if we perform the change

$$\beta(\omega) \to \beta(\omega) + \frac{i}{2}\alpha(\omega)\,. \quad (2.34)$$

The GNLSE in frequency domain can now be written

$$\frac{\partial \tilde{A}_i(z,\omega-\omega_0)}{\partial z} = i\sum_j \tilde{R}_{ij}^{(1)}(\omega)\tilde{A}_j(z,\omega-\omega_0) + i\gamma[1+(\omega-\omega_0)\eta]\,\tilde{P}_i^{NL}(z,\omega-\omega_0)\,, \quad (2.35)$$

where

$$\tilde{R}_{ij}^{(1)}(\omega) \equiv \beta(\omega) + \frac{i}{2}\alpha(\omega) - \frac{\omega}{2}\overleftrightarrow{B}_{ij}\,, \tag{2.36}$$

accounts for dispersive, loss and birefringence effects in the waveguide, and the nonlinear induced polarization $\tilde{P}_i^{NL}(z,\omega-\omega_0)$ is given by (2.23).

The GNLSE can be transformed to time domain, by expanding the propagation constant around the carrier frequency ω_0. In that case, we obtain

$$\frac{\partial A_i(z,t)}{\partial z} = i\sum_j \int_{-\infty}^{+\infty} R_{ij}^{(1)}(t-\tau)A_j(z,\tau)d\tau + i\gamma\left[1+i\eta\frac{\partial}{\partial t}\right]P_i^{NL}(z,t)\,, \tag{2.37}$$

where $R_{ij}^{(1)}(t-\tau)$ is the Fourier transform of $\tilde{R}_{ij}^{(1)}(\omega)$, which obeys the causality condition defined as $R_{ij}^{(1)}(t-\tau)=0$ for $t<\tau$. The nonlinear polarization in time domain is given by

$$P_i^{NL}(z,t) = \sum_{j,k,l} A_j(z,t)\int_{-\infty}^{+\infty} R_{ijkl}^{(3)}(t-\tau)A_k^*(z,\tau)A_l(z,\tau)d\tau\,. \tag{2.38}$$

Note that first term in right side of (2.37), can also be written as

$$i\int_{-\infty}^{+\infty} R_{ij}^{(1)}(t-\tau)A_j(z,\tau)d\tau \equiv \sum_{n=0}^{+\infty}\frac{i^{n+1}\beta_n}{n!}\frac{\partial^n A_i(z,t)}{\partial t^n} - \int_{-\infty}^{t}\frac{\alpha(t-\tau)}{2}A_i(z,\tau)d\tau$$
$$-\frac{i}{2}\overleftrightarrow{B}_{ij}\left(\omega_0 + i\frac{\partial}{\partial t}\right)A_j(z,t) \tag{2.39}$$

where

$$\beta_n = \left.\frac{d^n\beta}{d\omega^n}\right|_{\omega=\omega_0}\,, \tag{2.40}$$

is the nth-order dispersion coefficient [1].

The GNLSE in Frequency and Time Domains

The propagation of optical fields in $\chi^{(3)}$ waveguides is governed by the GNLSE. Here we present a summary of that nonlinear equation in frequency and time domains. In frequency domain the GNLSE can be written as

$$\frac{\partial\tilde{A}_i(z,\omega-\omega_0)}{\partial z} = i\sum_j \tilde{R}_{ij}^{(1)}(\omega)\tilde{A}_j(z,\omega-\omega_0) + i\gamma[1+(\omega-\omega_0)\eta]\,\tilde{P}_i^{NL}(z,\omega-\omega_0)\,, \tag{2.41}$$

where $\tilde{R}_{ij}^{(1)}(\omega)$ describes the linear dispersive properties of the waveguide including its loss and birefringence, given by

$$\tilde{R}_{ij}^{(1)}(\omega) \equiv \beta(\omega) + \frac{i}{2}\alpha(\omega) - \frac{\omega}{2}\overleftrightarrow{B}_{ij}\,. \tag{2.42}$$

In (2.41), the nonlinear polarization in frequency domain can be written as

$$\tilde{P}_i^{NL}(z,\omega-\omega_0) = \iint_{-\infty}^{+\infty} \frac{d\omega_1 d\omega_2}{(2\pi)^2} \sum_{j,k,l} \tilde{R}_{ijkl}^{(3)}(\omega_2-\omega_1)\tilde{A}_k^*(z,\omega_1-\omega_0)\tilde{A}_l(z,\omega_2-\omega_0) \times \tilde{A}_j(z,\omega+\omega_1-\omega_2-\omega_0). \tag{2.43}$$

In time domain we can write the GNLSE as follows

$$\frac{\partial A_i(z,t)}{\partial z} = i\sum_j \int_{-\infty}^{+\infty} R_{ij}^{(1)}(t-\tau)A_j(z,\tau)d\tau + i\gamma\left[1+i\eta\frac{\partial}{\partial t}\right]P_i^{NL}(z,t)\,, \tag{2.44}$$

where $R_{ij}^{(1)}(t-\tau)$ is the Fourier transform of $\tilde{R}_{ij}^{(1)}(\omega)$, and the nonlinear induced polarization is given by

$$P_i^{NL}(z,t) = \sum_{j,k,l} A_j(z,t) \int_{-\infty}^{+\infty} R_{ijkl}^{(3)}(t-\tau)A_k^*(z,\tau)A_l(z,\tau)d\tau\,. \tag{2.45}$$

Considerable simplification occurs if the nonlinear response is assumed to be instantaneous. In that case the nonlinear polarization in (2.38) can be written as [1]

$$P_i^{NL}(z,t) = \frac{1}{3}\sum_j \left[A_i^*(z,t)A_j^2(z,t) + 2A_i(z,t)|A_j(z,t)|^2\right]\,. \tag{2.46}$$

The assumption of instantaneous nonlinear response allow us to neglect the Raman effect in the waveguide. For silica fibers the vibrational the Raman response occurs over a time scale 60-70 fs. This mean that this approximation is valid for optical pulse widths higher than 1 ps. Moreover, the η parameter in (2.44) govern the effect of self-steepening [1]. However, for picosecond pulses the impact of η is quite small, but must be considered for ultrashort pulses withs. In that case, for optical pulse widths higher than 1 ps we can neglect that term in (2.44), making the approximation $\eta \approx 0$. Under this approximations, we can write the GNLSE as [1]

$$\frac{\partial A_i(z,t)}{\partial z} + \frac{\alpha(\omega_0)}{2}A_i(z,t) = \sum_{n=0}^{+\infty}\frac{i^{n+1}\beta_n}{n!}\frac{\partial^n A_i(z,t)}{\partial t^n} + i\frac{\gamma}{3}\sum_j\left[A_i^*(z,t)A_j^2(z,t) + 2A_i(z,t)|A_j(z,t)|^2\right], \tag{2.47}$$

where we neglect the polarization effects, assuming that the fiber had no birefringence. This approximation is valid for very low birefringence fibers or polarization maintaining optical waveguides [1].

2.1.4 Birefringence Effects in Long Optical Fibers

In long optical fibers the state of polarization (SOP) of an optical field does not remains the same at fiber input/output, since internal manufacturing imperfections and external environmental factors introduce perturbations to fiber properties and result in residual birefringence inside the waveguide [1, 12]. That residual birefringence not only randomizes the SOP in both its magnitude and orientation along the fiber length, but also induces differential polarization variations among waves of different frequencies through polarization mode dispersion (PMD)[1, 12].

The equations governing the evolution and interaction of the two polarization components of the field can be written in a compact form in the Jones space [13]. In this notation, the GNLSE in time domain, (2.44), for the field vector $|A(z,t)\rangle$ is given by [7]

$$\frac{\partial|A(z,t)\rangle}{\partial z}+\int_{-\infty}^{t}\frac{\alpha(t-\tau)}{2}|A(z,\tau)\rangle d\tau=\sum_{n=0}^{+\infty}\frac{i^{n+1}\beta_n}{n!}\frac{\partial^n|A(z,t)\rangle}{\partial t^n}-\frac{i}{2}\overleftrightarrow{\mathbf{B}}\left(\omega_0+i\frac{\partial}{\partial t}\right)|A(z,t)\rangle + i\gamma\left[1+i\eta\frac{\partial}{\partial t}\right]|P^{NL}(z,t)\rangle\,. \quad (2.48)$$

In the Jones space, $|A(z,t)\rangle$ and $|P^{NL}(z,t)\rangle$ are define as [13]

$$|A(z,t)\rangle=\begin{bmatrix}A_x(z,t)\\A_y(z,t)\end{bmatrix},\qquad\text{and}\qquad|P^{NL}(z,t)\rangle=\begin{bmatrix}P_x^{NL}(z,t)\\P_y^{NL}(z,t)\end{bmatrix}. \quad (2.49)$$

The nonlinear polarization vector is given by [7]

$$\begin{aligned}|P^{NL}(z,t)\rangle=\frac{1-f_R}{3}&\left[2\langle A(z,t)|A(z,t)\rangle+|A^*(z,t)\rangle\langle A^*(z,t)|\right]|A(z,t)\rangle\\&+f_R\left\{\int_{-\infty}^{t}R_a(t-\tau)\langle A(z,\tau)|A(z,\tau)\rangle d\tau\right\}|A(z,t)\rangle\\&+\frac{f_R}{2}\left\{\int_{-\infty}^{t}R_b(t-\tau)\left[|A(z,\tau)\rangle\langle A(z,\tau)|+|A^*(z,\tau)\rangle\langle A^*(z,\tau)|\right]d\tau\right\}|A(z,t)\rangle\,, \quad (2.50)\end{aligned}$$

where $\langle A(z,t)|$ and $|A^*(z,t)\rangle$ are the Hermitian and complex conjugates of $|A(z,t)\rangle$, respectively [14]. The birefringence tensor in (2.48) can be written in the form of Pauli spin vector $\overleftrightarrow{\mathbf{B}}=\boldsymbol{B}\cdot\boldsymbol{\sigma}$, where $\boldsymbol{B}$ is a three dimensional Stokes vector, that governs the birefringence-induced random SOP variations during the propagation of the optical field in the waveguide [7, 13–15]. Moreover, $\boldsymbol{\sigma}=\boldsymbol{\sigma}_1\hat{e}_1+\boldsymbol{\sigma}_2\hat{e}_2+\boldsymbol{\sigma}_3\hat{e}_3$, where $\hat{e}_1,\hat{e}_2,\hat{e}_3$ are the three unit vectors in the Stokes space [13], and

$$\boldsymbol{\sigma}_1=\begin{bmatrix}1&0\\0&-1\end{bmatrix},\qquad\boldsymbol{\sigma}_2=\begin{bmatrix}0&1\\1&0\end{bmatrix},\quad\text{and}\quad\boldsymbol{\sigma}_3=\begin{bmatrix}0&-i\\i&0\end{bmatrix}, \quad (2.51)$$

are the Pauli spin matrices [13]. In this notation, we can define the following relations [7, 13]

$$|A^*(z,t)\rangle\langle A^*(z,t)| = |A(z,t)\rangle\langle A(z,t)| - \langle A(z,t)|\boldsymbol{\sigma}_3|A(z,t)\rangle\boldsymbol{\sigma}_3 \tag{2.52}$$

$$|A(z,t)\rangle\langle A(z,t)| = \frac{1}{2}\left(\langle A(z,t)|A(z,t)\rangle + \langle A(z,t)|\boldsymbol{\sigma}|A(z,t)\rangle\cdot\boldsymbol{\sigma}\right). \tag{2.53}$$

The optical power at a given point z in the waveguide is given by [7]

$$\mathbf{P}_p(z,t) = \langle A(z,t)|\boldsymbol{\sigma}|A(z,t)\rangle. \tag{2.54}$$

The residual birefringence introduce rapid random polarization variations of the optical field over short fiber distance, since the beat length of residual birefringence is of the order of 1 m and the correlation length associated with residual birefringence is about 10 m [7]. We can remove such rapid SOP variations by adopting a rotating frame through an unitary transformation [14, 15]

$$|A(z,t)\rangle = \overleftrightarrow{\mathbf{T}}(z)|A'(z,t)\rangle, \tag{2.55}$$

where $\overleftrightarrow{\mathbf{T}}(z)$ is an unitary Jones matrix, that corresponds to random rotations of the Stokes vector on the Poincaré sphere that do not change the vector length [13, 15]. As $\overleftrightarrow{\mathbf{T}}(z)$ evolves only on a length scale of the birefringence correlation length, the SOPs of optical waves vary so rapidly and randomly during nonlinear interaction along the fiber that only the average SOPs have an effect on the nonlinear interactions [13–15]. In the Jones space, the unitary transformation matrix can be written in the form [13–15]

$$\overleftrightarrow{\mathbf{T}}(z) = \begin{bmatrix} \cos(\theta(z)/2)e^{-i(\phi_0(z)+\phi(z))/2} & -\sin(\theta(z)/2)e^{i(\phi_0(z)-\phi(z))/2} \\ \sin(\theta(z)/2)e^{-i(\phi_0(z)-\phi(z))/2} & \cos(\theta(z)/2)e^{i(\phi_0(z)+\phi(z))/2} \end{bmatrix}, \tag{2.56}$$

where $\phi_0(z)$ and $\phi(z)$ are uniformly distributed in the range $[0,2\pi]$, and $\cos(\theta(z))$ is uniformly distributed in the range $[-1,1]$ [7, 14, 15]. In (2.56), $\phi_0(z)$, $\phi(z)$, and $\cos(\theta(z))$ are three independent random variables [7]. In this new rotating frame, the GNLSE can be written as [7, 14, 15]

$$\frac{\partial|A'(z,t)\rangle}{\partial z} + \int_{-\infty}^{t}\frac{\alpha(t-\tau)}{2}|A'(z,\tau)\rangle d\tau = \sum_{n=0}^{+\infty}\frac{i^{n+1}\beta_n}{n!}\frac{\partial^n|A'(z,t)\rangle}{\partial t^n} + \frac{1}{2}\mathbf{b}\cdot\boldsymbol{\sigma}|A'(z,t)\rangle + i\gamma\left[1+i\eta\frac{\partial}{\partial t}\right]|[P^{NL}]'(z,t)\rangle, \tag{2.57}$$

where $\mathbf{b} = \overleftrightarrow{\mathbf{R}}^{-1}\mathbf{B}$ with $\overleftrightarrow{\mathbf{R}}^{-1}$ being a three-dimensional rotation matrix in the Stokes space with $\overleftrightarrow{\mathbf{R}}\boldsymbol{\sigma} = \overleftrightarrow{\mathbf{T}}^{\dagger}\boldsymbol{\sigma}\overleftrightarrow{\mathbf{T}}$ [7, 13–15]. The $\overleftrightarrow{\mathbf{R}}$ matrix can be written as follows [7]

$$\overleftrightarrow{\mathbf{R}} = \begin{bmatrix} \cos\theta & -\sin\theta\cos\phi_0 & \sin\theta\sin\phi_0 \\ \sin\theta\cos\phi & \cos\theta\cos\phi_0\cos\phi - \sin\phi_0\sin\phi & -\cos\theta\sin\phi_0\cos\phi - \cos\phi_0\sin\phi \\ \sin\theta\sin\phi & \cos\theta\cos\phi_0\sin\phi + \sin\phi_0\cos\phi & \cos\phi_0\cos\phi - \cos\theta\sin\phi_0\sin\phi \end{bmatrix}. \tag{2.58}$$

The nonlinear polarization vector in (2.57) is given by [7, 14, 15]

$$|[P^{NL}]'(z,t)\rangle = \frac{(1-f_R)}{3}\left[3\,\langle A'(z,t)|A'(z,t)\rangle - \langle A'(z,t)|\overleftrightarrow{\mathbf{T}}^{\dagger}\boldsymbol{\sigma}_3\overleftrightarrow{\mathbf{T}}|A'(z,t)\rangle\overleftrightarrow{\mathbf{T}}^{\dagger}\boldsymbol{\sigma}_3\overleftrightarrow{\mathbf{T}}\right]|A'(z,t)\rangle$$
$$+ f_R\left\{\int_{-\infty}^{t} R_a(t-\tau)\langle A'(z,\tau)|A'(z,\tau)\rangle d\tau\right\}|A'(z,t)\rangle$$
$$+\frac{f_R}{2}\left\{\int_{-\infty}^{t} R_b(t-\tau)\left[2\,|A'(z,\tau)\rangle\langle A'(z,\tau)| - \langle A'(z,\tau)|\overleftrightarrow{\mathbf{T}}^{\dagger}\boldsymbol{\sigma}_3\overleftrightarrow{\mathbf{T}}|A'(z,\tau)\rangle\overleftrightarrow{\mathbf{T}}^{\dagger}\boldsymbol{\sigma}_3\overleftrightarrow{\mathbf{T}}\right]d\tau\right\}|A'(z,t)\rangle\,. \tag{2.59}$$

After averaging over the fast variations induced by $\overleftrightarrow{\mathbf{T}}$, the GNLSE can be written as

$$\frac{\partial|A'(z,t)\rangle}{\partial z} + \int_{-\infty}^{t}\frac{\alpha(t-\tau)}{2}|A'(z,\tau)\rangle d\tau = \sum_{n=0}^{+\infty}\frac{i^{n+1}\beta_n}{n!}\frac{\partial^n|A'(z,t)\rangle}{\partial t^n} + \frac{1}{2}\mathbf{b}\cdot\boldsymbol{\sigma}|A'(z,t)\rangle$$
$$+ i\gamma\left[1+i\eta\frac{\partial}{\partial t}\right]|[P^{NL}]'(z,t)\rangle\,, \tag{2.60}$$

where the nonlinear polarization is given by [7, 14, 15]

$$|[P^{NL}]'(z,t)\rangle = \frac{8(1-f_R)}{9}\langle A'(z,t)|A'(z,t)\rangle|A'(z,t)\rangle +$$
$$f_R\left\{\int_{-\infty}^{t}\left[R_a(t-\tau)+\frac{1}{6}R_b(t-\tau)\right]\langle A'(z,\tau)|A'(z,\tau)\rangle d\tau\right\}|A'(z,t)\rangle$$
$$+\frac{2f_R}{3}\left\{\int_{-\infty}^{t} R_b(t-\tau)|A'(z,\tau)\rangle\langle A'(z,\tau)|d\tau\right\}|A'(z,t)\rangle\,. \tag{2.61}$$

In (2.61) we have used the result [14, 15]

$$\left\langle\langle A'(z,t)|\overleftrightarrow{\mathbf{T}}^{\dagger}\boldsymbol{\sigma}_3\overleftrightarrow{\mathbf{T}}|A'(z,t)\rangle\overleftrightarrow{\mathbf{T}}^{\dagger}\boldsymbol{\sigma}_3\overleftrightarrow{\mathbf{T}}\right\rangle = \frac{1}{3}\langle A'(z,t)|\boldsymbol{\sigma}|A'(z,t)\rangle\cdot\boldsymbol{\sigma}\,, \tag{2.62}$$

and $\langle\sin^2(\theta(z))\rangle = 2/3$, $\langle\cos^2(\theta(z))\rangle = 1/3$, $\langle\sin^2(\phi(z))\rangle = \langle\cos^2(\phi(z))\rangle = 0.5$, and similar relations [7]. Averaging over the random polarization variation induced by $\overleftrightarrow{\mathbf{T}}$ allows to remove the rapid variation of the SOP of the optical field [7, 14]. In that sense, that method is similar to the SVEA used in (2.26).

For optical pulse widths higher than 1 ps, the GNLSE for long optical fibers can be written

as [1, 16]

$$\frac{\partial|A'(z,t)\rangle}{\partial z}+\frac{\alpha(\omega_0)}{2}|A'(z,t)\rangle=\sum_{n=0}^{+\infty}\frac{i^{n+1}\beta_n}{n!}\frac{\partial^n|A'(z,t)\rangle}{\partial t^n}+\frac{1}{2}\mathbf{b}\cdot\boldsymbol{\sigma}|A'(z,t)\rangle \\ +i\frac{8\gamma}{9}\langle A'(z,t)|A'(z,t)\rangle|A'(z,t)\rangle\,. \quad (2.63)$$

From (2.47) and (2.63) we can observe that rapid SOP variations along the propagation of the optical field in the waveguide leads to a reduction of the nonlinear parameter, such that its effective value is $\gamma_{\text{eff}}=8\gamma/9$ [1]. That reduction arises from the fact that, if the polarization state changes randomly along the fiber length, we measure an average value of γ that is reduced by a factor of $8/9$, compared with the value expected for polarization maintaining waveguides. Averaging over rapid variations of the SOP over the Poincaré sphere leads to a reduction of γ [1].

2.2 Quantum Version of the Nonlinear Wave Equation

In section 2.1 we derive the GNLSE for an optical field that can be treated classically. Nevertheless, a complete theory for describing the evolution of a electromagnetic field in a dielectric waveguide, such as an optical fiber, must include a quantum description of the radiation field [17]. The effects of thermal vibration states of the fiber cause fluctuations on both the macroscopic and molecular scales, which leads to a time delayed fiber response due to the Raman effect [17]. In addition, the quantum description of the electromagnetic field propagation in the fiber accounts also with the quantum noise terms arising from the interaction between photons and optical phonons inside the waveguide, and arising from the coupling between photons and absorption reservoirs [17, 18].

The interaction between photons in a fiber is mediated through the dielectric material that constitutes the fiber [18]. The total Hamiltonian that describes that interaction takes into account the waveguide dispersion and loss, the electronic Kerr effect and the Raman-like nonlinearity. The optical fiber will be treated in this section as a single transverse mode waveguide with dispersion and nonlinearity [17, 18]. Moreover, we assume a single polarization direction. In the infinite volume limit, we can define the annihilation field operator $\hat{A}(z,t)$ associated with the slowly varying envelope of the electromagnetic field as [19, 20]

$$\hat{A}(z,t)=\frac{\sqrt{v_g}}{2\pi}\int dk\hat{b}(k,t)e^{i(k-k_0)z+i\omega_0 t}\,, \quad (2.64)$$

where $\hat{b}(k,t)$ is the annihilation operator at time t for modes with wave vector k and angular frequency $\omega(k)$, z is the waveguide longitudinal coordinate, k_0 is the central wavenumber within

a frequency bandwidth, and $\omega_0 = \omega(k_0)$ is the carrier frequency [17, 18, 20, 21]. We can expand $\omega(k)$ around k_0 until the m-th order [17, 18, 22]

$$\omega(k) \approx \omega_0 + \sum_{m=1}^{+\infty} \left[\left. \frac{\partial^m \omega}{\partial k^m} \right|_{k=k_0} \frac{(k-k_0)^m}{m!} \right], \tag{2.65}$$

where $v_g = [\partial\omega/\partial k]_{k=k_0}$ is the group velocity. Moreover, it is assumed that $\omega(k)$ describes the fiber linear response, in the limit of a spatially uniform environment [17, 18]. In (2.64), $\hat{b}(k)$ is a boson annihilation operator for modes with wave vector k, with commutation relation [17, 18]

$$\left[\hat{b}(k,t), \hat{b}^\dagger(k',t')\right] = 2\pi\delta(k-k')\delta(t-t'), \tag{2.66}$$

where $\hat{b}^\dagger(k',t')$ is the boson creation operator for modes with wave vector k' at time t'. The field operator $\hat{A}(z,t)$ in (2.64) obeys to the commutation relation [19, 20]

$$\left[\hat{A}(z,t), \hat{A}^\dagger(z',t')\right] = v_g\delta(z-z')\delta(t-t'). \tag{2.67}$$

Under the rotating-wave approximation, where the rapidly oscillating terms of the Hamiltonian are neglected, the fiber Hamiltonian can be written as [17, 18, 22]

$$\begin{aligned} \hat{H}_F = \frac{\hbar}{2}\int \Bigg\{ iv_g \left[\frac{\partial}{\partial z}\hat{A}^\dagger(z,t)\hat{A}(z,t) - \hat{A}^\dagger(z,t)\frac{\partial}{\partial z}\hat{A}(z,t) \right] + \omega_0'' \frac{\partial}{\partial z}\hat{A}^\dagger(z,t)\frac{\partial}{\partial z}\hat{A}(z,t) \\ - \frac{i}{6}\omega_0''' \left[\frac{\partial^3}{\partial z^3}\hat{A}^\dagger(z,t)\hat{A}(z,t) - \hat{A}^\dagger(z,t)\frac{\partial^3}{\partial z^3}\hat{A}(z,t) \right] \Bigg\} \frac{dz}{v_g} + \hat{H}_{NL}, \end{aligned} \tag{2.68}$$

where $\hbar$ is the Planck's constant over 2π, $\hat{A}^\dagger(z,t)$ is the creation field operator, and $\hat{A}^\dagger(z,t)\hat{A}(z,t)$ represents the flux of quanta (photons) at z [19, 20]. In (2.68) the waveguide dispersion was included up to the third-order with $\omega_0'' = \left[\partial^2\omega/\partial k^2\right]_{k=k_0}$, and $\omega_0''' = \left[\partial^3\omega/\partial k^3\right]_{k=k_0}$ [17, 18, 22]. In (2.68), $\hat{H}_{NL}$ describes the fiber nonlinearities, electronic and Raman, and is given by [19, 20]

$$\hat{H}_{NL} = -\hbar\kappa \int \hat{n}_{NL}(z,t)\hat{A}^\dagger(z,t)\hat{A}(z,t)dz, \tag{2.69}$$

where $\kappa = -v_g^{-1}\left[d\omega_0/dn\right]$ with n representing the local index of refraction. The Hermitian operator $\hat{n}_{NL}(z,t)$ commutes at equal times with the envelope operators and represents the matter degrees of freedom affecting the field [19, 20]. Since $\hat{n}_{NL}(z,t)$ couples to the envelope operators only through its intensity and since optical nonlinearities are very small, it is sufficient expand $\hat{n}_{NL}(z,t)$ up to first order in its dependence on the photon flux [19, 20]

$$\kappa\hat{n}_{NL}(z,\tau) = \int_{-\infty}^{\tau} R^{(3)}(\tau-\tau')\hat{A}^\dagger(z,\tau')\hat{A}(z,\tau')d\tau' + \hat{m}(z,\tau), \tag{2.70}$$

where we introduce the retarded time $\tau = t - z/v_g$. The function $R^{(3)}(\tau - \tau')$ describes the response of $\hat{n}_{NL}(z,\tau)$ to the optical field, given by [17–20]

$$R^{(3)}(\tau - \tau') = (\hbar\omega_0)\gamma R^{(3)}_{xxxx}(t - \tau)\,, \tag{2.71}$$

with γ representing the nonlinear parameter of the waveguide (2.31), and $R^{(3)}_{xxxx}$ is given by (2.15). The operator $\hat{m}(z,\tau)$ in (2.70) describes the quantum and thermal fluctuations present in $\hat{n}_{NL}(z,\tau)$ in the absence of optical field [19, 20]. Moreover, $\hat{m}(z,\tau)$ describes the coupling of the field to a collection of localized, independent, medium oscillators (optical phonon modes), given by [19–21, 23]

$$\hat{m}(z,\tau) = \int_0^{+\infty} d\Omega \frac{\sqrt{W(\Omega)}}{2\pi} \left\{ \hat{d}^{\dagger}_{\Omega}(z) e^{i\Omega\tau} + \hat{d}_{\Omega}(z) e^{-i\Omega\tau} \right\}, \tag{2.72}$$

where $W(\Omega)$ is a spectral weighting function given by [23, 24]

$$W(\Omega) = 2\mathrm{Im}\left[\tilde{R}^{(3)}(\Omega)\right], \tag{2.73}$$

with $\tilde{R}^{(3)}(\Omega)$ representing the Fourier transform of $R^{(3)}(\tau - \tau')$. The operators $\hat{d}^{\dagger}_{\Omega}(z)$ and $\hat{d}_{\Omega}(z)$ are independent from the envelope operators, and obeys to the commutation relation [19–21, 23]

$$\left[\hat{d}_{\Omega}(z), \hat{d}^{\dagger}_{\Omega'}(z')\right] = \delta(\Omega - \Omega')\delta(z - z')\,, \tag{2.74}$$

and each phonon mode is in thermal equilibrium

$$\langle \hat{d}^{\dagger}_{\Omega}(z)\hat{d}_{\Omega'}(z')\rangle = \delta(\Omega - \Omega')\delta(z - z')n_{th}(\Omega)\,, \tag{2.75}$$

with a mean phonon number given by

$$n_{th}(\Omega) = \frac{1}{e^{\hbar|\Omega|/k_B T} - 1}\,, \tag{2.76}$$

where k_B is the Boltzmann's constant, and T is the temperature. Note that the creation operator at each Ω frequency, $\hat{d}^{\dagger}_{\Omega}(z)$, oscillates as $e^{i\Omega\tau}$, a Stokes detuning frequency. The annihilation operator at each Ω frequency, $\hat{d}_{\Omega}(z)$, oscillates as $e^{-i\Omega\tau}$, an anti-Stokes detuning frequency [23]. We will call $\hat{m}(z,\tau)$ the Raman noise source since Raman scattering is caused by the dynamics of localized molecular oscillators [20].

A fully description of the evolution of the electromagnetic field inside a waveguide must consider the absorption of light by the waveguide [17, 18, 22]. The presence of an absorption coefficient is associated with the existence of noise sources in waveguide, an absorbing reservoir. This additional effect needs to included within the present Hamiltonian model for a fully

consistent quantum theory [17, 18, 22]. The absorption reservoir can be modeled by the field to a collection of localized, independent harmonic oscillators at resonant frequency ω. In that case the Hamiltonian that describes the absorption reservoir can be written as [17, 18, 22]

$$\hat{H}_A = \hbar \int_{-\infty}^{+\infty} dz \int_{0}^{+\infty} d\omega \Bigg\{ \frac{1}{\sqrt{v_g}} \left[\hat{A}(z,t)\hat{a}^{\dagger}(z,t,\omega)G(z,\omega) + \hat{A}^{\dagger}(z,t)\hat{a}(z,t,\omega)G^{*}(z,\omega) \right] + (\omega - \omega_0)\hat{a}^{\dagger}(z,t,\omega)\hat{a}(z,t,\omega) \Bigg\}, \quad (2.77)$$

where $G(z,\omega)$ provides the frequency-dependent coupling between the radiation modes and the absorption reservoir. The reservoir annihilation and creation operators, $\hat{a}(z,t,\omega)$ and $\hat{a}^{\dagger}(z,t,\omega)$, obey to the equal-time commutation relation [17, 18, 22]

$$\left[\hat{a}(z,t,\omega), \hat{a}^{\dagger}(z',t,\omega') \right] = \delta(z-z')\delta(\omega-\omega') . \quad (2.78)$$

The time evolution for the annihilation operator of the absorbing photon reservoir is given by

$$\frac{\partial \hat{a}(z,t,\omega)}{\partial t} = -i(\omega-\omega_0)\hat{a}(z,t,\omega) - iv_g^{-1}G(z,\omega)\hat{A}(z,t) . \quad (2.79)$$

Equation (2.79) can be solve analytically, and we obtain [17, 18, 22]

$$\hat{a}(z,t,\omega) = \hat{a}(z,t_0,\omega)e^{-i(\omega-\omega_0)(t-t_0)} - iv_g^{-1}G(z,\omega)\int_{t_0}^{t} e^{-i(\omega-\omega_0)(t-t')}\hat{A}(z,t')dt' , \quad (2.80)$$

where $\hat{a}(z,t_0,\omega)$ represents the annihilation operator of the absorbing photon reservoir at initial time t_0. The initial correlations for the reservoir operators in the far past, $t_0 \to -\infty$, are given by [17, 18, 22]

$$\langle \hat{a}^{\dagger}(z,t_0,\omega)\hat{a}(z',t_0,\omega') \rangle = n_{th}(\omega)\delta(z-z')\delta(\omega-\omega') \quad (2.81)$$

$$\langle \hat{a}(z,t_0,\omega)\hat{a}^{\dagger}(z',t_0,\omega') \rangle \rangle = \left(n_{th}(\omega)+1\right)\delta(z-z')\delta(\omega-\omega') . \quad (2.82)$$

The total optical fiber Hamiltonian, $\hat{H}_T$, can be written as

$$\hat{H}_T = \hat{H}_F + \hat{H}_A . \quad (2.83)$$

2.2.1 Generalized Quantum Nonlinear Schrödinger Equation

The evolution of the field operator propagating inside the fiber can be obtained from the Heisenberg equation of motion [19, 20]

$$\frac{d\hat{A}(z,t)}{dt} = \frac{i}{\hbar}\left[\hat{H}_F + \hat{H}_A, \hat{A}(z,t)\right] + \frac{\partial \hat{A}(z,t)}{\partial t} , \quad (2.84)$$

where the last derivative acts on the explicit time dependent of the envelope contained in the overall phase in (2.64). Introducing the retarded time $\tau = t - z/v_g$ we obtain [17–20]

$$\frac{\partial \hat{A}(z,\tau)}{\partial z} = -\int_{-\infty}^{\tau} \frac{\alpha(\tau-\tau')}{2}\hat{A}(z,\tau')d\tau' - i\frac{\beta_2}{2}\frac{\partial^2 \hat{A}(z,\tau)}{\partial \tau^2} + \frac{\beta_3}{6}\frac{\partial^3 \hat{A}(z,\tau)}{\partial \tau^3}$$
$$+ i(\hbar\omega_0)\gamma\hat{A}(z,\tau)\int_{-\infty}^{\tau} R^{(3)}_{xxxx}(\tau-\tau')\hat{A}^{\dagger}(z,\tau')\hat{A}(z,\tau')d\tau' + i\sqrt{\hbar\omega_0}\hat{m}(z,\tau)\hat{A}(z,\tau) + \hat{l}(z,\tau), \quad (2.85)$$

where $\alpha(\tau) = 2\alpha_A(\tau)$ is the usual linear absorption coefficient, with $\alpha_A(\tau)$ being the net linear response of the fiber that is due to coupling to linear absorption reservoirs, given by [18, 22]

$$\alpha_A(\tau) \approx \frac{\Theta(\tau)}{2\pi}\int_{-\infty}^{+\infty} |G(z,\omega)|^2 e^{-i(\omega-\omega_0)\tau}d\omega, \quad (2.86)$$

where $G(z,\omega)$ is defined in (2.77), and $\Theta(\tau)$ is the Heaviside step function. In (2.85), $\hat{l}(z,\tau)$ represents the photon absorption reservoir. That operator describes the noise introduced by the fiber loss mechanism, through the coupling of the optical field with a thermal photon reservoir with a population following the Boltzman distribution, and spectral weight proportional to the fiber loss coefficient [18, 22, 24]

$$\hat{l}(z,\tau) = \frac{-i}{2\pi}\int_{0}^{+\infty} G^*(z,\omega)e^{-i(\omega-\omega_0)(\tau-\tau_0)}\hat{a}(z,\tau_0,\omega)d\omega, \quad (2.87)$$

where $\hat{a}(z,\tau_0,\omega)$ is defined in (2.80).

In frequency domain, the evolution of the field operator can be written as

$$\frac{\partial \hat{A}(z,\omega-\omega_0)}{\partial z} + \frac{\alpha(\omega)}{2}\hat{A}(z,\omega-\omega_0) = i\left[\frac{(\omega-\omega_0)^2}{2}\beta_2 + \frac{(\omega-\omega_0)^3}{6}\beta_3\right]\hat{A}(z,\omega-\omega_0)$$
$$+ i\frac{\hbar\omega_0}{(2\pi)^2}\gamma\iint_{-\infty}^{+\infty} d\omega_1 d\omega_2 \tilde{R}^{(3)}_{xxxx}(\omega_2-\omega_1)\hat{A}^{\dagger}(z,\omega_1-\omega_0)\hat{A}(z,\omega_2-\omega_0)\hat{A}(z,\omega+\omega_1-\omega_2-\omega_0)$$
$$+ i\frac{\sqrt{\hbar\omega_0}}{2\pi}\int_{-\infty}^{+\infty} d\omega_1 \hat{m}(z,\omega-\omega_1)\hat{A}(z,\omega_1-\omega_0) + \hat{l}(z,\omega). \quad (2.88)$$

Note that, the quantum version of the nonlinear Schrödinger equation (2.88), is similar to the classical wave equation given by (2.41), excepted some minor changes related to a correct description of the quantum effects.

Vectorial Quantum Nonlinear Schrödinger Equation

A realist treatment of the waveguide eventually needs to take into account the mode structure, since the single mode waveguide can support two orthogonal polarization modes. In that case the evolution of the field operator inside the waveguide must be described by the vectorial nonlinear Schrödinger equation, that is the quantum version of the GNLSE obtained in section 2.1.3. The vectorial quantum nonlinear Schrödinger equation can be obtained from the Hamiltonian for a three-dimensional dielectric waveguide [17]. It turns out that, as in last section, the vectorial quantum version of the GNLSE exhibits a form quite similar to that presented in section 2.1.3, except for some minor changes related to a correct description of the quantum effects for a single mode waveguide that can support two orthogonal polarization modes [5, 17]. Here we provide only the final equations for the vectorial quantum nonlinear Schrödinger equation. As result, that equation in frequency domain can be written as [5, 17]

$$\frac{\partial \hat{A}_i(z,\omega-\omega_0)}{\partial z} = i\sum_j \tilde{R}^{(1)}_{ij}(\omega)\hat{A}_j(z,\omega-\omega_0) + i\frac{\sqrt{\hbar\omega_0}}{2\pi}\sum_j \int_{-\infty}^{+\infty} d\omega_1 \hat{m}_{ij}(z,\omega-\omega_1)\hat{A}_j(z,\omega_1-\omega_0)$$
$$+ i\frac{\hbar\omega_0}{(2\pi)^2}\gamma \iint_{-\infty}^{+\infty} d\omega_1 d\omega_2 \sum_{j,k,l} \tilde{R}^{(3)}_{ijkl}(\omega_2-\omega_1)\hat{A}^\dagger_k(z,\omega_1-\omega_0)\hat{A}_l(z,\omega_2-\omega_0)\hat{A}_j(z,\omega+\omega_1-\omega_2-\omega_0)$$
$$+ \hat{l}_i(z,\omega)\,, \quad (2.89)$$

where $i,j,k,l = x,y$, $\tilde{R}^{(1)}_{ij}(\omega)$ is given by (2.36) and accounts for, dispersion, loss and birefringence effects, and $\tilde{R}^{(3)}_{ijkl}(\Omega)$ is given by (2.17) and accounts for the nonlinear processes that occurs inside the waveguide [5, 17]. In (2.89), field operator satisfy the commutation relation [19, 20]

$$\left[\hat{A}_i(z,\omega), \hat{A}^\dagger_j(z',\omega')\right] = 2\pi\delta_{ij}\delta(z-z')\delta(\omega-\omega')\,. \quad (2.90)$$

Moreover, the noise operators in (2.89) satisfy the commutation relations [5, 17]

$$\left[\hat{m}_{ij}(z,\Omega), \hat{m}^\dagger_{kl}(z',\Omega')\right] = 2\pi\delta(z-z')\delta(\Omega-\Omega')2\gamma\,\mathrm{Im}\left[\tilde{R}^{(3)}_{ijkl}(\Omega)\right], \quad (2.91)$$

and

$$\left[\hat{l}_i(z,\omega), \hat{l}^\dagger_j(z',\omega')\right] = 2\pi\delta_{ij}\delta(z-z')\delta(\omega-\omega')2\,\mathrm{Im}\left[\tilde{R}^{(1)}_{ij}(\omega)\right]. \quad (2.92)$$

The expectation values for the reservoirs are given by [5, 17]

$$\langle \hat{m}^\dagger_{ij}(z,\Omega)\hat{m}_{kl}(z',\Omega')\rangle = 2\pi\delta(z-z')\delta(\Omega-\Omega')2\gamma\,\mathrm{Im}\left[\tilde{R}^{(3)}_{ijkl}(\Omega)\right](n_{th}(\Omega)+\Theta(-\Omega))\,, \quad (2.93)$$

and

$$\langle \hat{l}_i^{\dagger}(z,\omega)\hat{l}_j(z',\omega')\rangle = 2\pi\delta_{ij}\delta(z-z')\delta(\omega-\omega')2\,\mathrm{Im}\left[\tilde{R}_{ij}^{(1)}(\omega)\right] n_{th}(\omega) \tag{2.94}$$

$$\langle \hat{l}_i(z,\omega)\hat{l}_j^{\dagger}(z',\omega')\rangle = 2\pi\delta_{ij}\delta(z-z')\delta(\omega-\omega')2\,\mathrm{Im}\left[\tilde{R}_{ij}^{(1)}(\omega)\right] (n_{th}(\omega)+1)\,, \tag{2.95}$$

where $n_{th}(\omega)$ is given by (2.76).

In time domain the vectorial quantum nonlinear Schrödinger equation can be written as [5]

$$\frac{\partial \hat{A}_i(z,\tau)}{\partial z} = i\int_{-\infty}^{\tau}\sum_j R_{ij}^{(1)}(\tau-\tau')\hat{A}(z,\tau')d\tau' + i\sqrt{\hbar\omega_0}\sum_j \hat{m}_{ij}(z,\tau)\hat{A}_j(z,\tau) + \hat{l}_i(z,\tau) + i(\hbar\omega_0)\gamma\sum_j \hat{A}_j(z,\tau)\int_{-\infty}^{\tau} R_{ijkl}^{(3)}(\tau-\tau')\hat{A}_k^{\dagger}(z,\tau')\hat{A}_l(z,\tau')d\tau'\,, \tag{2.96}$$

where $R_{ij}^{(1)}(\tau-\tau')$ is the Fourier transform of $\tilde{R}_{ij}^{(1)}(\omega)$ and is given by (2.39), and $R_{ijkl}^{(3)}(\tau-\tau')$ is given by (2.15).

References

[1] G. P. Agrawal, *Nonlinear Fiber Optics*, 4th ed. San Diego: Academic Press, 2007.

[2] R. W. Boyd, *Nonlinear Optics*, 3rd ed. Academic Press, 2008.

[3] R. Hellwarth, J. Cherlow, and T.-T. Yang, "Origin and frequency dependence of nonlinear optical susceptibilities of glasses," *Phys. Rev. B*, vol. 11, pp. 964–967, 1975.

[4] R. W. Hellwarth, *Third-order optical susceptibilities of liquids and solids*. New York: Pergamon Press, Oxford, 1977.

[5] Q. Lin, F. Yaman, and G. P. Agrawal, "Photon-pair generation in optical fibers through four-wave mixing: Role of Raman scattering and pump polarization," *Phys. Rev. A*, vol. 75, p. 023803, 2007.

[6] C. Headley III and G. P. Agrawal, "Unified description of ultrafast stimulated Raman scattering in optical fibers," *J. Opt. Soc. Am. B*, vol. 13, pp. 2170–2177, 1996.

[7] Q. Lin and G. P. Agrawal, "Vector theory of stimulated Raman scattering and its application to fiber-based Raman amplifiers," *J. Opt. Soc. Am. B*, vol. 20, pp. 1616–1631, 2003.

[8] Q. Lin, "Polarization and fiber nonlinearities," Ph.D. dissertation, The Institute of Optics, The College School of Engineering and Applied Sciences - University of Rochester, Rochester, New York, 2006.

[9] F. Yaman, "Fiber-optic parametric amplifiers: Their advantages and limitations," Ph.D. dissertation, The Institute of Optics, The College School of Engineering and Applied Sciences - University of Rochester, Rochester, New York, 2006.

[10] R. Stolen and J. E. Bjorkholm, "Parametric amplification and frequency conversion in optical fibers," *IEEE Journal of Quantum Electronics*, vol. 18, pp. 1062–1072, 1982.

[11] X. Liu, X. Zhou, and C. Lu, "Multiple four-wave mixing self-stability in optical fibers," *Physical Review A*, vol. 72, p. 013811, 2005.

[12] I. Kaminow and T. Li, *Optical Fiber Telecommunications IV B*, 4th ed. San Diego: Academic Press, 2002, ch. Polarization-Mode Dispersion, pp. 725–861.

[13] J. P. Gordon and H. Kogelnik, "PMD fundamentals: Polarization mode dispersion in optical fibers," *PNAS*, vol. 97, pp. 4541–4550, 2000.

[14] Q. Lin and G. Agrawal, "Effects of polarization-mode dispersion on cross-phase modulation in dispersion-managed wavelength-division-multiplexed systems," *IEEE/OSA Journal of Lightwave Technology*, vol. 22, pp. 977–987, 2004.

[15] P. K. Wai and C. R. Menyuk, "Polarization mode dispersion, decorrelation, and diffusion in optical fibers with randomly varying birefringence," *IEEE/OSA Journal of Lightwave Technology*, vol. 14, pp. 148–157, 1996.

[16] P. K. A. Wai, C. R. Menyuk, and H. H. Chen, "Stability of solitons in randomly varying birefringent fibers," *Optics Letters*, vol. 16, pp. 1231–1233, 1991.

[17] P. D. Drummond, *Coherence and Quantum Optics VII*. Springer, 1996, ch. Quantum Theory of Fiber-Optics and Solitons, pp. 323–332.

[18] P. D. Drummond and J. F. Corney, "Quantum noise in optical fibers. I. Stochastic equations," *J. Opt. Soc. Am. B*, vol. 18, pp. 139–152, 2001.

[19] L. Boivin, F. X. Kärtner, and H. A. Haus, "Analytical solution to the quantum field theory of self-phase modulation with a finite response time," *Phys. Rev. Lett.*, vol. 73, pp. 240–243, 1994.

[20] L. Boivin, "Sagnac-loop squeezer at zero dispersion with a response time for the kerr nonlinearity," *Phys. Rev. A*, vol. 52, pp. 754–766, 1995.

[21] F. X. Kärtner, D. J. Dougherty, H. A. Haus, and E. P. Ippen, "Raman noise and soliton squeezing," *J. Opt. Soc. Am. B*, vol. 11, pp. 1267–1276, 1994.

[22] C. Shi-Hua, Z. Shao-Wu, and S. Du-Fang, "Quantum theory of femtosecond soliton propagation in single-mode optical fibers," *Communications in Theoretical Physics*, vol. 41, pp. 943–948, 2004.

[23] P. L. Voss and P. Kumar, "Raman-effect induced noise limits on (3) parametric amplifiers and wavelength converters," *Journal of Optics B: Quantum and Semiclassical Optics*, vol. 6, p. S762, 2004.

[24] P. L. Voss, K. G. Köprülü, and P. Kumar, "Raman-noise-induced quantum limits for $\chi(3)$ nondegenerate phase-sensitive amplification and quadrature squeezing," *J. Opt. Soc. Am. B*, vol. 23, pp. 598–610, 2006.

Chapter 3

Few-Photon Generation in Optical Fibers

SINGLE photon sources are basic elements for quantum key distribution (QKD) systems [1]. However, true or on-demand single photon sources are very complex to implement, since in general they demand cryogenic temperatures or most be operated in vacuum [1, 2]. Due to that, practical implementations of QKD in optical fibers rely on faint laser pulses as an approximation to a single photon source. Recently, the four-wave mixing (FWM) has been used in quantum optics experiments to generate single-photons and entangled photon-pairs [3–7]. Single-photons and entangled photon-pairs have been used for quantum cryptographic experiments, mainly for QKD. When compared with others techniques for single-photons and entangled photon-pairs generation, FWM has the advantage of generating the photons already inside the optical fiber. In these experiments, FWM is obtained with very low pump powers [8–10]. Therefore, an accurate description of the FWM process in this low power regime is required in order to guide this new kind of experiments.

In this Chapter we analyze theoretically and experimentally the classical process of FWM in optical fibers. From the experimental data we propose a new parameter, the effective nonlinear parameter, that accounts for the loss of efficiency in the FWM process due to the polarization decorrelation between all the optical fields involved in that nonlinear process during the evolution in the fiber. This Chapter is based on the references [11–15], and is organized as follows: Section 3.1 describes the experimental setup used to analyze the FWM process in a low power regime. In section 3.2 a new theoretical model to describe the FWM process in a low power regime is presented. We also discuss the role of the nonlinear contribution on the phase-matching condition. We also analyze the efficient generation of the idler wave outside the zero-dispersion of the fiber and with pump and signal far apart. In section 3.3 we analyze the polarization dependent effects in the efficiency of the FWM process. In section 3.4 we use the classical process

of FWM to obtain a source of few-photons, and we use that photons to implement a fiber-optic quantum channel. The main results presented in this Chapter are summarized in section 3.5. All the theoretical results presented in this Chapter are confronted with experimental data, obtained for a dispersion-shifted fiber (DSF).

3.1 Stimulated Four-Wave Mixing Process in a Low Power Regime

The classical process of FWM occurs when light of two or more frequencies (known as pump and signal fields) are launched into a fiber, giving rise to a new frequency (known as idler). At the same time that the idler is generated the signal is amplified [8]. FWM is a nonlinear process, described by the third-order nonlinear susceptibility, $\chi^{(3)}$, and its origin is in the nonlinear response of bound electrons to an applied optical field [8]. FWM is a major source of nonlinear crosstalk in wavelength-division multiplexing lightwave systems [16]. Besides that, FWM can be used to implement fiber-optic parametric amplifiers [17–19], wavelength converters [18, 20–22] and single-photons and entangled photon-pairs sources [10, 23, 24].

In 1974, the phase-matched nonlinear mixing in a silica fiber was observed [25]. Since then, generalized studies of FWM in optical fibers taking into account the stimulated Raman scattering (SRS) and polarization effects have been carried out [9, 26–29]. Most of the work related with FWM in optical fibers has been done around the zero-dispersion wavelength of the fiber [30–33], or with the pump and signal wavelengths placed very closely [34]. In these conditions the phase-matching is easily achieved and efficient FWM is obtained [30–34]. All these experiments were performed in a high power regime in order to enhance the FWM effect.

3.1.1 Experimental Setup and the Four-Wave Mixing Process

A schematic of our experimental setup is show in Fig. 3.1. This setup was used to measure the optical power of the idler wave generated through the FWM process in a low power regime. In the experimental setup, Fig. 3.1, a pump, λ_1 from a distributed feedback (DFB) laser source operating in a continuous mode passes through a polarization controller (PC)-1 before being coupled to another optical signal, λ_2 from a tunable laser source, that is modulated externally to produce optical pulses with a width at half maximum of approximately 1.6 ns and repetition rate of 610.3 kHz. The two optical fields are launched into a DSF, with incident powers $P_1(0)$ and $P_2(0)$ for pump and signal fields, respectively. The DSF has a dispersion slope at zero-dispersion

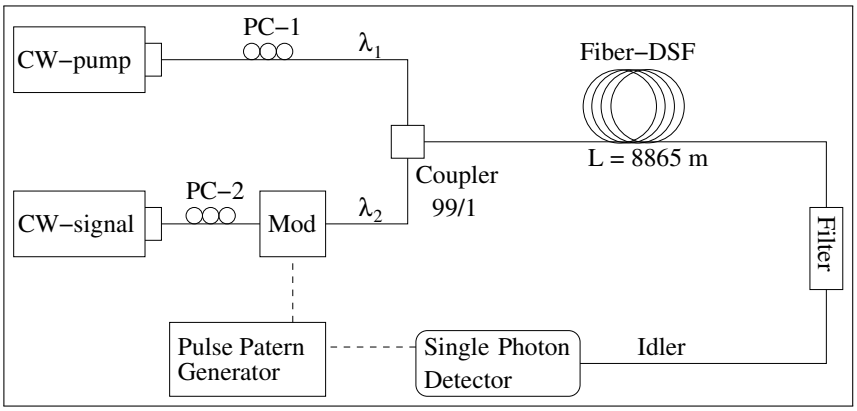

Figure 3.1: Experimental arrangement for measuring the optical power generated through FWM in a low power regime. The dashed lines represent electrical signals and the solid lines the optical path. Details of the experiment are presented in the text.

wavelength $dD_c/d\lambda = 0.069$ ps/nm^2-km, length $L = 8865$ m, zero-dispersion wavelength $\lambda_0 = 1547.34$ nm, attenuation $\alpha_{dB/km} = 0.2$ dB/km and nonlinear coefficient $\gamma = 2.36$ W^{-1}km^{-1}. The zero-dispersion wavelength and the dispersion slope of the fiber were measured with an *Optical Network Analyzer, 86038-90B01* from Agilent. At the fiber output, a filter blocks the pump and signal waves. The idler wave, $\lambda_3 = \lambda_1\lambda_2/(2\lambda_2 - \lambda_1)$ [8, 34], passes through the filter and reaches a single-photon detector. The single-photon detector is based on an avalanche photo diode (APD), operating in the so-called Geiger mode, being $T_g = 2.5$ ns the time during which the gate of the detector is open. The detector quantum efficiency is $\eta_{det} = 10\%$ and the dark count probability per gate is $Pr_{dc} = 5 \times 10^{-5}$ [35]. The noise equivalent power (NEQ) of the detector is NEQ $\approx 2.56 \times 10^{-16}$ W$/\sqrt{\text{Hz}}$, and the probability of having a count when a single-photon reaches the detector compared with the probability of having a count due to the dark counts is $Pr_{\text{eff}} = 5 \times 10^{-4}$ [36]. The optical power of the idler wave can be obtained from the average number of photons per pulse that arrive to the single-photon detector using

$$P_m = \frac{\langle n \rangle hc}{\lambda_3 T_g} 10^{\alpha_d/10}, \tag{3.1}$$

where P_m represents the measured idler power at the exit of the fiber, $\langle n \rangle$ is the average number of idler photons per pulse that arrive to the single-photon detector, h is the Planck constant, c is the speed of light in vacuum and α_d is the attenuation, in decibels, from the fiber output to the detector. From (3.1) with $\alpha_d = 0$ and with $\langle n \rangle$ replaced by $n \equiv 1$ we obtain the minimum measurable power of the detector, $P_m \approx 5 \times 10^{-11}$ W. In our experiment we perform the estimation of $\langle n \rangle$ using a measurement period of 20 s. The average number of idler photons that reaches to

the single-photon detector is given by [37, 38]

$$\langle n \rangle = \frac{1}{\eta_{det}} \ln\left(\frac{Pr_{dc}-1}{Pr_{av}-1}\right), \tag{3.2}$$

where Pr_{av} is the measured probability of avalanche per gate, i.e. the detector counting rate divided by the trigger frequency obtained from the pulse pattern generator, see Fig. 3.1.

The FWM process in optical fibers was investigated, theoretically and experimentally, by Hill *et al.* [39], and their work was latter reformulated by Shibata *et al.* [40] to include the dependence of the phase-matching. According with [30, 34, 40], the optical power evolution of the idler wave in the single pump case can be described by

$$P_3(z) = (\gamma P_1(0) z_{\text{eff}})^2 P_2(0) \exp\{-\alpha z\} \eta, \tag{3.3}$$

with

$$z_{\text{eff}} = \frac{1-\exp\{-\alpha z\}}{\alpha}, \tag{3.4}$$

where α is the fiber losses, and η is the efficiency of the process given by

$$\eta = \frac{\alpha^2}{\alpha^2+(\Delta\beta)^2}\left(1+\frac{4\exp\{-\alpha z\}\sin^2(\Delta\beta z/2)}{(1-\exp\{-\alpha z\})^2}\right), \tag{3.5}$$

and $\Delta\beta$ is the phase-matching condition

$$\Delta\beta = -\frac{2\pi c\lambda_0^3}{\lambda_1^3\lambda_2^2}\frac{dD_c}{d\lambda}\bigg|_{\lambda_0}(\lambda_1-\lambda_0)(\lambda_1-\lambda_2)^2. \tag{3.6}$$

3.2 Four-Wave Mixing in a Low Power Regime

We assume that all fields involved in the FWM process (pump, signal and idler) remain co-polarized along the propagation in the fiber, and in order to avoid multiple FWM processes in the optical fiber [41–43], the pump and signal powers are maintained in a low power regime. Under the slowly varying envelope approximation, the evolution of the electrical field complex amplitudes inside an optical fiber (A_1 for pump, A_2 for signal and A_3 for idler) are governed by the nonlinear Schrödinger equation (NSE) [8]

$$\frac{\partial A}{\partial z}+\frac{\alpha}{2}A = \sum_{m=0}^{+\infty}\frac{i^{m+1}\beta_m}{m!}\frac{\partial^m A}{\partial t^m}+i\gamma\left[1+\frac{i}{\omega_0}\frac{\partial}{\partial t}\right]P^{NL}(z,t), \tag{3.7}$$

where β_m is the m^{th} order dispersion coefficient and $P^{NL}(z,t)$ is the third-order nonlinear polarization given by

$$P^{NL}(z,t) = A(z,t)\int_{-\infty}^{+\infty} R(\tau)|A(z,t-\tau)|^2 d\tau, \tag{3.8}$$

where $R(\tau)$ is the fiber nonlinear response function [8]. Equation (3.7) is quite general in the sense that it includes the effects of group-velocity dispersion, attenuation, self-phase modulation (SPM), cross-phase modulation (XPM), SRS and FWM process. Equation (3.7) does not have an analytical solution. However, with some considerations an approximated analytical solution can be obtained. Assuming that each field component is not time dependent (continuous wave (CW) condition), that $|A_1|^2 \gg |A_{2,3}|^2$, undepleted-pump approximation [8], and instantaneous nonlinear response [8], we obtain

$$\frac{\partial A_1(z)}{\partial z} + \frac{\alpha}{2}A_1(z) \approx i\gamma A_1(z)P_1(z), \tag{3.9a}$$

$$\frac{\partial A_2(z)}{\partial z} + \frac{\alpha}{2}A_2(z) \approx i\gamma\Big[2A_2(z)P_1(z) + A_1^2(z)A_3^*(z)e^{-i\Delta\beta z}\Big], \tag{3.9b}$$

$$\frac{\partial A_3(z)}{\partial z} + \frac{\alpha}{2}A_3(z) \approx i\gamma\Big[2A_3(z)P_1(z) + A_1^2(z)A_2^*(z)e^{-i\Delta\beta z}\Big], \tag{3.9c}$$

where

$$\Delta\beta \;=\; \beta(\omega_2) + \beta(\omega_3) - 2\beta(\omega_1). \tag{3.10}$$

Equation (3.9a) has an analytical solution

$$A_1(z) = A_1(0)\exp\{i\phi(z)\}\exp\{-\alpha z/2\}, \tag{3.11}$$

where $P_1(0) = |A_1(0)|^2$ is the incident pump power, and

$$\phi(z) = \int_0^z \gamma P_1(z')dz' = \gamma P_1(0)\frac{1-\exp\{-\alpha z\}}{\alpha}, \tag{3.12}$$

is the nonlinear phase shift caused by the Kerr effect [44]. By introducing the substitutions [44]

$$A_2(z) = A_s(z)\exp\left[i\left(\phi(z) - \frac{\Delta\beta}{2}z\right) - \frac{\alpha}{2}z\right], \tag{3.13a}$$

$$A_3(z) = A_i(z)\exp\left[i\left(\phi(z) - \frac{\Delta\beta}{2}z\right) - \frac{\alpha}{2}z\right], \tag{3.13b}$$

and assuming that only the signal and pump waves are incident at the fiber input, and considering $\alpha = 0$, the signal and idler waves at distance z are given by

$$A_s(z) = A_s(0)\left(\cos(\kappa z) + \frac{i}{\kappa}\left[\frac{\Delta\beta}{2} + \gamma P_1(0)\right]\sin(\kappa z)\right), \tag{3.14}$$

and

$$A_i(z) = i\gamma P_1(0) A_s^*(0)\frac{\sin(\kappa z)}{\kappa}. \tag{3.15}$$

In (3.14) and (3.15) the parametric gain, κ, is given by

$$\kappa = \sqrt{\frac{\Delta\beta}{2}\left(\frac{\Delta\beta}{2} + 2\gamma P_1(0)\right)}. \tag{3.16}$$

The effect of fiber losses is taken into account by replacing $P_1(0)$ in (3.14) and (3.15) with $P_1(0)z_{\text{eff}}/z$, valid for low-loss fibers [44]. In this regime the parametric gain is written as

$$\kappa = \sqrt{\frac{\Delta\beta}{2}\left(\frac{\Delta\beta}{2} + 2\gamma P_1(0) z_{\text{eff}}/z\right)}, \tag{3.17}$$

where contributions from the phase-matching condition $\Delta\beta$ and nonlinear effects, $\gamma P_1(0)$, are included. If κ is real, the optical power of the idler wave can be express as

$$P_3(z) = (\gamma P_1(0) z_{\text{eff}})^2 P_2(0)\left|\frac{\sin(\kappa z)}{\kappa z}\right|^2 \exp\{-\alpha z\}. \tag{3.18}$$

From (3.6) and (3.17), κ is real for $\lambda_1 < \lambda_0$, or if $\lambda_1 > \lambda_0$ and

$$\frac{\Delta\beta}{2} + 2\gamma P_1(0) z_{\text{eff}}/z < 0. \tag{3.19}$$

However, the parametric gain κ becomes imaginary if $\lambda_1 > \lambda_0$ and [5]

$$\frac{\Delta\beta}{2} + 2\gamma P_1(0) z_{\text{eff}}/z > 0. \tag{3.20}$$

In that regime the parametric gain is written as

$$\kappa = i\sqrt{-\frac{\Delta\beta}{2}\left(\frac{\Delta\beta}{2} + 2\gamma P_1(0) z_{\text{eff}}/z\right)}, \tag{3.21}$$

and the optical power is expressed as

$$P_3(z) = (\gamma P_1(0) z_{\text{eff}})^2 P_2(0)\left|\frac{\sinh(\kappa z)}{\kappa z}\right|^2 \exp\{-\alpha z\}. \tag{3.22}$$

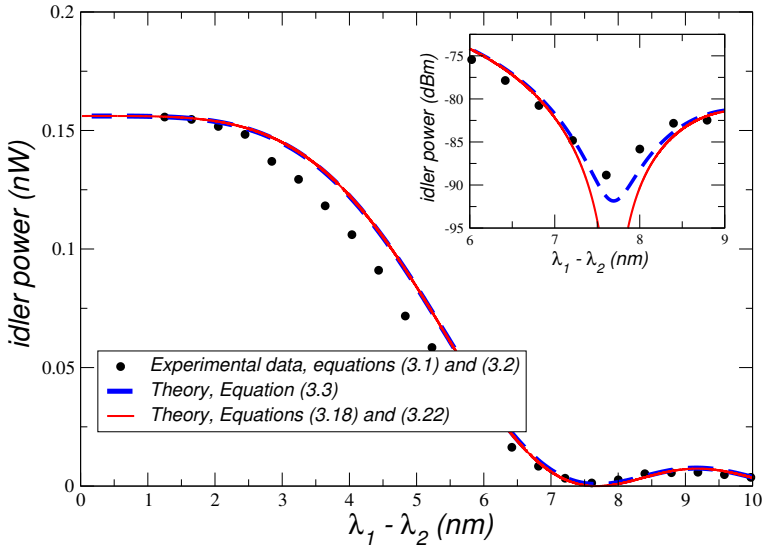

Figure 3.2: Optical power of idler wave as a function of wavelength separation between pump and signal fields.The circles represent the measured optical power, the dashed line represents the theoretical model given by (3.3) and the solid line represents the theoretical model given by (3.18). Incident pump and signal powers are $P_1(0) = 8.71$ mW and $P_2(0) = 3.73 \times 10^{-3}$ mW, respectively, and the pump wavelength is $\lambda_1 = 1547.57$ nm.

If fiber losses are neglected, equations (3.18) and (3.22) are equivalent to results presented in [8, 18, 45]. Comparing (3.3) with (3.18), the efficiency of the FWM process is now given by $\eta = |\sin(\kappa z)/\kappa z|^2$ and it is dependent of the nonlinear contribution $\gamma P_1(0)$. For high values of the nonlinear contribution (3.3) and (3.18) produce different results.

In Fig. 3.2 we plot the measured optical power and the theoretical predictions given by (3.3), (3.18) and (3.22) for the idler wave as a function of wavelength separation between pump and signal fields. From Fig. 3.2 we can see that for 2.8 nm $< \lambda_1 - \lambda_2 <$ 5 nm the theoretical models and the experimental data does not coincide. That difference is analyzed in section 3.3.

From (3.18) and (3.22) if $\lambda_1 = \lambda_0$ or if $\lambda_1 = \lambda_2$ the phase-matching condition becomes null (consequently $\kappa = 0$), and the optical power of the idler wave is maximum. However, efficient generation of idler wave can be achieved even when $\Delta\beta \neq 0$, making $\kappa = 0$. That particular case of interest occurs when the incident pump power is sufficiently strong so that

$$P_1(0) = -\frac{\Delta\beta}{4\gamma}\frac{z}{z_{\text{eff}}}, \tag{3.23}$$

and the system is operating in the anomalous-dispersion regime, $\lambda_1 > \lambda_0$. In this case, although $\lambda_1 \neq \lambda_0$ the optical power of the idler wave grows as if $\lambda_1 = \lambda_0$.

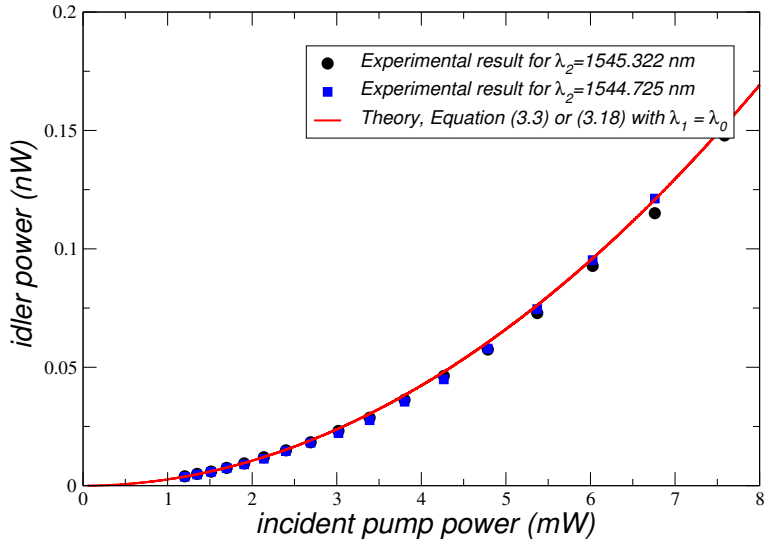

Figure 3.3: Optical power of idler wave as a function of incident pump power, in the zero-dispersion wavelength of the fiber. The circles and the squares represent the experimental data, and the line represents the theoretical model given by (3.3) or (3.18) with $\lambda_1 = \lambda_0$. The optical fiber input signal power used was $P_2(0) = 4.81 \times 10^{-3}$ mW.

In Fig. 3.3 we plot the optical power of the idler wave as a function of the pump power when $\lambda_1 = \lambda_0$, for two fixed values of the signal wavelength: $\lambda_2 = 1544.725$ nm and $\lambda_2 = 1545.322$ nm. We see from Fig. 3.3 that the idler power varies with the pump power quadratically (for the two distinct values of λ_2). This is expected from the theory, according with (3.3) and (3.18), when $\Delta\beta = 0$. We can also see that the idler power is almost independent of the signal wavelength. The fluctuations of the zero-dispersion wavelength along the fiber length can influence the FWM process [30, 46, 47]. However, fluctuations with short coherence length, $\gamma P_1(0) L_c \ll 1$ (where L_c is the length over which the fluctuations occurs), and narrow wavelength separations, can be neglected. [46, 47]. Even if we assume that $L_c \approx L$, we obtain in our case $\gamma P_1(0) L_c \approx 0.18$. Considering the good agreement between the theoretical predictions and the experimental data present in Fig. 3.3, we assume that the fluctuations of the fiber zero-dispersion has almost no impact in our experiment.

In Fig. 3.4 we analyze the possibility of efficient generation of the idler wave inside an optical fiber outside the zero-dispersion of the fiber and with pump and signal far apart. Fig. 3.4 shows the measured optical power for $\lambda_1 \neq \lambda_0$ with the incident pump power given by (3.23) and the theoretical model given by (3.18) with $\lambda_1 = \lambda_0$ for the idler wave as a function of incident pump power. The experimental results show a good agreement with theoretical predictions. This means that the generation of the idler field becomes the same as for the case when the pump wavelength

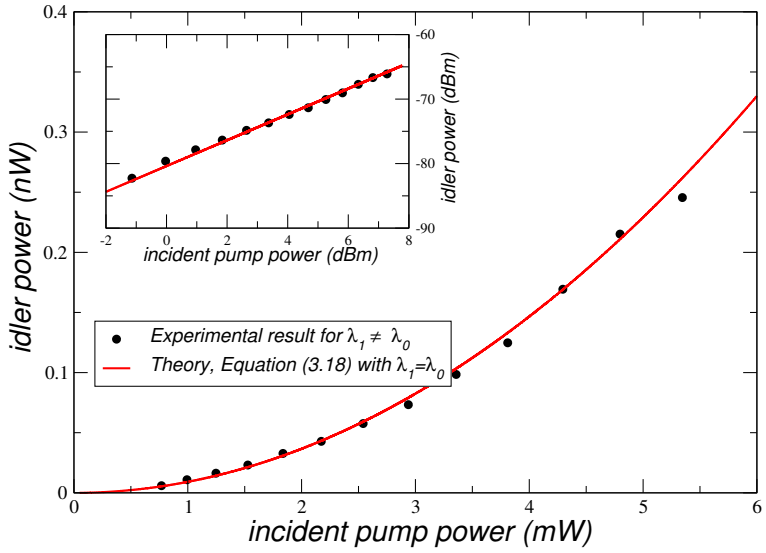

Figure 3.4: Representation of the measured optical power of the idler field as a function of incident pump power for $\lambda_1 = 1547.37$ nm. The line represents the theoretical model given by (3.18) when $\lambda_1 = \lambda_0$. The incident signal power used was $P_2(0) = 1.67 \times 10^{-2}$ mW and the signal wavelength varies between 1543.532 nm and 1545.92 nm. The experimental incident pump power was adjusted according with (3.23).

is in the zero-dispersion wavelength of the fiber or when the signal and pump wavelengths are placed very closely. The explanation of this result is only possible due to the inclusion of the nonlinear contribution in the parametric gain.

3.3 Polarization Effects on the Generation of the Idler Wave

The efficiency of the FWM process is dependent of the relative polarization of pump and signal fields [8]. The best efficiency is obtained when pump and signal are co-polarized, whereas the orthogonal scheme leads to the worst efficiency [8]. When pump and signal are orthogonal the optical power of the idler wave is about $1/9$ of the power obtained with the co-polarized scheme [8, 9]. In the results presented in Fig. 3.2, we can see that with the increase of the wavelength separation between pump and signal, the idler power measured experimentally is smaller than the theoretical predictions. In the theoretical model it was assumed that all fields remain co-polarized along the propagation in the fiber. However, when the wavelength separation between pump and signal is increased the fields go from an almost co-polarized situation to a decorrelated state of polarization (SOP). The loss of efficiency in the FWM process due to the polarization decorrelation can be seen as a reduction of the value of the nonlinear parameter γ [48–52]. This

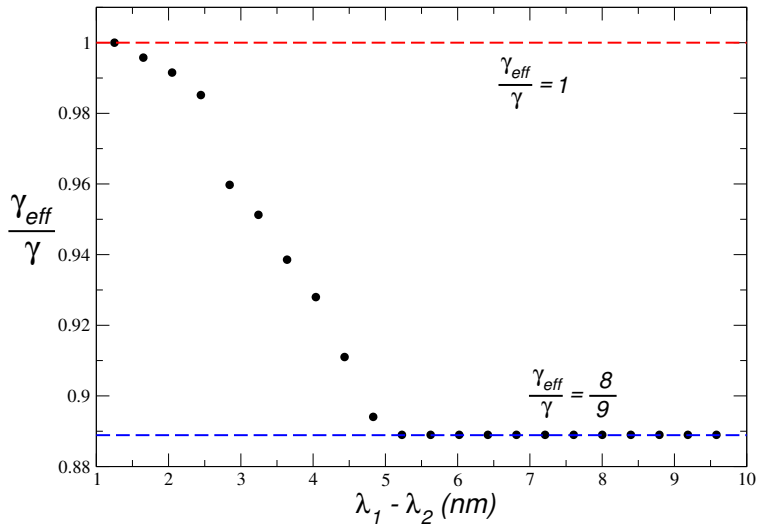

Figure 3.5: Representation of the γ_{eff} variation with the wavelength separation between pump and signal fields. The data presented in the figure is obtained by fitting the experimental data presented in Fig. 3.2 to (3.18) and (3.22), with γ replaced by γ_{eff}.

can be described through a new parameter called effective nonlinear parameter γ_{eff}, which is dependent of the wavelength separation between pump and signal fields. If the nonlinear parameter present in (3.18) and (3.22) is replaced by the effective nonlinear parameter, γ_{eff}, the loss of efficiency in the generation of idler wave due to polarization effects can also be described by these two equations.

It can be seen in Fig. 3.5 the variation of the effective nonlinear parameter with the wavelength separation between pump and signal fields. The points represented in Fig. 3.5 were obtained by fitting the experimental data present in Fig. 3.2 to (3.18) and (3.22), with γ replaced by γ_{eff}. The results show that the effective nonlinear parameter is approximately equals to γ for $\lambda_1 - \lambda_2 < 2.8$ nm. However, with the increasing separation between pump and signal fields, the value of γ_{eff} rapidly decreases to $8\gamma/9$, and remains constant for $\lambda_1 - \lambda_2 > 5$ nm. This value for the effective nonlinear parameter is in agreement with theoretical predictions for polarization dependent processes in a strong mode coupling [48–52].

In Fig. 3.6 we present the theoretical model given by (3.18) and (3.22) for two values of γ_{eff}, γ and $8\gamma/9$, and the measured optical power for the idler wave as a function of wavelength separation between pump and signal. The comparison, between the two plots in Fig. 3.6, shows that the polarization effects decrease the idler power approximately by 1 dB, due to the reduction of γ_{eff}. The results also show that, until $\lambda_1 - \lambda_2 < 2.8$ nm the experimental data and theoretical

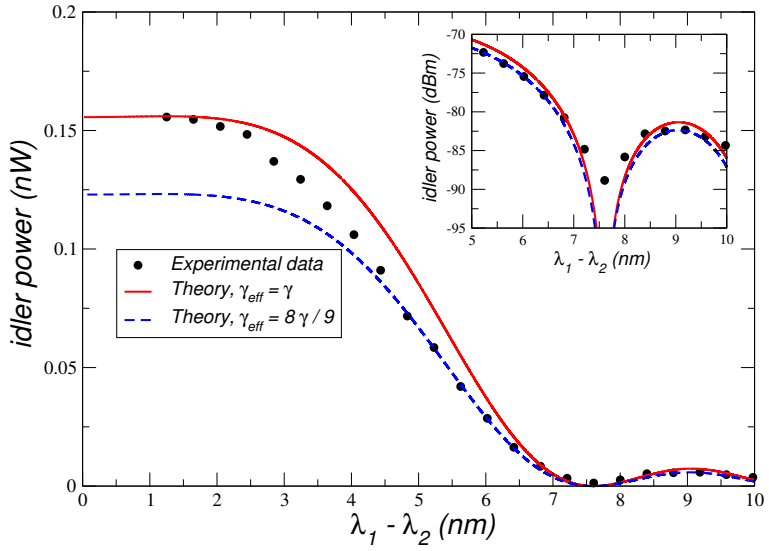

Figure 3.6: Measured optical power of the idler wave as a function of $\lambda_1 - \lambda_2$. The solid and the dashed lines represent (3.18) and (3.22) with $\gamma_{\text{eff}} = \gamma$ and with $\gamma_{\text{eff}} = 8\gamma/9$, respectively.

prediction with $\gamma_{\text{eff}} = \gamma$ present a quasi perfectly match. That means that for small wavelengths detunings the pump and signal fields remain approximately co-polarized along the optical fiber.

According with the theory of the principal states of polarisation (PSP) [53, 54], exist a small frequency range over which the polarization mode dispersion vector is reasonably constant

$$\Delta\omega_{\text{psp}} \approx \frac{\pi}{4\langle\Delta\tau\rangle}\,, \tag{3.24}$$

where $\langle\Delta\tau\rangle$ is the mean differential group delay (DGD). To evaluate the mean DGD we perform an experiment with the *Optical Network Analyzer*, and we find that $\langle\Delta\tau\rangle \simeq 0.362$ ps. For this value of mean DGD, the frequency range over which the SOP is reasonably constant is, $\Delta\omega_{\text{psp}} \simeq 2.17$ GHz. In terms of wavelength, the bandwidth is $\Delta\lambda_{\text{psp}} \simeq 2.75$ nm, which is in line with the value mentioned above, $\lambda_1 - \lambda_2 < 2.8$ nm. For $\lambda_1 - \lambda_2 > 5$ nm the experimental data is correctly describe with $\gamma_{\text{eff}} = 8\gamma/9$, which indicates that the pump and signal polarizations are mostly decorrelated. The comparison between the results presented in Fig. 3.6 also show that exist a transition region, 2.8 nm $< \lambda_1 - \lambda_2 <$ 5 nm, over which the optical power evolution of the idler wave with the wavelength separation between pump and signal fields is not described by $\gamma_{\text{eff}} = \gamma$ or by $\gamma_{\text{eff}} = 8\gamma/9$. In that region the optical fields go from an almost co-polarized situation to a decorrelated state of polarization.

In order to describe analytically the γ_{eff} variation with the wavelength separation between

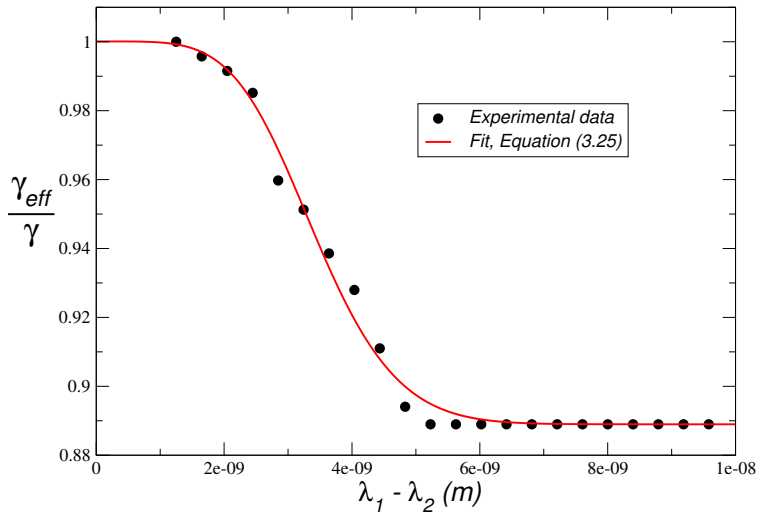

Figure 3.7: Comparison between the points obtained for the γ_{eff} parameter, Fig 3.5, and the fit with the hyperbolic secant function (3.25).

pump and signal, we fit the result present in Fig. 3.5 with an hyperbolic secant function given by

$$\gamma_{\text{eff}}(\Delta\lambda) = \frac{8\gamma}{9} + \frac{\gamma}{9}\text{sech}\left(\frac{(\Delta\lambda)^{A_0}}{T_0}\right), \tag{3.25}$$

where A_0 and T_0 are the fitting parameters, and $\Delta\lambda = \lambda_1 - \lambda_2$. In Fig. 3.7 we represent the analytical equation for γ_{eff} with $A_0 \approx 2.15$ and $T_0 \approx 5.47826 \times 10^{-19}$, and the experimental data as a function of wavelength separation between pump and signal. The results presented in Fig. 3.7 show that the hyperbolic secant function in (3.25) correctly describes the variation of the $\gamma_{\text{eff}}(\Delta\lambda)$ parameter with wavelength separation between pump and signal fields in the transition region 2.8 nm $< \lambda_1 - \lambda_2 <$ 5 nm.

Finally, in Fig. 3.8 we represent the measured optical power, plot (a), the average number of idler photons generated through FWM, plot (b), and the theoretical model for the idler wave as a function of wavelength separation between pump and signal. The results presented in Fig. 3.8 shows a good agreement between the experimental data and the theoretical model given by (3.18) and (3.22) with $\gamma_{\text{eff}}(\Delta\lambda)$ given by (3.25). Moreover, in Fig. 3.8(b) we can see that the photon source is capable of generating few-photons per pulse, and the average number of generated photons can be adjusted by simple tuning the wavelength separation between pump and signal fields. That can be seen in Table 3.1 where we present the average number of idler photons per pulse given by (3.2) and the spectral spacing between pump and signal fields. For high values of wavelength separation between pump and signal fields, the average number of idler photons generated through FWM is smaller than one, which is essential for QKD applications [1].

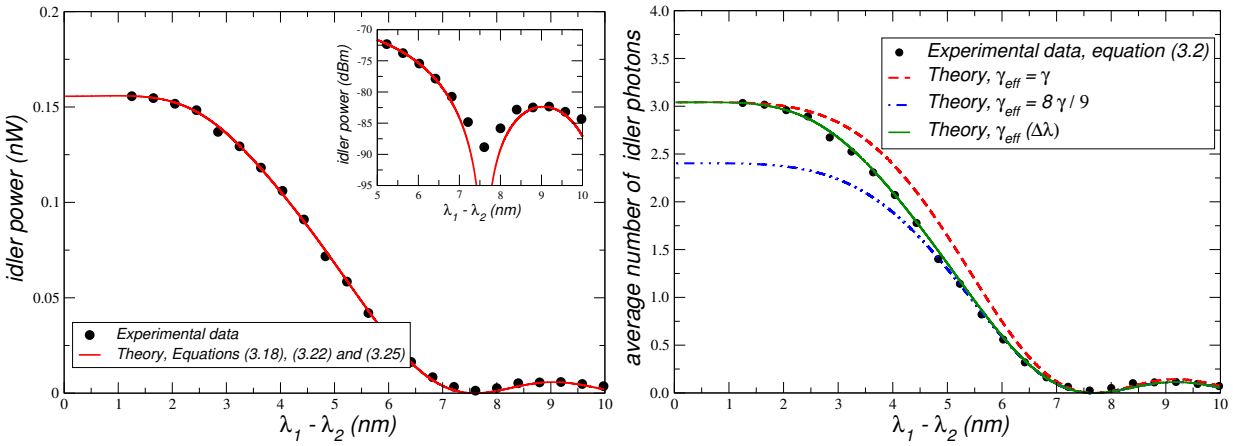

(a) (b)

Figure 3.8: Comparison between the experimental data for the idler power, plot (a), and for the average number of idler photons, plot (b), and the theoretical model given by (3.18), (3.22) with $\gamma_{\text{eff}}(\Delta\lambda)$ given by (3.25). The theoretical model and the experimental data show good agreement. The experimental parameters used are the same as the ones used to obtain Fig. 3.2.

Table 3.1: Average number of idler photons per pulse versus spectral spacing between pump and signal fields

$\lambda_1 - \lambda_2$ nm	$\langle n \rangle$	$\lambda_1 - \lambda_2$ nm	$\langle n \rangle$
1.251	3.034	5.626	0.821
1.65	3.016	6.022	0.559
2.049	2.959	6.418	0.320
2.447	2.894	6.814	0.164
2.845	2.673	7.210	0.064
3.243	2.525	7.606	0.025
3.640	2.308	8.001	0.051
4.038	2.071	8.397	0.102
4.435	1.778	8.792	0.107
4.832	1.401	9.186	0.115
5.229	1.142	9.581	0.009

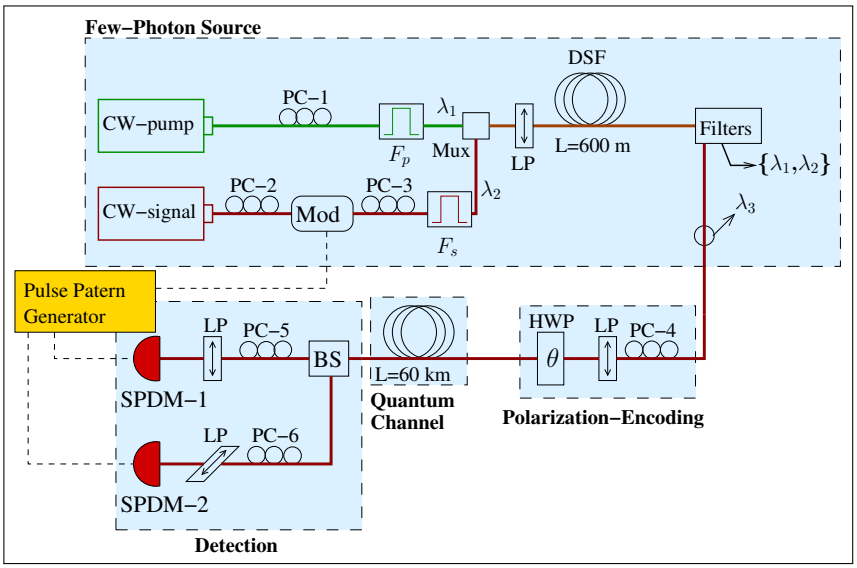

Figure 3.9: Experimental setup used to generate, encode, transmit and detect single photons from the classical process of FWM encoded into two non-orthogonal linear SOPs, $\theta = 0°$ and $\theta = 45°$. The dashed lines represent electrical signals and the solid lines the optical path. Details of the experiment are presented in the text.

3.4 Implementation of a Quantum Communication Link Using Few-Photons Obtained from the FWM Process

In order to validate the proposed few-photon source based on the classical FWM process, we implement in the laboratory a setup capable of transmit photons through a long standard single mode fiber (SSMF). The experimental setup was implemented by Á. J. Almeida [14, 15]. A schematic of the experimental setup is show in Fig. 3.9.

In the experimental setup, Fig. 3.9, a pump field from a tunable laser source (TLS) centered at $\lambda_1 = 1550.918$ nm, passes through a PC and a bandpass filter, F_P, before being coupled in a beam splitter (BS) to an optical signal from an external cavity laser (ECL) centered at $\lambda_2 = 1547.715$ nm. The signal passes through a PC, and is then externally modulated to produce optical pulses with a width at half maximum of approximately 1 ns and a repetition rate, $f_r \approx 1.22$ MHz. After the modulation, it passes through another PC, in order to assure that it will be co-polarized with the pump pulse at the input of the linear polarizer (LP) after the coupling. Optical filters, F_p, and F_s, are fixed flat-top type with 100 GHz passband width, and are used to eliminate the lasers sidebands from the pump and signal fields, respectively. After the LP, the two optical signals are launched into a DSF, with incident powers, $P_p(0) = 2.2$ mW, and $P_s(0) = 2.65 \times 10^{-3}$ mW, for the pump and signal, respectively. The DSF has a zero

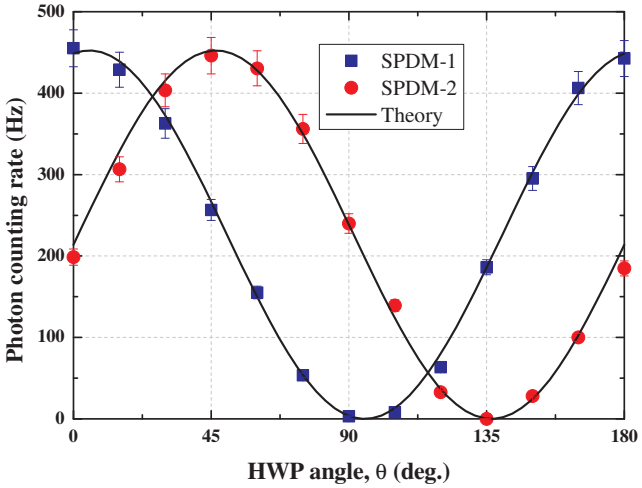

Figure 3.10: Idler photon counting rate as a function of the HWP angle, θ (degrees), for the two non-orthogonal SOPs with angles $\theta = 0^\circ$ and 45°, after propagation through a quantum channel with a length equal to 60 km. The theoretical model was taken from [14, 15].

dispersion wavelength, $\lambda_0 \approx 1550$ nm, a dispersion slope at the zero dispersion wavelength, $S(\lambda_0) \approx 0.071$ ps/nm^2/km, length, L = 600 m, attenuation, $\alpha \approx 0.2$ dB/km, and a nonlinear coefficient, $\gamma \approx 2.3$ W^{-1}km^{-1}. Due to the FWM process, the idler field is generated inside the DSF at $\lambda_3 = \lambda_1\lambda_2/(2\lambda_2 - \lambda_1)$ [8]. At the DSF output, optical filters suppress the pump and signal fields.

The idler photons passes through the filters and reaches the polarization-encoding stage, Fig. 3.9. At that stage, the idler photons passes through a PC to align photon's polarization with the axis of the LP. After the SOP of the idler photons is adjusted using a half wave plate (HWP), in order to obtain two non-orthogonal angles $\theta = 0^\circ$ and $\theta = 45^\circ$. The idler photons are transmitted through the quantum channel, an optical fiber with a length equal to 60 km. At the end of the quantum channel they pass through a BS, before reaching the single photon detector modules (SPDMs). Adjusting the PCs in each arm of the BS, the polarization changes inside the quantum channel can be compensated [55]. The LPs before the SPDMs work as polarization analyzers.

In Fig. 3.10, we present the average number of photon counts registered by SPDM-1 and SPDM-2 as a function of the HWP angle, θ, along with the theoretical model taken from [14, 15]. The results were obtained after the photons were transmitted through an optical fiber with a length equal to 60 km. From 3.10 it can be seen that the maximum counting rate is obtained when the polarization of the incident photons in the LPs is aligned with its transmission axes,

and the minimum when they are orthogonal. Moreover, it can be seen in Fig. 3.10 that even after the photons were transmitted through the long distance quantum channel, the 45° separation is still present. This indicates that we are able to decode the photons after they were transmitted through a quantum channel, with at least 60 km.

3.5 Summary

We investigated, both theoretically and experimentally, the FWM process in optical fibers in a low power regime. Using the coupled-equations, we derived a simple equation that governs the evolution of idler wave, for the case $P_1 \gg P_2$ with pump and signal powers maintained in a low power regime. We show that an accurate description of the FWM process in the low power regime can only be obtained by including the nonlinear contribution and polarization dependent effects in the scalar FWM theory. The theoretical results were validated experimentally through the measurement of the optical power generated in the idler wave through the FWM process in a DSF. We verify the possibility of efficient generation of idler wave outside of the zero-dispersion of the fiber and with pump and signal fields far apart. We also show experimentally that exist a transition region over which the pump and signal fields go from an almost co-polarized situation to a decorrelated SOP. In order to describe the influence of the polarization effects on the evolution of the idler power, we introduced the effective nonlinear parameter, $\gamma_{\text{eff}}(\Delta\lambda)$. We found that the $\gamma_{\text{eff}}(\Delta\lambda)$ varies as a hyperbolic secant with the wavelength separation between pump and signal. This result was obtained for a single sample of a DSF, a sample that we had available in our laboratory. Although we believe that this result can be generalized for other fibers, this should be validated in further studies. We show that if we use the FWM process to measure the fiber nonlinear parameter, what we obtain is the effective nonlinear parameter of the fiber, which is dependent of the wavelength separation between pump and signal fields.

We use the classical FWM process to obtain a few-photon source with adjustable linear SOP. This allow us to implement a quantum channel with length equal to 60 km. A correspondence between the emitted and the received idler photons was observed and the feasibility of the source was verified, since we observe a fringe visibility greater than 98%. This source, operating in a low power regime, can in principle be used for implementation of QKD systems using polarization-encoding schemes.

References

[1] N. Gisin, G. Ribordy, W. Tittel, and H. Zbinden, "Quantum cryptography," *Rev. Mod. Phys.*, vol. 74, pp. 145–195, 2002.

[2] M. D. Eisaman, J. Fan, A. Migdall, and S. V. Polyakov, "Invited review article: Single-photon sources and detectors," *Review of Scientific Instruments*, vol. 82, p. 071101, 2011.

[3] W. Tittel and G. Weihs, "Photonic entanglement for fundamental tests and quantum communication," *Quantum Information and Computation*, vol. 1, pp. 3–56, 2001.

[4] T. Jennewein, C. Simon, G. Weihs, H. Weinfurter, and A. Zeilinger, "Quantum cryptography with entangled photons," *Physical Review Letters*, vol. 84, pp. 4729–4732, 2000.

[5] L. J. Wang, C. K. Hong, and S. R. Friberg, "Generation of correlated photons via four-wave mixing in optical fibrer," *J. Opt. B: Quantum Semiclass*, vol. 3, pp. 346–352, 2001.

[6] H. Takesue and K. Inoue, "Generation of polarization-entangled photon pairs and violation of Bell's inequality using spontaneous four-wave mixing in a fiber loop," *Physical Review A*, vol. 70, p. 031802, 2004.

[7] H. Takesue and K. Inoue, "Generation of 1.5-μm band time-bin entanglement using spontaneous fiber four-wave mixing and planar light-wave circuit interferometers," *Physical Review A*, vol. 72, p. 041804, 2005.

[8] G. P. Agrawal, *Nonlinear Fiber Optics*, 3rd ed. San Diego: Academic Press, 2001.

[9] Q. Lin, F. Yaman, and G. P. Agrawal, "Photon-pair generation in optical fibers through four-wave mixing: Role of raman scattering and pump polarization," *Phys. Rev. A*, vol. 75, p. 023803, 2007.

[10] P. Antunes, P. S. André, and A. N. Pinto, "Single-photon source by means of four-wave mixing inside a dispersion-shifted optical fiber," in *FIO'06 - Frontiers in Optics*, USA, October 2006.

[11] N. A. Silva, N. J. Muga, and A. N. Pinto, "Effective nonlinear parameter measurement using FWM in optical fibers in a low power regime," *IEEE Journal of Quantum Electronics*, vol. 46, pp. 285–291, 2010.

[12] N. A. Silva, N. J. Muga, and A. N. Pinto, "Single-photon generation," in *Conf. on Telecommunications - ConfTele*, vol. 1, May 2009, pp. 35–38.

[13] N. A. Silva, N. J. Muga, and A. N. Pinto, "Measurement of the effective nonlinear parameter using FWM in random polarization optical fibers," in *European Conf. on Networks and Optical Communications - NOC*, vol. 1, June 2010, pp. 185–190.

[14] A. J. Almeida, N. A. Silva, N. J. Muga, and A. N. Pinto, "Single-photon source using stimulated FWM in optical fibers for quantum communication," in *International Conf. on Applications of Optics and Photonics - AOP2011*, vol. 8001, May 2011, pp. 80 013W–1 – 80 013W–7.

[15] A. J. Almeida, N. A. Silva, N. J. Muga, and A. N. Pinto, "Fiber-optical communication system using polarization-encoding photons," in *European Conf. on Networks and Optical Communications and Conf. on Optical Cabling and Infrastructure - NOC/OC*, vol. 1, June 2010, pp. 127–132.

[16] G. P. Agrawal, *Applications of Nonlinear Fiber Optics*. San Diego: Academic Press, 2001.

[17] B. P. Pal, *Guided Wave Optical Components and Devices*. San Diego: Academic Press, 2005, ch. Fiber-Optic Parametric Amplifiers for Lightwave Sysytems.

[18] R. H. Stolen and J. E. Bjorkholm, "Parametric amplification and frequency conversion in optical fibers," *IEEE Journal of Quantum Electronics*, vol. 18, pp. 1062–1072, 1982.

[19] J. Hanstyd, P. A. Andrekson, M. Westlund, J. Li, and P. Hedekvist, "Fiber-based optical parametric amplifiers and their applications," *IEEE Journal of Selected Topics in Quantum Electronics*, vol. 8, pp. 506–520, 2002.

[20] K. Inoue and H. Toba, "Wavelength conversion experiment using fiber four-wave mixing," *IEEE Photonics Technology Letters*, vol. 4, pp. 69–72, 1992.

[21] K. Inoue, "Tunable and selective wavelength conversion using fiber four-wave mixing with two pump ligths," *IEEE Photonics Technology Letters*, vol. 6, pp. 1451–1453, 1994.

[22] Q. Lin and G. P. Agrawal, "Effects of polarization-mode dispersion on fiber-based parametric amplification and wavelength conversion," *Optics Letters*, vol. 29, pp. 1114–1116, 2004.

[23] M. Fiorentino, P. L. Voss, J. E. Sharping, and P. Kumar, "All-fiber photon-pair source for quantum communications," *IEEE Photonics Technology Letters*, vol. 14, pp. 983–985, 2002.

[24] X. Li, J. Chen, P. Voss, J. Sharping, and P. Kumar, "All-fiber photon-pair source for quantum communications: Improved generation of correlated photons," *Optics Express*, vol. 12, pp. 3737–3744, 2004.

[25] R. H. Stolen, J. E. Bjorkholm, and A. Ashkin, "Phase-matched three-wave mixing in silica fiber optical waveguides," *Appl. Phys. Lett.*, vol. 27, pp. 308–310, 1974.

[26] Q. Lin and G. P. Agrawal, "Vector theory of four wave mixing: polarization effects in fiber optic parametric amplifiers," *J. Opt. Soc. Am. B*, vol. 21, pp. 1216–1224, 2004.

[27] E. A. Golovchenko and A. N. Pilipetskii, "Undified analysis of four-photon mixing, modulation instability, and stimulated raman scattering under various polarization conditions in fibers," *J. Opt. Soc. Am. B*, vol. 11, pp. 92–101, 1994.

[28] C. J. McKinstrie, A. V. Kanaev, and H. Kogelnik, "Nonlinear dynamics associated with a model of vector four-wave mixing," *Optics Express*, vol. 13, pp. 1580–1597, 2005.

[29] C. J. McKinstrie, H. Kogelnik, R. M. Jopson, S. Radic, and A. V. Kanaev, "Four-wave mixing in fibers with random birefringence," *Optics Express*, vol. 12, pp. 2033–2055, 2004.

[30] K. Inoue, "Four-wave mixing in an optical fiber in the zero-dispersion wavelength region," *IEEE/OSA Journal of of Lightwave Technology*, vol. 10, pp. 1553–1561, 1992.

[31] K. Washio, K. Inoue, and S. Kishida, "Efficient large-frequency-shifted three-wave mixing in low dispersion wavelength region in single-mode optical fiber," *Electronic Letters*, vol. 16, pp. 658–660, 1980.

[32] C. Lin, W. A. Reed, A. D. Pearson, and H. T. Shang, "Phase matching in the minimum-chromatic-dispersion region of single-mode fibers for stimulated four-photon mixing," *Optics Letters*, vol. 6, pp. 493–495, 1981.

[33] C. Lin, W. A. Reed, A. D. Pearson, H.-T. Shang, and P. F. Glodis, "Designing single-mode fibres for near-ir(1.1-1.7μm) frequency generation by phase-matched four-photon mixing in the minimum chromatic dispersion region," *Electronics Letters*, vol. 18, pp. 87–89, 1982.

[34] S. J. Jung, J. Y. Lee, and D. Y. Kim, "Novel phase-matching condition for a four wave mixing experiment in an optical fiber," *Optics Express*, vol. 14, pp. 35–43, 2005.

[35] id Quantique, "id 200 single-photon detector module," http://www.idquantique.com/products/files/id200-operating.pdf.

[36] A. Karlsson, M. Bourennane, G. Ribordy, H. Zbinden, J. Brendel, J. Rarity, and P. Tapster, "A single-photon counter for long-haul telecom," *IEEE Circuits and Devices Magazine*, vol. 15, pp. 34–40, 1999.

[37] A. Trifonov, D. Subacius, A. Berzanskis, and A. Zavriyev, "Single photon counting at telecom wavelength and quantum key distribution," *Journal of Modern Optics*, vol. 51, pp. 1399–1415, 2004.

[38] M. Liu, C. Hu, X. Bai, X. Guo, J. C. Campbell, Z. Pan, and M. M. Tashima, "High-performance InGaAs/InP single-photon avalanche photodiode," *IEEE Journal of Selected Topics in Quantum Electronics*, vol. 13, pp. 887–894, 2007.

[39] K. O. Hill, D. C. Johnson, B. S. Kawasaki, and R. I. MacDonald, "cw three-wave mixing in single-mode optical fibers," *J .Appl. Phys.*, vol. 49, pp. 5098–5106, 1978.

[40] N. Shibata, R. P. Braun, and R. G. Waarts, "Phase-mismatch dependence of efficiency of wave generation through four-wave mixing in a single-mode optical fiber," *IEEE Journal of Quantum Electronics*, vol. 23, pp. 1205–1210, 1987.

[41] J. R. Thompson and R. Roy, "Multiple four-wave mixing process in an optical fiber," *Optics Letters*, vol. 16, pp. 557–559, 1991.

[42] J. R. Thompson and R. Roy, "Nonlinear dynamics of multiple four-wave mixing processes in a single-mode fiber," *Physical Review A*, vol. 43, pp. 4987–4996, 1991.

[43] X. Liu, X. Zhou, and C. Lu, "Multiple four-wave mixing self-stability in optical fibers," *Physical Review A*, vol. 72, p. 013811, 2005.

[44] K. Kikuchi and Chaloemphon, "Design of highly efficient four-wave mixing devices using optical fibers," *IEEE Photonics Technology Letters*, vol. 6, pp. 992–994, 1994.

[45] R. W. McKerracher, J. L. Blows, and C. M. de Sterke, "Wavelength conversion bandwidth in fiber based optical parametric amplifiers," *Optics Express*, vol. 11, pp. 1002–1007, 2003.

[46] M. Farahmand and M. de Sterke, "Parametric amplification in presence of dispersion fluctuations," *Optics Express*, vol. 12, pp. 136–142, 2004.

[47] M. Karlsson, "Four-wave mixing in fibers with randomly varying zero-dispersion wavelength," *J. Opt. Soc. Am. B*, vol. 15, pp. 2269–2275, 1998.

[48] P. K. A. Wai, C. R. Menyuk, and H. H. Chen, "Stability of solitons in randomly varying birefringent fibers," *Optics Letters*, vol. 16, pp. 1231–1233, 1991.

[49] Q. Lin and G. P. Agrawal, "Polarization mode dispersion-induced fluctuations during raman amplifications in optical fibers," *Optics Letters*, vol. 27, pp. 2194–2196, 2002.

[50] S. G. E. Jr., L. F. Mollenauer, J. P. Gordon, and N. S. Bergano, "Polarization multiplexing with solitons," *IEEE/OSA Journal of of Lightwave Technology*, vol. 10, pp. 28–35, 1992.

[51] Q. Lin and G. P. Agrawal, "Impact of polarization-mode dispersion on measurement of zero-dispersion wavelength through four-wave mixing," *IEEE Photonics Technology Letters*, vol. 15, pp. 1719–1721, 2003.

[52] Q. Lin and G. P. Agrawal, "Effects of polarization-mode dispersion on fiber-based parametric amplification and wavelength conversion," *Optics Letters*, vol. 29, pp. 1114–1116, 2004.

[53] C. D. Poole and R. E. Wagner, "Phenomenological approach to polarisation dispersion in long single-mode fibres," *Electronics Letters*, vol. 22, pp. 1029–1031, 1986.

[54] R. M. Jopson, L. E. Nelson, and H.Kogelnik, "Measurement of second-order polarization-mode dispersion vectors in optical fibers," *IEEE Photonics Technology Letters*, vol. 11, pp. 1153–1155, 1999.

[55] N. J. Muga, A. Nolasco Pinto, M. F. S. Ferreira, and J. R. Ferreira da Rocha, "Uniform Polarization Scattering With Fiber-Coil-Based Polarization Controllers," *IEEE/OSA Journal of Lightwave Technology*, vol. 24, pp. 3932–3943, 2006.

Chapter 4

Influence of the Raman Scattering on the Four-Wave Mixing

THE four-wave mixing (FWM) process has been used to implement fiber-optic parametric amplifiers [1, 2], wavelength converters [2, 3], and single and entangled photon-pairs sources [4, 5]. The stimulated Raman scattering (SRS) in optical fibers has been used to implement broadband Raman amplifiers [6, 7] and tunable Raman lasers [8, 9]. These two nonlinear processes typically are discussed as independent processes, even if they inevitably occur simultaneously [10–13]. In this Chapter we present a comprehensive description of the combined process of SRS and FWM in birefringent fibers, in the single and dual pump configuration and considering both co-polarized and orthogonal schemes of polarization. This Chapter is based on the references [14, 15], and is divided into two main sections. In section 4.1 we analyze theoretically the impact of the SRS on the FWM process considering the single- and dual-pump configuration in both co-polarized and orthogonal polarization schemes. In section 4.2 we derive and solve analytically the combined processes of SRS and multiple FWM in the dual pump configuration, considering both co-polarized and orthogonal schemes of polarization. We also study the evolution of the first-order sidebands generated through three distinct FWM process inside a high birefringent (HiBi) optical fiber, as a function of the angle between the two pump polarizations. In section 4.3, the main results of this Chapter are summarized.

4.1 Combined Process of Raman Scattering and Four-Wave Mixing

Stimulated FWM and SRS in optical fibers are both third-order nonlinear processes. These two nonlinear processes can be described by the third-order nonlinear response function of the fiber

$R^{(3)}_{ijkl}(\tau)$ [16]. The stimulated FWM process occurs when light of two or more frequencies are launched into an optical fiber given rise to a new wave. Typically, the frequencies launched into the fiber are known as pump and signal fields, and the new wave is known as idler. At same time that the idler wave is created the signal field is amplified [16]. During the FWM process no energy between the optical fields and the fiber is transfered and in that sense this nonlinear process can be considered as a third-order elastic process [16]. The SRS process in optical fibers is an inelastic scattering process in which energy is transfered between the optical fields and the dielectric nonlinear medium. In this nonlinear process the optical frequencies from the pumps transfer their energy to lower frequencies (Stokes amplification) and to higher frequencies (anti-Stokes amplification), through molecular vibrations [16, 17].

Most of the work related with the FWM process has been done around the zero-dispersion of the fiber. In that case, the phase-matching condition is easily achieved and efficient FWM is obtained [18, 19]. Recent developments of photonic crystal fibers (PCFs) have enabled to produce fibers with high nonlinear coefficient and with zero-dispersion wavelength around 1550 nm [20]. Highly nonlinear fibers with zero-dispersion wavelength around 1550 nm can be useful for telecommunications applications such as parametric amplifiers [21], soliton generation [22], supercontinuum generation [23] and wavelength conversion [21]. The PCFs also allow the introduction of a polarization maintaining structure, characterized by a high birefringence, of the order of $\delta n \sim 1 \times 10^{-4}$ [20, 24]. Due to the PCFs properties the FWM and the SRS processes can be obtained very efficiently in this kind of fibers [25–27].

The combined process of SRS and FWM in optical fibers was investigated theoretically by Keith J. Blow *et al.* [28], and their work was latter extended to investigate the parametric wavevector mismatch on both processes [1, 29, 30], and to include the effect of the pump polarization [11, 31]. Recent studies on this topic have shown that for the single pump configuration in the co-polarized scheme the signal field is mostly dependent on the imaginary part of the Raman susceptibility, whereas the idler wave is strongly dependent on the real part [12, 13]. That dependence is more visible when phase-matching condition is achieved. All these studies mainly discuss the influence of the SRS on fiber-optic parametric amplifiers based on the FWM process. In this section we expand previous studies related with SRS and FWM process [1, 11, 28–31] to the co-polarized and orthogonal polarization schemes, in order to treat simultaneously both processes in the single and dual pump configurations. The obtained results are valid even when the shift between the pumps and signal lies inside the Raman band. This work can help to guide the development of optical signal processing devices using PCFs and based on FWM and SRS

processes.

4.1.1 Theoretical Formalism

The evolution of optical waves inside an almost lossless optical fiber is governed by the nonlinear Schrödinger equation (NSE) [16, 32]

$$\frac{\partial A_i(z,t)}{\partial z} = \sum_{m=0}^{+\infty} \frac{i^{m+1}\beta_{m,i}}{m!}\frac{\partial^m A_i(z,t)}{\partial t^m} + i\gamma A_j(z,t)\int_{-\infty}^{+\infty} R^{(3)}_{ijkl}(\tau)A^*_k(z,t-\tau)A_l(z,t-\tau)d\tau, \tag{4.1}$$

where $A_i(z,t)$ is the electrical field complex amplitude, $\beta_{m,i}$ is the m^{th} order dispersion coefficient, γ is the nonlinear parameter of the fiber and $R^{(3)}_{ijkl}(\tau)$ is the waveguide nonlinear response function [33, 34]

$$R^{(3)}_{ijkl}(\tau) = \frac{1-f_R}{3}\delta(\tau)\left(\delta_{ij}\delta_{kl}+\delta_{ik}\delta_{jl}+\delta_{il}\delta_{jk}\right) + f_R R_a(\tau)\delta_{ij}\delta_{kl} + \frac{f_R}{2}R_b(\tau)\left(\delta_{ik}\delta_{jl}+\delta_{il}\delta_{jk}\right), \tag{4.2}$$

where $R_a(\tau)$ and $R_b(\tau)$ are the isotropic and anisotropic Raman response, respectively, and f_R represents their fractional contribution to the nonlinear refractive index. The isotropic and anisotropic Raman response can be modeled, respectively, by [27, 28, 35]

$$R_a(\tau) = f_a\frac{\tau_1^2+\tau_2^2}{\tau_1\tau_2^2}\exp(-\tau/\tau_2)\sin(\tau/\tau_1)\Theta(\tau), \tag{4.3a}$$

$$R_b(\tau) = f_b\frac{1}{\tau_b}\left(2-\frac{\tau}{\tau_b}\right)\exp(-\tau/\tau_b)\Theta(\tau) + f_c\frac{\tau_1^2+\tau_2^2}{\tau_1\tau_2^2}\exp(-\tau/\tau_2)\sin(\tau/\tau_1)\Theta(\tau), \tag{4.3b}$$

where $\Theta(\tau)$ is the Heaviside function, $\tau_1 \simeq 12.2$ fs is the inverse of the phonon frequency, $\tau_2 \simeq 32$ fs is the phonon lifetime, $\tau_b \simeq 96$ fs accounts for the spectral width of the Boson peak [28, 35], $f_a = 0.75$, $f_b = 0.21$ and $f_c = 0.04$ represent the fractional contribution to $R_a(\tau)$ and $R_b(\tau)$, and $f_R = 0.245$ [35]. The values presented for τ_1, τ_2, τ_b, f_a, f_b, f_c, and f_R are typical values for silica based fibers [35]. The isotropic and anisotropic Raman responses are related with co-polarized and orthogonal Raman gain [33, 35]

$$g_{R\parallel}(\Omega) = 2\gamma f_R\left(\mathrm{Im}[\tilde{R}_a(\Omega)] + \mathrm{Im}[\tilde{R}_b(\Omega)]\right), \tag{4.4}$$

$$g_{R\perp}(\Omega) = \gamma f_R\left(\mathrm{Im}[\tilde{R}_b(\Omega)]\right), \tag{4.5}$$

where $g_{R\parallel}(\Omega)$ and $g_{R\perp}(\Omega)$ are the Raman gain coefficient for the co-polarized and orthogonal scheme of polarization, respectively, $\tilde{R}_a(\Omega)$ is the Fourier transform of $R_a(\tau)$, and $\tilde{R}_b(\Omega)$ is the Fourier transform of $R_b(\tau)$. In Fig. 4.1(a) we plot the real and the imaginary parts of $\tilde{R}_a(\Omega)$ and

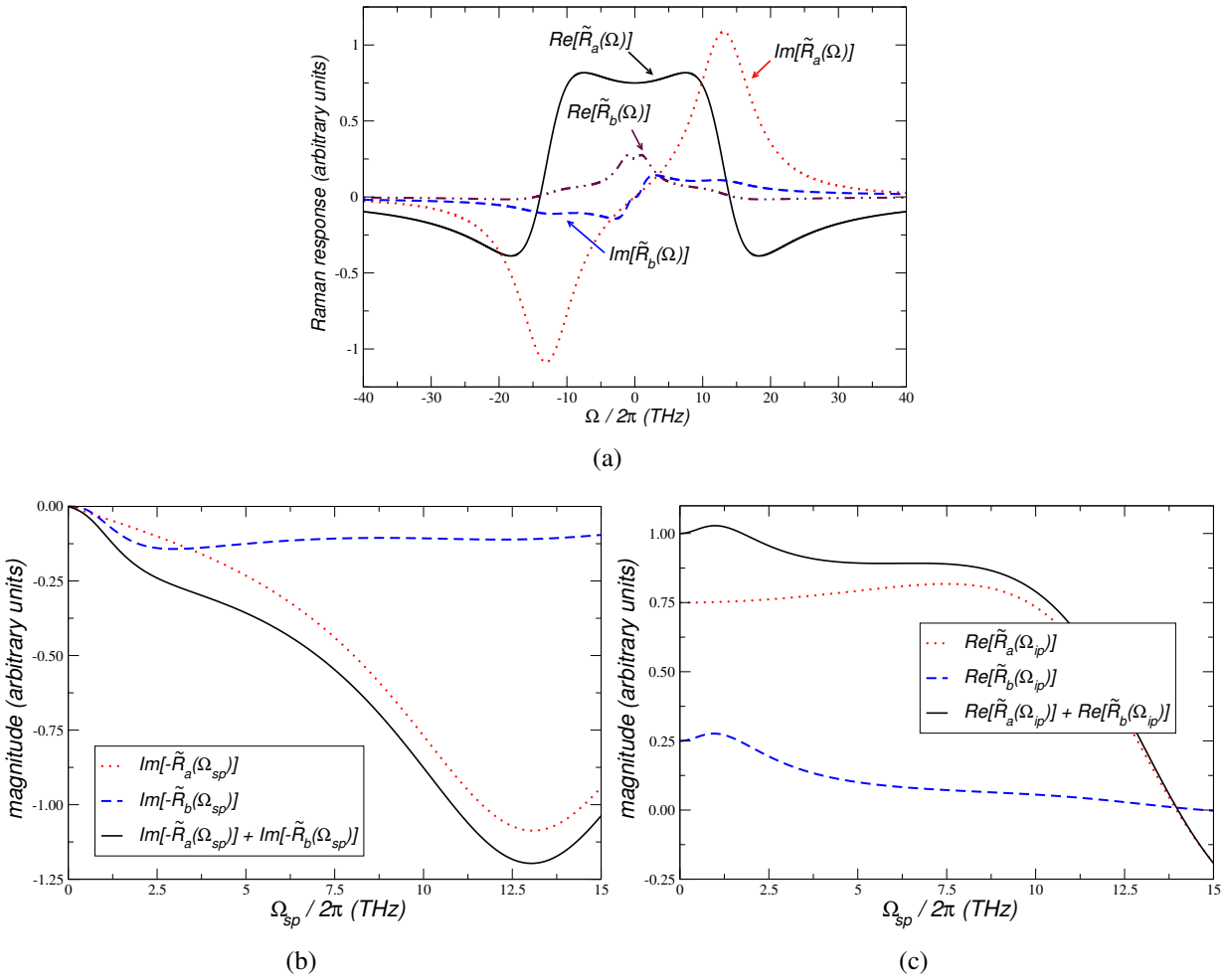

Figure 4.1: (a): Evolution of the isotropic and anisotropic Raman response with frequency detuning. Evolution of the imaginary and real parts of the Raman response function, plots (b) and (c), with frequency detuning.

$\tilde{R}_b(\Omega)$. In Fig. 4.1(b) and in Fig. 4.1(c) we plot the imaginary and real parts of $\tilde{R}_a(\Omega)$ and $\tilde{R}_b(\Omega)$, respectively. The real part of $\tilde{R}_a(\Omega)$ and $\tilde{R}_b(\Omega)$ leads to Raman-induced index change, whereas the imaginary part is proportional to the Raman gain [36].

In the sections 4.1.2 and 4.1.3, we use the theoretical model presented here in order to evaluate the influence of the SRS in the FWM process in highly nonlinear fibers with zero-dispersion around 1550 nm. The experimental fiber parameters used in the analytical models are $\gamma = 18 \times 10^{-3}$ W^{-1}m^{-1}, zero-dispersion of the fiber $\lambda_0 = 1552$ nm, birefringence $\delta n = 1.1 \times 10^{-4}$, dispersion slope at zero-dispersion wavelength $S = -250$ s/m^3 [24], length $L = 300$ m and input optical power for each pump equal 15 mW.

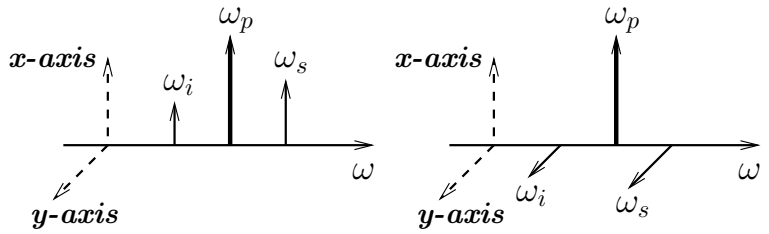

(a) Co-polarized scheme. (b) Orthogonal scheme.

Figure 4.2: Polarization schemes of the FWM process in the single pump configuration.

4.1.2 Single-Pump Configuration

In this section the FWM process is analyzed when only a pump and a signal with frequencies ω_p and ω_s, respectively, are launched into a fiber. Due to the FWM process the idler wave is created inside the fiber with frequency $\omega_i = 2\omega_p - \omega_s$ [16]. It is assumed that the pump is polarized along a principal axis of the fiber, the x axis, see Fig. 4.2. Under the continuous wave (CW) approximation the total optical field $A_j(z,t)$ can be written as [16]

$$A_j(z,t) = A_{px}(z)e^{-i\Omega_p t} + A_{sj}(z)e^{-i\Omega_s t} + A_{ij}(z)e^{-i\Omega_i t}, \tag{4.6}$$

where $j = x$ for the co-polarized scheme and $j = y$ for the orthogonal scheme of polarization, $\Omega_u = \omega_u - \omega_0$ where $u = p,s,i$ and ω_0 is the fiber zero-dispersion frequency, $A_{px}(z)$ represents the amplitude of the pump wave, $A_{sj}(z)$ and $A_{ij}(z)$ represent the amplitude of the signal and idler fields, respectively. The evolution of the complex amplitude for the pump wave is given by [16, 34]

$$A_{px}(z) = A_p(0)\Phi(z) = A_p(0)\exp[i(\beta_x(w_p) + \gamma P_0)z], \tag{4.7}$$

where $A_p(0)$ is the input pump amplitude, $P_0 = |A_p(0)|^2$ is the incident pump power and $\beta_x(w_p)$ is the pump propagation constant. The NSE equation for idler and signal fields can be written as

$$\frac{\partial A_{qj}(z)}{\partial z} = i\beta_j(\omega_q)A_{qj}(z) + i\gamma\zeta_j(\Omega_v)P_0A_{qj}(z) + i\gamma\rho_j(\Omega_v)A_{px}^2(z)A_{fj}^*(z), \tag{4.8}$$

where $q, f = s$ for the signal field and $q, f = i$ for the idler field with $q \neq f$, and

$$\zeta_x(\Omega_v) = 2 - f_R + f_R\tilde{R}_a(\Omega_v) + f_R\tilde{R}_b(\Omega_v), \tag{4.9}$$

$$\zeta_y(\Omega_v) = 2\frac{1-f_R}{3} + f_R\tilde{R}_a(0) + \frac{f_R}{2}\tilde{R}_b(\Omega_v), \tag{4.10}$$

$$\rho_x(\Omega_v) = 1 - f_R + f_R\tilde{R}_a(\Omega_v) + f_R\tilde{R}_b(\Omega_v), \tag{4.11}$$

$$\rho_y(\Omega_v) = \frac{1-f_R}{3} + \frac{f_R}{2}\tilde{R}_b(\Omega_v), \tag{4.12}$$

where $\Omega_v = \Omega_{sp} = \omega_s - \omega_p$ for the signal wave and $\Omega_v = \Omega_{ip} = \omega_i - \omega_p$ for the idler wave. In (4.8) $\rho_j(\Omega_v)$ is related with the efficiency of the FWM process. If $f_R = 0$ we obtain the description of the FWM process in the absence of Raman contribution.
The signal and idler complex amplitudes at a distance z are given by

$$\frac{A_{sj}(z)}{A_{sj}(0)} = \cosh(g_j(\Omega_{sp})z)\exp(i\delta\beta_j z/2)\Phi(z) + i\frac{\kappa_j(\Omega_{sp})}{2g_j(\Omega_{sp})}\sinh(g_j(\Omega_{sp})z)\exp(i\delta\beta_j z/2)\Phi(z), \tag{4.13}$$

and

$$\frac{A_{ij}(z)}{A^*_{sj}(0)} = i\frac{\gamma\rho_j(\Omega_{ip})}{g_j(\Omega_{ip})}\sinh(g_j(\Omega_{ip})z)A_p^2(0)\Phi(z)e^{-i\delta\beta_j z/2}, \tag{4.14}$$

where $\Phi(z)$ is given by (4.7), $\delta\beta_j = \beta_j(\omega_s) - \beta_j(\omega_i)$, $g_j(\Omega_v)$ is the parametric gain given by

$$g_j^2(\Omega_v) = (\gamma\rho_j(\Omega_v)P_0)^2 - (\kappa_j(\Omega_v)/2)^2, \tag{4.15}$$

and $k_j(\Omega_v)$ is phase-mismatch

$$\kappa_j(\Omega_v) = \Delta\beta_j + 2\gamma P_0(\zeta_j(\Omega_v) - 1), \tag{4.16}$$

where $\Delta\beta_j$ is the phase-matching condition given by [16, 37, 38]

$$\Delta\beta_j = \beta_j(\omega_s) + \beta_j(\omega_i) - 2\beta_x(\omega_p) = 2\frac{\omega_p}{c}\delta n + (\omega_p - \omega_0)(\omega_p - \omega_s)^2\beta_3, \tag{4.17}$$

where c is the speed of light in vacuum, $\delta n = n_y - n_x$ is the group birefringence, ω_0 is chosen at the zero-dispersion of the fiber and β_3 is the third order dispersion coefficient. For the co-polarized scheme we should consider $\delta n = 0$. The optical power evolution of signal and idler fields is given by

$$\frac{P_{sj}(z)}{P_{sj}(0)} = \left|\cosh(g_j(\Omega_{sp})z) + i\frac{\kappa_j(\Omega_{sp})}{2g_j(\Omega_{sp})}\sinh(g_j(\Omega_{sp})z)\right|^2, \tag{4.18}$$

and

$$\frac{P_{ij}(z)}{P_{sj}(0)} = (\gamma P_p(0)z)^2\left|\rho_j(\Omega_{ip})\right|^2\left|\frac{\sinh(g_j(\Omega_{ip})z)}{g_j(\Omega_{ip})z}\right|^2. \tag{4.19}$$

In Fig. 4.3 we plot the theoretical prediction for the signal field given by (4.18) as a function of frequency detuning. In Fig. 4.3(a) and in Fig. 4.3(b) we plot the evolution of the signal field in the co-polarized scheme, see Fig. 4.2(a), whereas in Fig. 4.3(c) and in Fig. 4.3(d) it is presented the evolution of the signal wave in the orthogonal polarization scheme, see Fig. 4.2(b).

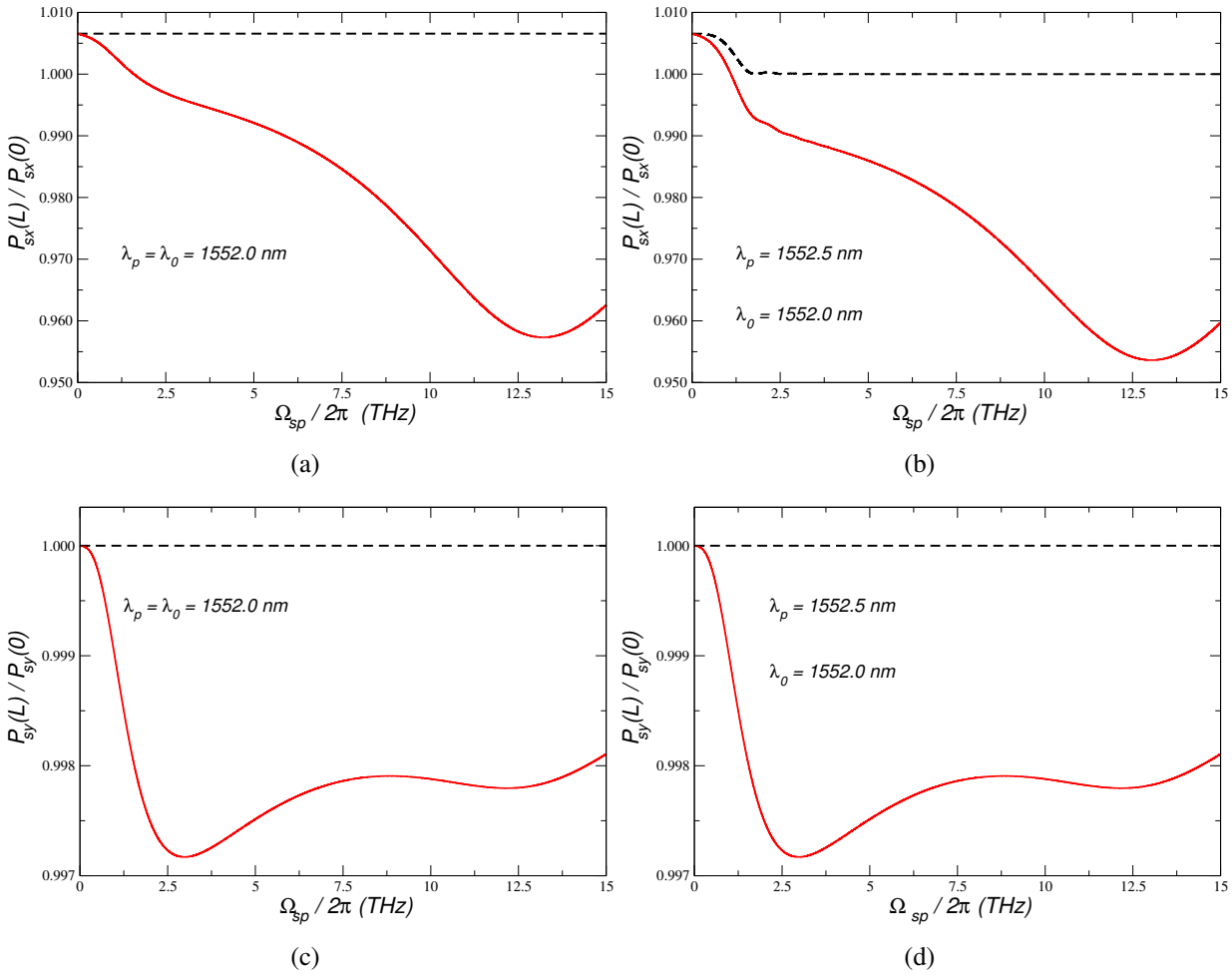

Figure 4.3: Theoretical predictions for the signal field given by (4.18) as a function of frequency detuning. Dashed lines represent the limit $f_R = 0$ and solid lines $f_R = 0.245$. Fig. 4.3(a) and Fig. 4.3(b) represent the co-polarized scheme, whereas Fig. 4.3(c) and Fig 4.3(d) describe the orthogonal polarization scheme. In plot (a) and (c) we represent the evolution of the signal field when the pump wavelength, λ_p, coincides with the zero-dispersion wavelength of the fiber, λ_0. Results show that the signal field is strongly influenced by the imaginary part of the fiber nonlinear response, which is proportional to the Raman gain parameter.

In Fig. 4.3(a) and in Fig. 4.3(c) the pump wavelength, λ_p, coincides with the zero-dispersion wavelength, λ_0, of the fiber. From Fig. 4.3(a) and Fig. 4.1(b) we can see that the evolution of the signal wave is mostly described by $(\mathrm{Im}[-\tilde{R}_a(\Omega_{sp})] + \mathrm{Im}[-\tilde{R}_b(\Omega_{sp})])$, which is proportional to the co-polarized Raman gain parameter given by (4.4). For high frequency detunings the magnitude of $\mathrm{Im}[-\tilde{R}_a(\Omega_{sp})]$ dominates, and the evolution of the signal wave is mostly described by that function, which leads to a minimum of efficiency in the signal wave around 13 THz. That value

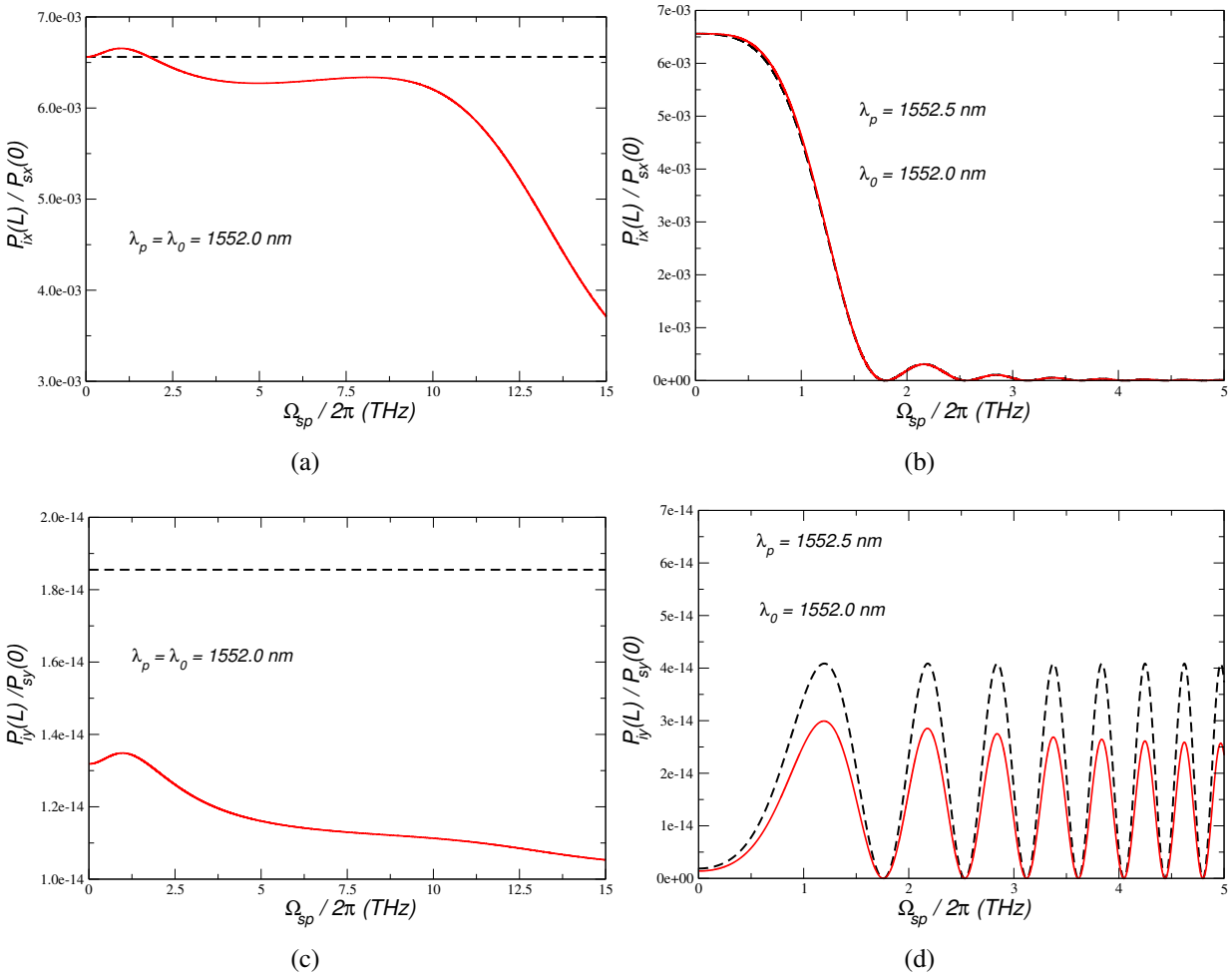

Figure 4.4: Theoretical predictions for the idler field given by Eq. (4.19) as a function of frequency detuning. Dashed lines represent the limit $f_R = 0$ and solid lines $f_R = 0.245$. In Fig. 4.4(a) and in Fig. 4.4(b) we plot the generation of the idler field in the co-polarized scheme, whereas in Fig. 4.4(c) and Fig. 4.4(d) we describe the idler field in the orthogonal polarization scheme. In Fig. 4.4(a) and Fig. 4.4(c) we plot the generation of the idler field when the pump wavelength, λ_p, coincides with the zero-dispersion wavelength of the fiber, λ_0. Results show that the idler field is strongly influenced by the real part of the fiber nonlinear response function, namely when the pump wavelength coincides with the fiber zero-dispersion wavelength.

of frequency detuning corresponds to the maximum of $\mathrm{Im}[\tilde{R}_a(\Omega)]$. From Fig. 4.3(a) we can see that the inclusion of SRS in the description of the FWM process leads to a frequency dependence on the evolution of the signal power. In Fig. 4.3(b) we plot the evolution of the signal field in the co-polarized scheme outside the fiber zero-dispersion wavelength. From Fig. 4.3(b) we can see that when $\lambda_p \neq \lambda_0$ the evolution of the signal field, for small frequency detunings, less than 2 THz, is described by both the real and imaginary parts of the fiber nonlinear response (4.2).

The real part contribution arises from the fact that $\Delta\beta_x \neq 0$ in (4.15) and (4.18). However, for frequency detunings higher than 2.5 THz, the evolution of the signal is field is mostly described by the imaginary part of the fiber nonlinear response function. In Fig. 4.3(c) and in Fig. 4.3(d) we plot the evolution of the signal field in the orthogonal polarization scheme. In Fig. 4.3(c) we use $\lambda_p = \lambda_0$, whereas in Fig. 4.3(d) the pump wavelength does not coincides with λ_0. We can see that does not exist a significant difference between both results, due to the high value of the group birefringence. The results presented in Fig. 4.3(c) and in Fig. 4.3(d) also show that the evolution of the signal wave is mostly described by $\mathrm{Im}[-\tilde{R}_b(\Omega_{sp})]$, which is proportional to the orthogonal Raman gain parameter given by (4.5).

In Fig. 4.4 we plot the theoretical prediction for the idler field given by (4.19) as a function of frequency detuning. In Fig. 4.4(a) and in Fig. 4.4(b) we plot the idler wave in the co-polarized scheme, see Fig. 4.2(a), whereas in Fig. 4.4(c) and in Fig. 4.4(d) it is presented the idler wave in the orthogonal polarization scheme, see Fig. 4.2(b). From Fig. 4.4(a) we can see that when the pump wavelength, λ_p, coincides with the fiber zero-dispersion wavelength, λ_0, the generation of the idler field is mostly described by the real part of the fiber nonlinear response function $(\mathrm{Re}[\tilde{R}_a(\Omega_{ip}) + \mathrm{Re}[\tilde{R}_b(\Omega_{ip})])$, see Fig. 4.1(c). Due to a maximum in the real part of $\tilde{R}_b(\Omega)$ around $\Omega/2\pi = 1$ THz, see Fig. 4.1(c), the presence of the SRS increases the efficiency of the generation of the idler wave, for small frequency detunings (less than 2 THz).
Outside the zero-dispersion wavelength, Fig. 4.4(b), the limit $f_R = 0$ is a quite good approximation to describe the generation of the idler wave. The evolution of the optical power of the idler wave, for $\lambda_p \neq \lambda_0$, is mostly described by the nonlinear instantaneous response of fiber, given by the first term on the right side of (4.2), and the evolution of the phase-matching condition with the frequency detuning given by (4.17) with $j = x$.
In Fig. 4.4(c) we plot the evolution of the idler wave in the orthogonal polarization scheme, and with $\lambda_p = \lambda_0$. From Fig. 4.4(c) we can see that the idler wave is mostly described by the real part of $\tilde{R}_b(\Omega_{ip})$, see Fig. 4.1(c). The results also show that this polarization scheme leads to an inefficient generation of the idler wave, due to high value of the group birefringence, and due to the presence of the SRS.
Outside the zero-dispersion and in the orthogonal polarization scheme, Fig. 4.4(d), the limit $f_R = 0$ is a good approximation, as it is the case presented in Fig. 4.4(b). The results plotted in Fig. 4.4(d) also show that the orthogonal scheme leads to an inefficient generation of the idler wave, mainly due to the high value of the group birefringence of the optical fiber.

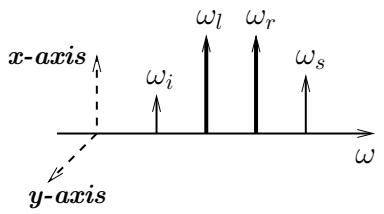

(a) Co-polarized scheme.

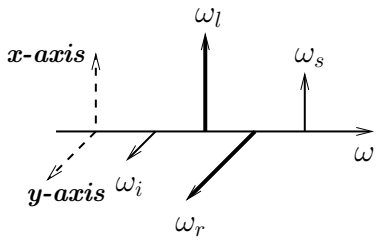

(b) Orthogonal, signal parallel to the left pump ω_l.

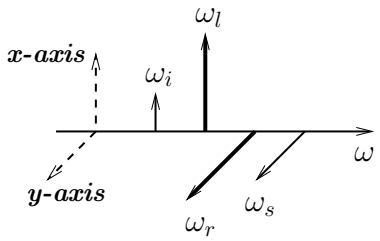

(c) Orthogonal, signal parallel to the right pump ω_r.

Figure 4.5: Polarization schemes of the FWM process in the dual pump configuration.

4.1.3 Dual-Pump Configuration

In this section we analyze the FWM process when two pumps (ω_l and ω_r) and a signal (ω_s) are launched into a fiber given rise to the idler wave, $\omega_i = \omega_l + \omega_r - \omega_s$ [16]. The FWM process in the dual pump configuration can be decomposed in three different polarization schemes [39], see Fig. 4.5. We assume that the pumps are always much more intense than the idler and signal waves. Hence, we use the undepleted-pump approximation. In order to avoid multiple FWM processes [40–42], the pumps and signal power are maintained in a low power regime. It is also assumed that the fiber length is much shorter than the walk-off length [16]. In that regime it is applicable the CW approximation [16]. Under these approximations the total optical field can be written as [16]

$$A_j(z,t) = A_{lj}(z)e^{-i\Omega_l t} + A_{rk}(z)e^{-i\Omega_r t} + A_{s\upsilon}(z)e^{-i\Omega_s t} + A_{i\varsigma}(z)e^{-i\Omega_i t}\,, \tag{4.20}$$

where $j,k,\upsilon,\varsigma = x,y$, depending on the polarization scheme, $\Omega_u = \omega_u - \omega_0$ where $u = l,r,s,i$ and ω_0 is the fiber zero-dispersion frequency, $A_{lj}(z)$ and $A_{rk}(z)$ represent the pumps amplitude, $A_{s\upsilon}(z)$ and $A_{i\varsigma}(z)$ represent the amplitude of the signal and idler fields, respectively. From (4.1) and (4.20) we can see that the two pumps, ω_l and ω_r, can interact with each other through the SRS, and their optical power evolution is given by

$$\frac{\partial P_{hj}(z)}{\partial z} = -g_{Rm}(\Omega_{ht})P_{hj}(z)P_{tk}(z)\,, \tag{4.21}$$

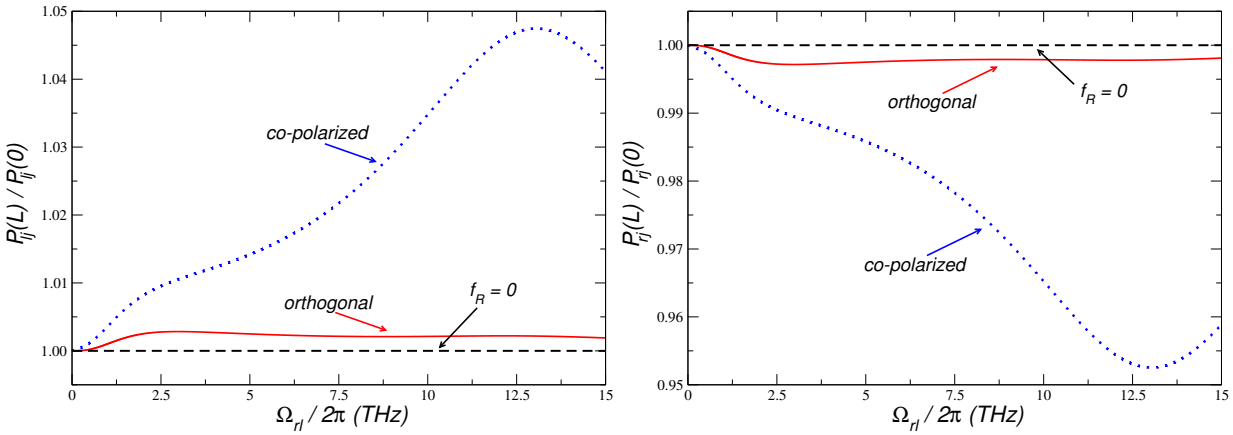

(a) Left pump evolution.

(b) Right pump evolution.

Figure 4.6: Optical power evolution of the pumps with frequency detuning Ω_{rl}. Results shows that for $\Omega_{rl}/2\pi < 3$ THz the energy transfer between the pumps is very small, less than 1% for the co-polarized scheme, and approximately 0.3% for the orthogonally scheme of polarization.

where $h,t = l,r$ with $h \neq t$. For the co-polarized scheme $j = k = x$ and $g_{Rm} = g_{R\parallel}$, and for the orthogonally scheme $j \neq k = x,y$ and $g_{Rm} = g_{R\perp}$. Solving (4.21) we obtain

$$P_{hj}(z) = \frac{P_{hj}(0)\left[g_{Rm}(\Omega_{th})P_{hj}(0) - g_{Rm}(\Omega_{ht})P_{tk}(0)\right]}{g_{Rm}(\Omega_{th})P_{hj}(0) - g_{Rm}(\Omega_{ht})P_{tk}(0)e^{-\Gamma(\Omega)z}}, \tag{4.22}$$

where $\Gamma(\Omega) = g_{Rm}(\Omega_{th})P_{hk}(0) - g_{Rm}(\Omega_{ht})P_{tj}(0)$. Typically, in FWM experiences the two pumps are placed closely to the zero-dispersion wavelength in order to achieve the phase-matching condition, and the pump powers are maintaining at a low power regime. Under these conditions the power transfer between the pumps is very small [43]. In Fig. 4.6 we plot the optical power evolution of the two pumps, given by (4.22), with the frequency detuning Ω_{rl}. From Fig. 4.6 we can see that for frequency detunings less than 3 THz the energy transfer between the pumps is very small, less than 1% for the co-polarized scheme, and it is even smaller for the orthogonal scheme of polarization, approximately 0.3%. In this regime of low optical powers and small frequency pump detunings, we can neglect the energy transfer between the pumps. Using this approximation, the evolution of the complex amplitudes of the pump fields along the fiber is given by

$$A_{hj}(z) = A_{hj}(0)\exp\{i\left[\beta_j(\omega_h) + \gamma P_{hj}(0) + 2\gamma P_{tk}(0)\right]z\}, \tag{4.23}$$

where $A_{hj}(0)$ is the input pump amplitude.

Co-Polarized Scheme

The NSE equation for the signal and idler fields in the co-polarized scheme, Fig. 4.5(a), can be written as

$$\frac{\partial A_{qx}(z)}{\partial z} = i\beta_x(\omega_q)A_{qx}(z) + i\gamma\zeta_x(\Omega_{ql})P_{lx}(0)A_{qx}(z) + i\gamma\left[\zeta_x(\Omega_{qr})P_{rx}(0)A_{qx}(z) + \varepsilon_x(\omega_q)A_{lx}(z)A_{rx}(z)A^*_{fx}(z)\right], \quad (4.24)$$

with

$$\varepsilon_x(w_q) = 2(1-f_R) + f_R\left[\tilde{R}_a(\Omega_{ql}) + \tilde{R}_b(\Omega_{ql})\right] + f_R\left[\tilde{R}_a(\Omega_{ql}) + \tilde{R}_b(\Omega_{qr})\right], \quad (4.25)$$

where $q, f = s$ for signal wave and $q, f = i$ for idler field with $q \neq f$. In (4.24) $\zeta_x(\Omega_{ql})$ and $\zeta_x(\Omega_{qr})$ are given by (4.9). If $f_R = 0$ we obtain the description of the FWM process in the absence of Raman contribution. The complex amplitudes for the signal and idler fields at a distance z are given by

$$\frac{A_{sx}(z)}{A_{sx}(0)} = \left(\cosh(g_x(\omega_s)z)e^{i\delta\beta_x(\omega_s)z/2} + i\frac{\kappa_x(\omega_s)}{2g_x(\omega_s)}\sinh(g_x(\omega_s)z)e^{i\delta\beta_x(\omega_s)z/2}\right)\phi_x(z), \quad (4.26)$$

and

$$\frac{A_{ix}(z)}{A^*_{sx}(0)} = i\frac{\gamma\varepsilon_x(\omega_i)}{g_x(\omega_i)}\sinh(g_x(\omega_i)z)A_{lx}A_{rx}\phi_x(z)e^{-i\delta\beta_x(\omega_i)z/2}, \quad (4.27)$$

where A_{lx} and A_{rx} are the input pump amplitudes, and

$$g_x^2(\omega_q) = (\gamma\varepsilon_x(\omega_q))^2P_{lx}(0)P_{rx}(0) - \left(\frac{\kappa_x(\omega_q)}{2}\right)^2, \quad (4.28)$$

$$\kappa_x(\omega_q) = \Delta\beta_{xx} + \gamma P_p(\zeta_x(\Omega_{ql}) + \zeta_x(\Omega_{qr}) - \zeta_x(0) - 1), \quad (4.29)$$

$$\delta\beta_x(\omega_q) = \beta_x(\omega_s) - \beta_x(\omega_i) + \gamma P_g[\zeta_x(\Omega_{qh}) - \zeta_x(\Omega_{qt})], \quad (4.30)$$

$$\phi_x(z) = \exp\{i(\beta_x(\omega_l) + \beta_x(\omega_r) + 3\gamma P_p)z/2\}, \quad (4.31)$$

where $h = l$ and $t = r$ for $q = s$, $h = r$ and $t = l$ for $q = i$, $P_g = P_{lx}(0) - P_{rx}(0)$, $P_p = P_{lx}(0) + P_{rx}(0)$ is the total pump input power, and $\Delta\beta_{xx}$ is the phase-matching condition [16, 37, 38]

$$\Delta\beta_{xx} = \beta_x(\omega_s) + \beta_x(\omega_i) - \beta_s(\omega_l) - \beta_x(\omega_r) \approx \frac{1}{2}(\omega_s - \omega_l)(\omega_s - \omega_r)(\omega_r + \omega_l - 2\omega_0)\beta_3, \quad (4.32)$$

where ω_0 is chosen at the zero-dispersion of the fiber and β_3 is the third order dispersion coefficient. The optical power evolution for the signal and idler fields is given by

$$\frac{P_{sx}(z)}{P_{sx}(0)} = \left|\cosh(g_x(\omega_s)z) + i\frac{\kappa_x(\omega_s)}{2g_x(\omega_s)}\sinh(g_x(\omega_s)z)\right|^2, \quad (4.33)$$

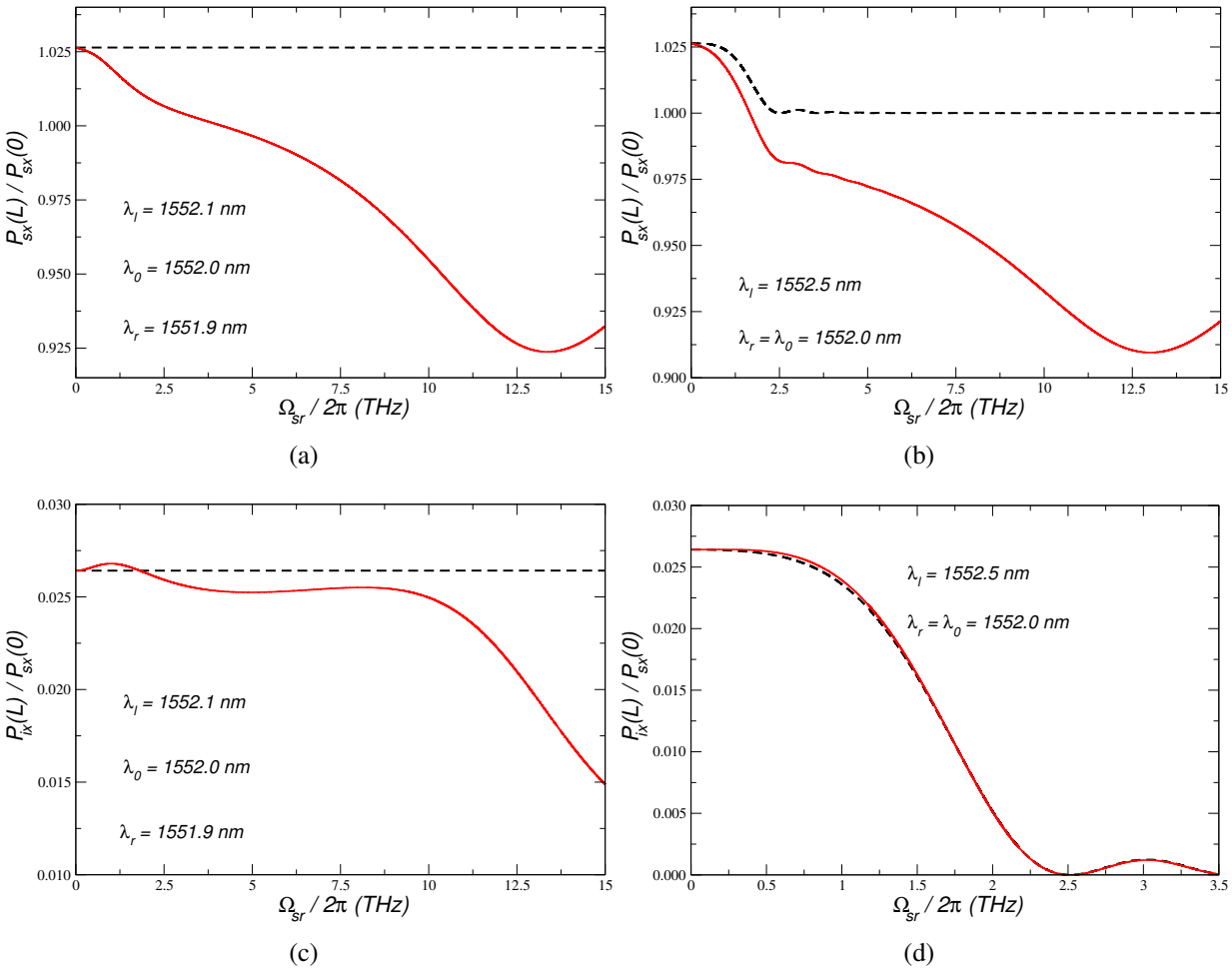

Figure 4.7: Theoretically predictions for the signal and idler fields given by (4.33) and (4.34) respectively, in the co-polarized dual pump FWM process, as a function of frequency detuning. Dashed lines represent the limit $f_R = 0$ and solid lines $f_R = 0.245$. Results show that when $\Delta\beta_{xx} = 0$, plots (a) and (c), the signal is mostly described by the imaginary part of the nonlinear response function, whereas the idler field is mostly described by the real part.

and

$$\frac{P_{ix}(z)}{P_{sx}(0)} = |\gamma\varepsilon_x(\omega_i)z|^2 P_{lx}(0)P_{rx}(0)\left|\frac{\sinh\left(g_x(\omega_i)z\right)}{g_x(\omega_i)z}\right|^2. \tag{4.34}$$

In Fig. 4.7 we plot the optical power evolution for both signal and idler fields in the co-polarized scheme, given by (4.33) and (4.34) respectively, as a function of frequency detuning, for the dual pump configuration, see Fig. 4.5(a). In Fig. 4.7(a) and in Fig. 4.7(b) we plot the optical power evolution of the signal field, whereas in Fig. 4.7(c) and in Fig. 4.7(d) we plot the optical power evolution of the idler wave. In Fig. 4.7(a) and in Fig. 4.7(c) the phase-matching condition (4.32) is achieved, $\Delta\beta_{xx} = 0$, whereas in Fig. 4.7(b) and in Fig. 4.7(d) the

wavelength of the right pump, λ_r, coincides with the fiber zero-dispersion wavelength, λ_0, and the left pump wavelength, λ_l, is higher than λ_0. From Fig. 4.7(a) we can see that the signal field is mostly described by $(\mathrm{Im}[-\tilde{R}_a(\Omega_{sl})] + \mathrm{Im}[-\tilde{R}_b(\Omega_{sl})] + \mathrm{Im}[-\tilde{R}_a(\Omega_{sr})] + \mathrm{Im}[-\tilde{R}_b(\Omega_{sr})])$, see Fig. 4.1(b), which is proportional to the Raman gain, given by (4.4). Increasing the frequency detuning the magnitude of $\mathrm{Im}[-\tilde{R}_a(\Omega)]$ dominates, and the signal field is mostly described by $(\mathrm{Im}[-\tilde{R}_a(\Omega_{sl})] + \mathrm{Im}[-\tilde{R}_a(\Omega_{sr})])$, which leads to a minimum of efficiency in the signal wave around 13 THz, see Fig. 4.1(b). The results plotted in Fig. 4.7(a) show that the SRS decreases the optical power of the signal wave of approximately 10%, when compared with the case $f_R = 0$. In Fig. 4.7(b) we plot the evolution of the signal wave when $\Delta\beta_{xx} \neq 0$. From Fig. 4.7(b) we can see that for $\Omega_{sr}/2\pi < 2.5$ THz, the signal field is mostly described by both the real and imaginary parts of the fiber nonlinear response given by (4.2). The dependence on the real part of the nonlinear fiber response arises from the fact that $\Delta\beta_{xx} \neq 0$ in (4.33). For higher frequency detunings the signal field is mostly described by $(\mathrm{Im}[-\tilde{R}_a(\Omega_{sl})] + \mathrm{Im}[-\tilde{R}_a(\Omega_{sr})])$. In Fig. 4.7(c) we plot the optical power of the idler wave, given by (4.34), as a function of frequency detuning, for $\Delta\beta_{xx} = 0$. From Fig. 4.7(c) we can see that the idler field is mostly described by the real part of the fiber nonlinear response function, given by $(\mathrm{Re}[\tilde{R}_a(\Omega_{il})] + \mathrm{Re}[\tilde{R}_b(\Omega_{il})] + \mathrm{Re}[\tilde{R}_a(\Omega_{ir})] + \mathrm{Re}[\tilde{R}_b(\Omega_{ir})])$, see Fig. 4.1(c). The results also show that the SRS increases the optical power of the idler wave for frequency detunings less than 2 THz, due to a maximum in the magnitude of $(\mathrm{Re}[\tilde{R}_a(\Omega_{il})] + \mathrm{Re}[\tilde{R}_a(\Omega_{ir})])$, around that frequency, see Fig. 4.1(c). However, for higher frequency detunings, the SRS decreases the optical power of the idler wave due to the reduction of the magnitude of the real part of $\tilde{R}_a(\Omega)$, see Fig. 4.1(c). In Fig. 4.7(d) we plot the evolution of the idler wave when $\Delta\beta_{xx} \neq 0$. From Fig. 4.7(d) we can see that the limit $f_R = 0$ is a good approximation to describe the idler wave. In that case the optical power evolution of the idler wave is mostly described by the nonlinear instantaneous response of the fiber, given by the first term on the right side of (4.2), and the phase-matching condition is given by (4.32).

Orthogonal Scheme of Polarization

The NSE equation for the signal and idler fields, for the two orthogonal polarization schemes, can be written as

$$\frac{\partial A_{sj}(z)}{\partial z} = i\beta_j(\omega_s)A_{sj}(z) + i\gamma\zeta_x(\Omega_{sh})P_{hj}(0)A_{sj}(z) + i\gamma\left[\zeta_y(\Omega_{st})P_{tk}(0)A_{sj}(z) + \xi_j(\omega_s)A_{lx}(z)A_{ry}(z)A^*_{ik}(z)\right], \quad (4.35)$$

and

$$\frac{\partial A_{ik}(z)}{\partial z} = i\beta_k(\omega_i)A_{ik}(z) + i\gamma\zeta_x(\Omega_{it})P_{tk}(0)A_{ik}(z) + i\gamma\left[\zeta_y(\Omega_{ih})P_{hj}(0)A_{ik}(z) + \xi_k(\omega_i)A_{lx}(z)A_{ry}(z)A^*_{sj}(z)\right], \quad (4.36)$$

where $j,k = x,y$ with $j \neq k$. For $j = x$, $h = l$ and $t = r$, and for $j = y$, $h = r$ and $t = l$. In (4.35) and (4.36) ζ_x and ζ_y are given by (4.9) and (4.10), respectively, and

$$\xi_x(\omega_q) = 2\frac{1-f_R}{3} + f_R\tilde{R}_a(\Omega_{ql}) + \frac{f_R}{2}\tilde{R}_b(\Omega_{qr}), \quad (4.37)$$

$$\xi_y(\omega_q) = 2\frac{1-f_R}{3} + f_R\tilde{R}_a(\Omega_{qr}) + \frac{f_R}{2}\tilde{R}_b(\Omega_{ql}). \quad (4.38)$$

The evolution of the signal and idler complex amplitudes inside the optical fiber are given by

$$\frac{A_{sj}(z)}{A_{sj}(0)} = \cosh(g_{jk}(\omega_s)z)\phi_{xy}(z)e^{i\delta\beta_{jk}(\omega_s)z/2} + i\frac{\kappa_{jk}(\omega_s)}{2g_{jk}(\omega_s)}\sinh(g_{jk}(\omega_s)z)\phi_{xy}(z)e^{i\delta\beta_{jk}(\omega_s)z/2}, \quad (4.39)$$

and

$$\frac{A_{ik}(z)}{A^*_{sj}(0)} = \frac{\gamma\xi_k(\omega_i)}{g_{jk}(\omega_i)}\sinh(g_{jk}(\omega_i)z)A_{lx}A_{ry}\phi_{xy}(z)e^{-i\delta\beta_{jk}(\omega_i)z/2}, \quad (4.40)$$

where A_{lx} and A_{ry} are the input pump amplitudes, and

$$g^2_{jk}(\omega_q) = (\gamma\xi_j(\omega_q))^2P_{lx}(0)P_{ry}(0) - \left(\frac{\kappa_{jk}(\omega_q)}{2}\right)^2, \quad (4.41)$$

$$\kappa_{jk}(\omega_q) = \Delta\beta_{jk} + \gamma P_p(\zeta_x(\Omega_{qh}) + \zeta_y(\Omega_{qt}) - \zeta_y(0) - 1), \quad (4.42)$$

$$\delta\beta_{jk}(\omega_q) = \beta_j(w_s) - \beta_k(w_i) + \gamma P_g[\zeta_j(\Omega_{qh}) - \zeta_k(\Omega_{qt})], \quad (4.43)$$

$$\phi_{xy}(z) = \exp\{i(\beta_x(w_l) + \beta_y(w_r) + \gamma P_p)(1 - \zeta_y(0))z/2\}, \quad (4.44)$$

where $P_p = P_{lx}(0) + P_{ry}(0)$ and $P_g = P_{lx}(0) - P_{ry}(0)$. The orthogonal scheme is separated in two different processes according with Fig. 4.5(b) and Fig. 4.5(c).

Signal Parallel to Left Pump The phase-matching condition in this configuration is given by [16, 37, 38]

$$\Delta\beta_{xy} = \beta_x(\omega_s) + \beta_y(\omega_i) - \beta_x(\omega_l) - \beta_y(\omega_r) \approx \frac{\omega_l - \omega_s}{c}\delta n + \frac{1}{2}(\omega_s - \omega_l)(\omega_s - \omega_r)(\omega_r + \omega_l - 2\omega_0)\beta_3, \quad (4.45)$$

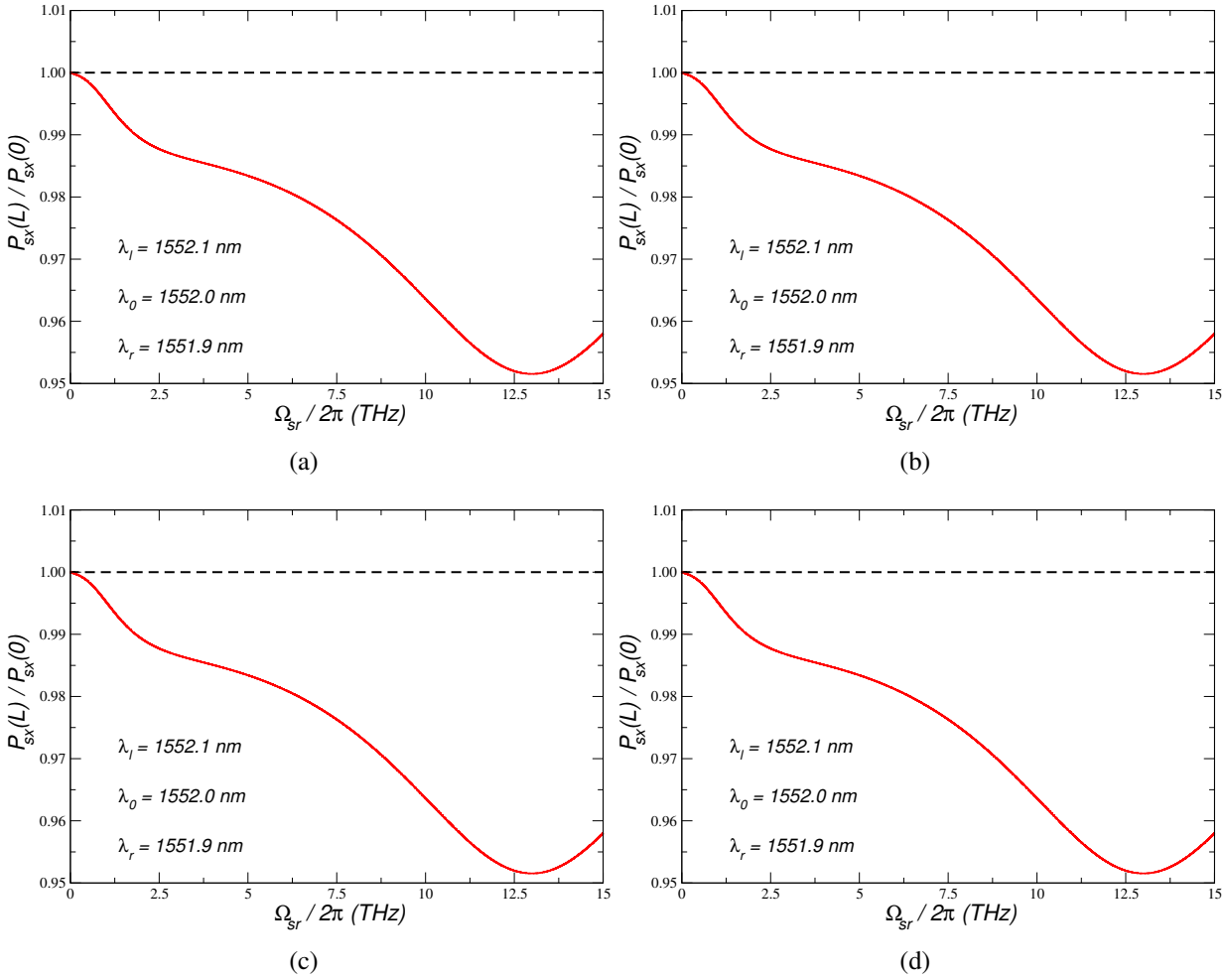

Figure 4.8: Optical power of the signal and idler fields in the orthogonal scheme of polarization, with signal launched parallel to the left pump ω_l, given by (4.46) and (4.47), respectively, as a function of frequency detuning. Dashed lines represent the limit $f_R = 0$ and solid lines $f_R = 0.245$. Results show that the signal field is mostly described by the imaginary part of the nonlinear response function, and also show that this polarization scheme leads to an inefficient generation of the idler wave.

where c is the speed of light in vacuum, and $\delta n = n_y - n_x$. The optical power of the signal and idler fields, according with (4.39) and (4.40), in this polarization scheme is given by

$$\frac{P_{sx}(z)}{P_{sx}(0)} = \left|\cosh(g_{xy}(\omega_s)z) + i\frac{\kappa_{xy}(\omega_s)}{2g_{xy}(\omega_s)}\sinh(g_{xy}(\omega_s)z)\right|^2, \tag{4.46}$$

and

$$\frac{P_{iy}(z)}{P_{sx}(0)} = \left|\gamma\xi_y(\omega_i)z\right|^2 P_{lx}(0)P_{ry}(0)\left|\frac{\sinh(g_{xy}(\omega_i)z)}{g_{xy}(\omega_i)z}\right|^2, \tag{4.47}$$

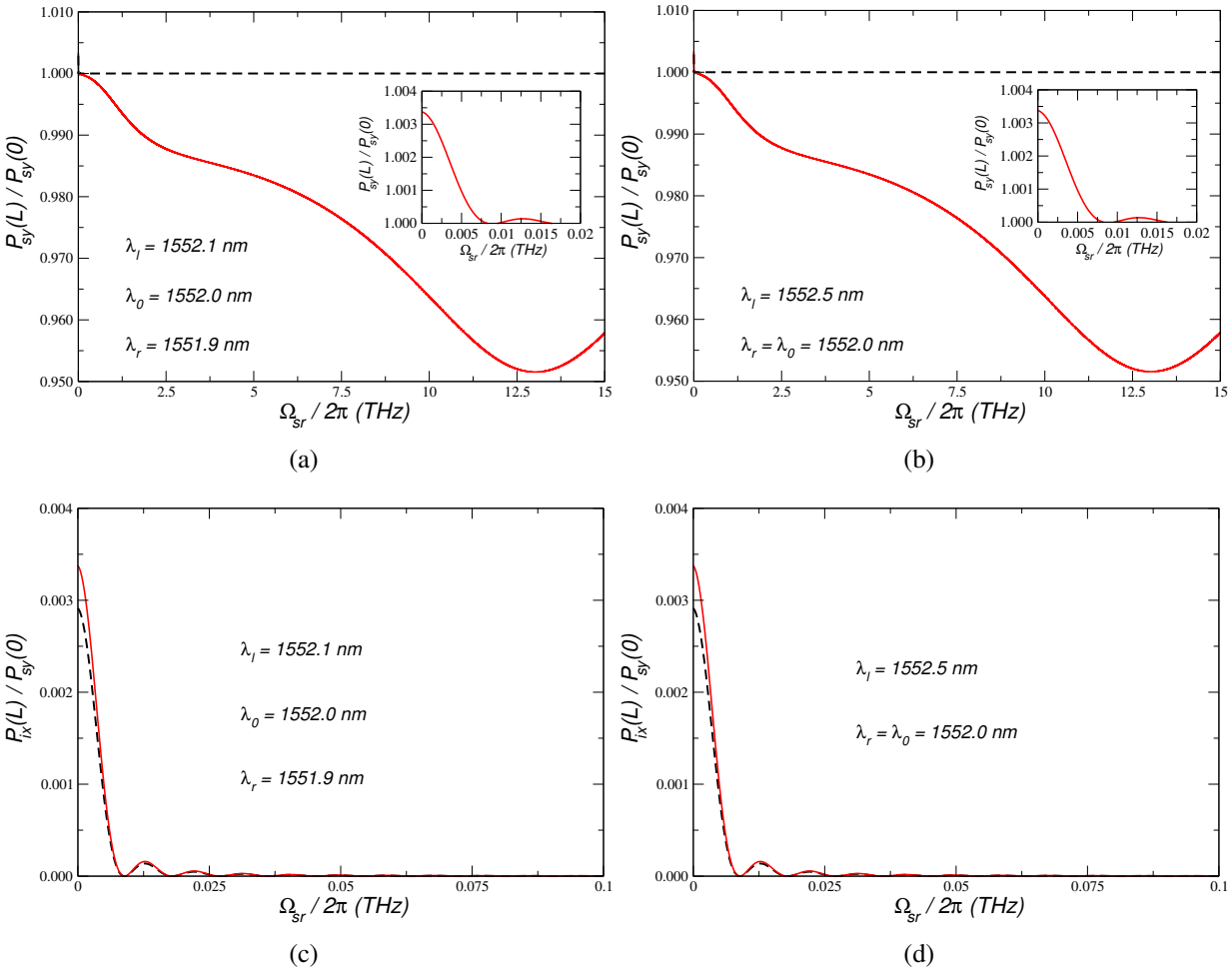

Figure 4.9: Optical power of the signal and idler fields in the orthogonal scheme of polarization, with signal launched parallel to the right pump ω_r, given by (4.49) and (4.50), respectively, as a function of frequency detuning. Dashed lines represent the limit $f_R = 0$ and solid lines $f_R = 0.245$. Results show that the generation of the idler wave and the amplification of the signal field in this polarization scheme is efficient for frequency detunings less than 0.01 THz, see inset in plots (a) and (b).

where ξ_y is given by (4.38).

Signal Parallel to Right Pump The phase-matching condition in this configuration is given by [16, 37, 38]

$$\Delta\beta_{yx} = \beta_y(\omega_s) + \beta_x(\omega_i) - \beta_x(\omega_l) - \beta_y(\omega_r) \approx \frac{\omega_s - \omega_r}{c}\delta n + \frac{1}{2}(\omega_s - \omega_l)(\omega_s - \omega_r)(\omega_r + \omega_l - 2\omega_0)\beta_3\,, \quad (4.48)$$

and the evolution of the optical power for the signal and idler fields according with (4.39) and (4.40) is given by

$$\frac{P_{sy}(z)}{P_{sy}(0)} = \left|\cosh(g_{yx}(\omega_s)z) + i\frac{\kappa_{yx}(\omega_s)}{2g_{yx}(\omega_s)}\sinh(g_{yx}(\omega_s)z)\right|^2, \tag{4.49}$$

and

$$\frac{P_{ix}(z)}{P_{sy}(0)} = |\gamma\xi_x(\omega_i)z|^2 P_{lx}(0)P_{ry}(0)\left|\frac{\sinh(g_{yx}(\omega_i)z)}{g_{yx}(\omega_i)z}\right|^2, \tag{4.50}$$

where ξ_x is given by (4.37).

In Fig. 4.8 we plot the optical power of the signal and idler fields, given by (4.46) and (4.47) respectively, as a function of the frequency detuning, see scheme in Fig. 4.5(b). In Fig. 4.8(a) and in Fig. 4.8(b) we plot the optical power evolution of the signal field, whereas in Fig. 4.8(c) and in Fig. 4.8(d) we plot the optical power evolution of the idler wave. In Fig. 4.8(a) and in Fig. 4.8(c) we use $\omega_l + \omega_r = 2\omega_0$ in (4.45), whereas in Fig. 4.8(b) and in Fig. 4.8(d) the wavelength of the right pump, λ_r, coincides with the fiber zero-dispersion wavelength, λ_0, and the left pump wavelength, λ_l, is higher than λ_0. From Fig. 4.8(a) and from Fig. 4.8(b) we can see that the signal field is mostly described by the sum of the imaginary parts of the fiber nonlinear response function, given by $(2\,\mathrm{Im}[-\tilde{R}_a(\Omega_{sl})] + \mathrm{Im}[-\tilde{R}_b(\Omega_{sr})])$, see Fig. 4.1(b). For $\Omega_{sr}/2\pi > 2.5$ THz, the magnitude of $\mathrm{Im}[-\tilde{R}_a(\Omega_{sl})]$ dominates, and the signal wave will be mostly described by that function, see Fig. 4.1(b). The optical power of the signal wave plotted in Fig. 4.8(a) is slightly higher than the presented in Fig. 4.8(b), due to the fact that in Fig. 4.8(a) we use $\omega_l + \omega_r = 2\omega_0$. From Fig. 4.8(a) and from Fig. 4.8(b) we can see that for $\Omega_{sr}/2\pi \approx 13$ THz the inclusion of the SRS on the description of the FWM process decreases the optical power of the signal wave of approximately 5%, when compared with the limit of $f_R = 0$. In Fig. 4.8(c) and in Fig. 4.8(d) we plot the generation of the idler wave, given by (4.47), as a function of frequency detuning. From Fig. 4.8(c) and from Fig. 4.8(d) we can see that the limit $f_R = 0$ is a good approximation. This results from the fact that the idler field in this polarization scheme is mostly described by both, the nonlinear instantaneous response of the fiber (4.2), and the phase-matching condition (4.45). In Fig. 4.8(c) the group birefringence leads to $\Delta\beta_{xy} \neq 0$. The group birefringence, δn, present in the phase-matching condition (4.45) leads to an inefficient generation of the idler wave. However, when $\omega_l + \omega_r = 2\omega_0$, see Fig. 4.8(c), the generation of the idler wave is more efficient than when $\omega_l + \omega_r \neq 2\omega_0$, see Fig. 4.8(d).

In Fig. 4.9 we plot the optical power of the signal and idler fields given by (4.49) and (4.50), respectively, as a function of the frequency detuning, see scheme in Fig. 4.5(c). In Fig. 4.9(a)

and in Fig. 4.9(b) we plot the optical power evolution of the signal field, whereas in Fig. 4.9(c) and in Fig. 4.9(d) we plot the optical power evolution of the idler wave. In Fig. 4.9(a) and in Fig. 4.9(c) we use $\omega_l + \omega_r = 2\omega_0$ in (4.48), whereas in Fig. 4.9(b) and in Fig. 4.9(d) the wavelength of the right pump, λ_r, coincides with the fiber zero-dispersion wavelength, λ_0, and the left pump wavelength, λ_l, is higher than λ_0. From Fig. 4.9(a) and from Fig. 4.9(b) we can see that the signal field is mostly described by $(2\,\mathrm{Im}[-\tilde{R}_a(\Omega_{sr})] + \mathrm{Im}[-\tilde{R}_b(\Omega_{sl})])$, see Fig. 4.1(b). For $\Omega_{sr}/2\pi < 0.01$ THz the phase-matching condition given by (4.48) is almost perfect, and the amplification of the signal wave is very efficient. For $0.01 < \Omega_{sr}/2\pi(\mathrm{THz}) < 2.5$ the signal field is mostly described by $\mathrm{Im}[-\tilde{R}_b(\Omega_{sl})]$, whereas for $\Omega_{sr}/2\pi > 2.5$ THz the signal wave will be mostly described by $\mathrm{Im}[-\tilde{R}_a(\Omega_{sr})]$, see Fig. 4.1(b). The optical power of the signal wave plotted in Fig. 4.9(a) is slightly higher than the presented in Fig. 4.9(b), due to the fact that in Fig. 4.9(a) we use $\omega_l + \omega_r = 2\omega_0$. From Fig. 4.9(a) and from Fig. 4.9(b) we can see that for $\Omega_{sr}/2\pi \approx 13$ THz the inclusion of the SRS on the description of the FWM process decreases the optical power of the signal wave of approximately 5%, when compared with $f_R = 0$. In Fig. 4.9(c) and in Fig. 4.9(d) we plot the generation of the idler wave, given by (4.50), as a function of frequency detuning. From Fig. 4.9(c) and from Fig. 4.9(d) we can see that the limit $f_R = 0$ is a good approximation. The results plotted in Fig. 4.9(c) and in Fig. 4.9(d) show that for $\Omega_{sr}/2\pi < 0.01$ THz the generation of the idler wave is very efficient in this polarization scheme, due to the fact that $\Delta\beta_{yx} \approx 0$, in that frequency range. However, for higher frequency detunings, this polarization scheme leads to an inefficient generation of the idler wave due to the high value of the group birefringence (4.48). From Fig. 4.9(c) and from Fig. 4.9(d) we can also see that when $\omega_l + \omega_r = 2\omega_0$, the generation of the idler wave is more efficient than when $\omega_l + \omega_r \neq 2\omega_0$.

4.2 Multiple FWM in the Dual-Pump Configuration

Typically, the single or dual pump FWM process involves only the generation of a new frequency. In these configurations, several studies of FWM process in optical fibers have been carried out, taken into account the quasi-instantaneous response of the nonlinear dielectric medium [44–46] and the delayed Raman response [1, 11, 14, 28]. For fiber lengths of the order of the effective length of interaction, the optical fiber can be considered an almost lossless medium. In that limit several new frequencies are generated inside the fiber through multiple FWM processes [40]. The multiple FWM process in optical fibers was investigated in [40, 41, 47], and their work was latter extended to investigate the conservation law [48] and the nonlinear dynamics [49] of dual frequency-pumped multiple FWM processes, as well to describe the dynamical evolu-

tion of the sidebands along an optical fiber [50]. Subsequent studies explored the interactions between pumps and the generated sidebands in highly birefringent fibers [51], and the role of stochasticity on multiple FWM processes [52]. Recently, the self-stability function of multiple FWM processes was studied in [53], and their work has extended in order to describe this process in the presence of multifrequency pumps [42]. In [14], we studied the influence of the SRS on the generation of one idler wave through the stimulated FWM process in the single and dual pump configurations. Potential applications of these nonlinear processes are wavelength converters [2, 3], modulation instability [51, 54], demultiplexing [55, 56] and phase conjugation [57, 58].

Existing theories cannot completely describe the simultaneous generation of two idler waves through multiple FWM processes in optical fibers. For this reason, numerical solution of the NSE is used for explain the experimental data [40–42, 47–53]. In this section we develop a theoretical model capable of describing the generation of two idler waves inside a birefringent optical fiber through three FWM processes in the dual pump configuration, and considering both the co-polarized and orthogonal polarization schemes. The obtained results take into account the delayed Raman response of the fiber. We use our model to quantify the impact of the delayed Raman response of the fiber on the generation of the two idler waves through three FWM processes. Since our theoretical model is vectorial, we are able to describe the evolution of the idler waves as function of the polarization angle between the two pumps.

4.2.1 Analytical Model

Using the model presented in section 4.1.1, we analyze in this section the generation of two new frequencies inside a HiBi optical fiber through multiple FWM processes. In this study, two pumps (at ω_1 and ω_2) are launched into a fiber, given rise to two new frequencies, ω_3 and ω_4, through three FWM processes, two degenerated and one non-degenerated. The two degenerate processes are given by $\omega_3 = 2\omega_1 - \omega_2$ and $\omega_4 = 2\omega_2 - \omega_1$, whereas the non-degenerated is given by $\omega_1 + \omega_2 = \omega_3 + \omega_4$. This multiple FWM process can be decomposed in two different polarization schemes, see Fig. 4.10. We assume that the pumps are always much more intense than the idlers, and it is also assumed that the fiber length is much shorter than the walk-off length [16]. In that regime, we can apply the quasi-CW approximation and the total optical field can be written as

$$A_j(z,t) = \sum_N A_{N,j}(z) \exp\{-i\Omega_N t\}\,, \tag{4.51}$$

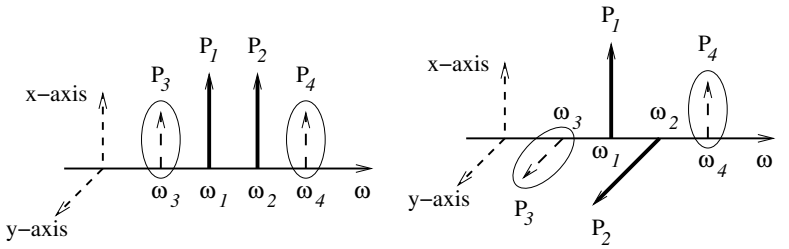

(a) Co-polarized scheme.

(b) Orthogonal polarization scheme.

Figure 4.10: Polarization schemes of the multiple FWM process.

where $N = 1,2,3,4$ represents all fields in the j state of polarization, and $\Omega_N = \omega_N - \omega_0$, with ω_0 being the fiber zero-dispersion frequency of the fiber. Substituting (4.51) in (4.1), the NSE for the pump fields, can be written as

$$\frac{\partial A_{u,j}(z)}{\partial z} = ik_j(\omega_u)A_{u,j}(z) + i\gamma P_{u,j}(z)A_{u,j}(z) + i\gamma\xi_m(\Omega_{u,v})P_{v,l}(z)A_{u,j}(z)\,, \tag{4.52}$$

where $u,v = 1,2$ represent the two pumps, according with the notation used in Fig. 4.10, with $u \neq v$, $\xi_m = \xi_{\parallel}$ for the co-polarized scheme, see Fig. 4.10(a), and $\xi_m = \xi_{\perp}$ for the orthogonal polarization scheme, see Fig. 4.10(b). In (4.52), $l = j = x$ for the co-polarized scheme. In the orthogonal polarization scheme $j = x$ and $l = y$ for $u = 1$, whereas for $u = 2$ we have $j = y$ and $l = x$. Finally, $P_{u,j}(z) = \left|A_{u,j}(z)\right|^2$ is the optical power of each pump field, and

$$k_j(\omega_u) = \sum_{m\geq 0} \frac{\beta_{m,j}}{m!}\Omega_u^m\,, \tag{4.53}$$

$$\xi_{\parallel}(\Omega_{u,v}) = 2 - f_R + f_R\left(\tilde{R}_a(\Omega_{u,v}) + \tilde{R}_b(\Omega_{u,v})\right)\,, \tag{4.54}$$

$$\xi_{\perp}(\Omega_{u,v}) = 2\frac{1-f_R}{3} + f_R\tilde{R}_a(0) + \frac{f_R}{2}\tilde{R}_b(\Omega_{u,v})\,, \tag{4.55}$$

where $\tilde{R}_a(\Omega)$ is the Fourier transform of $R_a(\tau)$, and $\tilde{R}_b(\Omega)$ is the Fourier transform of $R_b(\tau)$, and $\Omega_{u,v} = \omega_u - \omega_v$. After some mathematical manipulation, the complex amplitude for the pump fields at a distance z in the fiber can be written as

$$A_{u,j}(z) = A_{u,j}e^{i\left(k_j(\omega_u) - \gamma H_j(\omega_u)\right)z}F_j(0)^{-i\gamma G_j(\omega_u)}F_j(z)^{i\gamma G_j(\omega_u)}\,, \tag{4.56}$$

where $A_{u,j}$ is the input pump amplitudes, and

$$H_j(\omega_u) = \frac{P_{v,l} g_{Rm}^2(\Omega_{u,v}) + P_{u,j} g_{Rm}^2(\Omega_{v,u}) \xi_m(\Omega_{u,v})}{g_{Rm}(\Omega_{u,v}) g_{Rm}(\Omega_{v,u})}, \tag{4.57a}$$

$$G_j(\omega_u) = \frac{g_{Rm}(\Omega_{u,v}) + g_{Rm}(\Omega_{v,u}) \xi_m(\Omega_{u,v})}{g_{Rm}(\Omega_{u,v}) g_{Rm}(\Omega_{v,u})}, \tag{4.57b}$$

$$F_j(z) = g_{Rm}(\Omega_{2,1}) P_{1,x} e^{g_{Rm}(\Omega_{2,1}) P_{1,x} z} - g_{Rm}(\Omega_{1,2}) P_{2,l} e^{g_{Rm}(\Omega_{1,2}) P_{2,l} z}, \tag{4.57c}$$

where $g_{Rm} = g_{R\parallel}$ for the co-polarized scheme, whereas for the orthogonal polarization scheme $g_{Rm} = g_{R\perp}$, and $P_{u,j}$ represents the input pump power. From (4.56), we observe that the two pumps can transfer energy between them through the process of SRS. However, if the pumps are placed closely, $\Omega_{u,v}/2\pi < 3$ THz, and if their power is maintained at a low level [14, 34], the power transfer between the pumps is very small [14]. In that case, equation (4.56) can be written as

$$A_{u,j}(z) = A_{u,j} e^{i(k_j(w_u) + \gamma P_{u,j} + \gamma \xi_m(0) P_{v,l}) z}. \tag{4.58}$$

In the following sections we assume that we are operating around the fiber zero-dispersion wavelength, and we are assuming a typical HiBi optical fiber with the following parameters: $\gamma = 11$ W^{-1}km^{-1}, zero-dispersion wavelength $\lambda_0 = 1550.5$ nm, $\delta n = 10^{-5}$, third and fourth-order dispersion coefficients at zero-dispersion wavelength $\beta_{3,x} = \beta_{3,y} = -2.84 \times 10^{-2}$ ps^3/km and $\beta_{4,x} = \beta_{4,y} = 2.99 \times 10^{-4}$ ps^4/km [20, 24, 37, 59] and length $L = 500$ m. We are also assuming a continuous input optical power per pump of $P_1 = P_2 = P_p = 15$ mW.

4.2.2 Idlers Evolution in the Co-Polarized Scheme

The evolution of the idler fields in the co-polarized scheme is governed by the NSE equation, obtained from (4.1) and (4.51)

$$\begin{aligned}\frac{\partial A_{\nu,x}(z)}{\partial z} = {} & i\left[k_x(\omega_\nu) + \gamma \xi_{\parallel}(\Omega_{\nu,1}) P_{1,x}\right] A_{\nu,x}(z) + i\gamma \xi_{\parallel}(\Omega_{\nu,2}) P_{2,x} A_{\nu,x}(z) \\ & + i\gamma \rho_{\parallel}(\Omega_{\nu,u}) A_{u,x}^2(z) A_{v,x}^*(z) + i\gamma \eta_{\parallel}(\omega_\nu) A_{1,x}(z) A_{2,x}(z) A_{\sigma,x}^*(z), \end{aligned} \tag{4.59}$$

where $\nu \neq \sigma = 3,4$ represent the two idlers, according with the notation used in Fig. 4.10, $u \neq v = 1,2$, with $u = 1$ for $\nu = 3$ and $u = 2$ for $\nu = 4$, and

$$\rho_{\parallel}(\Omega_{\nu,u}) = 1 - f_R + f_R\left(\tilde{R}_a(\Omega_{\nu,u}) + \tilde{R}_b(\Omega_{\nu,u})\right), \tag{4.60}$$

$$\eta_{\parallel}(\omega_\nu) = 2(1 - f_R) + f_R\left(\tilde{R}_a(\Omega_{\nu,u}) + \tilde{R}_b(\Omega_{\nu,u})\right) + f_R\left(\tilde{R}_a(\Omega_{\nu,v}) + \tilde{R}_b(\Omega_{\nu,v})\right). \tag{4.61}$$

The evolution of the complex amplitudes of both idlers at a distance z in the fiber is given by

$$P_{\nu,x}(z) = |A_{\nu,x}(z)|^2 = \left| \left\{ e^{i\mathbb{K}_x(\omega_\nu)z} \left[i\frac{\gamma\rho_\parallel(\Omega_{\nu,u})}{g_x(\omega_\nu)} A_{u,x}^2 A_{v,x}^* \sinh(g_x(\omega_\nu)z) \right.\right.$$
$$\left.\left. + \Theta_{\nu,x}\left(i\frac{\mathbb{K}_x(\omega_\nu)}{g_x(\omega_\nu)} \sinh(g_x(\omega_\nu)z) - \cosh(g_x(\omega_\nu)z) \right) \right] + \Theta_{\nu,x} \right\} \Phi_{\nu,x}(z) \Bigg|^2, \quad (4.62)$$

where both idlers were assumed to have no optical power at $z = 0$, and

$$\Phi_{\nu,x}(z) = e^{i(2k_x(\omega_u) - k_x(\omega_v) + 3\gamma P_{v,x})z}, \quad (4.63a)$$
$$\mathbb{K}_x(\omega_3) = \Big[\Delta\beta_{x1} - \Delta\beta_{x2} + \gamma(P_{1,x} - P_{2,x})(\xi_\parallel(\Omega_{3,1}) - \xi_\parallel(\Omega_{3,2}) + 3) \Big]/2, \quad (4.63b)$$
$$\mathbb{K}_x(\omega_4) = \Big[\Delta\beta_{x2} - \Delta\beta_{x1} + \gamma(P_{2,x} - P_{1,x})(\xi_\parallel(\Omega_{4,2}) - \xi_\parallel(\Omega_{4,1}) + 3) \Big]/2, \quad (4.63c)$$
$$g_x^2(\omega_\nu) = (\gamma\eta_\parallel(\omega_\nu))^2 P_{1,x}P_{2,x} - \frac{1}{4}\big[\Delta\beta_{x3} + \gamma(P_{1,x} + P_{2,x})(\xi_\parallel(\Omega_{\nu,u}) + \xi_\parallel(\Omega_{\nu,v}) - 3) \big]^2. \quad (4.63d)$$

In (4.62), $\Theta_{3,x}$ and $\Theta_{4,x}$ are given by

$$\Theta_{3,x} = \frac{\gamma^2\eta_\parallel(\omega_3)\rho_\parallel(\Omega_{3,1})P_{2,x}A_{1,x}^2A_{2,x}^* - \gamma\varphi_\parallel(\omega_3)\rho_\parallel(\Omega_{3,1})A_{1,x}^2A_{2,x}^*}{\delta_\parallel(\omega_3)\varphi_\parallel(\omega_3) - (\gamma\eta_\parallel(\omega_3))^2 P_{1,x}P_{2,x}}, \quad (4.64a)$$
$$\Theta_{4,x} = \frac{\gamma^2\eta_\parallel(\omega_4)\rho_\parallel(\Omega_{4,2})P_{1,x}A_{2,x}^2A_{1,x}^* - \gamma\delta_\parallel(\omega_4)\rho_\parallel(\Omega_{4,2})A_{2,x}^2A_{1,x}^*}{\delta_\parallel(\omega_4)\varphi_\parallel(\omega_4) - (\gamma\eta_\parallel(\omega_4))^2 P_{1,x}P_{2,x}} \quad (4.64b)$$

where

$$\delta_\parallel(\omega_\nu) = \Delta\beta_{x1} + \gamma\xi_\parallel(\Omega_{\nu,u})P_{1,x} + \gamma P_{2,x}(\xi_\parallel(\Omega_{\nu,v}) - 3), \quad (4.65a)$$
$$\varphi_\parallel(\omega_\nu) = \Delta\beta_{x2} + \gamma\xi_\parallel(\Omega_{\nu,u})P_{2,x} + \gamma P_{1,x}(\xi_\parallel(\Omega_{\nu,v}) - 3). \quad (4.65b)$$

From (4.62) to (4.65) we can see that the efficiency of the three FWM processes are governed by three phase-matching conditions [16, 37]

$$\Delta\beta_{x1} = k_x(\omega_3) + k_x(\omega_2) - 2k_x(\omega_1)$$
$$= (\omega_1 - \omega_0)(\omega_1 - \omega_2)^2\beta_{3,x} + \frac{1}{2}(\omega_1 - \omega_2)^2\big[(\omega_1 - \omega_0)^2 + \frac{1}{6}(\omega_1 - \omega_2)^2\big]\beta_{4,x}, \quad (4.66a)$$

$$\Delta\beta_{x2} = k_x(\omega_4) + k_x(\omega_1) - 2k_x(\omega_2)$$
$$= (\omega_2 - \omega_0)(\omega_2 - \omega_1)^2\beta_{3,x} + \frac{1}{2}(\omega_2 - \omega_1)^2\big[(\omega_2 - \omega_0)^2 + \frac{1}{6}(\omega_2 - \omega_1)^2\big]\beta_{4,x}, \quad (4.66b)$$

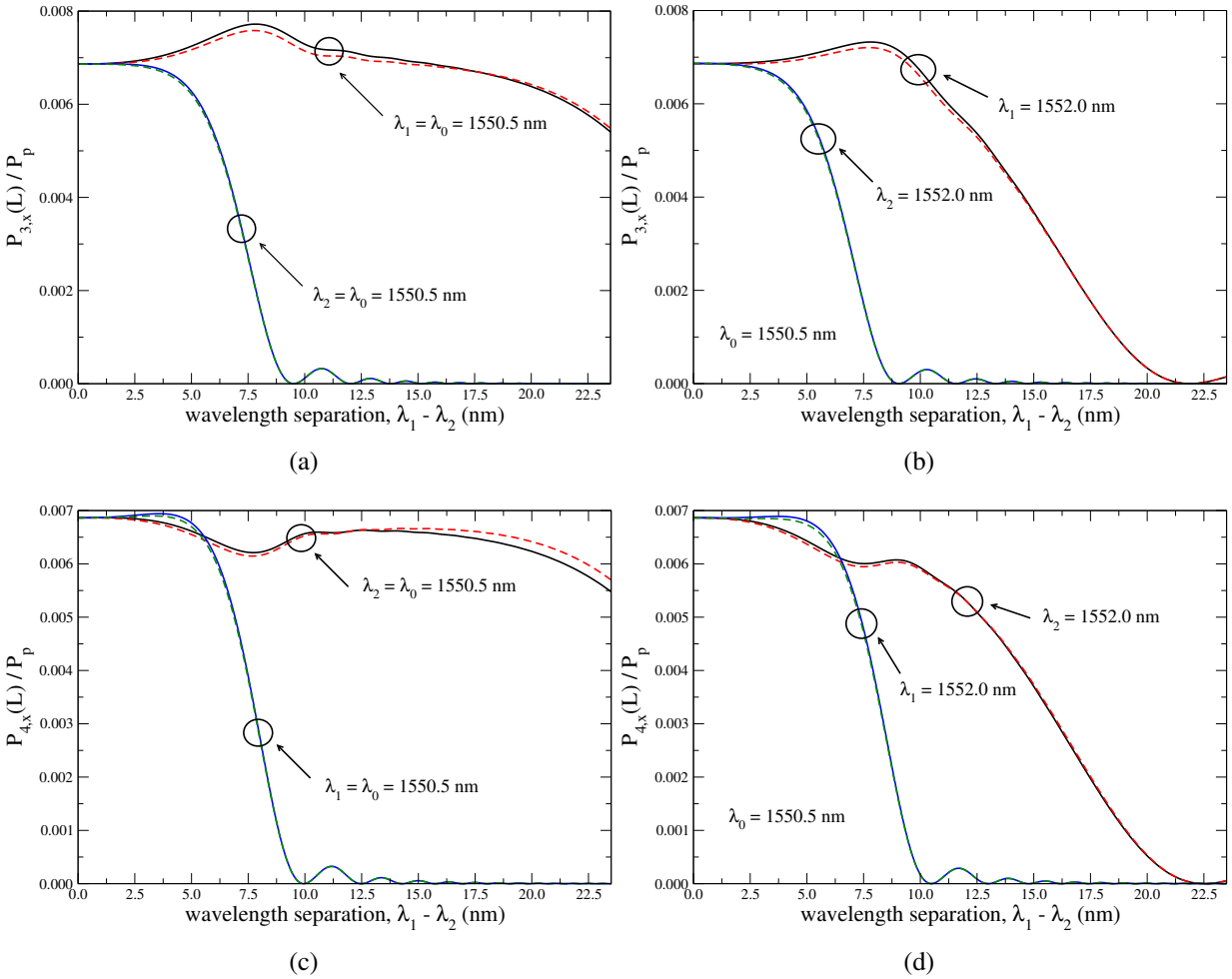

Figure 4.11: Optical power evolution for both idler waves, $P_{3,x}(L)$ and $P_{4,x}(L)$ given by (4.62), with the wavelength separation $\lambda_1 - \lambda_2$. The dashed lines represent the case $f_R = 0$, whereas the solid lines represent $f_R = 0.245$. Plots (a) and (b) describe the idler wave at ω_3, whereas plots (c) and (b) show the optical power of the field at ω_4.

$$\Delta\beta_{x3} = \Delta\beta_{x1} + \Delta\beta_{x2}\,. \tag{4.66c}$$

In Fig. 4.11, we plot the optical power evolution of both idler waves, given by (4.62), as a function of wavelength separation between the two pump fields, $\lambda_1 - \lambda_2$. In Fig. 4.11(a) and 4.11(b), we plot the evolution of the idler field at frequency ω_3, whereas in Fig. 4.11(c) and 4.11(d), we present the evolution of the idler at frequency ω_4, see the scheme of Fig. 4.10(a). In Fig. 4.11, we can see that the influence of the delayed Raman response on the idler waves is negligible in these cases. This shows that the process can mainly be described by the FWM

phase-matching conditions, given by (4.66a), (4.66b) and (4.66c). In the situations considered in Fig. 4.11, at least one of the phase-matching conditions is not null. According with [14], if the nonlinear process remains unmatched, the limit $f_R = 0$ is a good approximation to describe it, which is the case. In Fig. 4.11(a) and 4.11(c), we plot the evolution of the optical power $P_{3,x}(L)$ and $P_{4,x}(L)$, respectively, for two cases: $\lambda_1 = \lambda_0$, and $\lambda_2 = \lambda_0$. For $\lambda_1 = \lambda_0$ we have $\Delta\beta_{x1} \approx 0$, and for $\lambda_2 = \lambda_0$ we have $\Delta\beta_{x2} \approx 0$. In both cases, there exist two FWM processes that remains unmatched. We observe from Fig. 4.11(a) and 4.11(c) that the phase-matching condition $\Delta\beta_{x1} \approx 0$ (with $\Delta\beta_{x2} \neq 0$) leads to a high efficient generation of the ω_3 idler wave, and to a less efficient generation of the ω_4 idler wave. The opposite happens when $\Delta\beta_{x2} \approx 0$ (with $\Delta\beta_{x1} \neq 0$). This is due to the major or minor separation between the idler wave and the pump in the fiber zero-dispersion. It can be seen in Fig. 4.11(a) that, for $\lambda_1 = \lambda_0$ the optical power of the idler wave ω_3 increases with the wavelength separation until $\lambda_1 - \lambda_2 \approx 7.5$ nm. However, in Fig. 4.11(c) we can observe that for $\lambda_2 = \lambda_0$ the optical power of idler wave decreases with the wavelength separation between the pumps, and reaches a local minimum when $\lambda_1 - \lambda_2 \approx 7.5$ nm. This arises from the $\Theta_{v,x}$ contribution present in (4.62), that gives rise to the multiple FWM process. This happens because the phase-matching conditions for the idler wave in Fig. 4.11(a) remains approximately zero for the wavelength range considered, which leads to a high value of $\Theta_{3,x}$. The optical power increase due to the fact that the generation of the idler wave in the anomalous-dispersion regime is more efficient than in the normal-dispersion regime. In Fig. 4.11(c), the phase-matching conditions are also satisfied. However, we are in the normal-dispersion regime, and in that case the generation of the idler is inefficient, when compared with the anomalous-regime. These results show that the optical power of the idler wave can increase with the wavelength separation, because in the multiple FWM process, Fig. 4.11(a), we are not only transferring energy from the pump $P_{1,x}$ for $P_{3,x}$ but also from the pump $P_{2,x}$, and the two pumps also transfer energy between then (4.58). This mean that until $\Delta\beta_{x2}$ and $\Delta\beta_{x3}$ starts to deviates significantly from zero, the multiple FWM process continuous to amplify the idler wave, Fig. 4.11(a). The results presented in Fig. 4.11(a) for $\lambda_2 = \lambda_0$, and in Fig. 4.11(c) for $\lambda_1 = \lambda_0$, also show that, the optical power of the idler wave rapidly decreases with the increasing of $\lambda_1 - \lambda_2$. This is due to the fact that the phase-matching conditions starts to deviates from zero. In Fig. 4.11(b) and 4.11(d), we plot the evolution of the optical power $P_{3,x}(L)$ and $P_{4,x}(L)$, respectively, for two cases: $\lambda_1 = 1552$ nm and $\lambda_2 = 1552$ nm. We can see from Fig. 4.11(b) and 4.11(d) that the case $\lambda_1 = 1552$ nm leads to a high efficient generation of the idler wave ω_3, and a less efficiency in the generation of ω_4. The opposite happens for $\lambda_2 = 1552$ nm. It can also be seen in Fig. 4.11(b) that for $\lambda_2 = 1552$ nm the optical power of the idler wave decreases more rapidly with the evolution $\lambda_1 - \lambda_2$, than for

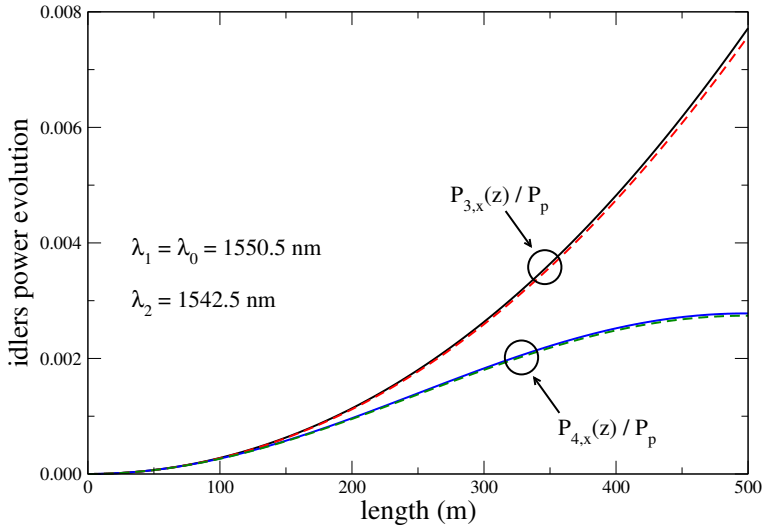

Figure 4.12: Optical power evolution for both idler waves along the fiber length. The dashed lines represent the case $f_R = 0$, whereas solid lines represent $f_R = 0.245$.

$\lambda_1 = 1552$ nm. The opposite result occurs when we analyze the idler wave ω_4, see Fig. 4.11(d). This happens because the difference $\lambda_1 - \lambda_0$ is smaller for $\lambda_1 = 1552$ nm than for $\lambda_2 = 1552$ nm, in Fig. 4.11(b), and the opposite happens in Fig. 4.11(d).

In Fig. 4.12, we plot the optical power evolution of both idler waves, given by (4.62), along the fiber length, for the case $\lambda_1 = \lambda_0$ and $\lambda_2 = 1542.5$ nm. It can be seen in Fig. 4.12 that the optical power of the idler wave at frequency ω_3, $P_{3,x}(z)$, grows monotonically along the length of the fiber, which is in line with numerical results presented in [41]. This is because the dominant process for the generation of the idler wave ω_3 is given by the FWM phase-matching condition $\Delta\beta_{x1} \approx 0$. From Fig. 4.12, we can also see that the optical power of idler wave at ω_4, $P_{4,x}(z)$, does not grows monotonically along the fiber length. This is due to the fact that the FWM process, given by the FWM phase-matching condition $\Delta\beta_{x2}$ remains unmatched. An analogous result can be achieved if we analyze the generation of the idler waves for $\lambda_2 = \lambda_0$ and $\lambda_1 = 1558.5$ nm.

In Fig. 4.13, we represent a comparison between this set of multiple FWM processes, given by (4.62), and the single and dual pump FWM configurations. The evolution of the idler wave in the single pump FWM configuration is given by (4.19). In the case of the dual pump FWM configuration the evolution of the idler wave is given by (4.34). In Fig. 4.13(a) we represent the evolution of the idler wave at ω_3 with $\lambda_1 - \lambda_2$, and in Fig. 4.13(b) we present the evolution along the fiber length. In Fig. 4.13(a) and 4.13(b), in the single pump configuration ω_3 is the idler, ω_1 is the pump, and ω_2 is the signal wave. In the dual pump configuration ω_3 is the idler, ω_1

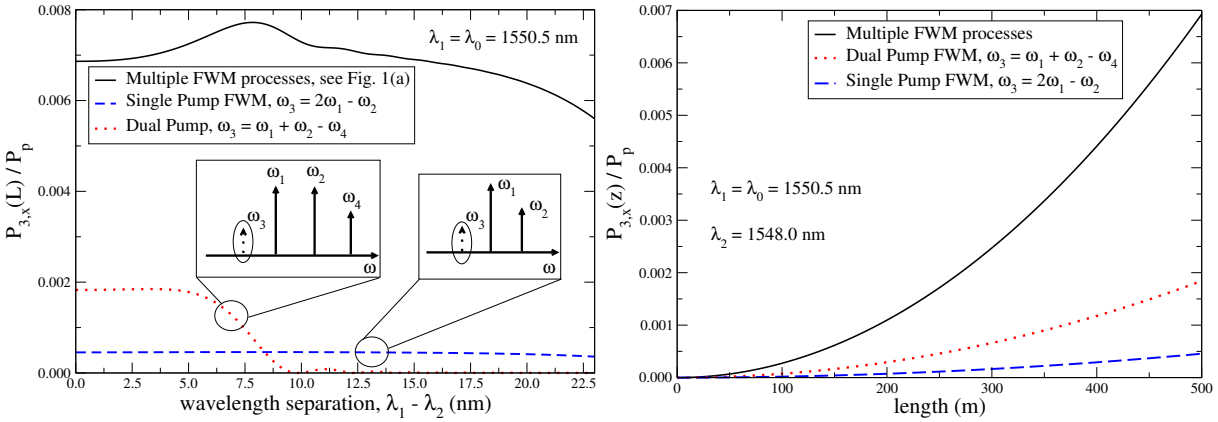

Figure 4.13: Comparison between this set of multiple FWM processes, given by (4.62), and the typically single and dual pump FWM, with $f_R = 0.245$. Plot (a) represents the evolution of the idler wave at ω_3 with $\lambda_1 - \lambda_2$, whereas plot (b) shows the evolution along the length of the fiber.

and ω_2 are the two pumps and $\omega_4 = 2\omega_2 - \omega_1$ is the signal wave. In both configurations, single and dual pump, the input signal power is 1 mW, and the input power per pump is 15 mW. In Fig. 4.13(a), we have used $\lambda_1 = \lambda_0$. In Fig. 4.13(b), we have used $\lambda_1 = \lambda_0$ and $\lambda_2 = 1548$ nm. In both figures the phase-matching condition for the single pump FWM configuration is almost null. In Fig. 4.13(a) and 4.13(b) the multiple FWM process is given by (4.62), and as aforementioned we assume that only the two pumps are launched into the fiber. Results present in Fig. 4.13 show that the idler wave grows more rapidly in this set of multiple FWM processes than in the single or dual pump FWM configurations. In the single and dual pump configurations the optical power grows of the idler wave is proportional to the square of the pump powers, while in the multiple FWM process the growth of the idler wave ω_3 involves the cube of the pump powers. This is due to the contribution given by the non-degenerated FWM process for the generation of the idler wave ω_3 in the multiple FWM configuration. Initially (for $z \approx 0$), the generation of the idler wave ω_3 in the multiple FWM configuration arises from the degenerated FWM process given by $2\omega_1 = \omega_2 + \omega_3$, subsequently the presence of this idler wave will stimulate a non-degenerate FWM process given by $\omega_1 + \omega_2 = \omega_3 + \omega_4$. This can be seen in (4.19) and (4.34). When $z \approx 0$ $P_{3,x}$ in (4.34) is null due to the fact that initially $P_{4,x}$ is null. However, $P_{3,x}$ in (4.19) is different from zero and the idler wave $P_{3,x}$ starts to grows from the degenerated FWM process $\omega_3 = 2\omega_1 - \omega_2$. At the same time the idler wave $P_{4,x}$ also starts to be generated inside the fiber due to the other degenerated FWM process, given by $\omega_4 = 2\omega_2 - \omega_1$. This can also be seen in (4.19), changing the subscript 3 by 4 and exchanging 1 by 2. When the idler

waves are generated these degenerated FWM processes gives rise to the non-degenerated FWM process described by (4.34), which is more efficient than the degenerated FWM process [60]. The combination of all these FWM processes, degenerated and non-degenerated, gives rise to the multiple FWM process, in which the generation of the idler waves is proportional to the cube of the pump power, instead of the square as is the case in (4.19) and (4.34).

4.2.3 Idlers Evolution in the Orthogonal Polarization Scheme

In the orthogonal polarization scheme and following (4.1) and (4.51) we find that the evolution of the idler waves in the fiber satisfy the NSE

$$\frac{\partial A'_{\nu,j}(z)}{\partial z} = i\left[k_j(\omega_\nu)+\gamma\xi_m(\Omega_{\nu,1})P_{1,x}\right]A'_{\nu,j}(z)+i\gamma\xi_n(\Omega_{\nu,2})P_{2,y}A'_{\nu,j}(z) + i\gamma\rho_\perp(\Omega_{\nu,u})A^2_{u,l}(z)A^*_{v,j}(z)+i\gamma\eta_\perp(\omega_\nu)A_{1,x}(z)A_{2,y}(z)A'^*_{\sigma,l}(z)\,, \quad (4.67)$$

where $j\neq l=x,y$, $\nu\neq\sigma=3,4$ represent the two idlers, according with the notation used in Fig. 4.10, $u\neq v=1,2$, with $u=1$ for $\nu=3$ and $u=2$ for $\nu=4$. For $j=x$ we have $\xi_m=\xi_\parallel$ and $\xi_n=\xi_\perp$, whereas for $j=y$ we have $\xi_m=\xi_\perp$ and $\xi_n=\xi_\parallel$. In (4.67)

$$\rho_\perp(\Omega_{\nu,u}) = \frac{1-f_R}{3}+\frac{f_R}{2}\tilde{R}_b(\Omega_{\nu,u})\,, \quad (4.68)$$

$$\eta_\perp(\omega_\nu) = 2\frac{1-f_R}{3}+f_R\tilde{R}_a(\Omega_{\nu,v})+\frac{f_R}{2}\tilde{R}_b(\Omega_{\nu,u})\,. \quad (4.69)$$

After some mathematical manipulation the evolution of both idlers inside the fiber in this polarization scheme is given by

$$P_{\nu,j}(z)=|A'_{\nu,j}(z)|^2=\left|\left\{e^{i\mathbb{K}_j(\omega_\nu)z}\left[i\frac{\gamma\rho_\perp(\Omega_{\nu,u})}{g_y(\omega_\nu)}A^2_{u,l}A^*_{v,j}\sinh(g_y(\omega_\nu)z) + \Theta_{\nu,y}\left(i\frac{\mathbb{K}_y(\omega_\nu)}{g_y(\omega_\nu)}\sinh(g_y(\omega_\nu)z)-\cosh(g_y(\omega_\nu)z)\right)\right]+\Theta_{\nu,y}\right\}\Phi_{\nu,j}(z)\right|^2, \quad (4.70)$$

where

$$\Phi_{\nu,j}(z)=\exp\left\{i\Big[2k_l(\omega_u)-k_j(\omega_v)+\gamma P_{u,l}(2-\xi_\perp(0))-\gamma P_{v,j}(1-2\xi_\perp(0))\Big]z\right\}, \quad (4.71a)$$

$$\mathbb{K}_y(\omega_3)=\Big[\Delta\beta_{y1}-\Delta\beta_{y2}+\gamma(P_{1,x}-P_{2,y})(\xi_\perp(\Omega_{3,1})-\xi_\parallel(\Omega_{3,2})+3\xi_\perp(0)-3)\Big]/2\,, \quad (4.71b)$$

$$\mathbb{K}_y(\omega_4)=\Big[\Delta\beta_{y2}-\Delta\beta_{y1}+\gamma(P_{2,y}-P_{1,x})(\xi_\perp(\Omega_{4,2})-\xi_\parallel(\Omega_{4,1})+3\xi_\perp(0)-3)\Big]/2\,, \quad (4.71c)$$

$$g_y^2(\omega_\nu)=(\gamma\eta_\perp(\omega_\nu))^2P_{1,x}P_{2,y}-\frac{1}{4}\big[\Delta\beta_{y3}+\gamma(P_{1,x}+P_{2,y})(\xi_\parallel(\Omega_{\nu,v})+\xi_\perp(\Omega_{\nu,u})-\xi_\perp(0)-1)\big]^2, \quad (4.71d)$$

and

$$\Theta_{3,y} = \frac{\gamma^2 \eta_\perp(\omega_3)\rho_\perp(\Omega_{3,1})P_{2,y}A_{1,x}^2A_{2,y}^* - \gamma\varphi_\perp(\omega_3)\rho_\perp(\Omega_{3,1})A_{1,x}^2A_{2,y}^*}{\delta_\perp(\omega_3)\varphi_\perp(\omega_3) - (\gamma\eta_\perp(\omega_3))^2P_{1,x}P_{2,y}}, \tag{4.72a}$$

$$\Theta_{4,y} = \frac{\gamma^2 \eta_\perp(\omega_4)\rho_\perp(\Omega_{4,2})P_{1,x}A_{2,y}^2A_{1,x}^* - \gamma\delta_\perp(\omega_4)\rho_\perp(\Omega_{4,2})A_{2,y}^2A_{1,x}^*}{\delta_\perp(\omega_4)\varphi_\perp(\omega_4) - (\gamma\eta_\perp(\omega_4))^2P_{1,x}P_{2,y}}, \tag{4.72b}$$

where

$$\delta_\perp(\omega_\nu) = \Delta\beta_{y1} + \gamma(\xi_\perp(\Omega_{\nu,u}) + \xi_\perp(0) - 2)P_{1,x} + \gamma P_{2,y}(\xi_\parallel(\Omega_{\nu,v}) + 1 - 2\xi_\perp(0)), \tag{4.73a}$$

$$\varphi_\perp(\omega_\nu) = \Delta\beta_{y2} + \gamma(\xi_\perp(\Omega_{\nu,u}) + \xi_\perp(0) - 2)P_{2,y} + \gamma P_{1,x}(\xi_\parallel(\Omega_{\nu,v}) + 1 - 2\xi_\perp(0)), \tag{4.73b}$$

with

$$\Delta\beta_{y1} = k_y(\omega_3) + k_y(\omega_2) - 2k_x(\omega_1) = 2\frac{\omega_1}{c}\delta n + \Delta\beta_{x1}, \tag{4.74a}$$

$$\Delta\beta_{y2} = k_x(\omega_4) + k_x(\omega_1) - 2k_y(\omega_2) = -2\frac{\omega_2}{c}\delta n + \Delta\beta_{x2}, \tag{4.74b}$$

$$\Delta\beta_{y3} = \Delta\beta_{y1} + \Delta\beta_{y2}, \tag{4.74c}$$

where c is the speed of light in vacuum, and $\Delta\beta_{x1}$ and $\Delta\beta_{x2}$ are given by (4.66). It was assumed that $A_{\nu,j}(z=0) = 0$, i.e. there are no idler fields at the fiber input.

In Fig. 4.14 we plot the optical power evolution of both idler waves given by (4.70) as a function of wavelength separation between the two pump fields, $\lambda_1 - \lambda_2$, in the orthogonal polarization scheme, see Fig. 4.10(b). In Fig. 4.14 we can see that the SRS process decreases the optical power of the both idler waves, when compared with the limit $f_R = 0$. This arises from the contribution of the imaginary part of $\tilde{R}_a(\Omega_{\nu,v})$ and $\tilde{R}_b(\Omega_{\nu,v})$ in the $\Theta_{\nu,y}$ function, present in (4.70). In Fig. 4.14(a) and 4.14(b), we plot the optical power $P_{3,y}(L)$, given by (4.70), as a function of $\lambda_1 - \lambda_2$. In Fig. 4.14(a) we have used $\lambda_1 = \lambda_0$, whereas in Fig. 4.14(b) we have used $\lambda_1 = 1552$ nm. Results show that the optical power of the idler wave plotted in Fig. 4.14(a) is higher than the presented in Fig. 4.14(b). This is due to the fact that the values of $\Delta\beta_{y1}$ and $\Delta\beta_{y2}$ are smaller for $\lambda_1 = \lambda_0$, Fig. 4.14(a), than for $\lambda_1 = 1552$ nm, Fig. 4.14(b). In Fig. 4.14(c) and in Fig. 4.14(d), we present the optical power evolution of the idler wave ω_4, given by (4.70), as a function of $\lambda_1 - \lambda_2$. In Fig. 4.14(c) we have used $\lambda_2 = \lambda_0$, whereas in Fig. 4.14(d) we have used $\lambda_2 = 1552$ nm. Results show that the generation of the idler wave ω_4 is less efficient when neither of the pumps coincide with the fiber zero-dispersion wavelength, Fig. 4.14(d). This fact emerges from the phase-matching conditions presented in (4.74), that are closer to zero when $\lambda_2 = \lambda_0$. It can also be seen in Fig. 4.14 that, this polarization scheme, Fig. 4.10(b), leads to

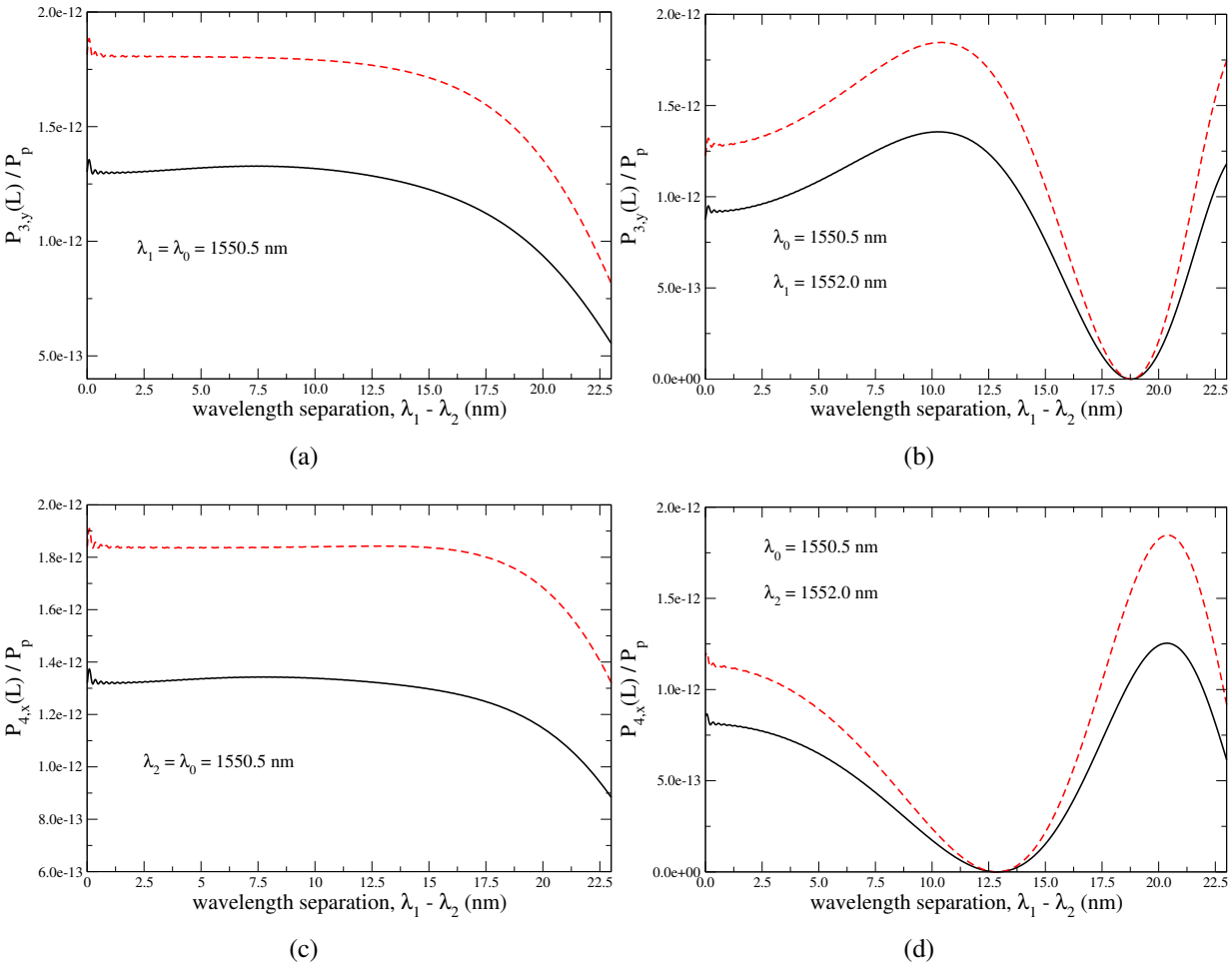

Figure 4.14: Optical power evolution for both idler waves, $P_{3,y}(L)$ and $P_{4,x}(L)$, in the orthogonal polarization scheme given by (4.70) with $\lambda_1 - \lambda_2$. The dashed line represents the case $f_R = 0$, whereas the solid line represents $f_R = 0.245$. Plots (a) and (b) describe the idler wave at ω_3, whereas plots (c) and (b) show the optical power of the field at ω_4.

an inefficient generation of the idler waves at frequencies ω_3 and ω_4, when compared with the co-polarized scheme, Fig.4.10(a). This is due to the high value of δn. Decreasing the value of δn, the optical power of the idler waves rapidly increases.

In Fig. 4.15, we plot the optical power evolution of the idler waves, given by (4.70), along 250 m of fiber, in the orthogonal polarization scheme. Fig. 4.15(a) shows the optical power for the idler wave ω_3, whereas in Fig. 4.15(b) we present the evolution of $P_{4,x}(z)$. In both figures we have used $\lambda_1 = \lambda_0$ and $\lambda_2 = 1542.5$ nm. Results show that the optical power evolution of both idlers waves, $P_{3,y}(z)$ and $P_{4,x}(z)$ is periodic with length. This behavior of the first-order sidebands evolution, ω_3 and ω_4, is related with the periodically energy exchange with the pumps. From

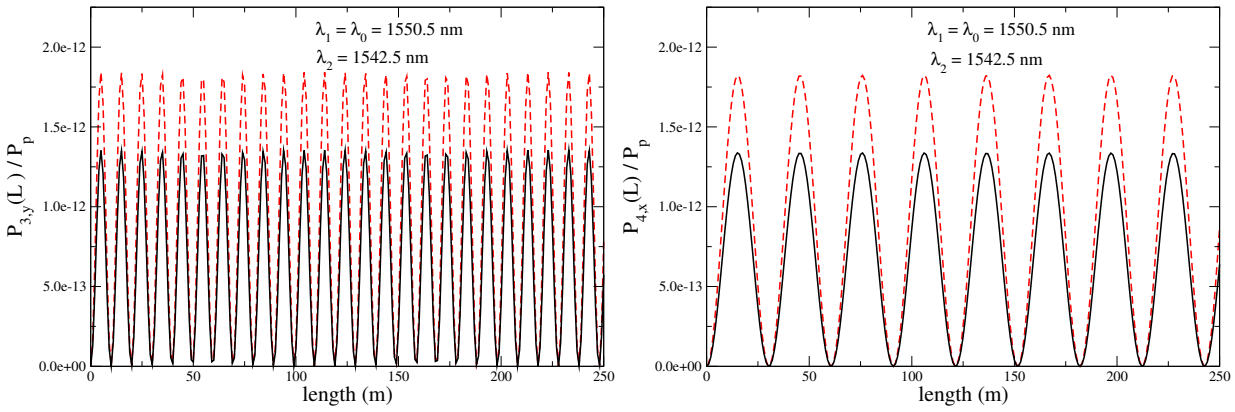

Figure 4.15: Optical power evolution for both idler waves along the fiber length. The dashed line represents the case $f_R = 0$, whereas the solid line represents $f_R = 0.245$. Plot (a) shows the idler field at ω_3, whereas plot (b) represent the optical field at frequency ω_4.

Fig. 4.15(a) and 4.15(b) we can see that the SRS decreases the efficiency of generation of both idler waves, when compared with the limit $f_R = 0$.

4.2.4 Polarization Sensitivity of the Idler Waves

In this section we analyze the generation of the idler waves as a function of the polarization angle between the two pumps. The pump at ω_1 is aligned with x-axis of the fiber. The pump at ω_2 makes an angle ϕ with the x-axis of the fiber [61]. The change of the angle ϕ from 0° to 90° means that we are evolving from the co-polarized to the orthogonal polarization scheme, see Fig. 4.10. In this scheme the optical power of both idlers at a given z inside the fiber can be written as [61, 62]

$$P_3(z) = |A_{3,x}(z)|^2 + |A'_{3,y}(z)|^2, \tag{4.75}$$

where $|A_{3,x}(z)|^2$ is given by (4.62) with $P_{2,x} = P_2\cos^2(\phi)$, and $|A'_{3,y}(z)|^2$ is given by (4.70) with $P_{2,y} = P_2\sin^2(\phi)$, and

$$P_4(z) = |A_{4,x}(z)|^2 + |A'_{4,x}(z)|^2, \tag{4.76}$$

where $|A_{4,x}(z)|^2$ is given by (4.62) with $P_{2,x} = P_2\cos^2(\phi)$, and $|A'_{4,x}(z)|^2$ is obtained from (4.70) with $P_{2,y} = P_2\sin^2(\phi)$.

To describe the polarization sensitivity of the generation of the idler waves, we present in Fig. 4.16 the variation of the optical power of both idler waves with the angle ϕ. Fig. 4.16 shows the optical power of both idler waves given by (4.75) and (4.76), for the case $\lambda_1 = \lambda_0$ and

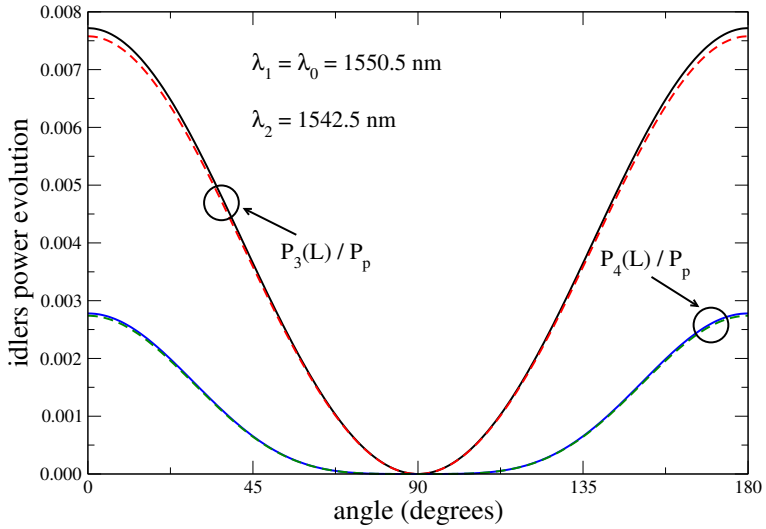

Figure 4.16: Optical power of both idler fields, given by (4.75) and (4.76) respectively, as a function of the polarization angle of the pump wave, ω_2. The dashed lines represent the case $f_R = 0$, whereas the solid lines represent $f_R = 0.245$.

$\lambda_2 = 1542.5$ nm. From Fig. 4.16 we can see that the optical power of $P_3(L)$ and $P_4(L)$ decreases rapidly with the evolution of the angle ϕ. This decreases is more evident for $P_4(L)$ due to the fact that the higher contribution for the generation of the idler wave at ω_4 arises from the photons that are annihilated from the pump P_2. From Fig. 4.16 we can see that exist a large angle range around $\phi = 90^\circ$ where $P_4(L)$ is almost null. This arises from the small contribution given by the orthogonal polarization scheme to the optical power of the idler wave at ω_4. It can also be seen in Fig. 4.16 that the SRS process does not change significantly the evolution of the idler waves with the angle ϕ.

4.3 Summary

We investigate the combined processes of SRS and FWM in optical fibers in the single and dual pump configurations, under several polarization schemes. Using the coupled-equations, we derive the equations that govern the evolution of the signal and idler waves, for the case in which the pump power is much higher than the signal power. In the dual pump configuration the pump powers are maintained in a low power regime. We show that an accurate description of the FWM process is obtained by including the SRS in the theory of the FWM process. We verify that in the single and dual pump configuration the signal wave is mostly described by the imaginary part of the fiber nonlinear response function. We also show that the generation of the idler wave in

the co-polarized scheme is dependent of the real part of the fiber nonlinear response function. That dependence is more visible when the phase-matching condition is achieved. For frequency detunings less than 3 THz the approximation $f_R = 0$ is quite good. The orthogonal scheme leads to an inefficient generation of the idler wave due to the high value of the group birefringence. However, in the dual pump configuration when the signal is launched into the fiber parallel to the right pump the generation of the idler wave is very efficient for small frequency detunings, less than 0.01 THz. When compared with the single pump configuration, the dual pump is a more efficient process in the amplification of the signal wave and generation of the idler field.

We also investigate the generation of two idler waves inside a HiBi optical fiber, considering three FWM processes and the SRS. Using the coupled-equations we solve analytically the equations that govern the evolution of the complex amplitudes for two pumps inside the fiber, considering that the pumps interact between them through the FWM and SRS process. We also derive and solve the equations that governs the generation of two idler waves inside a optical birefringent fiber in two polarization schemes. We show that in the co-polarized scheme the SRS does not change dramatically the optical power evolution of the two idler waves with the wavelength separation between the pumps, even when the pump wavelength coincide with λ_0. We verify that, although one phase-matching condition is almost achieved, two other remains unmatched. We show that the contribution of several FWM processes to the generation of idler wave can increase the efficiency of the process, for certain wavelengths detunings. We also show theoretically that the optical power of the idler waves grows monotonically along the fiber length, when the pumps coincide with λ_0. This fact is due to the three FWM contributions to the optical power of the idler wave. The orthogonal polarization scheme leads to an inefficient generation of the idler waves, due to the high value of δn. We verify that the SRS decreases the optical power of the idler waves when compared with limit $f_R = 0$. We show that the evolution from the co-polarized to the orthogonal polarization scheme leads to a continuous loss of efficiency on the generation of the idlers waves. Results also show that the generation of first-order sidebands from three FWM processes is physically quite different from the typically single and dual pump FWM configurations.

References

[1] R. H. Stolen and J. E. Bjorkholm, "Parametric amplification and frequency conversion in optical fibers," *IEEE Journal of Quantum Electronics*, vol. 18, pp. 1062–1072, 1982.

[2] J. Hanstyd, P. A. Andrekson, M. Westlund, J. Li, and P. Hedekvist, "Fiber-based optical parametric

amplifiers and their applications," *IEEE Journal of Selected Topics in Quantum Electronics*, vol. 8, pp. 506–520, 2002.

[3] K. Inoue and H. Toba, "Wavelength conversion experiment using fiber four-wave mixing," *IEEE Photonics Technology Letters*, vol. 4, pp. 69–72, 1992.

[4] P. Antunes, P. S. André, and A. N. Pinto, "Single-photon source by means of four-wave mixing inside a dispersion-shifted optical fiber," in *FIO'06 - Frontiers in Optics*, USA, October 2006.

[5] H. Takesue and K. Inoue, "Generation of polarization-entangled photon pairs and violation of Bell's inequality using spontaneous four-wave mixing in a fiber loop," *Physical Review A*, vol. 70, p. 031802, 2004.

[6] M. C. Fugihara and A. N. Pinto, "Low-cost Raman amplifier for CWDM systems," *Microwave and Optical Technology Letters*, vol. 50, pp. 297–301, 2008.

[7] S. Cui, J. Liu, and X. Ma, "A novel efficient optimal design method for gain-flattened multiwavelength pumped fiber Raman amplifier," *IEEE Photonics Technology Letters*, vol. 16, pp. 2451–2453, 2004.

[8] P.-G. Yan, S.-C. Ruan, C.-Y. Guo, Y.-Q. Yu, and L. Li, "Efficient, tunable photonic crystal fiber Raman laser," *Microwave and Optical Technology Letters*, vol. 49, pp. 395–397, 2007.

[9] D. I. Chang, D. S. Lim, M. Y. Jeon, H. K. Lee, K. H. Kim, and T. Park, "Dual-wavelength cascaded Raman fibre laser," *Electronics Letters*, vol. 36, pp. 1356–1358, 2000.

[10] F. Vanholsbeeck, P. Emplit, and S. Coen, "Complete experimental characterization of the influence of parametric four-wave mixing on stimulated Raman gain," *Optics Letters*, vol. 28, pp. 1960–1962, 2003.

[11] S. Trillo and S. Wabnitz, "Parametric and Raman amplification in birefringent fibers," *J. Opt. Soc. Am. B*, vol. 9, pp. 1061–1082, 1992.

[12] A. S. Y. Hsieh, G. K. L. Wong, S. G. Murdoch, S. Coen, F. Vanholsbeeck, R. Leonhardt, and J. D. Harvey, "Combined effect of Raman and parametric gain on single-pump parametric amplifiers," *Optics Express*, vol. 15, pp. 8104–8114, 2007.

[13] A. S. Y. Hsieh, S. G. Murdoch, S. Coen, R. Leonhardt, and J. D. Harvey, "Influence of Raman susceptibility on optical parametric amplification in optical fibers," *Optics Letters*, vol. 32, pp. 521–523, 2007.

[14] N. A. Silva, N. J. Muga, and A. N. Pinto, "Influence of the stimulated Raman scattering on the four-wave mixing process in birefringent fibers," *IEEE/OSA Journal of Lightwave Technology*, vol. 27, pp. 4979–4988, 2009.

[15] N. A. Silva, N. J. Muga, and A. N. Pinto, "Evolution of first-order sidebands from multiple FWM processes in HiBi optical fibers," *Optics Communications*, vol. 284, pp. 3408 – 3415, 2011.

[16] G. P. Agrawal, *Nonlinear Fiber Optics*, 3rd ed. San Diego, California, USA: Academic Press, 2001.

[17] N. Bloembergen and Y. R. Shen, "Coupling between vibrations and light waves in Raman laser media," *Physical Review Letters*, vol. 12, pp. 504–507, 1964.

[18] K. Washio, K. Inoue, and S. Kishida, "Efficient large-frequency-shifted three-wave mixing in low dispersion wavelength region in single-mode optical fiber," *Electronic Letters*, vol. 16, pp. 658–660, 1980.

[19] C. Lin, W. A. Reed, A. D. Pearson, and H. T. Shang, "Phase matching in the minimum-chromatic-dispersion region of single-mode fibers for stimulated four-photon mixing," *Optics Letters*, vol. 6, pp. 493–495, 1981.

[20] K. P. Hansen, J. R. Jensen, C. Jacobsen, H. R. Simonsen, J. Broeng, P. M. W. Skovgaard, and A. Petersson, "Highly nonlinear photonic crystal fiber with zero-dispersion at 1.55μm," in *Conference on Optical Fiber Communication OFC*, Anaheim, California, 2002.

[21] J. Hansryd and P. A. Andrekson, "Broad-band continuous-wave-pumped fiber optical parametric amplifier with 49-dB gain and wavelength-conversion efficiency," *IEEE Photonics Technology Letters*, vol. 13, pp. 194–196, 2001.

[22] A. Ferrando, M. Zacarés, P. F. de Córdoba, D. Binosi, and J. A. Monsoriu, "Spatial soliton formation in photonic crystal fibers," *Optics Express*, vol. 11, pp. 452–459, 2003.

[23] P. A. Andersen, C. Peucheret, K. M. Hilligsøe, K. S. Berg, K. P. Hansen, and P. Jeppesen, "Supercontinuum generation in a photonic crystal fiber using picosecond pulses at 1550 nm," in *5th International Conference on Transparent Optical Networks: ICTON*, vol. 1, Warsaw, Poland, 2003, pp. 66–69.

[24] A. I. Siahlo, L. K. Oxenløwe, K. S. Berg, A. T. Clausen, P. A. Andersen, C. Peucheret, A. Tersigni, P. Jeppesen, K. P. Hansen, and J. R. Folkenberg, "A high-speed demultiplexer based on a nonlinear optical loop mirror with a photonic crystal fiber," *IEEE Photonics Technology Letters*, vol. 15, pp. 1147–1149, 2003.

[25] M. Bottacini, F. P. A. Cuciotta, and S. Selleri, "Modeling of photonic crystal fiber Raman amplifiers," *IEEE/OSA Journal of of Lightwave Technology*, vol. 22, pp. 1707–1713, 2004.

[26] J. E. Sharping, M. Fiorentino, A. Coker, and P. Kumar, "Four-wave mixing in a microstructure fiber," *Optics Letters*, vol. 26, pp. 1048–1050, 2001.

[27] F. Biancalana, D. V. Skryabin, and P. S. J. Russell, "Four-wave mixing instabilities in photonic-crystal and tapered fibers," *Physical Review E*, vol. 68, p. 046603, 2003.

[28] K. J. Blow and D. Wood, "Theoretical description of transient stimulated Raman scattering in optical fibers," *IEEE Journal of Quantum Electronics*, vol. 25, pp. 2665–2673, 1989.

[29] Y. Chen, "Combined processess of stimulated Raman scattering and four-wave mixing in optical fibers," *J. Opt. Soc. Am. B*, vol. 7, pp. 43–52, 1990.

[30] E. A. Golovchenko and A. N. Pilipetskii, "Undified analysis of four-photon mixing, modulational instability, and stimulated Raman scattering under various polarization conditions in fibers," *J. Opt. Soc. Am. B*, vol. 11, pp. 92–101, 1994.

[31] E. Golovchenko, P. V. Mamyshev, A. N. Pilipetskii, and E. M. Dianov, "Mutual influence of the parametric effects and stimulated scattering in optical fibers," *IEEE Journal of Quantum Electronics*, vol. 26, pp. 1815–1820, 1990.

[32] P. V. Mamyshev and S. V. Chernikov, "Ultrashort-pulse propagation in optical fibers," *Optics Letters*, vol. 15, pp. 1076–1078, 1990.

[33] R. W. Hellwarth, "Third-order optical susceptibilities of liquids and solids," *Prog. Quant. Electron.*, vol. 5, pp. 1–68, 1977.

[34] Q. Lin, F. Yaman, and G. P. Agrawal, "Photon-pair generation in optical fibers through four-wave mixing: Role of Raman scattering and pump polarization," *Physical Review A*, vol. 75, p. 023803, 2007.

[35] Q. Lin and G. P. Agrawal, "Raman response function for silica fibers," *Optics Letters*, vol. 31, pp. 2086–3088, 2006.

[36] C. Headley and G. P. Agrawal, *Raman Amplification in Fiber Optical Communication Systems*. San Diego: Academic Press, 2005.

[37] R. H. Stolen, M. A. Bösch, and C. Lin, "Phase matching in birefringent fibers," *Optics Letters*, vol. 6, pp. 213–215, 1981.

[38] E. Lantz, D. Gindre, H. Maillotte, and J. Monneret, "Phase matching for parametric amplification in a single mode birefringent fiber: influence of non-phase-matched waves," *J. Opt. Soc. Am. B*, vol. 14, pp. 116–125, 1997.

[39] Q. Lin and G. P. Agrawal, "Vector theory of four-wave mixing: polarization effects in fiber-optic parametric amplifiers," *J. Opt. Soc. Am. B*, vol. 21, pp. 1216–1224, 2004.

[40] J. R. Thompson and R. Roy, "Multiple four-wave mixing process in an optical fiber," *Optics Letters*, vol. 16, pp. 557–559, 1991.

[41] J. R. Thompson and R. Roy, "Nonlinear dynamics of multiple four-wave mixing processes in a single-mode fiber," *Physical Review A*, vol. 43, pp. 4987–4996, 1991.

[42] X. M. Liu, "Theory and experiments for multiple four-wave-mixing processes with multifrequency pumps in optical fibers," *Physical Review A*, vol. 77, p. 043818, 2008.

[43] Q. Lin, F. Yaman, and G. P. Agrawal, "Photon-pair generation by four-wave mixing in optical fibers," *Optics Letters*, vol. 31, pp. 1286–1288, 2006.

[44] K. O. Hill, D. C. Johnson, B. S. Kawasaki, and R. I. MacDonald, "cw three-wave mixing in single-mode optical fibers," *Journal of Applied Physics*, vol. 49, pp. 5098–5106, 1978.

[45] N. Shibata, R. Braun, and R. Waarts, "Phase-mismatch dependence of efficiency of wave generation through four-wave mixing in a single-mode optical fiber," *IEEE Journal of Quantum Electronics*, vol. 23, pp. 1205–1210, 1987.

[46] N. A. Silva, N. J. Muga, and A. N. Pinto, "Effective nonlinear parameter measurement using FWM in optical fibers in a low power regime," *IEEE Journal of Quantum Electronics*, vol. 46, pp. 285–291, 2010.

[47] J. R. Thompson and R. Roy, "Statistical fluctuations in multiple four-wave mixing in a single-mode optical fiber," *Phys. Rev. A*, vol. 44, pp. 7605–7614, 1991.

[48] D. L. Hart, A. Judy, T. A. B. Kennedy, R. Roy, and K. Stoev, "Conservation law for multiple four-wave-mixing processes in a nonlinear optical medium," *Phys. Rev. A*, vol. 50, pp. 1807–1813, 1994.

[49] S. Trillo, S. Wabnitz, and T. A. B. Kennedy, "Nonlinear dynamics of dual-frequency-pumped multi-wave mixing in optical fibers," *Phys. Rev. A*, vol. 50, pp. 1732–1747, 1994.

[50] D. L. Hart, A. F. Judy, R. Roy, and J. W. Beletic, "Dynamical evolution of multiple four-wave-mixing processes in an optical fiber," *Phys. Rev. E*, vol. 57, pp. 4757–4774, 1998.

[51] G. Millot, "Multiple four-wave mixing-induced modulational instability in highly birefringent fibers," *Opt. Lett.*, vol. 26, pp. 1391–1393, 2001.

[52] B. Khubchandani, P. N. Guzdar, and R. Roy, "Influence of stochasticity on multiple four-wave-mixing processes in an optical fiber," *Phys. Rev. E*, vol. 66, p. 066609, 2002.

[53] X. Liu, X. Zhou, and C. Lu, "Multiple four-wave mixing self-stability in optical fibers," *Phys. Rev. A*, vol. 72, p. 013811, 2005.

[54] A. Hasegawa, "Generation of a train of soliton pulses by induced modulational instability in optical fibers," *Opt. Lett.*, vol. 9, pp. 288–290, 1984.

[55] P. Andrekson, N. Olsson, J. Simpson, T. Tanbun-Ek, R. Logan, and M. Haner, "16 Gbit/s all-optical demultiplexing using four-wave mixing," *Electronics Letters*, vol. 27, pp. 922–924, 1991.

[56] P. Hedekvist and P. Andrekson, "Demonstration of fibre four-wave mixing optical demultiplexing with 19 db parametric amplification," *Electronics Letters*, vol. 32, pp. 830–831, 1996.

[57] A. Yariv, D. Fekete, and D. M. Pepper, "Compensation for channel dispersion by nonlinear optical phase conjugation," *Opt. Lett.*, vol. 4, pp. 52–54, 1979.

[58] P. Hedekvist, M. Karlsson, and P. Andrekson, "Polarization dependence and efficiency in a fiber four-wave mixing phase conjugator with orthogonal pump waves," *Photonics Technology Letters, IEEE*, vol. 8, pp. 776–778, 1996.

[59] F. Poli, A. Cucinotta, and S. Selleri, *Photonic Crystal Fibers: Properties and Applications*, 1st ed. Springer Netherlands, 2007.

[60] B. P. Pal, *Guided Wave Optical Components and Devices*. San Diego: Academic Press, 2005, ch. Fiber-Optic Parametric Amplifiers for Lightwave Sysytems, pp. 101–118.

[61] C. J. McKinstrie, S. Radic, and C. Xie, "Phase conjugation driven by orthogonal pump waves in birefringent fibers," *J. Opt. Soc. Am. B*, vol. 20, pp. 1437–1446, 2003.

[62] N. J. Muga, N. A. Silva, M. F. Ferreira, and A. N. Pinto, "Evolution of the degree of co-polarization in high-birefringence fibers," *Optics Communications*, vol. 283, pp. 2125 – 2132, 2010.

Chapter 5

Photon Statistics of the Stimulated Four-Wave Mixing Process

THE quantum key distribution (QKD) systems have evolved from point-to-point fiber links to optical fiber networks. In that scenario, the quantum channel used in the QKD setup share the same fiber with other classical optical signals [1]. In that scenario, the inter-channel nonlinear effects that occurs inside the fiber can potentially degrade the performance of the QKD system [2]. In a wavelength-division multiplexing (WDM) lightwave system, the interaction between the classical optical signals will generate noise photons through stimulated four-wave mixing (FWM) and through spontaneous and stimulated Raman scattering [3, 4]. The statistical characterization of the quantum channel is essential to correctly estimate the quantum bit error rate (QBER). Changes in the QBER are used in several QKD protocols to detect the presence of an eavesdropper.

The focus of this Chapter is to understand the impact of noise photons generated by FWM and Raman scattering on the statistics of a coherent quantum channel used for QKD. In this study, we admit that the spectral bandwidth of the noise photons coincide with the wavelength of the quantum channel. We quantify the photon statistics of the quantum channel by means of the second-order coherence function. We present a quantum description of the FWM process in optical fibers considering both stimulated and spontaneous Raman scattering. The photon number distribution of the idler wave generated through stimulated FWM is studied in two distinct cases. First, we assume that the idler photons are fully generated inside the fiber. In a second scenario, we admit that at the fiber input there exists a coherent quantum signal and idler photons will be created at that frequency. This Chapter is based on the references [5–7], and is organized as follows: Section 5.1 provides an introduction to the photon statistics state of the art. In section 5.2, we present a quantum version of the stimulated FWM process. In section 5.3 we discuss the

second-order coherence function for the stimulated FWM process. Section 5.4 reports the theoretical results obtained for the statistics of the idler wave. Section 5.5 describes the experimental setup used to reconstruct the photon statistics of a single-photon source based on the stimulated FWM process. The main conclusions of this Chapter are summarized in section 5.6.

5.1 Photon statistics: An introduction

In a WDM scenario, the quantum channel used in the QKD setup share the same fiber with other classical optical signals [1]. In that scenario, the inter-channel nonlinear effects that occurs inside the fiber can potentially degrade the performance of the QKD system [2]. In [8], the quantum channel and the classical signal shared the same fiber, but they were placed in different bands. However, there are important advantages in placing the QKD channel on the C-band, as fiber losses and most of the installed optical components are optimized for the C-band [9, 10]. Recently in [11], authors demonstrated that quantum channels can successfully coexist with classical optical signals in the same optical band, in a WDM architecture [11]. In a WDM lightwave system, the interaction between the classical optical signals will generate noise photons through stimulated FWM and through spontaneous and stimulated Raman scattering [3, 4]. These physical impairments were investigated in recent works in this coexisting architecture [2, 4, 12]. The statistical characterization of the quantum channel is essential to correctly estimate the QBER. Changes in the QBER are used in several QKD protocols to detect the presence of an eavesdropper [1]. However, the theoretical statistical characterization of the quantum channel in this coexisting architecture remains an open issue, to the best of our knowledge.

The experimental statistical characterization of an optical field can be performed with several different techniques [13–17]. A method based on quantum tomography was used in [13]. That particular method requires phase-matching with a local oscillator and homodyne detection. A different experiment approach to measure the statistics of an optical field was implemented in [14]. In that case, authors have used a photomultiplier tube to reconstruct the statistics of an incoming quantum state. In [15], authors reconstruct the photon statistics by using on/off detectors assisted by the maximum-likelihood estimation algorithm. Recently, the second-order coherence function, $g^{(2)}(0)$, was measured experimentally for a heralded single photon source based on the spontaneous FWM process inside an optical fiber [16–20]. The photon number statistics of the heralded single-photon source based on spontaneous FWM process was also studied in [21] through the Wigner function. Moreover, in [18] authors measured the unconditional second-order correlation function for the spontaneous FWM process inside a microstruture fiber.

In [13], authors report measurements of the photon statistics of a fiber-optic parametric amplifier. In that experimental work, the idler wave is fully generated inside the fiber, and they measure the statistics of the signal field for a high gain fiber-optic parametric amplifier based on the FWM process.

5.2 Stimulated Four-Wave Mixing: A Quantum Approach

In this section, we present a quantum description of the generation of the idler wave through the FWM process inside an optical fiber. In Fig. 5.1, we present a schematic arrangement of a typical FWM experimental setup. We assume that all fields remain co-polarized along the propagation on the fiber, and the fiber attenuation is negligible. In that conditions, the quantum evolution of the idler annihilation operator in the frequency domain inside the optical fiber is given by the input/output relation [22, 23]

$$\hat{A}(L,\omega_i) = \Big(\Lambda_i(L)\hat{A}(0,\omega_Q) + \Gamma_i(L)e^{-2i\theta_p}\hat{A}^{\dagger}(0,\omega_s) + \hat{M}(L,\omega_i)\Big)\Theta(L)\,, \tag{5.1}$$

where θ_p is the phase of the optical pump coherent field, ω_Q is the frequency of the input quantum channel, ω_i is the frequency of the idler photons generated through FWM process and Raman scattering inside the fiber, which we assume coincident with ω_Q. In (5.1), $\Theta(L) = \exp\{i(k_p + \gamma P_p)L\}$, where k_p is the pump propagation constant, P_p is the fiber input pump power, γ is the fiber nonlinear parameter, L is the fiber length. In (5.1)

$$\Lambda_i(L) = \left(\cosh(g_{ip}L) + i\frac{\kappa_{ip}}{2g_{ip}}\sinh(g_{ip}L)\right)e^{i\frac{k_i-k_s}{2}L}\,, \tag{5.2}$$

$$\Gamma_i(L) = i\frac{\gamma\eta_{ip}}{g_{ip}}A_p^2\sinh(g_{ip}L)e^{i\frac{k_i-k_s}{2}L}\,, \tag{5.3}$$

and

$$\hat{M}(L,\omega_i) = i\int_0^L \hat{m}_{ip}(z)\Big(A_p e^{-i\theta_p}\Lambda_i(L-z) - A_p^* e^{i\theta_p}\Gamma_i(L-z)\Big)dz\,, \tag{5.4}$$

where $\hat{m}_{ip}(z)$ is the Hermitian phase noise operator, and A_p is the pump field envelop such that $P_p = |A_p|^2$. In (5.2)-(5.4)

$$g_{ip}^2 = \left((\gamma\eta_{ip}P_p)^2 - (\kappa_{ip}/2)^2\right)\,, \tag{5.5a}$$

$$\kappa_{ip} = \Delta\beta + 2\gamma P_p\eta_{ip}\,, \tag{5.5b}$$

$$\eta_{ip} = 1 - f_R + f_R\left(\tilde{R}_a(\omega_i-\omega_p) + \tilde{R}_b(\omega_i-\omega_p)\right)\,, \tag{5.5c}$$

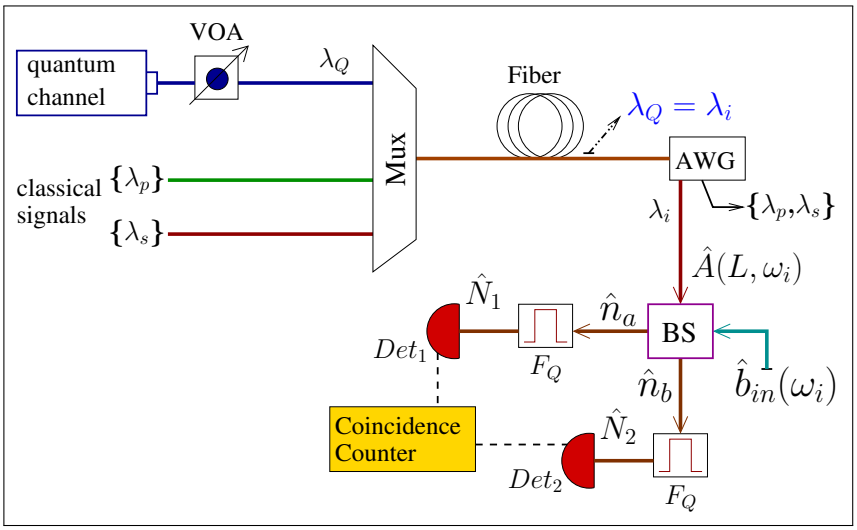

Figure 5.1: Setup for obtain the photon counting statistics of the stimulated FWM process. The dashed lines represents electrical signals and the solid lines the optical path. Details of the setup are presented in the text.

where $\Delta\beta$ is the phase-matching condition given by [24]

$$\Delta\beta \approx \beta_3(\omega_p-\omega_0)(\omega_p-\omega_s)^2+\frac{\beta_4}{2}\left[(\omega_p-\omega_0)^2+\frac{1}{6}(\omega_p-\omega_s)^2\right](\omega_p-\omega_s)^2\,, \tag{5.6}$$

where ω_p and ω_s are the pump and signal frequencies, respectively, ω_0 is fiber zero-dispersion frequency, and β_3 and β_4 are the third and fourth order dispersion coefficients, respectively. In (5.5), $f_R = 0.245$ is the fractional contribution of the Raman process to the nonlinear refractive index, $\tilde{R}_a(\omega_i-\omega_p)$ and $\tilde{R}_b(\omega_i-\omega_p)$ are the isotropic and anisotropic Raman response, respectively, defined in [3, 25–27]. In (5.1), the field operator satisfies the commutation relation [22]

$$\left[\hat{A}(0,\omega_u),\hat{A}^\dagger(0,\omega_u')\right] = 2\pi\delta(\omega_u-\omega_u')\,, \tag{5.7}$$

where $u = s$ or Q, and the noise quantum operator [22, 28]

$$\left[\hat{M}(L,\omega_i),\hat{M}^\dagger(L,\omega_i')\right] = 2\pi\left(|\Lambda_i(L)|^2-|\Gamma_i(L)|^2-1\right)\delta(\omega_i-\omega_i')\,. \tag{5.8}$$

The photon number distribution of the idler wave can be obtained through the setup shown in Fig. 5.1 [16, 29]. In Fig. 5.1, a pump, λ_p, a classical signal λ_s, and a quantum channel λ_Q are coupled by a multiplexer (MUX) and sent to an optical fiber. The quantum channel λ_Q is highly attenuated with a variable optical attenuator (VOA). Note that if the idler wave is fully generated inside the fiber, the quantum channel path present in Fig. 5.1 does not exist. Inside the fiber idler photons are created due to the both stimulated and spontaneous FWM and Raman scattering

processes. Since we assume that the idler photons have wavelength $\lambda_i = \lambda_Q$, noise photons will be added to the quantum channel launched to the fiber. At the fiber output, the three optical fields passes through an arrayed waveguide grating (AWG) to separate the pump and signal fields from the quantum channel λ_Q. The output photons from the AWG are launched into a non-polarizing beam splitter (BS), where they can be combined with other quantum states given by the $\hat{b}_{in}(\omega)$ operator. At the BS output the photons are spectrally filtered (F_Q) and collected by the photon counting modules, Det_1 and Det_2. Single and coincidence measurements are performed in order to obtain $g^{(2)}(0)$ [17].

5.2.1 Expectation values

We are now interested on the evaluation of the expectation values for the photon flux spectral density and the normally ordered second moment, for the idler photons generated through FWM and Raman scattering processes. We take at the input of the fiber the signal field and the quantum channel as a continuous mode coherent state, as well states $|f\rangle$ that accounts the phonon reservoir inside the fiber. The general state can be written as [16, 28, 30]

$$|\Psi\rangle = \exp\left\{\int d\omega_s \left(\vartheta(\omega_s)\hat{A}^\dagger(0,\omega_s) - c.c.\right)\right\}|0_s\rangle \times \exp\left\{\int d\omega_Q \left(\varphi(\omega_Q)\hat{A}^\dagger(0,\omega_Q) - c.c.\right)\right\}|0_Q\rangle\,, \quad (5.9)$$

where $c.c.$ represents the complex conjugate, $|0_u\rangle$ is the vacuum state for the $u = s\,\text{or}\,Q$ mode, $\vartheta(\omega_s)$ and $\varphi(\omega_Q)$ are the fiber incident amplitudes for the fields $\hat{A}(0,\omega_s)$ and $\hat{A}(0,\omega_Q)$, respectively. That amplitudes contain the mean photon flux and the phase of the optical field. The expectation values for the noise operator $\hat{M}(L,\omega_i)$ are given by [28]

$$\langle f|\hat{M}^\dagger(L,\omega_i)|f\rangle = \langle f|\hat{M}(L,\omega_i)|f\rangle = 0\,, \quad (5.10a)$$

$$\langle f|\hat{M}(L,\omega_i)\hat{M}(L,\omega_i')|f\rangle = \langle f|\hat{M}^\dagger(L,\omega_i)\hat{M}^\dagger(L,\omega_i')|f\rangle = 0, \quad (5.10b)$$

and

$$\langle f|\hat{M}^\dagger(L,\omega_i)\hat{M}(L,\omega_i')|f\rangle = 2\pi\left(n_{th}(\omega_i-\omega_p)+1\right)\left(|\Lambda_i(L)|^2 - |\Gamma_i(L)|^2 - 1\right)\delta(\omega_i-\omega_i')\,, \quad (5.11)$$

where $n_{th}(\Omega) = \left[e^{\hbar|\Omega|/k_BT} - 1\right]^{-1}$. The fourth-order noise correlation function of the noise operator used for obtain the normally ordered second moment is expressed in terms of second-order

correlation [28]

$$\langle f|\hat{M}^{\dagger}(L,\omega_i)\hat{M}^{\dagger}(L,\omega_i')\hat{M}(L,\omega_i'')\hat{M}(L,\omega_i''')|f\rangle$$
$$= \langle f|\hat{M}^{\dagger}(L,\omega_i)\hat{M}(L,\omega_i'')|f\rangle\langle f|\hat{M}^{\dagger}(L,\omega_i')\hat{M}(L,\omega_i''')|f\rangle$$
$$+ \langle f|\hat{M}^{\dagger}(L,\omega_i)\hat{M}(L,\omega_i''')|f\rangle\langle f|\hat{M}^{\dagger}(L,\omega_i')\hat{M}(L,\omega_i'')|f\rangle\,, \quad (5.12)$$

and each expectation noise value is evaluated using (5.11). The expectation value for the signal quantum operator is given by [31–33]

$$\langle\Psi\left|\left(\hat{A}^{\dagger}(0,\omega_s')\right)^m\left(\hat{A}(0,\omega_s'')\right)^n\right|\Psi\rangle$$
$$= \left(\langle\Psi|\hat{A}^{\dagger}(0,\omega_s')|\Psi\rangle\right)^m\left(\langle\Psi|\hat{A}(0,\omega_s'')|\Psi\rangle\right)^n = \left(\vartheta^*(\omega_s')\right)^m\left(\vartheta(\omega_s'')\right)^n\,. \quad (5.13)$$

A similar expression is obtained for the input coherent quantum channel ω_Q. Although (5.13) is null if $\vartheta(\omega_s)$=0, idler photons are generated inside the fiber due to the fact that, the anti-normal ordered moments that arises from (5.1) are not null even when $\vartheta(\omega_s)$=0.

5.2.2 Beam Splitter Input/Output Relations

The second-order coherence parameter can be experimentally obtained with one non-polarizing beam splitter [17, 18] through the setup shown in Fig. 5.1. In that setup, we consider that the arm $\hat{b}_{in}$ of the beam splitter is left in its vacuum state given by $|0_b\rangle$. In reality beam splitters exhibit some losses. This mean that some of the incident idler photons are absorbed by the beam splitter. In Fig. 5.1, $\hat{n}_a = \hat{a}_{out}^{\dagger}(\omega_i)\hat{a}_{out}(\omega_i)$ and $\hat{n}_b = \hat{b}_{out}^{\dagger}(\omega_i)\hat{b}_{out}(\omega_i)$ where [34]

$$\hat{a}_{out}(\omega_i) = t(\omega_i)\hat{A}(L,\omega_i) + r(\omega_i)\hat{b}_{in}(\omega_i) + \hat{F}_a(\omega_i)\,, \quad (5.14)$$
$$\hat{b}_{out}(\omega_i) = t(\omega_i)\hat{b}_{in}(\omega_i) + r(\omega_i)\hat{A}(L,\omega_i) + \hat{F}_b(\omega_i)\,, \quad (5.15)$$

where $r(\omega_i)$ and $t(\omega_i)$ are the beam splitter reflection and transmission coefficients, respectively, and $\hat{F}_v(\omega_i)$ is the Langevin noise operator, with $v = a,b$, which satisfy the commutation relations [34]

$$\left[\hat{F}_v(\omega_i),\hat{F}_v^{\dagger}(\omega_i')\right] = 2\pi\left(1-|t_i|^2-|r_i|^2\right)\delta(\omega_i-\omega_i')\,, \quad (5.16a)$$
$$\left[\hat{F}_v(\omega_i),\hat{F}_l^{\dagger}(\omega_i')\right] = -2\pi\left(t_i r_i^* + r_i t_i^*\right)\delta(\omega_i-\omega_i')\,, \quad (5.16b)$$

with $l \neq v = a,b$. The expectation values for the Langevin noise operators are [34]

$$\langle\hat{F}_v(\omega_i)\rangle = \langle\hat{F}_v^{\dagger}(\omega_i)\rangle = 0\,, \quad (5.17a)$$
$$\langle\hat{F}_v(\omega_i)\hat{F}_v^{\dagger}(\omega_i')\rangle = 2\pi\left(1-|t_i|^2-|r_i|^2\right)\delta(\omega_i-\omega_i')\,, \quad (5.17b)$$
$$\langle\hat{F}_v(\omega_i)\hat{F}_l^{\dagger}(\omega_i')\rangle = -2\pi\left(t_i r_i^* + r_i t_i^*\right)\delta(\omega_i-\omega_i')\,, \quad (5.17c)$$

where $t_i = t(\omega_i)$ and $r_i = r(\omega_i)$.

5.3 The Second-Order Coherence Function

In this section, we examine the photon counting statistics of the idler wave fully generated inside the fiber, and how the idler photons generated through FWM and Raman scattering processes affects the photon number distribution of an incident coherent quantum channel. The photon number distribution is studied theoretically in terms of the second-order coherence function, $g^{(2)}(0)$. The second-order coherence function is defined as [16]

$$g^{(2)}(0) = \frac{\langle : \hat{N}_1 \hat{N}_2 : \rangle}{\langle \hat{N}_1 \rangle \langle \hat{N}_2 \rangle}, \tag{5.18}$$

where $\hat{N}_1$ and $\hat{N}_2$ are the photon number operators, according with Fig. 5.1, and :: denotes operator normal ordering. A vanishing $g^{(2)}(0)$ corresponds to a perfect single photon source, while $g^{(2)}(0) < 1$ determines the nonclassical nature of the optical field. Otherwise, $g^{(2)}(0) \geq 1$ represents the classical nature of the field being measured. In addition, it can be shown that $g^{(2)}(0) = 1$ corresponds to a Poissonian statistics, such as a coherent laser, and $g^{(2)}(0) = 2$ determines a source with thermal statistics, such as spontaneous Raman scattering [16, 18, 20].

As seen in Fig. 5.1 after the beam splitter the optical field is filtered using an optical filter to remove out-band photons, mainly from the pump and signal fields. In that case, the filtered idler field in time domain can be written as [22, 28]

$$\hat{a}_i(t) = \frac{1}{2\pi} \int d\omega_i H(\omega_i) \hat{a}_{out}(\omega_i) e^{-i\omega_i t}, \tag{5.19}$$

$$\hat{b}_i(t) = \frac{1}{2\pi} \int d\omega_i H(\omega_i) \hat{b}_{out}(\omega_i) e^{-i\omega_i t}, \tag{5.20}$$

where $H(\omega_i)$ is the filter function centered at $\bar{\omega}_i$, with angular frequency bandwidth, $\sigma_{\bar{\omega}_i}$, equals to $\sigma_{\bar{\omega}_i} = 2\pi(\Delta\nu_{\bar{\omega}_i})$. We assume that $g^{(2)}(0)$ is measured by direct photo-detection, and there is no background noise at the detection stage. Note that in a direct detection configuration the background noise does not affect the value of $g^{(2)}(0)$, for a coherent optical field [35, 36]. For a thermal field the background noise slightly decrease the $g^{(2)}(0)$ parameter [35, 36]. Assuming

ideal detection, the expectation value for the dimensionless number operator is given by [28]

$$\langle \hat{N}_n \rangle = \int_{t_0}^{t_0+T_0} dt \langle \hat{c}_i^\dagger(t)\hat{c}_i(t)\rangle$$
$$= \frac{1}{(2\pi)^2}\int_{t_0}^{t_0+T_0} dt \int d\omega_i' \int d\omega_i'' H^*(\omega_i')H(\omega_i'')\langle \hat{c}_{out}^\dagger(\omega_i')\hat{c}_{out}(\omega_i'')\rangle e^{i(\omega_i'-\omega_i'')t}\,, \quad (5.21)$$

where $\hat{c} = \hat{a}$ for $n = 1$ and $\hat{c} = \hat{b}$ for $n = 2$. In Fig. 5.1, $n = 1$ corresponds to Det_1, whereas $n = 2$ corresponds to Det_2. The normally ordered second moment can be written as [28]

$$\langle :\hat{N}_1\hat{N}_2: \rangle = \frac{1}{(2\pi)^4}\iint_{t_0}^{t_0+T_0} dt\,dt' \int d\omega_i' \int d\omega_i'' \int d\omega_i''' \int d\omega_i'''' H^*(\omega_i')H^*(\omega_i'')H(\omega_i''')$$
$$\times H(\omega_i'''')\langle \hat{a}_{out}^\dagger(\omega_i')b_{out}^\dagger(\omega_i'')\hat{b}_{out}(\omega_i''')\hat{a}_{out}(\omega_i'''')\rangle e^{i(\omega_i'-\omega_i'''')t}e^{i(\omega_i''-\omega_i''')t'}\,, \quad (5.22)$$

where $t_0 + T_0$ is a period of time in which the photo-current of the direct detection measurements is integrated.

In this work, we admit that all fields sent to the fiber are from different lasers, in which only a single mode is excited. In that case

$$\vartheta(\omega_s) = (2\pi I_s)^{1/2} e^{-i\theta_s}\delta(\omega_Q - \bar{\omega}_Q)\,, \quad (5.23a)$$
$$\varphi(\omega_Q) = (2\pi I_Q)^{1/2} e^{-i\theta_Q}\delta(\omega_Q - \bar{\omega}_Q)\,, \quad (5.23b)$$

where $\omega_s = 2\omega_p - \omega_Q$, $\bar{\omega}_Q$ is the laser excited mode, which coincides with the filter central frequency $\bar{\omega}_i$. In (5.23), I_s and I_Q are the signal field and coherent quantum channel input mean photon flux, given by

$$I_u = P_u/(\hbar\omega_u)\,. \quad (5.24)$$

If we assume that $\sigma_{\bar{\omega}_i} \ll \omega_i$ and $\sigma_{\bar{\omega}_i} T_0 \ll 1$ the multiple integrals in (5.21) and (5.22) can be carried out

$$\langle \hat{N}_n \rangle \simeq (T_0\Delta\nu_{\bar{\omega}_i})\,|X_i|^2\Big(\bar{n}_Q|\Lambda_i|^2 + (1+\bar{n}_s)|\Gamma_i|^2 + (\bar{n}_{th}+1)\left(|\Lambda_i|^2 - |\Gamma_i|^2 - 1\right)$$
$$+ 2\mathrm{Re}\Big[\Lambda_i\Gamma_i^* e^{-i\Delta\theta}\Big](\bar{n}_Q\bar{n}_s)^{1/2}\Big)\,, \quad (5.25)$$

where the number operator was obtained from the state given by (5.9), $X_i = t(\bar{\omega}_i)$ for $n = 1$ and $X_i = r(\bar{\omega}_i)$ for $n = 2$, and $\Delta\nu_{\bar{\omega}_i} = (1/2\pi)\int |H(\omega_i)|^2 d\omega_i$. In (5.25), $\bar{n}_Q$ and $\bar{n}_s$ are the fiber input

mean photon fluxes per unit of angular frequency bandwidth $\sigma_{\bar{\omega}_i}$. Finally, the normally ordered second moment is given by

$$\begin{aligned}\langle :\hat{N}_1\hat{N}_2: \rangle \simeq (T_0\Delta\nu_{\bar{\omega}_i})^2\,|\bar{r}_i|^2|\bar{t}_i|^2\Big(&\bar{n}_Q^2|\Lambda_i|^4+4\bar{n}_Q(1+\bar{n}_s)|\Lambda_i|^2|\Gamma_i|^2+2\bar{n}_Q\bar{n}_s\mathrm{Re}\Big[\Lambda_i^2\Gamma_i^{*2}e^{-2i\Delta\theta}\Big]\\&+4(\bar{n}_Q\bar{n}_s)^{1/2}\mathrm{Re}\Big[\Lambda_i\Gamma_i^*e^{-i\Delta\theta}\Big]\left(\bar{n}_Q|\Lambda_i|^2+(2+\bar{n}_s)|\Gamma_i|^2\right)\\&+4(\bar{n}_{th}+1)\left(|\Lambda_i|^2-|\Gamma_i|^2-1\right)\left(\bar{n}_i|\Lambda_i|^2+(1+\bar{n}_s)|\Gamma_i|^2\right)\\&+8(\bar{n}_s\bar{n}_Q)(\bar{n}_{th}+1)\left(|\Lambda_i|^2-|\Gamma_i|^2-1\right)\mathrm{Re}\Big[\Lambda_i\Gamma_i^*e^{-i\Delta\theta}\Big]\\&+(2+4\bar{n}_s+\bar{n}_s^2)|\Gamma_i|^4+2(\bar{n}_{th}+1)^2\left(|\Lambda_i|^2-|\Gamma_i|^2-1\right)^2\Big),\end{aligned}\quad(5.26)$$

where $\bar{r}_i = r(\bar{\omega}_i)$, $\bar{t}_i = t(\bar{\omega}_i)$, $\Delta\theta = \theta_i + \theta_s - 2\theta_p$, $\Lambda_i \equiv \Lambda_i(L)$, $\Gamma_i \equiv \Gamma_i(L)$, and $\bar{n}_{th} \equiv n_{th}(\bar{\omega}_i - \omega_p)$. In (5.26), when $\bar{n}_Q \neq 0$ the relative phase $\Delta\theta$ stays at $\pi/2$, which means that the optical power flows from the pump to the classical signal and to the quantum channel [24, 37]. Note that the second momentum number operator $\langle :\hat{N}_1\hat{N}_2: \rangle$ given by (5.26) contains 81 different terms, of which according with the expectation values present in (5.10)-(5.13), 33 are not null.

If the idler wave is fully generated inside the fiber $\bar{n}_Q = 0$. If both $\bar{n}_Q$ and $\bar{n}_s$ are null the FWM process is spontaneous and according with (5.25) and (5.26) $g^{(2)}(0) = 2$, which is in-line with previous theoretical [22] and experimental results [13].

5.4 Theoretically Results

In this section, we present the results obtained for the evolution of $g^{(2)}(0)$ with the fiber input optical power, in two distinct cases. First, we assume that there is no quantum channel, λ_Q, at fiber input. Second we admit that idler photons generated by FWM are created at wavelength λ_Q. In this work, we are assuming a filter bandwidth of 100 GHz, and an optical fiber with the following parameters: $\gamma = 2$ W^{-1}/km, zero-dispersion wavelength $\lambda_0 = 1550.92$ nm, third and fourth-order dispersion coefficients at zero-dispersion wavelength $\beta_3 = 0.1$ ps^3/km and $\beta_4 = 10^{-4}$ ps^{-4}/km, respectively, and length $L = 2.5$ km [38].

5.4.1 Idler Wave Fully Generated Inside the Fiber

In a low power regime, the FWM process produces only a few photons in the idler field [39]. In this section we analyze the $g^{(2)}(0)$ function in that regime.

In Fig. 5.2, we present the evolution of the $g^{(2)}(0)$ function given by (5.18) with the fiber input power. In that figure, the pump wavelength coincides with the fiber zero-dispersion wavelength.

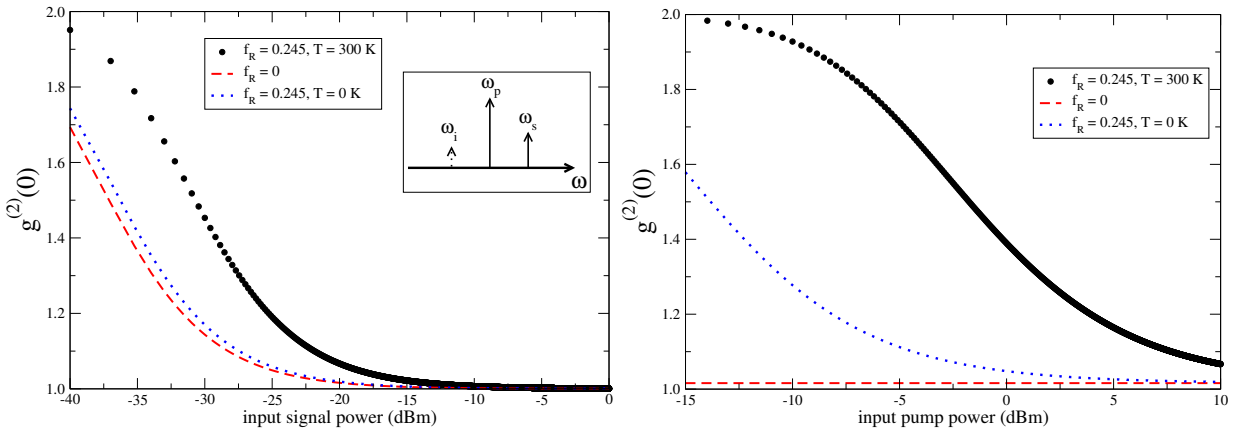

Figure 5.2: Evolution of the $g^{(2)}(0)$ parameter with the fiber input power for the case $P_Q = 0$ W. In (a) $P_p = 10$ dBm, and in plot (b) $P_s = -20$ dBm. The dots represent the case $f_R = 0.245$, the dashed lines represent $f_R = 0$, and the dot line represent the case $T = 0$ K. We have used $\lambda_p = \lambda_0$ and $\lambda_s = 1547.72$ nm. At fiber output the expected idler optical power is $P_Q < 0.4$ μW for plot (a), and $P_Q < 5$ nW for plot (b).

In Fig. 5.2(a), we plot $g^{(2)}(0)$ as a function of the input signal power, whereas in Fig. 5.2(b) we plot the evolution of $g^{(2)}(0)$ with the input pump power. In both figures the idler wave is fully generated inside the fiber. From Fig. 5.2(a) we can see that, the idler field is mostly described by a thermal statistics, when the input signal power is maintained at a low level. Increasing the signal power the statistics of the idler wave at fiber output evolves from thermal to Poissonian. After that, a continuous increase of the signal power does not change the statistics of the idler wave. The results plotted in Fig. 5.2(a) show that, the Raman scattering increases the variance of the photon distribution of the idler wave when compared with the limit $f_R = 0$. This increase leads a high value on the $g^{(2)}(0)$ function. Fig. 5.2(a) also shows that, at zero temperature the variance of the idler photons decrease when compared with the case $T = 300$ K. This arises from (5.11) where $n_{th}(\Omega)$ is null when $T = 0$ K. It can be seen in Fig. 5.2(b) that, the statistics of the idler wave is very dependent on the Raman scattering process. In a low pump and signal power limit the dominant process inside the fiber is the spontaneous Raman scattering [22]. Due to that, the statistics of the idler wave remains approximately thermal over a high range of input pump power. This is also verified when $T = 0$ K, due to the fact that (5.11) is different from zero even at that temperature. This mean that at zero temperature the spontaneous Raman scattering continues to be a dominant process of creation of photons on the idler wave. When we ignore the Raman scattering process, $f_R = 0$, we observe that $g^{(2)}(0) \gtrsim 1$. This reveals the bunched nature

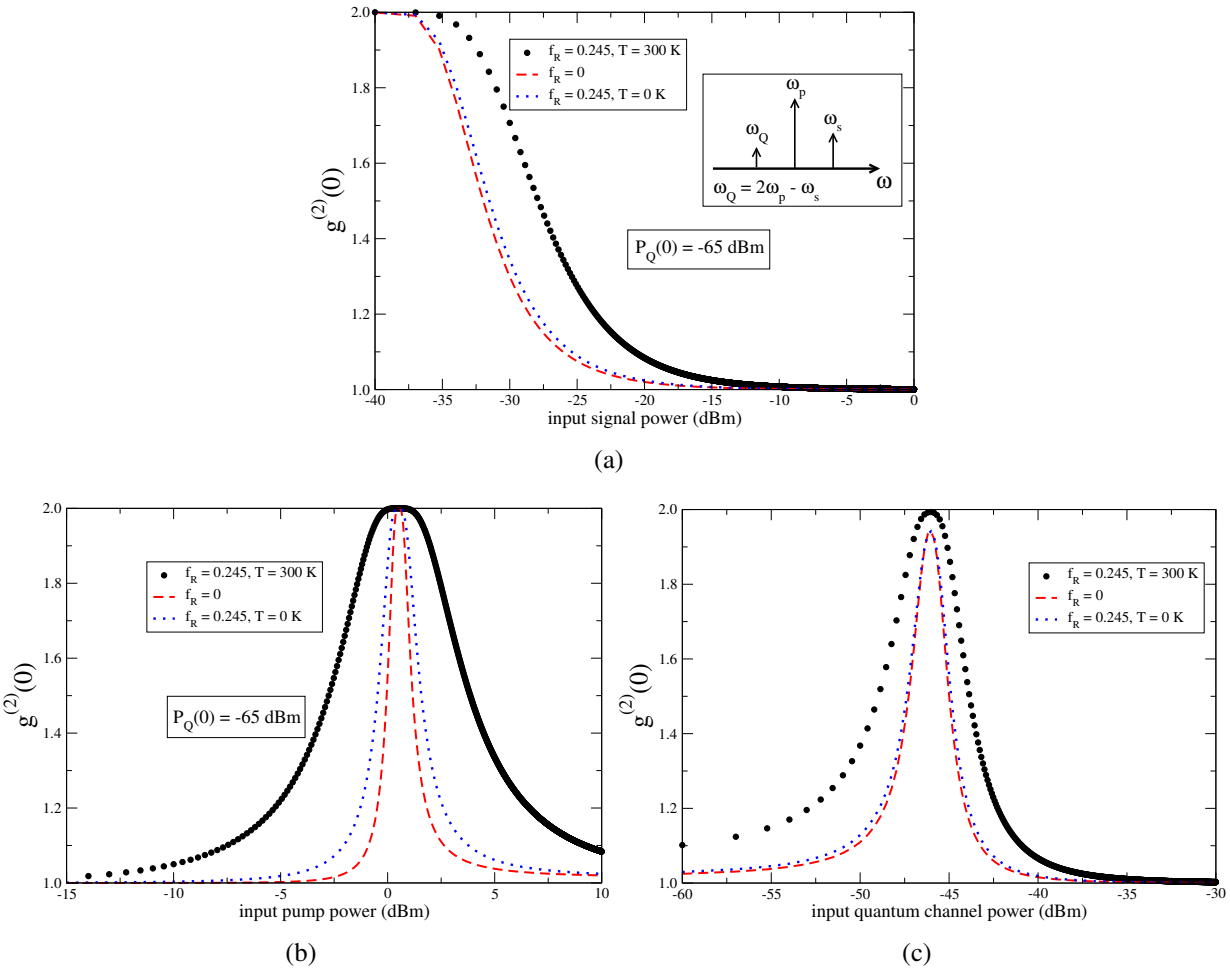

Figure 5.3: Evolution of the $g^{(2)}(0)$ parameter with the fiber input power. In (a) $P_p = 10$ dBm and $P_Q = -65$ dBm, in (b) $P_s = -20$ dBm and $P_Q = -65$ dBm, and in plot (c) $P_p = 10$ dBm and $P_s = -20$ dBm. The dots represent the case $f_R = 0.245$, the dashed lines represent $f_R = 0$, and the dot line represent the case $T = 0$ K. We have used $\lambda_p = \lambda_0$ and $\lambda_s = 1547.72$ nm. At fiber output the expected idler optical power is $P_Q < 0.4$ μW for plot (a), $P_Q < 4$ nW for plot (b), and $P_Q < 0.2$ μW for plot (c).

of the photons generated by the FWM process.

5.4.2 Idler Photons Generated at λ_Q

In this section, we admit that at the fiber input there exist a coherent quantum channel, ω_Q, and idler photons, ω_i, will be created at ω_Q. The idler photons are generated inside the optical fiber through the combined processes of FWM and Raman scattering. The coherent quantum channel ω_Q at fiber input contains only a few photons in that frequency mode, and it is described by a

Poissonian statistics, see Fig. 5.1. At fiber output the coherent quantum channel contains photons created by both FWM and Raman scattering processes. In that scenario, the FWM and Raman photons can be seen as noise sources with respect to the quantum channel [4]. Since that noise photons are generated at frequency ω_Q, they cannot be removed from the quantum channel by using spectral filters on the detection stage, they must be seen as in-band noise [2, 4, 12].

In Fig. 5.3, we plot the variation of $g^{(2)}(0)$ given by (5.18), with the fiber input power. In Fig. 5.3(a), we plot $g^{(2)}(0)$ as a function of the input signal power, whereas Fig. 5.3(b) and 5.3(c) show the evolution of $g^{(2)}(0)$ with the fiber input pump and quantum channel power, respectively. From Fig. 5.3(a) we can see that, the quantum channel changes its own statistics, from a Poissonian distribution at fiber input to a thermal statistics at the fiber output, when the input signal power is maintained in a low level. This change on the statistics arises from the spontaneous photons generated through FWM and Raman processes inside the fiber. Increasing the signal power the statistics of the quantum channel rapidly tends to a Poissonian distribution at both fiber input/output. This reveals the single mode nature of the quantum channel. Results plotted in Fig. 5.3(a) show that, the Raman scattering process does not dramatically change the statistics of that field. In Fig. 5.3(b), we plot the evolution of $g^{(2)}(0)$ with the input pump power. From Fig. 5.3(b) we can see that, for low pump power levels the second-order coherence function remains approximately constant, $g^{(2)}(0) \approx 1$ at fiber output. This is an expected result since in that pump power limit, the unique contribution for the generation of photons arises from the expectation value of the noise operator given by (5.11), which is a very small contribution when compared with the input fiber mean photon flux for the quantum channel field (5.24). However, an increase on the input pump power leads to a rapidly change on the statistics of the quantum channel, from a Poissonian, at fiber input, to a thermal at fiber output. This change is mainly due to spontaneous processes that occurs inside the optical fiber. Moreover, if we continue to increase the pump power the statistics at fiber output changes again from a thermal to Poissonian. This is due to the increase of the stimulated FWM process, in which the variance of the mean photon number is smaller when compared with the Raman scattering process. This happens because stimulated FWM is almost a single frequency mode process. When we compare the cases $T = 0$ K with $T = 300$ K we see that the Raman noise given by (5.11) dominates the evolution of $g^{(2)}(0)$ with the input pump power. In Fig. 5.3(c), we show the evolution of $g^{(2)}(0)$ as a function of the fiber input power of the quantum channel. From Fig. 5.3(c) we can see that, for low input power the statistics of the quantum channel remains approximately Poissonian at fiber input/output. However, an increase on the input power leads to a rapidly evolution of the statistics of that optical field, from Poissonian to thermal, revealing the spontaneous nature of

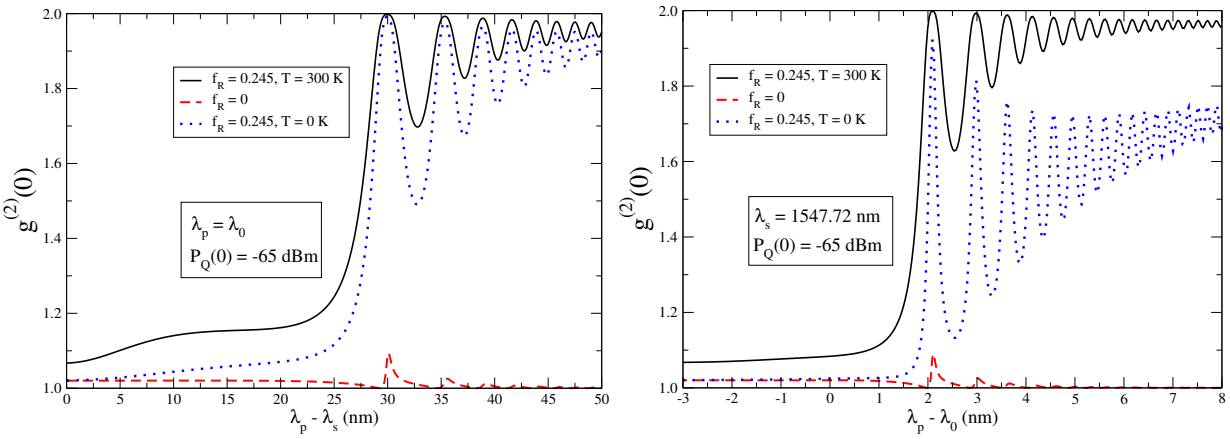

(a) (b)

Figure 5.4: Evolution of the $g^{(2)}(0)$ parameter with wavelength detuning. In plot (a) we show the evolution of the $g^{(2)}(0)$ with the wavelength separation between pump and signal field, whereas in plot (b) we present the $g^{(2)}(0)$ parameter as a function of $\lambda_p - \lambda_0$. At fiber output the expected idler optical power is $P_Q < 4$ nW for both plot (a) and plot (b).

FWM and Raman processes that occurs inside the fiber. For high power levels, the dominant process is the stimulated FWM, and the quantum channel evolves from a thermal statistics to a Poissonian. Since (5.11) does not depend on the input mean photon flux of the quantum channel the Raman noise does not affect the statistics of that field. Results present in Fig. 5.3(c) show that the presence of the Raman scattering increase the variance of the quantum channel, when compared with the limit $f_R = 0$.

In Fig. 5.4, we plot $g^{(2)}(0)$, given by (5.18), as a function of wavelength detuning between pump and signal fields, Fig. 5.4(a), and between pump and fiber zero-dispersion wavelength, Fig. 5.4(b). It can be seen in Fig. 5.4(a) and in Fig. 5.4(b) that, $g^{(2)}(0)$ tends to a thermal distribution at fiber output with the increase of the wavelength detuning. This happens because the frequency of the quantum channel approaches the maximum Raman gain. For small values of wavelength detuning the $g^{(2)}(0)$ function is slightly higher than one in both Fig. 5.4(a) and Fig. 5.4(b). This is due to photons generated on the quantum channel through the Raman scattering process inside the fiber. This can be seen in Fig. 5.4 when we compared the case $f_R = 0.245$ with $f_R = 0$. It can also be seen in Fig. 5.4(a) that, the Raman noise given by (5.11) does not change significantly the evolution of $g^{(2)}(0)$ with $\lambda_p - \lambda_s$. Otherwise, in Fig. 5.4(b) at zero temperature the value of $g^{(2)}(0)$ is smaller when compared with $T = 300$ K. This is due to the phase-matching condition given by (5.6) which takes a small value in the case presented in

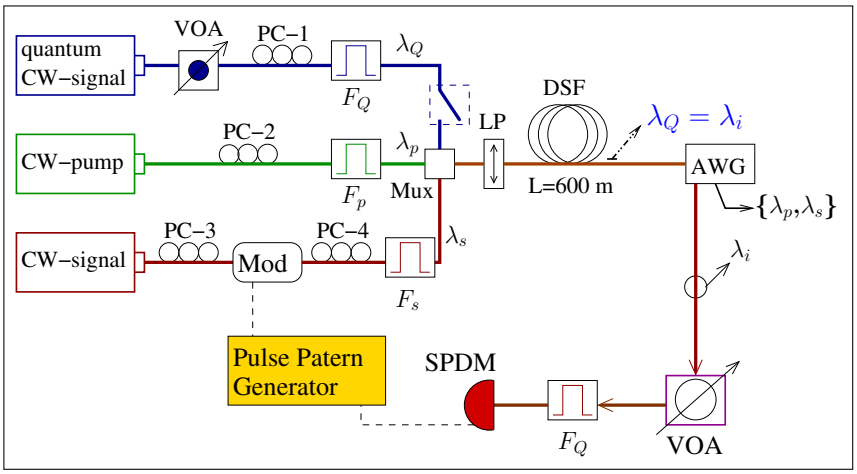

Figure 5.5: Experimental arrangement for measuring the photon counting statistics of the stimulated FWM process. The dashed lines represents electrical signals and the solid lines the optical path. Details of the experiment are presented in the text.

Fig. 5.4(a) than in Fig 5.4(b), due to the fact that $\lambda_p = \lambda_0$ in Fig. 5.4(a). This leads to a high generation of photons through stimulated FWM process, instead of Raman scattered photons.

5.5 Experimental Estimation of the Photon Statistics

In order to validate the proposed theoretical model for the statistics of the classical FWM process, we implement in the laboratory a setup capable of measure the photon distribution of that nonlinear process. The experimental setup was implemented by Á. J. Almeida [6]. A schematic of the experimental setup used to numerical reconstruct the photon number distribution of the idler wave is shown in Fig. 5.5. In Fig. 5.5, a pump, λ_p, at a wavelength of 1550.92 nm from a continuous wave (CW) tunable laser source passes through a polarization controller (PC) before being multiplexed with another two optical fields, λ_s and λ_Q. The signal field, $\lambda_s = 1547.72$ nm, from an external cavity laser (ECL) was modulated externally into pulses with a 1 ns width and a 1.22 MHz repetition frequency using a Mach-Zehnder modulator (Mod). The quantum CW signal, $\lambda_Q = 1554.13$ nm, from an ECL passes from a PC and reaches the MUX. Before being coupled by the MUX each optical field is spectrally filtered to remove laser noise with 100 GHz bandwidth flat-top bandpass optical filters. After the MUX, the three optical fields pass through a linear polarizer (LP) to assure that they are sent to the dispersion-shifted fiber (DSF) in the same linear polarization state, and in that sense obtain the highest efficiency on the generation of idler photons through FWM inside the DSF. The DSF has a nonlinear parameter $\gamma = 2.3$ W^{-1}/km, zero-dispersion wavelength $\lambda_0 = 1549.7$ nm, dispersion-slope at λ_0 of $dD_c/d\lambda = 0.071$ ps/(nm^2-

km) and length $L = 600$ m. At the fiber output, the three optical fields passes through a flat-top AWG with 200 GHz channel spacing to separate the pump, signal and idler photons. The output photons from the AWG idler port are launched into a cascade of 100 GHz bandwidth flat-top bandpass optical filters to further suppress the pump and signal photons. The idler wave passes through the filters and reaches a variable optical attenuator (VOA) and a single photon detector module (SPDM). The VOA allow us to obtain several different click probabilities on the SPDM for the same average photon number, which is essential for the numerical reconstruction of the photon number distribution. The SPDM is based on an avalanche photo diode (APD) operating in the Geiger mode, being 5 ns the gate duration of the photo-detector and 10 μs the dead-time. The quantum detection efficiency of the SPDM is $\eta_D = 7.1\%$ and the probability of dark count is $P_{dc} = 5.1 \times 10^{-6}$ per ns. The outcome of the SPDM is the number of clicks in a time interval of 20 s, and the total number of gates that were open by the detector in the same time interval, for a chosen efficiency value on the VOA.

5.5.1 Numerical Reconstruction Method

The numerical method for the reconstruction of the photon number distribution through on/off detection (click/no-click events) was introduced in [40] and implemented in [15, 41]. Here we use the same ideas for numerical estimate of the statistics of our photon source based on the stimulated FWM process. The statistics of no-click events from the SPDM is given by [41, 42]

$$p_{\nu}^{\text{off}}(\eta_{\nu}) = (1 - P_{dc}) \sum_{n=0} (1 - \eta_{\nu})^n \rho_n \,, \tag{5.27}$$

where η_{ν} with $\nu = 1 \ldots K$ are the values of the combined efficiencies of the SPDM and the VOA, and ρ_n is the probability of obtain n photons. Since this is a linear model, the solution for ρ_n can be obtained by maximum likelihood estimation method [41, 42]

$$\rho_n^{(i+1)} = \frac{\rho_n^{(i)}}{\sum_{\nu=1}^{K} A_{\nu n}} \sum_{\nu=1}^{K} \frac{A_{\nu n} f_{\nu}}{p_{\nu}^{\text{off}}[\{\rho_n^{(i)}\}]} \,, \tag{5.28}$$

where $A_{\nu n} = (1 - P_{dc})(1 - \eta_{\nu})^n$, f_{ν} is the experimental frequencies of the no-click events for the efficiency η_{ν}, and $p_{\nu}^{\text{off}}[\{\rho_n^{(i)}\}]$ is the no-click probability obtained from the reconstructed distribution $\{\rho_n^{(i)}\}$. In our algorithm, we limit the upper limit in the sum (5.27) with $N \leq K + 1 = 30$. This allow us to verify the condition $\sum_{n=0}^{N} \rho_n \approx 1$. The absolute error in the reconstruction process at the i-th iteration is given by [41]

$$\varepsilon^{(i)} = \sum_{\nu=1}^{K} \left| f_{\nu} - p_{\nu}^{\text{off}}[\{\rho_n^{(i)}\}] \right| . \tag{5.29}$$

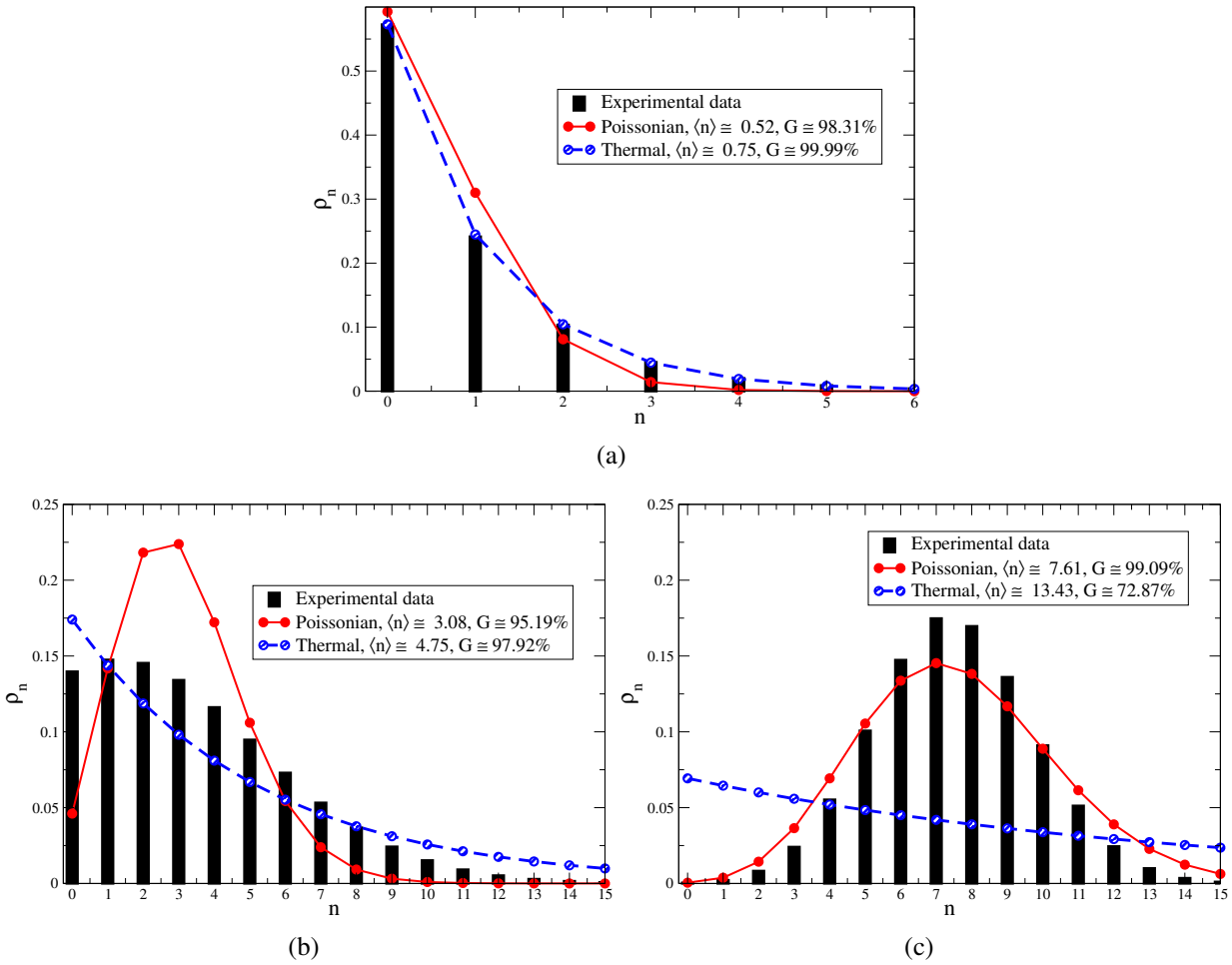

Figure 5.6: Reconstructed photon number distribution for three different values of fiber input signal power. In plot (a) we have used $P_s(0) = -28.99$ dBm, in plot (b) we used $P_s(0) = -22.91$ dBm, whereas in plot (c) $P_s(0) = -18.86$ dBm. In the figure we have used $P_p(0) = 8.81$ dBm. The line represents a Poissonian fit to the experimental data, whereas the dashed line represents the thermal fit.

Since we don't know the photon number distribution of the source, and the numerical reconstruction is an iterative process, we stop the numerical method when the number of iterations is $N_i = 1.22 \times 10^6$. The fidelity between the reconstructed, $\rho_n^{(i)}$, and theoretical, ρ_n, distributions is given by [41]

$$G^{(i)} = \sum_{n=0}^{N} \sqrt{\rho_n \rho_n^{(i)}}\,. \tag{5.30}$$

In Fig 5.6 we plot the experimental results and the theoretical fits for the reconstructed pho-

ton number distribution for the specific case when the idler field is fully generated inside the fiber, for three different fiber input signal powers. It can be seen in Fig 5.6 that the statistics of the idler field is thermal when the optical power of the signal wave is maintained in a low regime, Fig. 5.6(a). In that case the fidelity of the reconstructed method is $G \approx 0.9999$ for the thermal distribution, and the error $\varepsilon^{(N_i+1)} \approx 1.43 \times 10^{-3}$. From Fig. 5.6(b) we can observe both thermal and coherent photons. This indicates the presence of a multithermal statistics. In the last case, Fig. 5.6(c), we can observe a majority of coherent idler photons at the fiber output, due to stimulated processes. The statistics of the idler wave tends to a Poissonian distribution with the

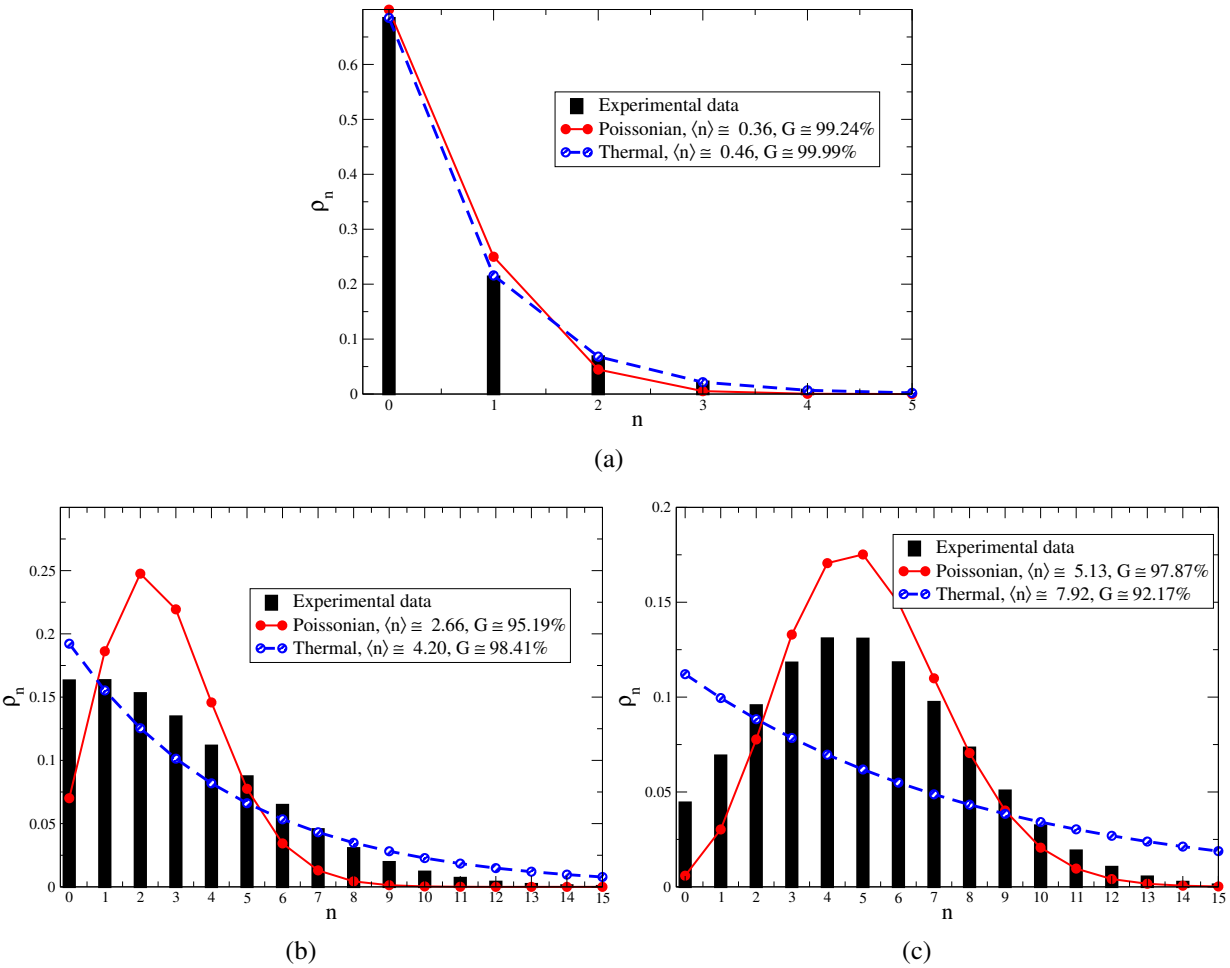

Figure 5.7: Reconstructed photon number distribution for three different values of fiber input idler power. In plot (a) we have used $P_i(0) = -69$ dBm, in plot (b) we used $P_i(0) = -62$ dBm, whereas in plot (c) $P_i(0) = -59$ dBm. In the figure we have used $P_p(0) = 2.12$ dBm, and $P_s(0) = -15.17$ dBm. The line represents a Poissonian fit to the experimental data, whereas the dashed line represents the thermal fit.

increase of the fiber input signal power. These results are also in-line with the theoretical analysis performed in section 5.4.1. In Fig. 5.6(b) we obtain $G \approx 0.9792$ for the thermal distribution, and $\varepsilon^{(N_i+1)} \approx 1.12 \times 10^{-2}$. Finally, in Fig. 5.6(c) we obtain $G \approx 0.9909$ for the Poisson distribution, and $\varepsilon^{(N_i+1)} \approx 3.03 \times 10^{-2}$.

In Fig 5.7 we show the experimental results and the theoretical fits for the reconstructed photon number distribution for the quantum signal, at three different fiber input powers for that optical field. It can be seen in Fig 5.7 that the statistics of the quantum signal field is thermal when the optical power is maintained in a low regime, Fig. 5.7(a). In that case the fidelity of the reconstructed method is $G \approx 0.9999$ for the thermal distribution, and the error $\varepsilon^{(N_i+1)} \approx 9.76 \times 10^{-4}$. This indicates that the statistics of the quantum signal changed from Poissonian to thermal after co-propagation with other classical signals. Increasing the power on the quantum signal, Fig. 5.7(b), we observe a multithermal statistics for the quantum signal. Finally, in Fig. 5.7(c) we can see that the statistics of the quantum signal tends to a Possonian distribution with the increase of the fiber input optical power of that field, the statistics of the quantum signal remains the same at fiber input/output. These results are in-line with the theoretical analysis performed in section 5.4.2. In Fig. 5.7(b) we obtain $G \approx 0.9519$ for the Poisson distribution, and $\varepsilon^{(N_i+1)} \approx 8.7 \times 10^{-3}$. Finally, in Fig. 5.7(c) we obtain $G \approx 0.9787$ for the Poisson distribution, and $\varepsilon^{(N_i+1)} \approx 1.23 \times 10^{-2}$.

5.6 Summary

We show that the statistics of the idler wave generated through FWM follows a thermal distribution when the fiber input power is maintained in a low level. This arises from the thermal nature of the photons generated through spontaneous FWM and through Raman scattering inside the fiber. That happens because those nonlinear processes create photons in several different frequency modes (large frequency bandwidth) with short coherence time. However, an increase on the input power rapidly leads to a Poissonian distribution for the idler photons, at the fiber output. This change on the statistics happens when the stimulated FWM becomes the dominant process, and the photons are created at a single frequency mode, ω_i. Our results also show that the in-band noise photons created by FWM and Raman scattering processes can change the statistics of a quantum channel used for QKD. At low power level the statistics of the coherent quantum channel can evolve from Poissonian to thermal. Our findings also show that when we increase the wavelength detuning between the pump and signal the coherent quantum channel evolves from a Poissonian statistics to a thermal one. This is due to the fact that the quantum channel

approaches the maximum Raman gain. In addition, we have shown that for small wavelength detunings between pump and signal fields the impact of the Raman scattering on the quantum channel is almost negligible, and the statistics of that channel remains the same through propagation.

We have presented a numerical reconstruction of the statistics of a single-photon source based on the stimulated FWM process. The reconstruction was performed using the maximum likelihood estimation method, through the expectation-maximization algorithm. Results have shown that in a low power regime, the statistics of the photons is a thermal. Increasing the power of the signal leads to a multithermal statistics that converges to a Poissonian statistics in a moderate power regime. Regarding the impact of the FWM process on the statistics of a co-propagating coherent quantum signal, we observe that when the quantum signal is in a low power regime, its statistics changes from Poissonian, at the fiber input, to thermal at the fiber output. With the increase on the power of the quantum signal, a multithermal statistics is verified. In a moderate power regime it was verified that the quantum signal does not change its statistics, since it remains Poissonian at the input and at the output of the fiber.

References

[1] N. Gisin, G. Ribordy, W. Tittel, and H. Zbinden, "Quantum cryptography," *Rev. Mod. Phys.*, vol. 74, pp. 145–195, 2002.

[2] P. Eraerds, N. Walenta, M. Legré, N. Gisin, and H. Zbinden, "Quantum key distribution and 1 Gbps data encryption over a single fibre," *New Journal of Physics*, vol. 12, p. 063027, 2010.

[3] N. Silva, N. Muga, and A. Pinto, "Influence of the stimulated Raman scattering on the four-wave mixing process in birefringent fibers," *IEEE/OSA Journal of Lightwave Technology*, vol. 27, pp. 4979–4988, 2009.

[4] N. A. Peters, P. Toliver, T. E. Chapuran, R. J. Runser, S. R. McNown, C. G. Peterson, D. Rosenberg, N. Dallmann, R. J. Hughes, K. P. McCabe, J. E. Nordholt, and K. T. Tyagi, "Dense wavelength multiplexing of 1550 nm QKD with strong classical channels in reconfigurable networking environments," *New Journal of Physics*, vol. 11, p. 045012, 2009.

[5] N. A. Silva, A. J. Almeida, and A. N. Pinto, "Interference in a quantum channel due to classical four-wave mixing in optical fibers," *IEEE Journal of Quantum Electronics*, vol. 48, pp. 472 –479, 2012.

[6] Á. J. Almeida, N. A. Silva, P. S. André, and A. N. Pinto, "Four-wave mixing: Photon statistics and the impact on a co-propagating quantum signal," *Optics Communications*, vol. 285, pp. 2956 – 2960, 2012.

[7] N. A. Silva, A. J. Almeida, and A. N. Pinto, "Statistical characterization of a single-photon source based on stimulated FWM in optical fibers," in *Conf. on Telecommunications - ConfTele*, vol. 1, April 2011, pp. 1–4.

[8] P. Townsend, "Simultaneous quantum cryptographic key distribution and conventional data transmission over installed fibre using wavelength-division multiplexing," *Electronics Letters*, vol. 33, pp. 188 –190, 1997.

[9] G. Agrawal, *Lightwave Technology: Telecommunication Systems*. Wiley-Interscience, 2005.

[10] N. Muga, M. Ferreira, and A. Pinto, "QBER estimation in QKD systems with polarization encoding," *IEEE/OSA Journal of Lightwave Technology*, vol. 29, pp. 355 –361, 2011.

[11] T. Xia, D. Chen, G. Wellbrock, A. Zavriyev, A. Beal, and K. Lee, "In-band quantum key distribution (QKD) on fiber populated by high-speed classical data channels," in *Optical Fiber Communication Conference, 2006 and the 2006 National Fiber Optic Engineers Conference. OFC 2006*, march 2006, p. 3.

[12] B. Qi, W. Zhu, L. Qian, and H.-K. Lo, "Feasibility of quantum key distribution through a dense wavelength division multiplexing network," *New Journal of Physics*, vol. 12, p. 103042, 2010.

[13] P. L. Voss, R. Tang, and P. Kumar, "Measurement of the photon statistics and the noise figure of a fiber-optic parametric amplifier," *Opt. Lett.*, vol. 28, pp. 549–551, 2003.

[14] G. Zambra, M. Bondani, A. S. Spinelli, F. Paleari, and A. Andreoni, "Counting photoelectrons in the response of a photomultiplier tube to single picosecond light pulses," *Review of Scientific Instruments*, vol. 75, pp. 2762–2765, 2004.

[15] G. Zambra, A. Andreoni, M. Bondani, M. Gramegna, M. Genovese, G. Brida, A. Rossi, and M. G. A. Paris, "Experimental reconstruction of photon statistics without photon counting," *Phys. Rev. Lett.*, vol. 95, p. 063602, 2005.

[16] R. Loudon, *The Quantum Theory of Light*, 3rd ed. Oxford University Press, USA, 2000.

[17] M. Beck, "Comparing measurements of $g^{(2)}(0)$ performed with different coincidence detection techniques," *J. Opt. Soc. Am. B*, vol. 24, pp. 2972–2978, 2007.

[18] E. A. Goldschmidt, M. D. Eisaman, J. Fan, S. V. Polyakov, and A. Migdall, "Spectrally bright and broad fiber-based heralded single-photon source," *Phys. Rev. A*, vol. 78, p. 013844, 2008.

[19] H. J. McGuinness, M. G. Raymer, C. J. McKinstrie, and S. Radic, "Quantum frequency translation of single-photon states in a photonic crystal fiber," *Phys. Rev. Lett.*, vol. 105, p. 093604, 2010.

[20] J. A. Slater, J.-S. Corbeil, S. Virally, F. Bussières, A. Kudlinski, G. Bouwmans, S. Lacroix, N. Godbout, and W. Tittel, "Microstructured fiber source of photon pairs at widely separated wavelengths," *Opt. Lett.*, vol. 35, pp. 499–501, 2010.

[21] D. de Brito and R. Ramos, "Analysis of heralded single-photon source using four-wave mixing in optical fibers via wigner function and its use in quantum key distribution," *IEEE Journal of Quantum Electronics*, vol. 46, pp. 721 –727, 2010.

[22] Q. Lin, F. Yaman, and G. P. Agrawal, "Photon-pair generation in optical fibers through four-wave mixing: Role of Raman scattering and pump polarization," *Phys. Rev. A*, vol. 75, p. 023803, 2007.

[23] E. Brainis, "Four-photon scattering in birefringent fibers," *Phys. Rev. A*, vol. 79, p. 023840, 2009.

[24] G. Agrawal, *Nonlinear Fiber Optics*, 3rd ed. Academic Press, 2001.

[25] R. W. Hellwarth, *Third-order optical susceptibilities of liquids and solids*. Pergamon Press, Oxford ; New York, 1977.

[26] Q. Lin and G. P. Agrawal, "Raman response function for silica fibers," *Opt. Lett.*, vol. 31, pp. 3086–3088, 2006.

[27] N. A. Silva, N. J. Muga, and A. N. Pinto, "Evolution of first-order sidebands from multiple FWM processes in HiBi optical fibers," *Optics Communications*, vol. 284, pp. 3408 – 3415, 2011.

[28] M. Artoni and R. Loudon, "Propagation of nonclassical light through an absorbing and dispersive slab," *Phys. Rev. A*, vol. 59, pp. 2279–2290, 1999.

[29] M. Fox, *Quantum optics: An introduction*. Oxford University Press, USA, 2006.

[30] K. J. Blow, R. Loudon, S. J. D. Phoenix, and T. J. Shepherd, "Continuum fields in quantum optics," *Phys. Rev. A*, vol. 42, pp. 4102–4114, 1990.

[31] S. Barnett and P. Radmore, *Methods in Theoretical Quantum Optics*. Oxford University Press, USA, 2002.

[32] R. Chiao and J. Garrison, *Quantum Optics*. Oxford University Press, USA, 2008.

[33] W. H. Louisell, A. Yariv, and A. E. Siegman, "Quantum fluctuations and noise in parametric processes. I." *Phys. Rev.*, vol. 124, pp. 1646–1654, 1961.

[34] S. M. Barnett, J. Jeffers, A. Gatti, and R. Loudon, "Quantum optics of lossy beam splitters," *Phys. Rev. A*, vol. 57, pp. 2134–2145, 1998.

[35] G. Li, T. C. Zhang, Y. Li, and J. M. Wang, "Photon statistics of light fields based on single-photon-counting modules," *Phys. Rev. A*, vol. 71, p. 023807, 2005.

[36] G. Li, T. Zhang, Y. Li, and J. Wang, "Correction of photon statistics of quantum states in single-photon detection," in *Quantum Optics and Applications in Computing and Communications II*, G.-C. Guo, H.-K. Lo, M. Sasaki, and S. Liu, Eds., vol. 5631, no. 1. SPIE, 2005, pp. 134–142.

[37] K. Inoue and T. Mukai, "Signal wavelength dependence of gain saturation in a fiber optical parametric amplifier," *Opt. Lett.*, vol. 26, pp. 10–12, 2001.

[38] B. P. Pal, *Guided Wave Optical Components and Devices*. San Diego: Academic Press, 2005, ch. Fiber-Optic Parametric Amplifiers for Lightwave Systems.

[39] N. A. Silva, N. J. Muga, and A. N. Pinto, "Effective nonlinear parameter measurement using FWM in optical fibers in a low power regime," *IEEE Journal of Quantum Electronics*, vol. 46, pp. 285–291, 2010.

[40] D. Mogilevtsev, "Diagonal element inference by direct detection," *Optics Communications*, vol. 156, pp. 307 – 310, 1998.

[41] A. R. Rossi, S. Olivares, and M. G. A. Paris, "Photon statistics without counting photons," *Phys. Rev. A*, vol. 70, p. 055801, 2004.

[42] T. Moroder, M. Curty, and N. Ltkenhaus, "Detector decoy quantum key distribution," *New Journal of Physics*, vol. 11, p. 045008, 2009.

Chapter 6

Characterization of a Heralded Single Photon Source Based on Four-Wave Mixing

SINGLE photon sources at telecom band are basic elements for quantum key distribution (QKD) systems [1]. However, perfect single photon sources are very complex to implement, since in general they demand cryogenic temperatures or must be operated in vacuum [1, 2]. Due to that, practical implementations of QKD protocols tend to rely on faint laser pulses, as an approximation to a source of single photons [1]. Nevertheless, a faint laser pulses obeys to a Poissonian statistics, which could lead to a loss of security [1]. An alternative approach for single photon generation relies on sources of quantum correlated photon-pairs [3]. In this kind of sources, typically known as heralded single photon sources, the detection of one photon of the pair heralds the presence of its twin photon [3, 4]. In this Chapter we focus on the theoretical evaluation of the conditioned second-order coherence function. Our goal is to quantify the impact of the Raman scattering and the propagation loss effects on the statistics of a heralded single photon source. We identify regimes for the pump power and frequency detuning that minimizes the $g_c^{(2)}$ function. We verify the nonclassical nature of the photon source over a high frequency bandwidth. We consider the presence of noise photons from the Raman scattering process and from a room temperature absorption reservoir. This Chapter is based on the references [5, 6], and is divided as follows: Section 6.1 provides an introduction to the spontaneous four-wave mixing (FWM) process in optical fibers. In section 6.2, we present the theoretical model that describes the generation of quantum-correlated photon pairs through the FWM process, considering the Raman scattering process and the presence of noise photons that are coupled to the propagation fiber due to the presence of a photon absorption reservoir. In section 6.3, we discuss

the conditioned second-order coherence function for the heralded single photon source. Section 6.4 reports the theoretical results. The main conclusions of this Chapter are summarized in section 6.5.

6.1 Spontaneous Four-Wave Mixing Process in $\chi^{(3)}$ Waveguides

The spontaneous FWM process appears as a natural solution to obtain time correlated photon-pairs in $\chi^{(3)}$ materials [7–18]. Moreover, when implemented in dispersion-shifted fibers (DSFs) the spontaneous FWM process can efficiently produce photon-pairs at the 1550 nm telecom window [8]. Nevertheless, inside the DSF and simultaneously with the FWM occurs the Raman scattering process, which generates uncorrelated (noise) photons. The generation of quantum correlated photon-pairs through spontaneous FWM in optical fibers was investigated in [7, 8, 19], and their work was latter extended to account for the spectral shape of pump pulses [20–22]. Subsequent studies have include the spontaneous Raman scattering that occurs inside the optical fiber, and inevitably accompanies the FWM process [23–27]. Recently, in [28, 29] was investigated the impact of fiber loss on the generation of quantum correlated photon-pairs through FWM. The FWM process as a source of heralded single photons was investigated experimentally in [30–34], through the measurement of the second-order correlation function. Subsequent studies [35], characterize the photon statistics of that source through the analysis of the Wigner function, and its performance in a QKD system. In [36] was investigated a synchronous heralded single photon source based on FWM in a liquid nitrogen cooled optical fiber. Recently, in [37] was shown that for a heralded single photon source based on FWM narrow band filters are not mandatory to obtain a high heralding efficiency. In [38] were investigated different schemes that best mitigate the trade-off between high purity and high photon generation rate. Recently, in [39] was presented a quantum theory for the heralded single photon source based on FWM that takes into account the spectral shape of pump pulses. Moreover, in [39] were also reported experimental results for the conditioned second-order coherence function and heralding efficiency.

6.2 The Heralded Single Photon Source

In this section, we present a quantum model for the generation of the signal and idler photon-pairs through spontaneous FWM inside a DSF [8], and for the propagation of the signal photons in a standard single mode fiber (SSMF). We consider the Raman scattering that inevitably ac-

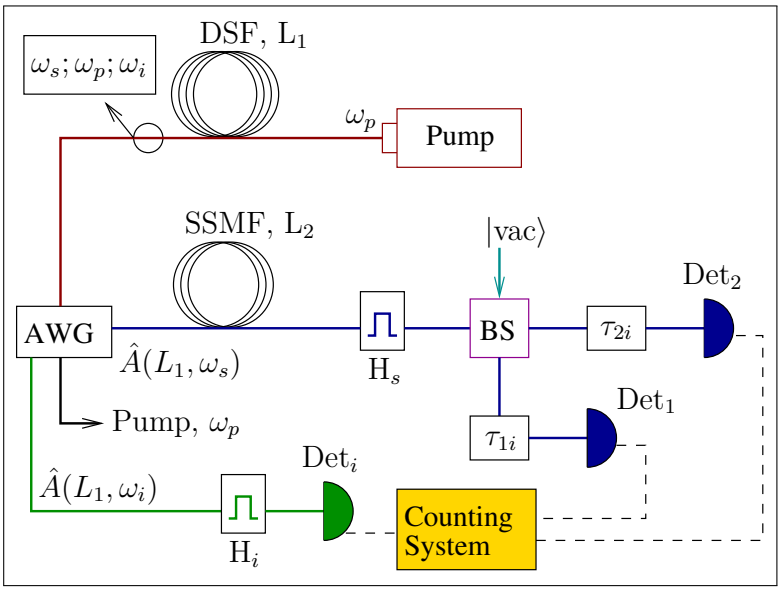

Figure 6.1: Schematic setup to obtain the photon counting statistics of the heralded single photon source based on spontaneous FWM in optical fibers. The dashed lines represents electrical signals and the solid lines the optical path. Details of the setup are presented in the text.

companies the FWM process during the generation of the signal and idler photons inside the DSF. We also take into account the loss mechanism that affect the propagation of the signal photons in the SSMF.

The photon number distribution of the heralded single photon source can be obtained through the setup shown in Fig. 6.1. In the figure, a pump at ω_p, is sent through a DSF with length L_1. Inside the DSF two pump photons are annihilated, and two new photons are created at frequencies ω_s (signal field) and ω_i (idler field), such that $2\omega_p = \omega_s + \omega_i$, with $\omega_s > \omega_i$. Inside the DSF are also generated Raman noise photons, that inevitably accompanies the FWM process. At the DSF output, the three optical fields plus noise passes through an arrayed waveguide grating (AWG) to separate the pump from the signal and idler fields. The output idler photons are spectrally filtered (H_i) and collected by the photon detector module, Det$_i$. The signal photons passes through a SSMF with length L_2 and an optical filter H_s, before been launched into a non-polarizing beam splitter (BS). Note that, we consider two identical filters with central frequency $\overline{\omega}_i$ for H_i and $\overline{\omega}_s$ for H_s, such that $2\omega_p = \overline{\omega}_s + \overline{\omega}_i$. At the BS output the signal photons are collected by the photon detector modules, Det$_1$ and Det$_2$. In Fig. 6.1, τ_{1i} and τ_{2i} represents an adjustable time delay in each arm of the beam splitter. The counting system in Fig. 6.1 measures the delays between a trigger click in Det$_i$ and the clicks in Det$_1$ and Det$_2$, i.e. $t_1 - t_i + t_R$ and $t_2 - t_i + t_R$, with t_1, t_2, and t_i representing the time detection event in detector Det$_1$, Det$_2$, and Det$_i$, respectively, and t_R is a

reference time. The reference time t_R is adjusted in order to compensate for the path delay difference between signal and idler photons. Single and coincidence measurements can be performed in order to obtain $g_c^{(2)}(t_1,t_2|t_i)$ [30, 39].

6.2.1 Photon-Pair Generation Inside the DSF

We focus on the single undepleted pump configuration, where a unique pump is used to induced the FWM process, see Fig. 6.1. In this configuration, the signal and idler annihilation operators in the frequency domain at DSF output are given by [27, 40, 41]

$$\hat{A}(\mathrm{L}_1,\omega_u) = \Big(\Lambda_u(\mathrm{L}_1)\hat{A}(0,\omega_u) + \Gamma_u(\mathrm{L}_1)\hat{A}^\dagger(0,\omega_v) + \hat{N}(\mathrm{L}_1,\omega_u)\Big)\Phi(\mathrm{L}_1), \tag{6.1}$$

with $\langle \hat{A}^\dagger(\mathrm{L}_1,\omega_u)\hat{A}(\mathrm{L}_1,\omega_u)\rangle$ representing the mean spectral photon-flux density, where $u \neq v = s \,\mathrm{or}\, i$ denote the signal and idler field [42]. In (6.1), $\Phi(\mathrm{L}_1) = \exp\{i(k_p + \gamma P_0)\mathrm{L}_1\}$, where k_p is the pump propagation constant, γ is the DSF nonlinear parameter, L_1 is the DSF length, and P_0 is the input pump power. In (6.1), the field operator satisfies the commutation relation [27]

$$\left[\hat{A}(\mathrm{L}_1,\omega), \hat{A}^\dagger(\mathrm{L}_1,\omega')\right] = 2\pi\delta(\omega-\omega')\,. \tag{6.2}$$

where ω and ω' are two angular frequencies. The coefficients $\Lambda_u(\mathrm{L}_1)$ and $\Gamma_u(\mathrm{L}_1)$ appearing in (6.1) are given by [27]

$$\Lambda_u(\mathrm{L}_1) = \left(\cosh(g_{up}\mathrm{L}_1) + i\frac{\kappa_{up}}{2g_{up}}\sinh(g_{up}\mathrm{L}_1)\right) e^{i\frac{k_u-k_v}{2}\mathrm{L}_1} \tag{6.3a}$$

$$\Gamma_u(\mathrm{L}_1) = i\frac{\gamma\eta_{up}}{g_{up}}A_p^2\sinh(g_{up}\mathrm{L}_1)e^{i\frac{k_u-k_v}{2}\mathrm{L}_1}, \tag{6.3b}$$

with

$$g_{up}^2 = \left((\gamma\eta_{up}P_0)^2 - (\kappa_{up}/2)^2\right) \tag{6.4a}$$

$$\kappa_{up} = \Delta\beta + 2\gamma P_0\eta_{up} \tag{6.4b}$$

$$\eta_{up} = 1 - f_R + f_R\tilde{R}_a(\omega_u-\omega_p) + f_R\tilde{R}_b(\omega_u-\omega_p)\,, \tag{6.4c}$$

with ω_p representing the pump frequency, A_p is the pump field envelop such that $P_0 = |A_p|^2$, $\Delta\beta$ is the linear phase-mismatch parameter [43, 44]. In (6.4), $f_R = 0.18$ is the fractional contribution of the Raman process to the nonlinear refractive index [43], $\tilde{R}_a(\omega_u-\omega_p)$ and $\tilde{R}_b(\omega_u-\omega_p)$ are the isotropic and anisotropic Raman response, respectively, defined as in [45]. In (6.3), k_u and k_v are the propagation constants for the signal $u \neq v = s$ or idler field $u \neq v = i$, with $u,v = s\,\mathrm{or}\,i$.

The noise operator in (6.1) is given by [27]

$$\hat{N}(\mathrm{L}_1,\omega_u) = i\int_0^{\mathrm{L}_1} \hat{m}(z,\Omega_{up})\Big(A_p\Lambda_u(\mathrm{L}_1-z) - A_p^*\Gamma_u(\mathrm{L}_1-z)\Big)dz, \tag{6.5}$$

where $\hat{m}(z,\Omega_{up})$ is the Hermitian phase noise operator which accounts for the spontaneous Raman scattering, defined as in [46], $\Omega_{up} = \omega_u - \omega_p$, and the frequency-space correlation for the noise operator is given by [47]

$$\langle \hat{m}^\dagger(z,\Omega_{up})\hat{m}(z',\Omega'_{up})\rangle = 2\pi\delta(\Omega_{up}-\Omega'_{up})\delta(z-z')|g_R(\Omega_{up})|\left(n_{th}(\Omega_{up})+\Theta(-\Omega_{up})\right), \tag{6.6}$$

where $g_R(\Omega_{up})$ is the Raman gain coefficient [45, 48–50], $n_{th}(\Omega_{up}) = \left[e^{\hbar|\Omega_{up}|/k_BT}-1\right]^{-1}$ is the phonon population at temperature T, and $\Theta(-\Omega_{up})$ is the Heaviside step function.

6.2.2 Signal Propagation in the SSMF

We model the SSMF by a continuous array of beam splitters. In that case, the annihilation operator for signal photons at SSMF output is given by [51, 52]

$$\hat{a}(\mathrm{L}_2,\omega_s) = \exp\left\{\left(i\beta(\omega_s)-\frac{\alpha(\omega_s)}{2}\right)\mathrm{L}_2\right\}\hat{A}(\mathrm{L}_1,\omega_s) + i\sqrt{\alpha(\omega_s)}\int_0^{\mathrm{L}_2} e^{\left(i\beta(\omega_s)-\frac{\alpha(\omega_s)}{2}\right)(\mathrm{L}_2-z)}\hat{b}(z,\omega_s)dz, \tag{6.7}$$

where $\beta(\omega_s)$ and $\alpha(\omega_s)$ are the SSMF propagation constant and loss coefficient at frequency ω_s. The propagation constant of the SSMF is expanded to first order in frequency as $\beta(\omega_s) \approx \beta(\overline{\omega}_s) + (\omega_s-\overline{\omega}_s)/v_g(\overline{\omega_s})$, where $v_g(\overline{\omega_s})$ is the group velocity at frequency $\overline{\omega_s}$ [52]. In (6.7), $\hat{A}(\mathrm{L}_1,\omega_s)$ is given by (6.1), and $\hat{b}(z,\omega_s)$ refers to light that is scattered into a guided fiber frequency mode ω_s, due to the coupling with a thermal photon reservoir, with commutation relation [51, 52]

$$\left[\hat{b}(z,\omega),\hat{b}^\dagger(z',\omega')\right] = 2\pi\delta(z-z')\delta(\omega-\omega'), \tag{6.8}$$

and expectation value [51, 52]

$$\langle \hat{b}^\dagger(z,\omega)\hat{b}(z',\omega')\rangle = 2\pi n_{th}(\omega)\delta(z-z')\delta(\omega-\omega'), \tag{6.9}$$

where $n_{th}(\omega) = \left[e^{\hbar\omega/k_BT}-1\right]^{-1}$.

6.3 Statistics of the Heralded Single Photon Source

In this section, we examine the statistics of the heralded single photon source based on spontaneous FWM process in optical fibers. We study the statistics of the source through the analysis of the second order coherence function for the signal field conditioned on observing an idler event [53–55]

$$g_c^{(2)}(t_1,t_2|t_i) = \frac{\langle \hat{E}_s^\dagger(t_1)\hat{E}_s^\dagger(t_2)\hat{E}_s(t_2)\hat{E}_s(t_1)\rangle_{\rm pm}}{\langle \hat{E}_s^\dagger(t_1)\hat{E}_s(t_1)\rangle_{\rm pm}\langle \hat{E}_s^\dagger(t_2)\hat{E}_s(t_2)\rangle_{\rm pm}} = \frac{\langle \hat{E}_i^\dagger(t_i)\hat{E}_s^\dagger(t_1)\hat{E}_s^\dagger(t_2)\hat{E}_s(t_2)\hat{E}_s(t_1)\hat{E}_i(t_i)\rangle\langle \hat{E}_i^\dagger(t_i)\hat{E}_i(t_i)\rangle}{\langle \hat{E}_i^\dagger(t_i)\hat{E}_s^\dagger(t_1)\hat{E}_s(t_1)\hat{E}_i(t_i)\rangle\langle \hat{E}_i^\dagger(t_i)\hat{E}_s^\dagger(t_2)\hat{E}_s(t_2)\hat{E}_i(t_i)\rangle}, \quad (6.10)$$

where $\langle\cdot\rangle_{\rm pm}$ is the average over the post-measurement state, after detection of an idler event [53–55], and

$$\hat{E}_s(t_1) = \frac{1}{2\pi}\int H_s(\omega-\overline{\omega}_s)\hat{a}(\mathrm{L}_2,\omega)e^{-i\omega t_1}d\omega \quad (6.11a)$$

$$\hat{E}_s(t_2) = \frac{1}{2\pi}\int H_s(\omega-\overline{\omega}_s)\hat{a}(\mathrm{L}_2,\omega)e^{-i\omega t_2}d\omega \quad (6.11b)$$

$$\hat{E}_i(t_i) = \frac{1}{2\pi}\int H_i(\omega-\overline{\omega}_i)\hat{A}(\mathrm{L}_1,\omega)e^{-i\omega t_i}d\omega. \quad (6.11c)$$

A $g_c^{(2)}(t_1,t_2|t_i) < 1$ determines the nonclasical nature of the photon source, with $g_c^{(2)}(t_1,t_2|t_i)$ equals to zero for a perfect conditional single photon source. Otherwise, $g_c^{(2)}(t_1,t_2|t_i) \geq 1$ represents the classical nature of the field. Moreover, $g_c^{(2)}(t_1,t_2|t_i) = 1$ corresponds to a Poissonian statistics, and $g_c^{(2)}(t_1,t_2|t_i) = 2$ represents a thermal statistics [30, 41, 52].

To obtain $g_c^{(2)}(t_1,t_2|t_i)$ it is necessary obtain the fourth- and six-order moments given respectively by

$$\langle \hat{E}_i^\dagger(t_i)\hat{E}_s^\dagger(t_j)\hat{E}_s(t_j)\hat{E}_i(t_i)\rangle = \langle \hat{E}_i^\dagger(t_i)\hat{E}_i(t_i)\rangle\langle \hat{E}_s^\dagger(t_j)\hat{E}_s(t_j)\rangle + \left|\langle \hat{E}_s(t_j)\hat{E}_i(t_i)\rangle\right|^2, \quad (6.12)$$

where $j = 1\,\text{or}\,2$, and

$$\begin{aligned}\langle \hat{E}_i^\dagger(t_i)\hat{E}_s^\dagger(t_1)\hat{E}_s^\dagger(t_2)\hat{E}_s(t_2)\hat{E}_s(t_1)\hat{E}_i(t_i)\rangle &= \langle \hat{E}_i^\dagger(t_i)\hat{E}_i(t_i)\rangle\langle \hat{E}_s^\dagger(t_1)\hat{E}_s(t_1)\rangle\langle \hat{E}_s^\dagger(t_2)\hat{E}_s(t_2)\rangle \\ &+ \langle \hat{E}_i^\dagger(t_i)\hat{E}_i(t_i)\rangle\left|\langle \hat{E}_s^\dagger(t_1)\hat{E}_s(t_2)\rangle\right|^2 + \langle \hat{E}_s^\dagger(t_1)\hat{E}_s(t_1)\rangle\left|\langle \hat{E}_s(t_2)\hat{E}_i(t_i)\rangle\right|^2 \\ &+ \langle \hat{E}_s^\dagger(t_2)\hat{E}_s(t_2)\rangle\left|\langle \hat{E}_s(t_1)\hat{E}_i(t_i)\rangle\right|^2 + 2\,\mathrm{Re}\left[\langle \hat{E}_s^\dagger(t_1)\hat{E}_s(t_2)\rangle\left(\langle \hat{E}_s(t_2)\hat{E}_i(t_i)\rangle\right)^*\langle \hat{E}_s(t_1)\hat{E}_i(t_i)\rangle\right],\end{aligned} \quad (6.13)$$

where we use the quantum form of the Gaussian moment-factoring theorem [56], in order to expand the fourth- and six-order moments. For a filter bandwidth ($\Delta\omega_u$) much narrow than the filter central frequency $\Delta\omega_u \ll \omega_u$ [57], the signal and idler photon-fluxes appearing in (6.10), (6.12), and (6.13) are given by

$$\langle \hat{E}_i^\dagger(t_i)\hat{E}_i(t_i)\rangle \approx \phi_i S(\mathrm{L}_1,\overline{\omega}_i) \tag{6.14a}$$

$$\langle \hat{E}_s^\dagger(t_j)\hat{E}_s(t_j)\rangle \approx \phi_s |Y_j|^2 \left(S(\mathrm{L}_1,\overline{\omega}_s)e^{-\alpha(\overline{\omega}_s)\mathrm{L}_2} + \left(1-e^{-\alpha(\overline{\omega}_s)\mathrm{L}_2}\right) n_{th}(\overline{\omega}_s)\right), \tag{6.14b}$$

where

$$\phi_u = \frac{1}{2\pi}\int |H_u(\omega-\overline{\omega}_u)|^2\, d\omega. \tag{6.15}$$

In (6.14), $Y_j = t(\overline{\omega}_s)$ for $j=1$, and $Y_j = r(\overline{\omega}_s)$ for $j=2$, with $t(\overline{\omega}_s)$ and $r(\overline{\omega}_s)$ representing the transmission and reflection beam splitter coefficients, see Fig. 6.1. The mean spectral photon-flux density for the signal and idler wave are given by [27]

$$S(\mathrm{L}_1,\overline{\omega}_u) = |\Gamma_u(\mathrm{L}_1)|^2 + \left(n_{th}(\overline{\Omega}_{up}) + \Theta(-\overline{\Omega}_{up})\right)\left|g_R(\overline{\Omega}_{up})\right| \times \int_0^{\mathrm{L}_1} \left|A_p\Lambda_u(\mathrm{L}_1-z) - A_p^*\Gamma_u(\mathrm{L}_1-z)\right|^2 dz, \tag{6.16}$$

with $\overline{\Omega}_{up} = \overline{\omega}_u - \omega_p$. The self temporal correlation for signal photons in (6.12) and (6.13) is given by

$$\langle \hat{E}_s^\dagger(t_1)\hat{E}_s(t_2)\rangle \approx \phi_s(\tau_{21})t^*(\overline{\omega}_s)r(\overline{\omega}_s)\left(S(\mathrm{L}_1,\overline{\omega}_s)e^{-\alpha(\overline{\omega}_s)\mathrm{L}_2} + \left(1-e^{-\alpha(\overline{\omega}_s)\mathrm{L}_2}\right) n_{th}(\overline{\omega}_s)\right), \tag{6.17}$$

where $\tau_{21} = t_2 - t_1$, and

$$\phi_s(\tau_{21}) = \frac{1}{2\pi}\int |H_u(\omega-\overline{\omega}_u)|^2 e^{-i\omega\tau_{21}} d\omega. \tag{6.18}$$

Finally, in (6.12) and (6.13) the cross temporal correlation between signal and idler photons is given by

$$\langle \hat{E}_s(t_j)\hat{E}_i(t_i)\rangle \approx \phi_{si}(\tau_{ji})Y_jF_{si}(\mathrm{L}_1,\overline{\omega}_s,\overline{\omega}_i)\Phi^2(\mathrm{L}_1)\, e^{-2i\omega_p t_i} e^{-i\overline{\omega}_s\tau_d} e^{(i\beta(\overline{\omega}_s)-\alpha(\overline{\omega}_s)/2)\mathrm{L}_2}. \tag{6.19}$$

where $\tau_{ji} = t_j - t_i - \tau_d$, with $\tau_d = \mathrm{L}_2/v_g(\overline{\omega_s})$ being the propagation time of the signal photons in the SSMF, which can be compensated by the counting system in Fig. 6.1, by making $t_R = \tau_d$. In that case we can consider the measured time delay as $\tau_{ji} = t_j - t_i$. In (6.19), $F_{si}(\mathrm{L}_1,\overline{\omega}_s,\overline{\omega}_i)$ is given by [27]

$$F_{si}(\mathrm{L}_1,\overline{\omega}_s,\overline{\omega}_i) = \Lambda_u(\mathrm{L}_1)\Gamma_u(\mathrm{L}_1) - \left(n_{th}(\overline{\Omega}_{ip}) + \Theta(-\overline{\Omega}_{ip})\right) \times \left|g_R(\overline{\Omega}_{ip})\right| \int_0^{\mathrm{L}_1} \left(A_p\Lambda_s(\mathrm{L}_1-z) - A_p^*\Gamma_s(\mathrm{L}_1-z)\right)\left(A_p\Lambda_i(\mathrm{L}_1-z) - A_p^*\Gamma_i(\mathrm{L}_1-z)\right) dz, \tag{6.20}$$

and $\phi_{si}(\tau_{ji})$ is given by

$$\phi_{si}(\tau_{ji}) = \frac{1}{2\pi}\int H_s(\omega-\overline{\omega}_s)H_i(\overline{\omega}_s-\omega)e^{-i\omega\tau_{ji}}d\omega. \tag{6.21}$$

We assume that the transmission function of the signal and idler filters is Gaussian shaped

$$H_u(\omega-\overline{\omega}_u) = \exp\left\{-\frac{(\omega-\overline{\omega}_u)^2}{2(\Delta\omega_u)^2}\right\}, \tag{6.22}$$

where $\Delta\omega_u = (2\pi)\Delta\nu_u/(2\sqrt{\ln 2})$, and $\Delta\nu_u$ is the filter full width at half maximum (FWHM). We admit that $\Delta\omega_u$ have the same value for the signal and idler fields, $\Delta\omega_u = \Delta\omega$ and consequently $\Delta\nu_u = \Delta\nu$. In that case

$$\phi_s(\tau_{21}) = \frac{1}{2\sqrt{\pi}}\Delta\omega e^{-\left(\frac{\Delta\omega}{2}\tau_{21}\right)^2}e^{-i\overline{\omega}_s\tau_{21}} \tag{6.23a}$$

$$\phi_{si}(\tau_{ji}) = \frac{1}{2\sqrt{\pi}}\Delta\omega e^{-\left(\frac{\Delta\omega}{2}\tau_{ji}\right)^2}e^{-i\overline{\omega}_s\tau_{ji}}, \tag{6.23b}$$

and $\phi_u = \Delta\omega/2\sqrt{\pi}$.

6.4 Theoretical Results

In this section, we present results for the evolution of $g_c^{(2)}(t_1,t_2|t_i)$ with time, and with frequency detuning between pump and signal fields. Moreover, it is also presented the evolution of $g_c^{(2)}(t_1,t_2|t_i)$ with the fiber input pump power, and with fiber length, L_2. We present the results in two different cases. First, we do not consider the SSMF, $L_2 = 0$. Second, we admit that the signal photons generated through FWM propagate in the SSMF.

We assume a temperature for both fibers of $T = 300$ K. The DSF length is $L_1 = 600$ m, and $\gamma = 2.3$ W^{-1}km^{-1}. The Raman response functions were taken from [58]. Moreover, we admit an ideal linear phase-mismatch condition, $\Delta\beta = 0$, in order to obtain efficient generation of signal and idler photons through FWM. This can be achieved by using a pump frequency close to the zero-dispersion frequency of the DSF, and considering a fourth order dispersion coefficient, β_4, of the order of 10^{-6} ps^4/km. Finally, we consider a loss coefficient for the SSMF of $\alpha(\overline{\omega}_s) = 0.25$ dB/km, and signal and idler filters bandwidth at FWHM of $\Delta\nu = 50$ GHz. In the following sections, we denote the idler as the Stokes wave with $\omega_i < \omega_p$, and the signal as the anti-Stokes wave with $\omega_s > \omega_p$.

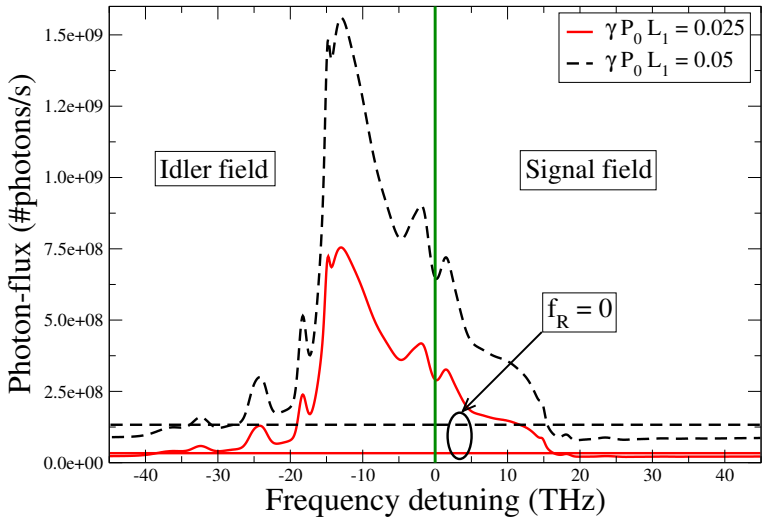

Figure 6.2: Signal and idler photon-fluxes, given by (6.14), as a function of frequency detuning between pump and signal, for a filter bandwidth of 50 GHz and two different values of $\gamma P_0 L_1$. In the figure when $f_R = 0$ the photons are generated only by the FWM process. In the plot we have used $L_2 = 0$. The fiber parameters used are presented in the text.

6.4.1 Statistics at Source Output

We first consider a back-to-back configuration, $L_2 = 0$ in Fig. 6.1. In Fig. 6.2 we present the signal and idler photon-fluxes, given by (6.14), as a function of frequency detuning between pump and signal, $\overline{\Omega}_{sp}/2\pi$, for a filter bandwidth of 50 GHz and for two different values of $\gamma P_0 L_1$. In Fig. 6.2 when $\overline{\Omega}_{sp}/2\pi$ is negative we obtain the idler photon flux, since $-\overline{\Omega}_{sp} = \overline{\Omega}_{ip}$. Moreover, when $f_R = 0$ the Raman scattering process that occurs inside the DSF is ignored. It can be seen in Fig. 6.2 that for $|\overline{\Omega}_{sp}|/2\pi < 15$ THz most of the signal and idler photons are generated through the Raman scattering process. However, for $|\overline{\Omega}_{sp}|/2\pi > 15$ THz we observe a vanish of the noise photons produced by the Raman scattering process [27]. In that scenario, the FWM process becomes dominant, and most of the signal and idler photons are generated through that nonlinear process. Moreover, it can be seen in Fig. 6.2 that for low values of pump power, $\gamma P_0 L_1 = 0.025$, and high frequency detunings, $|\overline{\Omega}_{sp}|/2\pi > 15$ THz, the signal and idler photon-fluxes are of the order of 3×10^7 photons/s.

In Fig. 6.3 we present the evolution of $g_c^{(2)}(t_1, t_2|t_i)$, given by (6.10), with the time delay between the idler and the two signal photon detectors, τ_{1i} and τ_{2i}, see Fig. 6.1. It can be seen in Fig. 6.3 three different regimes for $g_c^{(2)}(t_1, t_2|t_i)$. First, at trigger time $\tau_{1i} = \tau_{2i} = 0$, we obtain an almost perfect conditional single photon source with $g_c^{(2)}(t_1, t_2|t_i) \approx 0$. Second, when $\tau_{2i} = 0$ and $|\tau_{1i}| > (\Delta\nu)^{-1}$ the photon source is described by a Poissonian statistics, since $g_c^{(2)}(t_1, t_2|t_i) \approx 1$.

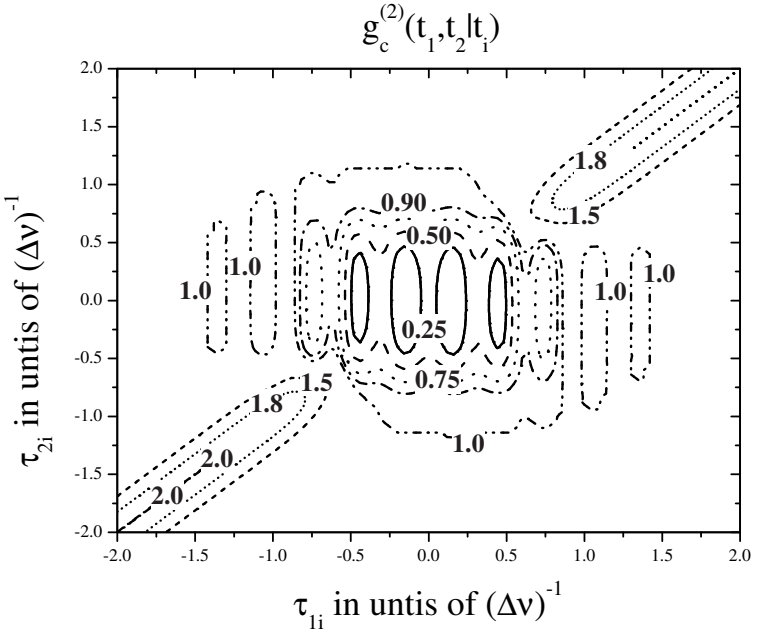

Figure 6.3: Conditioned second order coherence function, given by (6.10), as a function of time delay between the idler and the two signal photon detectors, τ_{1i} and τ_{2i}. In the plot we have used $\overline{\Omega}_{sp}/2\pi = 3$ THz, $\gamma P_0 L_1 = 0.1$, and $L_2 = 0$. The fiber parameters used are presented in the text.

The heralded single photon source has a coherence time of the order of $(\Delta\nu)^{-1}$. This mean that the probability of obtain a detection click on Det_1 in Fig. 6.1 is the same for all values of $|\tau_{1i}| > (\Delta\nu)^{-1}$. The same conclusion is achieved when $\tau_{1i} = 0$ and $|\tau_{2i}| > (\Delta\nu)^{-1}$. Finally, when $|\tau_{1i}| > (\Delta\nu)^{-1}$ and $|\tau_{2i}| > (\Delta\nu)^{-1}$, we obtain $g_c^{(2)}(t_1,t_2|t_i) \approx 2$, the source is described by a thermal statistics. There is no relation between the trigger event and the signal detection on Det_1 and Det_2 in Fig. 6.1. In this case, we are simple measuring the statistics of the unheralded signal photons, which is described by a thermal distribution.

Figure 6.4 shows the evolution of $g_c^{(2)}(t_i,t_2|t_i)$, given by (6.10), with both τ_{2i} and frequency detuning between pump and signal. Results show that for $\tau_{2i} < 1.5(\Delta\nu)^{-1}$ we operate in a nonclassical regime for all values of frequency detuning between pump and signal field, since $g_c^{(2)}(t_i,t_2|t_i) < 1$ which represents the antibunched nature of the light source. Moreover, for $\tau_{2i} \approx 0$ and $\overline{\Omega}_{sp}/2\pi > 13$ THz (the peak of the Raman gain) $g_c^{(2)}(t_i,t_2|t_i)$ decreases with the increases of the frequency detuning between pump and signal. This is a consequence of the decrease of the number of generated Raman scattered photons in the range $13 < \overline{\Omega}_{sp}/2\pi < 45$ THz.

Figure 6.5 shows the evolution of $g_c^{(2)}(t_i,t_i|t_i)$, given by (6.10), with the frequency detuning between pump and signal, for three different values of $\gamma P_0 L_1$. In Fig. 6.5 when $f_R = 0$ the

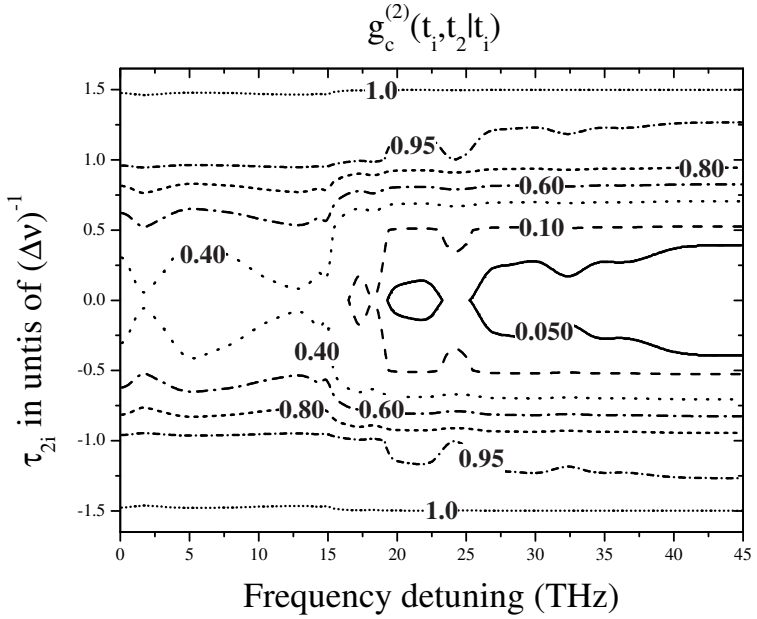

Figure 6.4: Conditioned second order coherence function, given by (6.10), as a function of τ_{2i} and frequency detuning between pump and signal. In the plot we have used $t_1 = t_i$, and $L_2 = 0$. The remaining parameters used are equal to the ones used in Fig. 6.3.

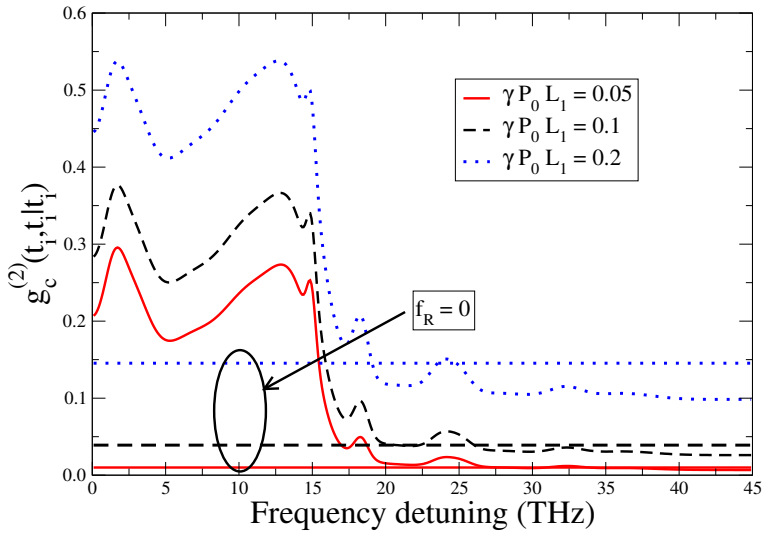

Figure 6.5: Conditioned second order coherence function, given by (6.10), as a function of frequency detuning between pump and signal, for three different values of $\gamma P_0 L_1$. In the figure when $f_R = 0$ the photons are generated only by the FWM process. In the plot we have used $t_1 = t_2 = t_i$, and $L_2 = 0$. The remaining parameters used are equal to the ones used in Fig. 6.3.

Raman scattering process is ignored. Results show that the Raman scattering process degrades the source of single photons, since $g_c^{(2)}(t_i,t_i|t_i)$ increases when $f_R = 0.18$ in (6.10). This is due to

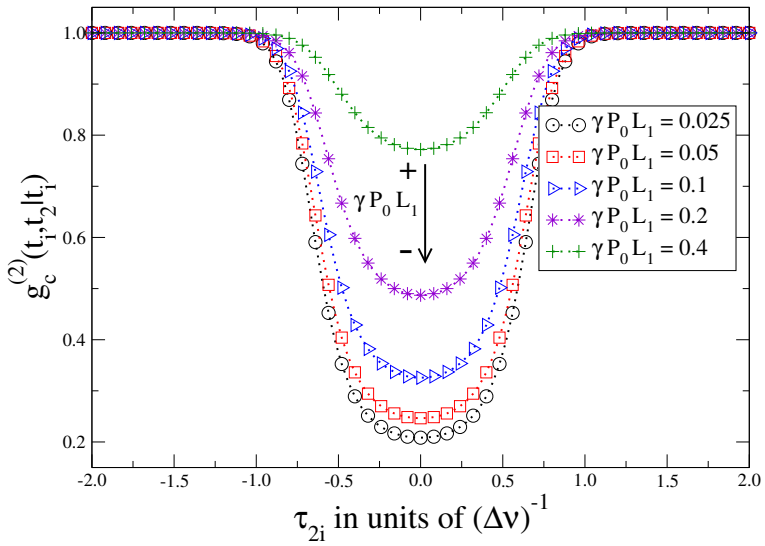

Figure 6.6: Conditioned second order coherence function, given by (6.10), as a function of τ_{2i}, for several different values of input pump power. In the plot we have used $t_1 = t_i$, $\overline{\Omega}_{sp}/2\pi =$ 3 THz, and $L_2 = 0$. The remaining parameters used are equal to the ones used in Fig. 6.3.

the fact that the Raman scattering process generates uncorrelated photons. Moreover, it can be seen in Fig. 6.5 that an increase on the fiber (L_1) input power leads to an increase on the value of $g_c^{(2)}(t_i,t_i|t_i)$ in both cases, $f_R = 0$ and $f_R = 0.18$. This is due to an increase of the number of uncorrelated Raman scattered photons, and due to an increase on the probability of generating multiple signal-idler photon pairs. For $\gamma P_0 L_1 = 0.05$ and $f_R = 0$, we can obtain an almost perfect conditional single photon source, since $g_c^{(2)}(t_i,t_i|t_i) \approx 9.9 \times 10^{-3}$.

In Fig. 6.6, we present the evolution of $g_c^{(2)}(t_i,t_2|t_i)$, given by (6.10), with τ_{2i}, for five different values of $\gamma P_0 L_1$. For all values of $\gamma P_0 L_1$ it is observed a central dip, around $\tau_{2i} = 0$. The depth of the central deep is higher for low values of pump power. In that regime, most of the photons are signal-idler pairs generated through spontaneous FWM.

In Fig. 6.7 we present the evolution of $g_c^{(2)}(t_i,t_i|t_i)$, given by (6.10), with $\gamma P_0 L_1$, for four different values of frequency detuning between pump and signal. It can be seen in Fig. 6.7 that a continuous increase on $\gamma P_0 L_1$ leads to a transition from a nonclassical regime, $g_c^{(2)}(t_i,t_i|t_i) < 1$, to a classical ones, with $g_c^{(2)}(t_i,t_i|t_i) \geq 1$. This is also observed when we ignore the Raman scattering process, $f_R = 0$ in (6.10). From Fig. 6.5 and Fig. 6.7 we can see two different frequency regimes for $g_c^{(2)}(t_i,t_i|t_i)$. First, when $\overline{\Omega}_{sp}/2\pi < 13$ THz $g_c^{(2)}(t_i,t_i|t_i)$ assumes a high value for $f_R = 0.18$ than for $f_R = 0$. Second, when $\overline{\Omega}_{sp}/2\pi \gtrsim 20$ THz, $g_c^{(2)}(t_i,t_i|t_i)$ assumes a high value for $f_R = 0$ than for $f_R = 0.18$. This is due to the fact that, in a high pump power level the idler photon

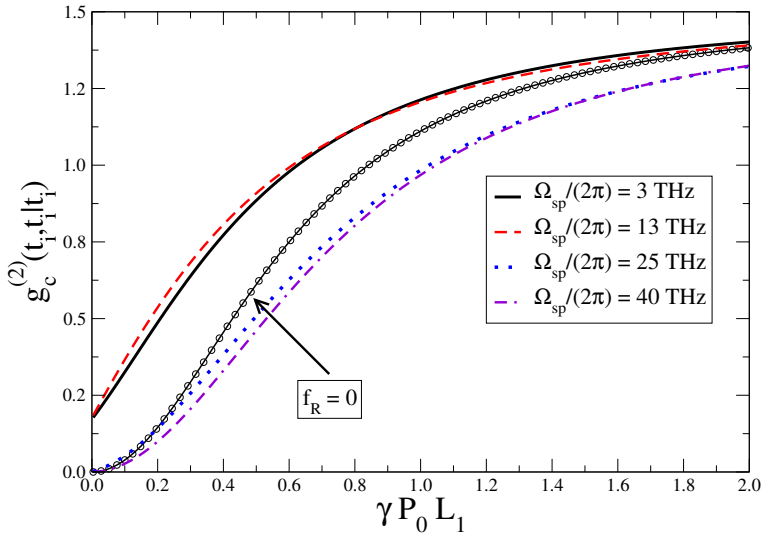

Figure 6.7: Conditioned second order coherence function, given by (6.10), as a function of $\gamma P_0 L_1$, for several different values of frequency detuning between pump and signal. In the figure when $f_R = 0$ the photons are generated only by the FWM process. In the plot we have used $t_1 = t_2 = t_i$, $\overline{\Omega}_{sp}/2\pi = 3$ THz, and $L_2 = 0$. The remaining parameters used are equal to the ones used in Fig. 6.3.

flux decreases with the increase of the frequency detuning [49]. In that regime, the idler wave is mostly described by the real part of the fiber response function, $\left(\tilde{R}_a(\overline{\Omega}_{up}) + \tilde{R}_b(\overline{\Omega}_{up})\right)$, which leads to a decrease on the idler wave intensity, for high frequency shifts, when compared with the limit $f_R = 0$. This results on a decrease on the value $g_c^{(2)}(t_i,t_i|t_i)$.

6.4.2 Propagation of the Signal Photons Inside a SSMF

In this section we assume that between the heralded photon source and the detection there exist a SSMF with length L_2 and loss $\alpha \equiv \alpha(\overline{\omega}_s)$. Only the signal photons travels in the SSMF, see Fig. 6.1.

In Fig. 6.8 we present the evolution of $g_c^{(2)}(t_i,t_i|t_i)$, given by (6.10), with both αL_2 and frequency detuning between pump and signal. It can be seen in Fig. 6.8 that for $\alpha L_2 < 40$ we operate always in a nonclassical regime, with $g_c^{(2)}(t_i,t_i|t_i) < 1$. However, an increase on the value of αL_2 leads to a $g_c^{(2)}(t_i,t_i|t_i) > 1$. This is due to the fact that in (6.14b) $S(L_1,\overline{\omega}_s)e^{-\alpha(\overline{\omega}_s)L_2}$ becomes smaller than $\left(1 - e^{-\alpha(\overline{\omega}_s)L_2}\right) n_{th}(\overline{\omega}_s)$. The flux of signal photons generated through FWM that reaches the detector is smaller than the noise photons obtained from the thermal reservoir. Those noise photons presents a thermal statistics.

Figure 6.9 shows $g_c^{(2)}(t_i,t_i|t_i)$, given by (6.10), as a function of both αL_2 and $\gamma P_0 L_1$. Results

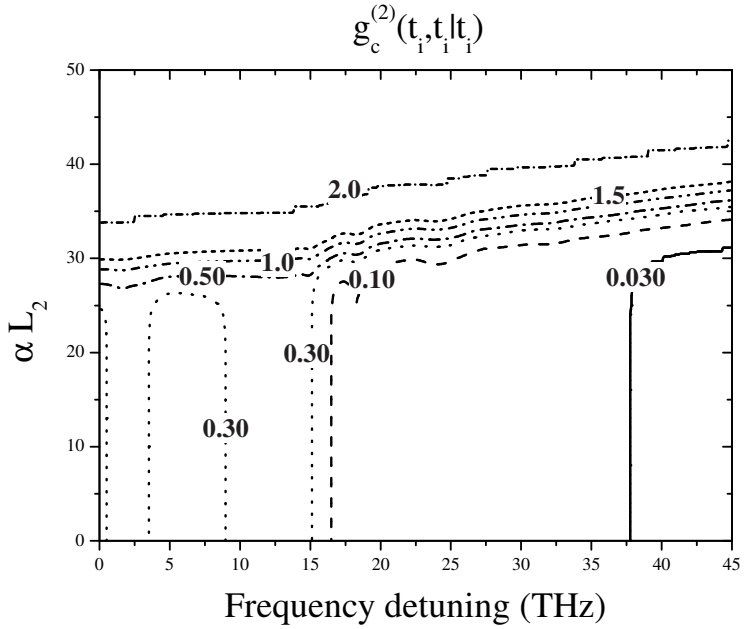

Figure 6.8: Conditioned second order coherence function, given by (6.10), as a function of αL_2 and frequency detuning between pump and signal. In the plot we have used $\gamma P_0 L_1 = 0.1$, and $t_1 = t_2 = t_i$. The remaining parameters used are equal to the ones used in Fig. 6.3.

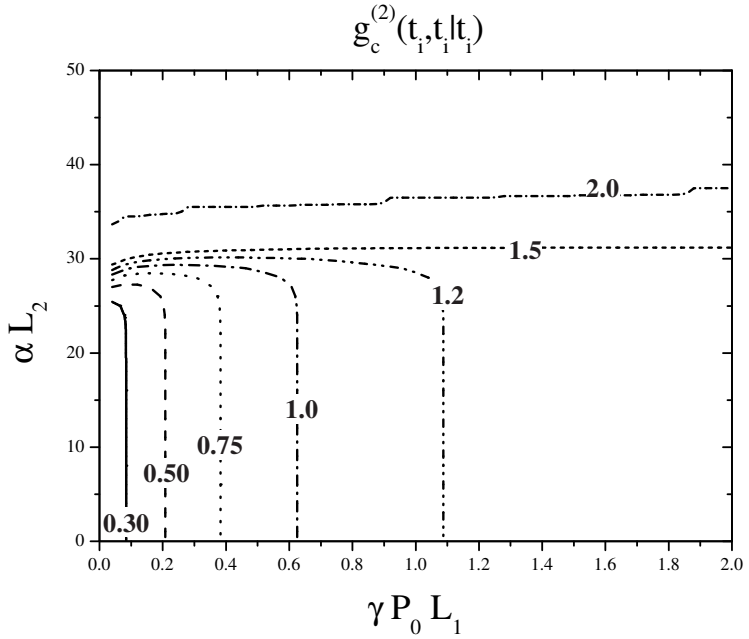

Figure 6.9: Conditioned second order coherence function, given by (6.10), as a function of αL_2 and $\gamma P_0 L_1$. In the plot we have used $\overline{\Omega}_{sp}/2\pi = 3$ THz, and $t_1 = t_2 = t_i$. The remaining parameters used are equal to the ones used in Fig. 6.3.

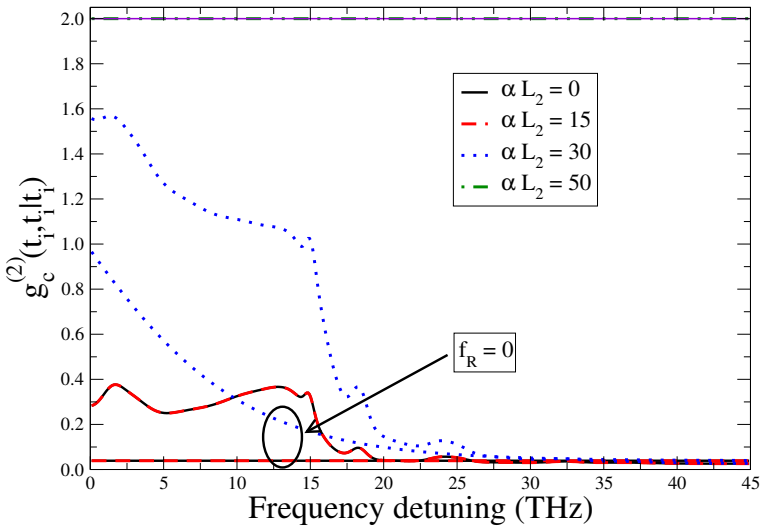

Figure 6.10: Conditioned second order coherence function, given by (6.10), as a function of frequency detuning between pump and signal, for several different values of αL_2. In the figure when $f_R = 0$ the photons are generated only by the FWM process. Note that $g_c^{(2)}(t_i,t_i|t_i)$ assumes the same value for $\alpha L_2 = 0$ and $\alpha L_2 = 15$. When $\alpha L_2 = 50$, $g_c^{(2)}(t_i,t_i|t_i)$ assumes the same value for $f_R = 0.18$ and $f_R = 0$. In the plot we have used $\gamma P_0 L_1 = 0.1$, and $t_1 = t_2 = t_i$. The remaining parameters used are equal to the ones used in Fig. 6.3.

show that an increase on fiber (L_1) input pump power does not counterbalances the increase on $g_c^{(2)}(t_i,t_i|t_i)$ of the heralded single photon source due to the propagation of the signal photons in the SSMF. This is due to the fact that an increase on $\gamma P_0 L_1$ leads to an increase on the number of generated Raman scattered photons, and on the generation of multiple signal-idler pairs.

Figure 6.10 shows $g_c^{(2)}(t_i,t_i|t_i)$, given by (6.10), as a function of frequency detuning between pump and signal, for four different values of αL_2. Results show that for $\alpha L_2 = 30$ and for $\overline{\Omega}_{sp}/2\pi < 25$ THz the Raman scattered photons generated inside the fiber L_1 increases significantly the value of $g_c^{(2)}(t_i,t_i|t_i)$. Moreover, for $\alpha L_2 = 0$ and $\alpha L_2 = 15$, $g_c^{(2)}(t_i,t_i|t_i)$ assumes the same value for both cases. The flux of noise photons generated inside the SSMF is very low for that values of αL_2. Otherwise, for $\alpha L_2 = 50$, the flux of noise photons generated inside the SSMF is much higher than the flux of signal photons generated through FWM. In that case we obtain $g_c^{(2)}(t_i,t_i|t_i) = 2$ for both $f_R = 0$ and $f_R = 0.18$.

Finally, in Fig. 6.11 we present the evolution of $g_c^{(2)}(t_i,t_i|t_i)$, given by (6.10), with αL_2, for four different values of $\gamma P_0 L_1$. It can be seen in Fig. 6.11 that $g_c^{(2)}(t_i,t_i|t_i)$ remains constant with the evolution of αL_2, until $\alpha L_2 \approx 25$. In that αL_2 range, $g_c^{(2)}(t_i,t_i|t_i)$ is smaller for $f_R = 0$ than for $f_R = 0.18$ for the heralded single photon source. After that, $g_c^{(2)}(t_i,t_i|t_i)$ rapidly increases and

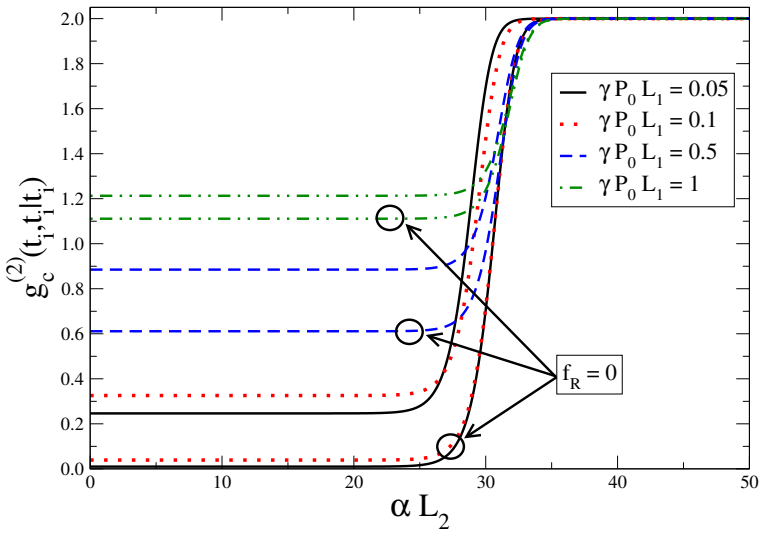

Figure 6.11: Conditioned second order coherence function, given by (6.10), as a function of αL_2, for several different values of $\gamma P_0 L_1$. In the figure when $f_R = 0$ the photons are generated only by the FWM process. In the plot we have used $\overline{\Omega}_{sp}/2\pi = 3$ THz, and $t_1 = t_2 = t_i$. The remaining parameters used are equal to the ones used in Fig. 6.3.

reach the value $g_c^{(2)}(t_i,t_i|t_i) = 2$. This is observed for all the values of $\gamma P_0 L_1$. This mean that the heralded single photons can be distributed for distances no longer than $\alpha L_2 \approx 25$, in a regime of low fiber (L_1) input pump power, to avoid the Raman scattered photons.

6.5 Summary

We investigate the impact of noise photons in a heralded single photon source based on FWM in optical fibers. We show that the Raman noise photons degrades the heralded single photon source, since that nonlinear process increases the value of $g_c^{(2)}(t_i,t_i|t_i)$. Nevertheless, for low values of pump power we still observe the nonclassical nature of the photon source, even in the presence of Raman noise photons. In the absence of Raman scattering process, we obtain $g_c^{(2)}(t_i,t_i|t_i) \approx 9.9 \times 10^{-3}$, which represents an almost perfect conditional source of single photons. Even in that particular case, $g_c^{(2)}(t_i,t_i|t_i) > 0$ due to the fact that the probability of generating multipair photons through FWM is not null. Our analysis also show that, to avoid the Raman noise photons, we need to operate in a high frequency detuning regime, $\overline{\Omega}_{sp} > 20$ THz. In that case, it is possible to obtain an almost perfect conditional source of single photons even in the presence of Raman noise photons. Our results also show that, a continuous increase of the pump power level leads to a Poissonian and to a multithermal statistics of the photon source. This

happens when the stimulated FWM and Raman scattering processes becomes dominant, over the spontaneous FWM. Our findings also show that, the photon absorption reservoir in the SSMF only changes significantly the statistics of the photon source for high values of αL_2. In that regime, the photon flux of thermal noise photons is higher than the flux of FWM photons. In that case, we obtain $g_c^{(2)}(t_i,t_i|t_i) = 2$. For low values of αL_2, the statistics of the source does not change significantly due to propagation.

References

[1] N. Gisin, G. Ribordy, W. Tittel, and H. Zbinden, "Quantum cryptography," *Rev. Mod. Phys.*, vol. 74, pp. 145–195, 2002.

[2] M. D. Eisaman, J. Fan, A. Migdall, and S. V. Polyakov, "Invited review article: Single-photon sources and detectors," *Review of Scientific Instruments*, vol. 82, p. 071101, 2011.

[3] S. A. Castelletto and R. E. Scholten, "Heralded single photon sources: a route towards quantum communication technology and photon standards," *The European Physical Journal - Applied Physics*, vol. 41, pp. 181–194, 2008.

[4] S. Fasel, O. Alibart, S. Tanzilli, P. Baldi, A. Beveratos, N. Gisin, and H. Zbinden, "High-quality asynchronous heralded single-photon source at telecom wavelength," *New Journal of Physics*, vol. 6, p. 163, 2004.

[5] N. A. Silva and A. N. Pinto, "Comprehensive characterization of a heralded single photon source based on four-wave mixing in optical fibers," 2013, submitted to: Optics Communications.

[6] N. A. Silva and A. N. Pinto, "Characterization of a fiber based heralded single photon source at telecom wavelength," in *RIAO/OPTILAS 2013*, vol. 8785, July 2013, pp. 8785F0–1 – 8785F0–5.

[7] J. E. Sharping, M. Fiorentino, and P. Kumar, "Observation of twin-beam-type quantum correlation in optical fiber," *Opt. Lett.*, vol. 26, pp. 367–369, 2001.

[8] M. Fiorentino, P. Voss, J. Sharping, and P. Kumar, "All-fiber photon-pair source for quantum communications," *IEEE Photonics Technology Letters*, vol. 14, pp. 983 –985, 2002.

[9] J. Sharping, J. Chen, X. Li, P. Kumar, and R. Windeler, "Quantum-correlated twin photons from microstructure fiber," *Opt. Express*, vol. 12, pp. 3086–3094, 2004.

[10] X. Li, J. Chen, P. Voss, J. Sharping, and P. Kumar, "All-fiber photon-pair source for quantum communications: Improved generation of correlated photons," *Opt. Express*, vol. 12, pp. 3737–3744, 2004.

[11] J. Rarity, J. Fulconis, J. Duligall, W. Wadsworth, and P. Russell, "Photonic crystal fiber source of correlated photon pairs," *Opt. Express*, vol. 13, pp. 534–544, 2005.

[12] J. Fulconis, O. Alibart, W. Wadsworth, P. Russell, and J. Rarity, "High brightness single mode source of correlated photon pairs using a photonic crystal fiber," *Opt. Express*, vol. 13, pp. 7572–7582, 2005.

[13] H. Takesue and K. Inoue, "1.5-μm band quantum-correlated photon pair generation in dispersion-shifted fiber: suppression of noise photons by cooling fiber," *Opt. Express*, vol. 13, pp. 7832–7839, 2005.

[14] J. Fan, A. Migdall, and L. J. Wang, "Efficient generation of correlated photon pairs in a microstructure fiber," *Opt. Lett.*, vol. 30, pp. 3368–3370, 2005.

[15] J. Fan, A. Dogariu, and L. J. Wang, "Generation of correlated photon pairs in a microstructure fiber," *Opt. Lett.*, vol. 30, pp. 1530–1532, 2005.

[16] J. Fan and A. Migdall, "Generation of cross-polarized photon pairs in a microstructure fiber with frequency-conjugate laser pump pulses," *Opt. Express*, vol. 13, pp. 5777–5782, 2005.

[17] J. Fan and A. Migdall, "A broadband high spectral brightness fiber-based two-photon source," *Opt. Express*, vol. 15, pp. 2915–2920, 2007.

[18] J. Fan, A. Migdall, J. Chen, and E. Goldschmidt, "Microstructure-fiber-based source of photonic entanglement," *IEEE Journal of Selected Topics in Quantum Electronics*, vol. 15, pp. 1724 –1732, 2009.

[19] L. J. Wang, C. K. Hong, and S. R. Friberg, "Generation of correlated photons via four-wave mixing in optical fibres," *Journal of Optics B: Quantum and Semiclassical Optics*, vol. 3, p. 346, 2001.

[20] J. Chen, X. Li, and P. Kumar, "Two-photon-state generation via four-wave mixing in optical fibers," *Phys. Rev. A*, vol. 72, p. 033801, 2005.

[21] O. Alibart, J. Fulconis, G. K. L. Wong, S. G. Murdoch, W. J. Wadsworth, and J. G. Rarity, "Photon pair generation using four-wave mixing in a microstructured fibre: theory versus experiment," *New Journal of Physics*, vol. 8, p. 67, 2006.

[22] X. Li, X. Ma, Z. Y. Ou, L. Yang, L. Cui, and D. Yu, "Spectral study of photon pairs generated in dispersion shifted fiber with a pulsed pump," *Opt. Express*, vol. 16, pp. 32–44, 2008.

[23] P. L. Voss and P. Kumar, "Raman-effect induced noise limits on $\chi^{(3)}$ parametric amplifiers and wavelength converters," *Journal of Optics B: Quantum and Semiclassical Optics*, vol. 6, p. S762, 2004.

[24] P. L. Voss and P. Kumar, "Raman-noise-induced noise-figure limit for $\chi(3)$ parametric amplifiers," *Opt. Lett.*, vol. 29, pp. 445–447, 2004.

[25] P. L. Voss, K. G. Köprülü, and P. Kumar, "Raman-noise-induced quantum limits for $\chi(3)$ nondegenerate phase-sensitive amplification and quadrature squeezing," *J. Opt. Soc. Am. B*, vol. 23, pp. 598–610, 2006.

[26] Q. Lin, F. Yaman, and G. P. Agrawal, "Photon-pair generation by four-wave mixing in optical fibers," *Opt. Lett.*, vol. 31, pp. 1286–1288, 2006.

[27] Q. Lin, F. Yaman, and G. P. Agrawal, "Photon-pair generation in optical fibers through four-wave mixing: Role of Raman scattering and pump polarization," *Phys. Rev. A*, vol. 75, p. 023803, 2007.

[28] N. A. Silva and A. N. Pinto, "Role of absorption on the generation of quantum-correlated photon pairs through FWM," *IEEE Journal of Quantum Electronics*, vol. 48, pp. 1380 –1388, 2012.

[29] N. A. Silva and A. N. Pinto, "Effects of losses and nonlinearities on the generation of polarization entangled photons," *IEEE/OSA Journal of Lightwave Technology*, vol. 31, pp. 1309–1317, 2013.

[30] E. A. Goldschmidt, M. D. Eisaman, J. Fan, S. V. Polyakov, and A. Migdall, "Spectrally bright and broad fiber-based heralded single-photon source," *Phys. Rev. A*, vol. 78, p. 013844, 2008.

[31] J. A. Slater, J.-S. Corbeil, S. Virally, F. Bussières, A. Kudlinski, G. Bouwmans, S. Lacroix, N. Godbout, and W. Tittel, "Microstructured fiber source of photon pairs at widely separated wavelengths," *Opt. Lett.*, vol. 35, pp. 499–501, 2010.

[32] H. J. McGuinness, M. G. Raymer, C. J. McKinstrie, and S. Radic, "Quantum frequency translation of single-photon states in a photonic crystal fiber," *Phys. Rev. Lett.*, vol. 105, p. 093604, 2010.

[33] C. Söller, O. Cohen, B. J. Smith, I. A. Walmsley, and C. Silberhorn, "High-performance single-photon generation with commercial-grade optical fiber," *Phys. Rev. A*, vol. 83, p. 031806, 2011.

[34] J. Fulconis, O. Alibart, J. L. O'Brien, W. J. Wadsworth, and J. G. Rarity, "Nonclassical interference and entanglement generation using a photonic crystal fiber pair photon source," *Phys. Rev. Lett.*, vol. 99, p. 120501, 2007.

[35] D. de Brito and R. Ramos, "Analysis of heralded single-photon source using four-wave mixing in optical fibers via Wigner function and its use in quantum key distribution," *IEEE Journal of Quantum Electronics*, vol. 46, pp. 721 –727, 2010.

[36] Q. Zhou, W. Zhang, J. rong Cheng, Y. dong Huang, and J. de Peng, "Properties of optical fiber based synchronous heralded single photon sources at 1.5 μm," *Physics Letters A*, vol. 375, pp. 2274 – 2277, 2011.

[37] Y.-P. Huang, J. B. Altepeter, and P. Kumar, "Heralding single photons without spectral factorability," *Phys. Rev. A*, vol. 82, p. 043826, 2010.

[38] Y.-P. Huang, J. B. Altepeter, and P. Kumar, "Optimized heralding schemes for single photons," *Phys. Rev. A*, vol. 84, p. 033844, 2011.

[39] L. Yang, X. Ma, X. Guo, L. Cui, and X. Li, "Characterization of a fiber-based source of heralded single photons," *Phys. Rev. A*, vol. 83, p. 053843, 2011.

[40] E. Brainis, "Four-photon scattering in birefringent fibers," *Phys. Rev. A*, vol. 79, p. 023840, 2009.

[41] N. A. Silva, A. J. Almeida, and A. N. Pinto, "Interference in a quantum channel due to classical four-wave mixing in optical fibers," *IEEE Journal of Quantum Electronics*, vol. 48, pp. 472 –479, 2012.

[42] E. Brainis, S. Clemmen, and S. Massar, "Spontaneous growth of raman stokes and anti-stokes waves in fibers," *Opt. Lett.*, vol. 32, pp. 2819–2821, 2007.

[43] G. Agrawal, *Nonlinear Fiber Optics*, 3rd ed. Academic Press, 2001.

[44] N. A. Silva, N. J. Muga, and A. N. Pinto, "Effective nonlinear parameter measurement using FWM in optical fibers in a low power regime," *IEEE Journal of Quantum Electronics*, vol. 46, pp. 285–291, 2010.

[45] Q. Lin and G. P. Agrawal, "Raman response function for silica fibers," *Opt. Lett.*, vol. 31, pp. 3086–3088, 2006.

[46] L. Boivin, F. X. Kärtner, and H. A. Haus, "Analytical solution to the quantum field theory of self-phase modulation with a finite response time," *Phys. Rev. Lett.*, vol. 73, pp. 240–243, 1994.

[47] P. D. Drummond and J. F. Corney, "Quantum noise in optical fibers. i. stochastic equations," *J. Opt. Soc. Am. B*, vol. 18, pp. 139–152, 2001.

[48] R. W. Hellwarth, *Third-order optical susceptibilities of liquids and solids*. Pergamon Press, Oxford ; New York, 1977.

[49] N. Silva, N. Muga, and A. Pinto, "Influence of the stimulated Raman scattering on the four-wave mixing process in birefringent fibers," *IEEE/OSA Journal of Lightwave Technology*, vol. 27, pp. 4979–4988, 2009.

[50] N. A. Silva, N. J. Muga, and A. N. Pinto, "Evolution of first-order sidebands from multiple FWM processes in HiBi optical fibers," *Optics Communications*, vol. 284, pp. 3408 – 3415, 2011.

[51] J. R. Jeffers, N. Imoto, and R. Loudon, "Quantum optics of traveling-wave attenuators and amplifiers," *Phys. Rev. A*, vol. 47, pp. 3346–3359, 1993.

[52] R. Loudon, *The Quantum Theory of Light*, 3rd ed. Oxford University Press, USA, 2000.

[53] M. Razavi, I. Söllner, E. Bocquillon, C. Couteau, R. Laflamme, and G. Weihs, "Characterizing heralded single-photon sources with imperfect measurement devices," *Journal of Physics B: Atomic, Molecular and Optical Physics*, vol. 42, p. 114013, 2009.

[54] E. Bocquillon, C. Couteau, M. Razavi, R. Laflamme, and G. Weihs, "Coherence measures for heralded single-photon sources," *Phys. Rev. A*, vol. 79, p. 035801, 2009.

[55] D. Höckel, L. Koch, and O. Benson, "Direct measurement of heralded single-photon statistics from a parametric down-conversion source," *Phys. Rev. A*, vol. 83, p. 013802, 2011.

[56] J. H. Shapiro and K.-X. Sun, "Semiclassical versus quantum behavior in fourth-order interference," *J. Opt. Soc. Am. B*, vol. 11, pp. 1130–1141, 1994.

[57] L. Mandel and E. Wolf, *Optical coherence and quantum optics*, 1st ed. New York: Cambridge University Press, 1995.

[58] D. Hollenbeck and C. D. Cantrell, "Multiple-vibrational-mode model for fiber-optic Raman gain spectrum and response function," *J. Opt. Soc. Am. B*, vol. 19, pp. 2886–2892, 2002.

Chapter 7

Impact of Absorption on the Generation Rate of Photon-Pairs

QUANTUM-correlated photon pairs are essential for quantum technologies, such as quantum information [1]. In this context, the generation of correlated photon pairs inside optical waveguides appears as important topic for quantum key distribution (QKD) [1]. The four-wave mixing (FWM) process provides an efficient method of generating correlated photon pairs already inside a waveguide. Those photons, obtained through FWM, has been used mainly in quantum key distribution experiments, through the implementation of heralded single photon sources [2] and entangled photon sources [3, 4]. In this Chapter we present a complete description of the generation of photon-pairs through the combined processes of FWM and Raman scattering in a medium with non-negligible loss. We expand previous studies related with the generation of quantum-correlated photon pairs in order to include the waveguide absorption [5–7]. The obtained results can help to guide the implementation of on-chip quantum technologies. This Chapter is based on the references [8–11], and is divided as follows: Section 7.1 provides an introduction to the generation of quantum correlated photon pairs in a lossy waveguide. In section 7.2, we present the formalism of the evolution of the optical field operator in a medium with non-negligible loss. In section 7.3, we apply that formalism to the co-polarized spontaneous FWM process in the single-pump configuration. We describe the impact of the waveguide absorption on the photon-flux and on the second-order coherence function. Moreover, in section 7.3, we also discuss the influence of waveguide loss on the Cauchy-Schwarz correlation parameter and on the Clauser, Horne, Shimony, and Holt (CHSH) inequality. In section 7.4 we present the experimental setup used to generate and detect time correlated and polarization-entangled photon pairs generated through spontaneous FWM. The main results of this Chapter are summarized in section 7.5.

7.1 Generation of Signal and Idler Photon Pairs in a Lossy Waveguide

Efficient generation of quantum-correlated photon pairs through spontaneous FWM demands perfect phase-matching condition and waveguides with high value of nonlinear coefficient [7, 12, 13]. Recent developments of photonic crystal fibers (PCFs) and chalcogenide glass waveguides have enable to produce optical waveguides with high nonlinear coefficient and a near-zero dispersion wavelength [14, 15]. Waveguides with high nonlinear coefficient can be used for efficient generation of photon pairs over short distances [16, 17]. This is essential to implement integrated on-chip quantum technologies [18]. However, waveguides with high nonlinear coefficient usually presents high values of loss [14–16]. A complete description of the generation of quantum-correlated photon pairs through spontaneous FWM in loss waveguides remains an open issue, to the best of our knowledge.

The spontaneous FWM in optical fibers as a source of photon pairs was investigated experimentally in [19, 20] in the single-pump configuration. In [21] authors report the generation of correlated photon pairs by means of a reversed degenerate FWM process. Recently, in [22] authors investigate the generation of identical photons using a dual-pump counter-propagating scheme. Subsequent studies have used the FWM process to implement polarization [17, 23–26], time-bin [27, 28], and frequency [29] entangled photon pair sources. The generation of quantum-correlated photon pairs was already studied experimentally in chalcogenide glass waveguides, see for instance [14, 16, 30].

The spontaneous FWM was also studied theoretically in [31], and their work was latter extend to include the pump pulsed regime [32, 33], and to include the impact of the spontaneous Raman scattering that occurs inside the fiber [5, 6, 34, 35]. A vectorial theory of the combined processes of FWM and Raman scattering was presented in [7], considering various pumping configurations. In [35], authors present a quantum theory of phase-sensitive parametric amplifier in $\chi^{(3)}$ materials, including the effect of linear loss. Recently, in [36] authors investigated the generation of correlated photon pairs through FWM using silicon waveguides, in the presence of three different sources of losses.

7.2 Signal and Idler Equations and Pair Correlation

In this section, we present the equation of motion of the optical field annihilation operator inside an optical fiber, for each of the polarization modes $j = x \text{or} y$. Under the rotating-wave

approximation, the quantum version of the nonlinear Schrödinger equation in optical fibers in the frequency domain is given by [7, 35, 37–40]

$$\frac{\partial \hat{A}_j(z,\omega)}{\partial z} = i\sum_k \tilde{R}^{(1)}_{jk}(\omega)\hat{A}_k(z,\omega) + i\frac{\sqrt{\hbar\omega_0}}{2\pi}\sum_k \int d\omega_1 \hat{m}_{jk}(z,\omega-\omega_1)\hat{A}_k(z,\omega_1) + \hat{l}_j(z,\omega) + i\frac{\hbar\omega_0}{(2\pi)^2}\sum_{klm}\iint d\omega_1 d\omega_2 \tilde{R}^{(3)}_{jklm}(\omega_2-\omega_1)\hat{A}^\dagger_l(z,\omega_1)\hat{A}_m(z,\omega_2)\hat{A}_k(z,\omega+\omega_1-\omega_2), \quad (7.1)$$

where $j,k,l,m = x \text{or} y$, ω_0 is the carrier frequency of the electromagnetic field, $\hat{A}_j(z,\omega)$ is the slowly varying field annihilation operator in the frequency domain, which satisfies the commutation relation

$$\left[\hat{A}_j(z,\omega), \hat{A}^\dagger_k(z,\omega')\right] = 2\pi\delta_{jk}\delta(\omega-\omega'), \quad (7.2)$$

$\tilde{R}^{(1)}_{jk}(\omega)$ is the Fourier transform of $R^{(1)}_{jk}(\tau)$, and represents the linear response function of the fiber, given by sec. 2.1 of [12], and [41]

$$\tilde{R}^{(1)}_{jk}(\omega) = \beta_j(\omega) + \frac{i}{2}\alpha_j(\omega) - \frac{\omega}{2}\mathbf{B}_{jk}, \quad (7.3)$$

which includes both dispersion $\beta_j(\omega)$ and birefringence $\mathbf{B}_{jk}$ properties of the fiber, as well the fiber losses $\alpha_j(\omega)$, see for instance sec. 1.2 of [12], and [42]. In (7.1), $\tilde{R}^{(3)}_{jklm}(\Omega)$ is the third-order nonlinear response function of the optical fiber, given by [7, 43–45]

$$\tilde{R}^{(3)}_{jklm}(\Omega) = \gamma\frac{1-f_R}{3}\left(\delta_{jk}\delta_{lm}+\delta_{jl}\delta_{km}+\delta_{jm}\delta_{kl}\right) + \gamma f_R \tilde{R}_a(\Omega)\delta_{jk}\delta_{lm} + \gamma\frac{f_R}{2}\tilde{R}_b(\Omega)\left(\delta_{jl}\delta_{km}+\delta_{jm}\delta_{kl}\right), \quad (7.4)$$

and governs the nonlinear processes that occurs inside the fiber such as FWM and Raman scattering. In (7.4), Ω is the Stokes ($\Omega<0$) or anti-Stokes ($\Omega>0$) frequency shift, γ is the nonlinear coefficient of the fiber, $f_R = 0.18$ [46] is the fractional contribution of the Raman process to the nonlinear refractive index, $\tilde{R}_a(\Omega)$ and $\tilde{R}_b(\Omega)$ are the isotropic and anisotropic Raman response, respectively, in the frequency domain [47]. The co-polarized and orthogonal Raman gain is obtained from (7.4), and are given by $g_{Rx}(\Omega) = 2\,\text{Im}[\tilde{R}^{(3)}_{xxxx}(\Omega)]$, and $g_{Ry}(\Omega) = 2\,\text{Im}[\tilde{R}^{(3)}_{xyxy}(\Omega)]$ [7, 43–45]. In (7.1), $\hat{m}_{jk}(z,\Omega)$ is the noise operator due to the presence of a phonon reservoir, and $\hat{l}_j(z,\omega)$ represents the photon absorption reservoir. The $\hat{m}_{jk}(z,\Omega)$ noise operator accounts for the spontaneous Raman scattering process in optical fibers. The Raman noise operator is modeled as a collection of localized and independent harmonic oscillators with spectral weight proportional to the imaginary part of the third-order nonlinear response of the fiber. Moreover, it is assumed that the initial state of the phonons is in thermal equilibrium, with occupation number following

the Boltzman distribution [35, 37–39]. The $\hat{l}_j(z,\omega)$ operator describes the noise introduce by the fiber loss mechanism, through the coupling of the optical field with a thermal photon reservoir with a population following the Boltzman distribution, and spectral weight proportional to the fiber loss coefficient [35–38]. The noise operators satisfy the commutation relations [7, 35, 38]

$$\left[\hat{m}_{jk}(z,\Omega),\hat{m}^{\dagger}_{lm}(z',\Omega')\right] = 2\pi\delta(z-z')\delta(\Omega-\Omega')2\,\mathrm{Im}\left[\tilde{R}^{(3)}_{jklm}(\Omega)\right], \tag{7.5}$$

and

$$\left[\hat{l}_j(z,\omega),\hat{l}^{\dagger}_k(z',\omega')\right] = 2\pi\delta_{jk}\delta(z-z')\delta(\omega-\omega')\alpha_j(\omega). \tag{7.6}$$

The expectation values for the reservoirs are given by

$$\langle\hat{m}^{\dagger}_{jk}(z,\Omega)\hat{m}_{lm}(z',\Omega')\rangle = 2\pi\delta(z-z')\delta(\Omega-\Omega')2\,\mathrm{Im}\left[\tilde{R}^{(3)}_{jklm}(\Omega)\right](\mathcal{N}_{th}+\Theta(-\Omega)), \tag{7.7}$$

$$\langle\hat{l}^{\dagger}_j(z,\omega)\hat{l}_k(z',\omega')\rangle = 2\pi\delta_{jk}\delta(z-z')\delta(\omega-\omega')\alpha_j(\omega)\mathcal{N}_{th}, \tag{7.8}$$

where $\mathcal{N}_{th} = [\exp\{\hbar|\Omega|/(k_BT)-1\}]^{-1}$, k_B is the Boltzmann's constant, T is the temperature, and $\Theta(-\Omega)$ is the Heaviside step function.

In the following sections, we will use the formalism presented in (7.1)-(7.8), in order to quantify the impact of fiber absorption on the generation of quantum-correlated photon pairs through spontaneous FWM process.

7.2.1 Combined Effects of FWM, Raman Scattering and Losses

In the single-pump configuration, the FWM process can be decomposed in two different polarization schemes, co-polarized and orthogonal. In the co-polarized the signal and idler photons are generated parallel to the pump field, whereas in the orthogonal they are generated perpendicular to the pump [7, 44]. In this work, we focus only on the co-polarized scheme. We assume that, the fiber length is much shorter than the walk-off length. In that regime, we can apply the quasi-continuous wave approximation, described in sec. 7.4 of [12]. Moreover, we consider that the pump field is much more intense than the signal and idler waves, and remains undepleted, see for instance sec. 10.2 of [12]. Hence, the pump field can be treated classically, ignoring the pump quantum fluctuations [35]. Separating (7.1) into the frequency components, the evolution of the pump, signal and idler waves inside the fiber can be written as [35]

$$\bar{A}_p(z) = \bar{A}_p(0)\exp\left\{(i\beta_p z+\gamma P_x(0)z_e)-\frac{\alpha_p}{2}z\right\}, \tag{7.9a}$$

$$\frac{\partial\hat{A}_u(z)}{\partial z} = i\left(\beta_u+\frac{i}{2}\alpha_u+\gamma\xi(\Omega_{up})P_x(z)\right)\hat{A}_u(z)+i\gamma\eta(\Omega_{up})\bar{A}^2_p(z)\hat{A}^{\dagger}_v(z) + i\hat{m}(z,\Omega_{up})\bar{A}_p(z)+\hat{l}(z,\omega_u), \tag{7.9b}$$

where $\hat{A}_u(z) \equiv \hat{A}_x(z,\omega_u)$, $\beta_u \equiv \beta_x(\omega_u)$, $\hat{m}(z,\Omega) \equiv \hat{m}_{xx}(z,\Omega)$, $\hat{l}(z,\omega_u) \equiv \hat{l}_x(z,\omega_u)$, and $\alpha_u \equiv \alpha_x(\omega_u)$. In (7.9b) $u \neq v = s$ or i and represent the signal and idler fields, and $\Omega_{up} = \omega_u - \omega_p$. $\bar{A}_p(z)$ is such that $P_x(z) = |\bar{A}_p(z)|^2$ is the pump power, z_e is the effective length of the fiber at pump frequency at a given distance z, given by sec. 4.1 of [12]

$$z_e = \frac{1 - e^{-\alpha_p z}}{\alpha_p}. \tag{7.10}$$

In (7.9b), $\xi(\Omega_{up})$ and $\eta(\Omega_{up})$ are given by [7, 44]

$$\xi(\Omega_{up}) = 2 - f_R + f_R\left(\tilde{R}_a(\Omega_{up}) + \tilde{R}_b(\Omega_{up})\right), \tag{7.11a}$$

$$\eta(\Omega_{up}) = 1 - f_R + f_R\left(\tilde{R}_a(\Omega_{up}) + \tilde{R}_b(\Omega_{up})\right), \tag{7.11b}$$

In the most general case, when the pump power loss is taken into account, equation (7.9b) only have a power series solution [35]. In that case, after some mathematical manipulation, the evolution of the signal and idler annihilation operators at a given distance L in the fiber are given by

$$\hat{A}_u(L) = \mu_u(L,0)\hat{A}_u(0) + \nu_u(L,0)\hat{A}_v^\dagger(0) + \hat{N}(L,\omega_u) + \int_0^L dz\left(\hat{l}(z,\omega_u)\mu_u(L,z) + \hat{l}^\dagger(z,\omega_v)\nu_u(L,z)\right), \tag{7.12}$$

where

$$\hat{N}(L,\omega_u) = i\int_0^L \hat{m}(z,\Omega_{up})\left(\bar{A}_p(z)\mu_u(L,z) - \bar{A}_p^*(z)\nu_u(L,z)\right)dz. \tag{7.13}$$

In (7.12) and (7.13)

$$\mu_s(L,z) = e^{p(L,z,\omega_s)}\sum_{n=0} s_n(z)L_e^n(z), \tag{7.14a}$$

with $s_0 = 1$ and $a_0^* = 0$,

$$\nu_s(L,z) = e^{p(L,z,\omega_s)}\sum_{n=0} s_n(z)L_e^n(z), \tag{7.14b}$$

with $s_0 = 0$ and $a_0^* = 1$,

$$\mu_i(L,z) = e^{p(L,z,\omega_i)}\sum_{n=0} a_n(z)L_e^n(z), \tag{7.14c}$$

with $s_0 = 0$ and $a_0^* = 1$,

$$\nu_i(L,z) = e^{p(L,z,\omega_i)}\sum_{n=0} a_n(z)L_e^n(z), \tag{7.14d}$$

with and $s_0 = 1$ and $a_0^* = 0$.

In (7.14)

$$L_e(z) = (1 - \exp\{-\alpha_p(L-z)\})/\alpha_p, \tag{7.15}$$

and

$$p(L,z,\omega_u) = -\frac{\alpha_s + \alpha_i + 2i\Delta\beta}{4}(L-z) + i\left(\beta_u(L-z) + \gamma P_x(0)L_e(z)\right), \tag{7.16}$$

where $\Delta\beta$ is the phase-matching condition, given by [44]

$$\Delta\beta = \beta_3(\omega_p - \omega_0)(\omega_p - \omega_s)^2, \tag{7.17}$$

where β_3 is the third-order dispersion coefficient at zero-dispersion frequency, ω_0. In (7.14), the coefficients s_1 and a_1 are given by

$$s_1(z) = i\gamma P_x(z)\left(\xi(\Omega_{sp}) - 1\right)s_0 + i\gamma\eta(\Omega_{sp})\bar{A}_p^2(z)a_0^* - \frac{\alpha_s + \alpha_i + 2i\Delta\beta}{4}s_0, \tag{7.18a}$$

$$a_1^*(z) = -i\gamma P_x(z)\left(\xi^*(\Omega_{ip}) - 1\right)a_0^* - i\gamma\eta^*(\Omega_{ip})\bar{A}_p^{2*}(z)s_0 + \frac{\alpha_s + \alpha_i + 2i\Delta\beta}{4}a_0^*. \tag{7.18b}$$

For $n \geq 1$ the coefficients s_{n+1} and a_{n+1} are given by

$$s_{n+1}(z) = \frac{n}{n+1}\alpha_p s_n(z) - \frac{\alpha_s + \alpha_i + 2i\Delta\beta}{4(n+1)}s_n(z) + i\frac{\gamma P_x(z)}{n+1}\left(\xi(\Omega_{sp}) - 1\right)\left(s_n(z) - \alpha_p s_{n-1}(z)\right) + i\frac{\gamma\eta(\Omega_{sp})}{n+1}\bar{A}_p^2(z)\left(a_n^*(z) - \alpha_p a_{n-1}^*(z)\right), \tag{7.19a}$$

$$a_{n+1}^*(z) = \frac{n}{n+1}\alpha_p a_n^*(z) + \frac{\alpha_s + \alpha_i + 2i\Delta\beta}{4(n+1)}a_n^*(z) - i\frac{\gamma P_x(z)}{n+1}\left(\xi^*(\Omega_{ip}) - 1\right)\left(a_n^*(z) - \alpha_p a_{n-1}^*(z)\right) - i\frac{\gamma\eta^*(\Omega_{ip})}{n+1}\bar{A}_p^{2*}(z)\left(s_n(z) - \alpha_p s_{n-1}(z)\right). \tag{7.19b}$$

In the case of orthogonal FWM polarization scheme, where the pump evolves on the x fiber axis and the signal-idler photons are created on the y axis, it is necessary to change some parameters on the theoretical model present in (7.9)-(7.19). The loss and dispersion coefficients for the signal and idler waves should be replaced by $\alpha_x(\omega_u) \equiv \alpha_y(\omega_u)$, and $\beta_x(\omega_u) \equiv \beta_y(\omega_u)$, respectively. In this polarization scheme, the phase matching condition is given by [44]

$$\Delta\beta_y = 2\frac{\omega_p}{c}\delta n + \Delta\beta, \tag{7.20}$$

where δn is the refractive-index difference between the fiber two axis, and $\Delta\beta$ is given by (7.17). Moreover, for the orthogonal polarization scheme $\xi(\Omega_{up})$ and $\eta(\Omega_{up})$ should be replaced by [7]

$$\xi_y(\Omega_{up}) = 2(1 - f_R)/3 + f_R\left(\tilde{R}_a(0) + \tilde{R}_b(\Omega_{up})/2\right), \tag{7.21a}$$

$$\eta_y(\Omega_{up}) = (1 - f_R)/3 + f_R\tilde{R}_b(\Omega_{up})/2. \tag{7.21b}$$

7.3 Numerical Results

In this section, we show results for the evolution of the signal and idler photon fluxes with the frequency detuning between pump and signal field, in a medium with no-negligible loss coefficient. We also study theoretically the statistics of the individual signal and idler frequency modes in a loss media in terms of the second-order coherence function. Moreover, we analyze the impact of fiber absorption on the generation of quantum-correlated photon pairs through spontaneous FWM in optical fibers. We analyze the degree of quantum correlation in terms of the Cauchy-Schwarz inequality, and the degree of polarization entanglement in terms of the CHSH inequality. It also analyzed the visibility of the quantum-correlated photon source. Finally, we show results for the evolution of the true and accidental counting rates as a function of frequency detuning.

7.3.1 Photon-Flux and the Second-Order Coherence Function

In this section, we focus on the impact of the fiber absorption on the photon-flux generated through spontaneous FWM process. We also examine the statistics of the individual signal and idler frequency modes in a loss media in terms of the second-order coherence function, $g_u^{(2)}(0)$.

The photon-flux for the signal and idler fields is given by [7]

$$I_u(L,\tau) = \langle \hat{B}_u^{\dagger}(L,\tau)\hat{B}_u(L,\tau)\rangle = \frac{1}{(2\pi)^2}\iint d\omega_u d\omega_{u'} e^{i(\omega_u-\omega_{u'})\tau} H_u^*(\omega_u)H_u(\omega_{u'})\mathcal{F}_u(L), \quad (7.22)$$

where $\mathcal{F}_u(L) = \langle \hat{A}^{\dagger}(L,\omega_u)\hat{A}(L,\omega_{u'})\rangle$ is the photon-flux spectral density, $H_u(\omega_u)$ is a filter function centered at $\bar{\omega}_u$. For the signal field the filter central frequency is $\bar{\omega}_s$, whereas for the idler is $\bar{\omega}_i$, such that $2\omega_p = \bar{\omega}_s + \bar{\omega}_i$. For a filter bandwidth much smaller than its mid-frequency, $\Delta\omega_u = 2\pi\Delta\nu_u \ll \bar{\omega}_u$ [48], and according with (7.7), (7.8) and (7.12) the photon-flux can be written as

$$I_u(L,\tau) \approx \Delta\nu_u\, \mathcal{F}_{\bar{u}}(L). \quad (7.23)$$

In (7.23) $\Delta\nu_u = 1/(2\pi)\int d\omega_u |H_u(\omega_u)|^2$, and the photon-flux spectral density $\mathcal{F}_u(L)$ is calculated at frequency $\bar{\omega}_u$

$$\mathcal{F}_{\bar{u}}(L) = \langle \hat{A}^{\dagger}(L,\bar{\omega}_u)\hat{A}(L,\bar{\omega}_u)\rangle = |\nu_{\bar{u}}(L,0)|^2 + \alpha_{\bar{u}}\mathcal{N}_{\bar{u}}\int_0^L dz|\mu_{\bar{u}}(L,z)|^2$$
$$+\alpha_{\bar{v}}(\mathcal{N}_{\bar{v}}+1)\int_0^L dz|\nu_{\bar{u}}(L,z)|^2 + (\mathcal{N}_{\bar{u}p}+\Theta_{\bar{u}p})g_R(\bar{\Omega}_{up})\int_0^L dz\left|\bar{A}_p(z)\mu_{\bar{u}}(L,z) - \bar{A}_p^*(z)\nu_{\bar{u}}(L,z)\right|^2, \quad (7.24)$$

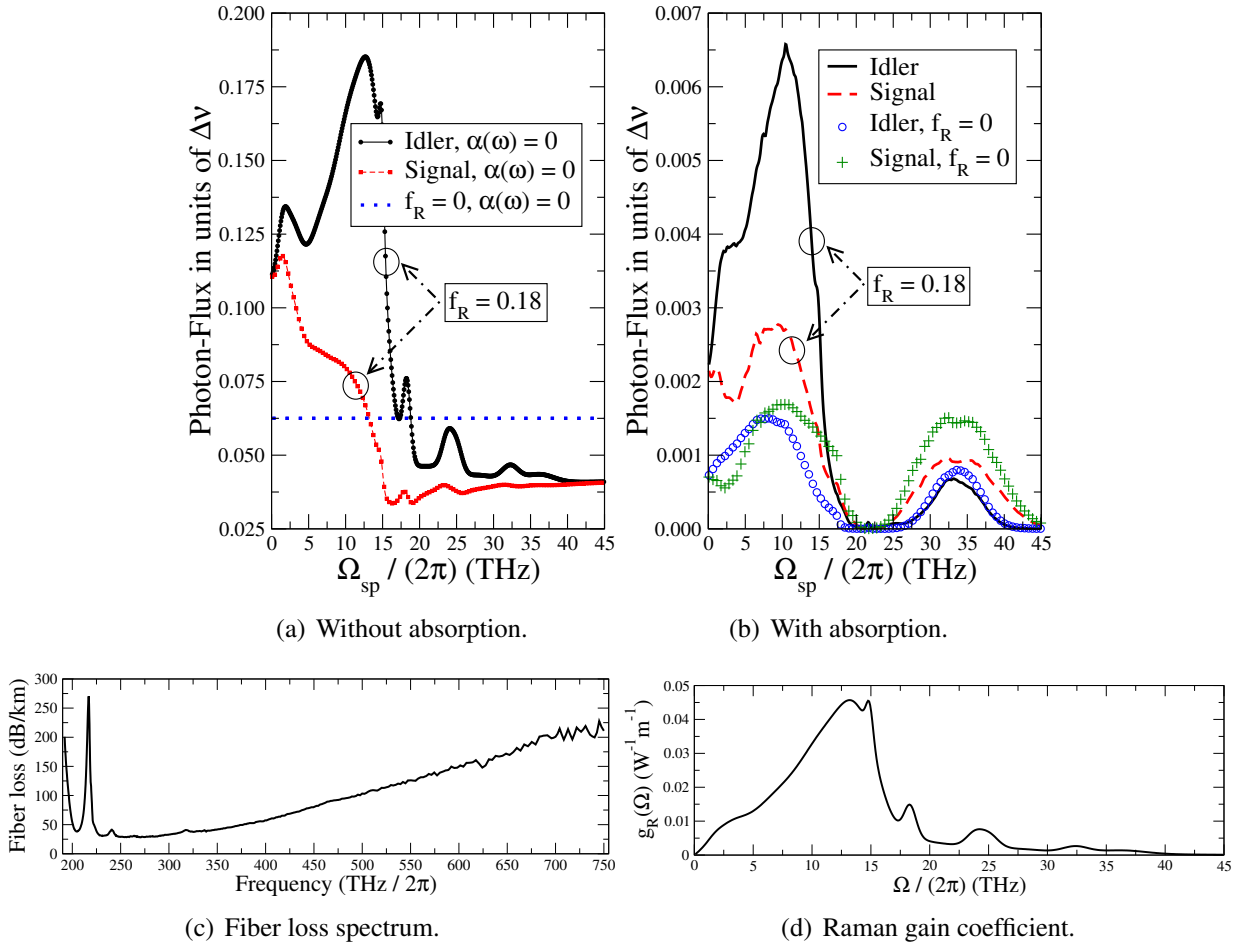

(a) Without absorption.

(b) With absorption.

(c) Fiber loss spectrum.

(d) Raman gain coefficient.

Figure 7.1: (a) and (b): Idler and signal photon-flux per unit of filter bandwidth, $\Delta\nu$, as a function of the frequency separation between pump and signal fields. In both plots when $f_R = 0$ the photons are generated only by the FWM process; (c): Fiber loss spectrum [15]. In (a) we do not consider the fiber loss, $\alpha(\omega) = 0$, whereas in (b) the fiber loss present in (c) is taken into account; (d) Raman gain coefficient [46].

where $\bar{u} \equiv \bar{\omega}_u$, $\Theta_{\bar{u}p} \equiv \Theta(-\bar{\Omega}_{up})$, $\bar{\Omega}_{up} = \bar{\omega}_u - \omega_p$, and

$$\mathcal{N}_{\bar{u}} \equiv [\exp\{\hbar|\bar{\omega}_u|/(k_B T) - 1\}]^{-1} \tag{7.25a}$$

$$\mathcal{N}_{\bar{u}p} \equiv [\exp\{\hbar|\bar{\Omega}_{up}|/(k_B T) - 1\}]^{-1} \tag{7.25b}$$

In Fig. 7.1, we present the photon-flux, given by (7.23), as a function of frequency detuning between pump and signal fields, Fig. 7.1(a) and Fig. 7.1(b). In the figure it is also presented the fiber loss spectrum, Fig. 7.1(c), and the Raman gain coefficient, Fig. 7.1(d). The silica based high nonlinear photonic crystal fiber parameters are $\gamma = 95$ W^{-1}km^{-1}, zero-dispersion wavelength $\lambda_0 = \lambda_p = 1257.45$ nm, $\beta_3 = -0.356$ ps^3/km, $\alpha_p = 37.2$ dB/km [15, 49], $\Delta\beta = 0$, $T = 300$ K,

length $L = 600 > 1/\alpha_p$ m, and $P_x(0) = 22.7$ mW such that $\gamma P_x(0) z_e = 0.25$. When $\alpha(\omega) = 0$ we obtain $P_x(0) = 4.4$ mW due to the fact that $z_e = L$. These values were obtained from the fiber manufacturer. We use this fiber in order to be able to operate in the $\alpha(\omega)L \gg 1$ regime. The fiber Raman response function, $\tilde{R}_a(\Omega_{up}) + \tilde{R}_b(\Omega_{up})$, was taken from [46], and the fiber loss spectrum was obtained from NKT Photonics [15]. Moreover, we assume an identical rectangular shape for both signal and idler optical filters.

Figure 7.1(a) and Fig. 7.1(b) show the signal and idler photon-fluxes, given by (7.23), as a function of frequency detuning between pump and signal fields. In Fig. 7.1(a), we do not consider the fiber loss, $\alpha(\omega) = 0$ in (7.23), whereas in Fig. 7.1(b), the fiber loss spectrum present in Fig. 7.1(c) is taken into account. In both figures, Fig. 7.1(a) and Fig. 7.1(b), when $f_R = 0$ the Raman scattering process is ignored. It can be seen in Fig. 7.1(a) and in Fig. 7.1(b), that the wavelength dependence of the fiber loss coefficient changes significantly the spectrum of both signal and idler photon-fluxes. Results also show that the fiber loss reduces the photon-flux due to the fiber absorption of the signal and idler photons, and due to the fact that the pump field, given by (7.9a), is attenuated during the propagation on the fiber. When $20 < \Omega_{sp}/(2\pi) < 25$ (THz) the photon-flux for signal and idler fields is almost null. This is due to the fact that, the idler frequency corresponds to the peak on the spectrum of the fiber loss presented on Fig. 7.1(c). According with (7.24) the signal photon-flux is proportional to the idler absorption coefficient. Since $\alpha_{\bar{i}} \approx 300$ dB/km this leads to an almost null photon-flux for the signal wave. This mean that, the number of photons generated in the signal field depends on the fiber absorption coefficient on the idler wave. The opposite is also true (7.24).

The statistics of the individual signal and idler frequency modes in a loss medium can be assessed through the analysis of the second-order coherence function defined as [50, 51]

$$g_u^{(2)}(0) = \frac{\iint_{t_0}^{t_0+T_0} \langle : I_u(L,t) I_u(L,t') : \rangle dt\, dt'}{\iint_{t_0}^{t_0+T_0} I_u(L,t)\, I_u(L,t') dt\, dt'}, \tag{7.26}$$

where $I_u(L,\tau) = \hat{B}_u^\dagger(L,t)\hat{B}_u(L,t)$, :: denotes operator normal ordering, and T_0 is the time detection window. Using (7.12), (7.22), and (7.23)

$$\begin{aligned} \langle : I_u(L,t) I_u(L,t') : \rangle &= \left| \langle \hat{B}_u^\dagger(L,t') \hat{B}_u(L,t) \rangle \right|^2 + I_u(L,t)\, I_u(L,t') \\ &= \left| \phi_u(t,t') \right|^2 |\mathcal{F}_{\bar{u}}(L)|^2 + (\Delta\nu_u\, \mathcal{F}_{\bar{u}}(L))^2, \end{aligned} \tag{7.27}$$

which represents the self-correlation amplitude for the signal or idler waves. In (7.27), $\mathcal{F}_{\bar{u}}(L)$ is given by (7.24) and

$$\phi_u(t,t') = \frac{1}{2\pi}\iint d\omega_u d\omega_{u'} H_u^*(\omega_u) H_u(\omega_{u'}) e^{i(\omega_u t' - \omega_{u'} t)}. \tag{7.28}$$

Finally, the second-order coherence function is given by

$$g_{\bar{u}}^{(2)}(0) = 1 + \frac{\iint |H_u(\omega_u)|^2 |H_u(\omega_{u'})|^2 \left(\frac{2-2\cos\left(T_0(\omega_u - \omega_{u'})\right)}{(\omega_u - \omega_{u'})^2} \right) d\omega_u d\omega_{u'}}{(\Delta\omega_u T_0)^2}. \tag{7.29}$$

From (7.29) we can see that, the absorption reservoir does not change the statistics of the signal or idler fields. However, depending of the value of $\Delta\omega_u T_0$ we obtain different statistical regimes for the signal and idler fields. If $\Delta\omega_u T_0 \ll 1$ we obtain $g_{\bar{u}}^{(2)}(0) = 2$, which represents a thermal statistics. However, if $\Delta\omega_u T_0 \gg 1$ we obtain $g_{\bar{u}}^{(2)}(0) = 1$, a Poissonian distribution. For all the other values of $\Delta\omega_u T_0$ the second-order coherence function varies between $1 < g_{\bar{u}}^{(2)}(0) < 2$, which represents a multithermal statistics. This is in-line with previous reported experimental works, see for instance [52, 53]

7.3.2 Two-Photon Correlation

In this section, we analyze the impact of fiber absorption on the generation of quantum-correlated photon pairs through spontaneous FWM in optical fibers. We analyze the degree of quantum correlation in terms of the Cauchy-Schwarz inequality, and the degree of polarization entanglement in terms of the CHSH inequality. A violation of the Cauchy-Schwarz inequality, given by (7.30), determines the nonclassical nature of the photons, whereas a violation of the CHSH inequality, given by (7.36), represents the nonlocality of light [54, 55].

The Cauchy-Schwarz inequality can be written as [54, 56]

$$\mathcal{G}^{CS}(\tau) = \frac{G_{(si)}^{(2)}(\tau)}{\sqrt{G_s^{(2)}(\tau)\, G_i^{(2)}(\tau)}} \leq 1, \tag{7.30}$$

where the nonclassical regime is obtained when $\mathcal{G}^{CS}(\tau) > 1$. This mean that, the photons of different modes have a higher correlation than the photons of the same mode. A larger value of $\mathcal{G}^{CS}(\tau)$ corresponds to a larger degree of nonclassical correlation. In (7.30), $G_{(si)}^{(2)}(\tau)$ is the cross-correlation between signal and idler frequency modes, given by

$$G_{(si)}^{(2)}(\tau) = \langle \hat{B}_i^\dagger(L,t)\hat{B}_s^\dagger(L,t+\tau)\hat{B}_s(L,t+\tau)\hat{B}_i(L,t)\rangle = \left|\langle \hat{B}_s(L,t+\tau)\hat{B}_i(L,t)\rangle\right|^2 + I_i(L,t)\, I_s(L,t+\tau), \tag{7.31}$$

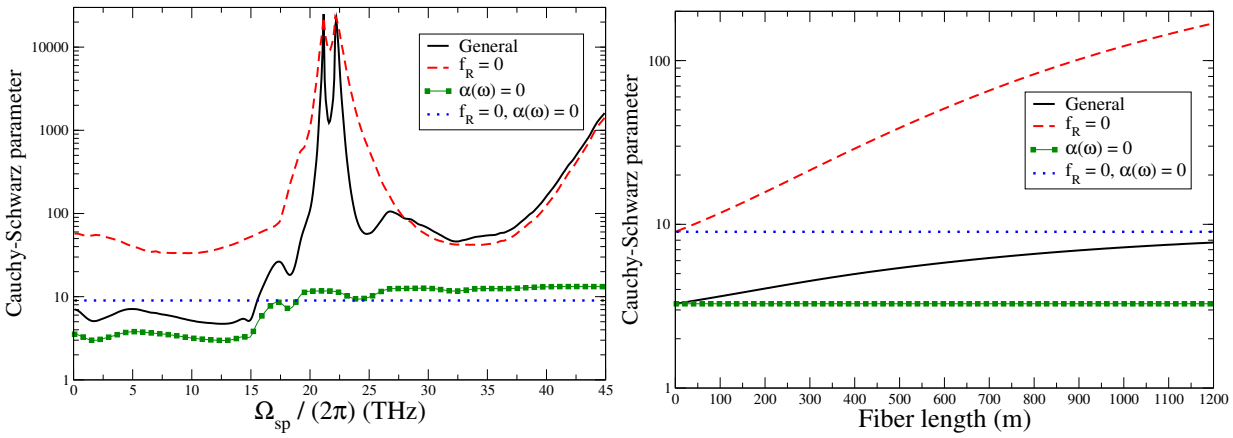

(a) (b)

Figure 7.2: Cauchy-Schwarz correlation parameter, $\mathcal{G}^{CS}(0)$, given by (7.30) as a function of frequency detuning, plot (a), and as a function of fiber length, plot (b). In plot (b) $\Omega_{sp}/(2\pi) = 3$ (THz). The fiber parameters used are equal to the ones used in Fig. 7.1.

where, according with (7.7), (7.8) and (7.12)

$$\left|\langle \hat{B}_s(L,t+\tau)\hat{B}_i(L,t)\rangle\right|^2 \approx |\phi_c(\tau)|^2\,|\mathcal{F}^c(L,\bar{\omega}_s,\bar{\omega}_i)|^2\,. \tag{7.32}$$

In (7.32), $\phi_c(\tau)$ is given by

$$\phi_c(\tau) = \frac{1}{2\pi}\int d\omega H_s(\omega-\bar{\omega}_s)H_i(\bar{\omega}_s-\omega)e^{-i\omega\tau}, \tag{7.33}$$

and

$$\begin{aligned}\mathcal{F}^c(L,\bar{\omega}_s,\bar{\omega}_i) = \langle \hat{A}(L,\bar{\omega}_s)\hat{A}(L,\bar{\omega}_i)\rangle &= \mu_{\bar{s}}(L,0)\nu_{\bar{i}}(L,0) + \alpha_{\bar{s}}(\mathcal{N}_{\bar{s}}+1)\int_0^L dz\mu_{\bar{s}}(L,z)\nu_{\bar{i}}(L,z)\\ &+\alpha_{\bar{i}}\mathcal{N}_{\bar{i}}\int_0^L dz\nu_{\bar{s}}(L,z)\mu_{\bar{i}}(L,z) - (\mathcal{N}_{\bar{i}p}+\Theta_{\bar{i}p})g_R(\bar{\Omega}_{ip})\\ &\times\int_0^L \left(\bar{A}_p(z)\mu_{\bar{s}}(L,z)-\bar{A}_p^*(z)\nu_{\bar{s}}(L,z)\right)\left(\bar{A}_p(z)\mu_{\bar{i}}(L,z)-\bar{A}_p^*(z)\nu_{\bar{i}}(L,z)\right)dz.\end{aligned} \tag{7.34}$$

The $G_u^{(2)}(\tau)$ coefficient is the self-correlation amplitude, and it is given by (7.27), with $t' = t+\tau$. From (7.23), (7.33) and (7.34) we can evaluate the true and the accidental coincidences counting

rates, given respectively by [7]

$$R_{\text{pair}} = \int_0^{\tau_c} |\phi_c(\tau)|^2 |\mathcal{F}^c(L, \bar{\omega}_s, \bar{\omega}_i)|^2 d\tau, \tag{7.35a}$$

$$R_{\text{acc}} = \int_0^{\tau_c} (\Delta\nu)^2 \mathcal{F}_{\bar{s}}(L) \mathcal{F}_{\bar{i}}(L) d\tau, \tag{7.35b}$$

where τ_c is the coincidence time window.

Figure 7.2 shows the Cauchy-Schwarz correlation parameter, $\mathcal{G}^{CS}(0)$, given by (7.30), as a function of the frequency detuning between pump and signal, Fig. 7.2(a), and as a function of fiber length, Fig. 7.2(b). It can be seen in Fig. 7.2(a) that the fiber loss increases the degree of non-classical correlation between signal and idler photons. Nevertheless, the presence of the Raman scattering process tends to degrade the photon pair correlation, since the Raman scattering process generates uncorrelated signal and idler photons. This degradation can be seen in Fig. 7.2(a) where $\mathcal{G}^{CS}(0)$ tends to take a high value when $f_R = 0$. When $20 < \Omega_{sp}/(2\pi) < 25$ (THz) the $\mathcal{G}^{CS}(0)$ parameter reaches its maximum value, which corresponds to the minimum of the signal and idler photon-fluxes, see Fig. 7.1(b). That maximum on the $\mathcal{G}^{CS}(0)$ parameter is due to the decrease on the accidental coincidences, given by $I_i(L,t)\, I_s(L,t+\tau)$ in (7.31). That term is almost null when $20 < \Omega_{sp}/(2\pi) < 25$ (THz), due to the fact that $\alpha_{\bar{i}}$ reaches its maximum value. It can be seen in Fig. 7.2(b) that the $\mathcal{G}^{CS}(0)$ parameter increases with the increase of the fiber length. This is due to the fact that the coefficient $\alpha(\omega)L$ increases, which leads to a decrease on the accidental coincidences, and due to the increase on the fiber input pump power with the increase of the fiber length, since we use $\gamma P_x(0) z_e = 0.25$. Results also show that for fiber lengths $L > 800$ m, the scenario where we consider fiber loss and Raman scattering is almost equal to the one where $f_R = 0$ and $\alpha(\omega) = 0$.

In optical fibers, the spontaneous FWM process can be used to create polarization entangled states through a fiber loop [57]. The fiber loop give rises to two co-polarized FWM processes, one clockwise and other counterclockwise, creating a polarization entangled Bell state of $|\Phi^{\pm}\rangle = (|H\rangle_s |H\rangle_i \pm |V\rangle_s |V\rangle_i)/\sqrt{2}$, where H and V denote horizontal and vertical linear polarizations, respectively [23, 57]. The degree of quantum entanglement can be tested with the CHSH form of the Bell's inequality [55]. The violation of CHSH inequality in optical fibers using spontaneous FWM process has been reported in several experimental works [17, 23–26, 58]. According with [7], the CHSH parameter $\mathcal{S}(\tau)$ is given by

$$\mathcal{S}(\tau) = 2\sqrt{2} V(\tau) \leq 2, \tag{7.36}$$

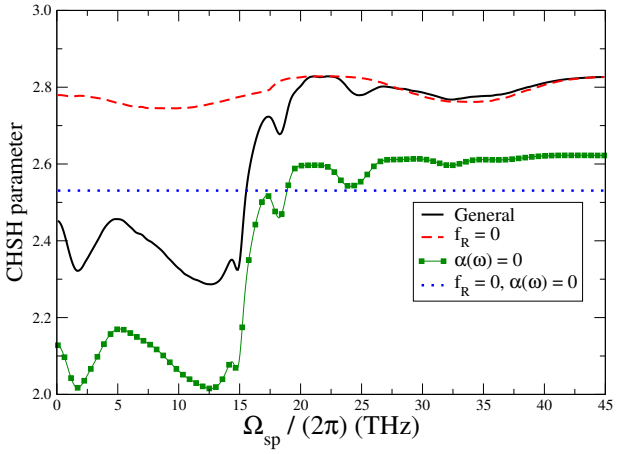

(a)

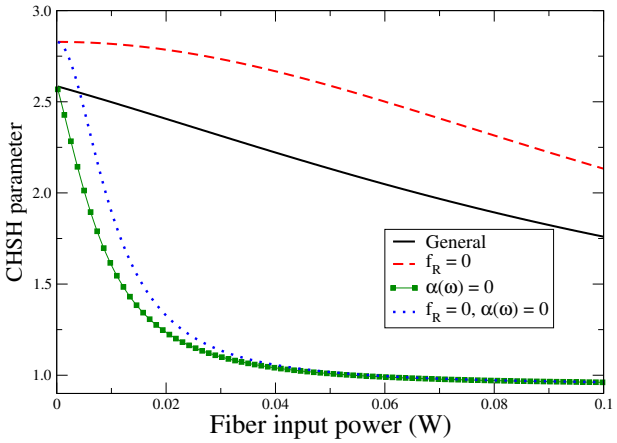

(b)

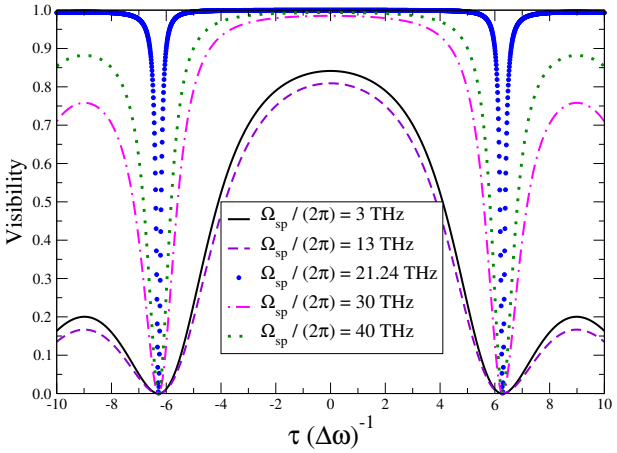

(c)

Figure 7.3: CHSH parameter, $\mathcal{S}(0)$, given by (7.36) as a function of frequency detuning, plot (a), and as a function of fiber input pump power, plot (b). In plot (b) $\Omega_{sp}/(2\pi) = 3$ (THz). (c) Visibility, $V(\tau)$, given by (7.37) as a function of time delay between signal-idler photon pairs. In (c) the signal and idler optical filters are assumed to have a bandwidth of $\Delta\nu = 100$ GHz. The fiber parameters used are equal to the ones used in Fig. 7.1.

where $V(\tau)$ is the fringe pattern visibility, given by

$$V(\tau) = \frac{G^{(2)}_{(si)}(\tau) - I_i(L,t)\, I_s(L,t+\tau)}{G^{(2)}_{(si)}(\tau) + I_i(L,t)\, I_s(L,t+\tau)}, \tag{7.37}$$

where I_u and $G^{(2)}_{(si)}$ are given by (7.22) and (7.31), respectively. For more details about the derivation of CHSH parameter see Appendix 7.A. A violation of the CHSH inequality happens when $\mathcal{S}(\tau) > 2$.

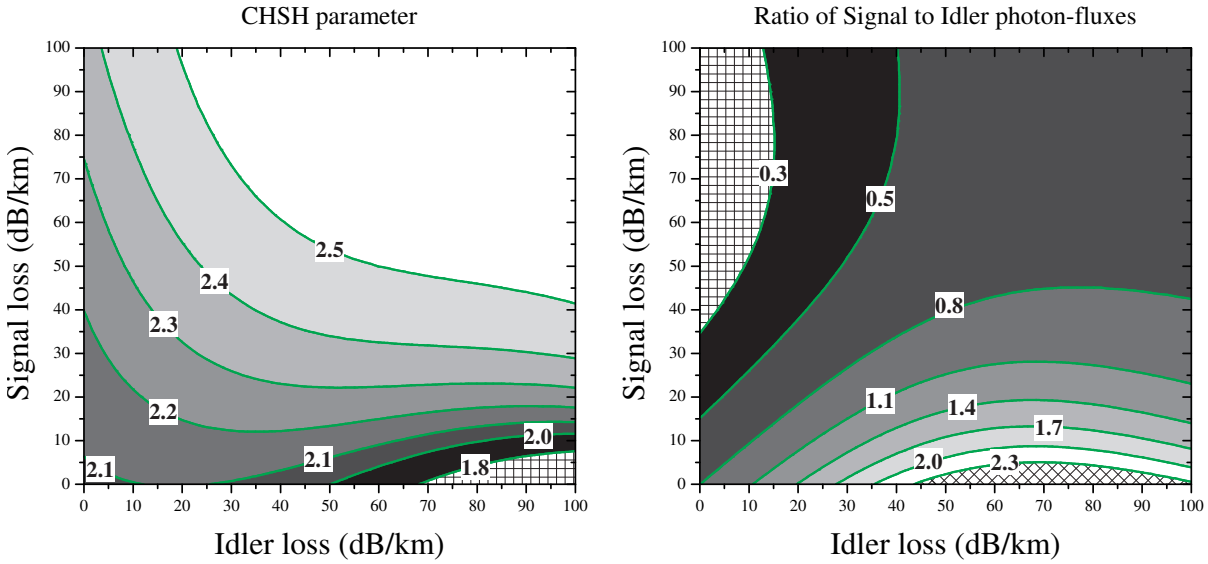

(a) (b)

Figure 7.4: (a) Contour plot for the CHSH parameter, $\mathcal{S}(0)$, given by (7.36) as a function of idler loss, $\alpha_{\bar{i}}$, and as a function of signal loss, $\alpha_{\bar{s}}$. (b) Contour plot for the ratio $I_s(L,0)/I_i(L,0)$, given by (7.23) as a function of $\alpha_{\bar{i}}$ and $\alpha_{\bar{s}}$. In the figure we use $\Omega_{sp}/(2\pi) = 3$ (THz). The fiber parameters used are equal to the ones used in Fig. 7.1.

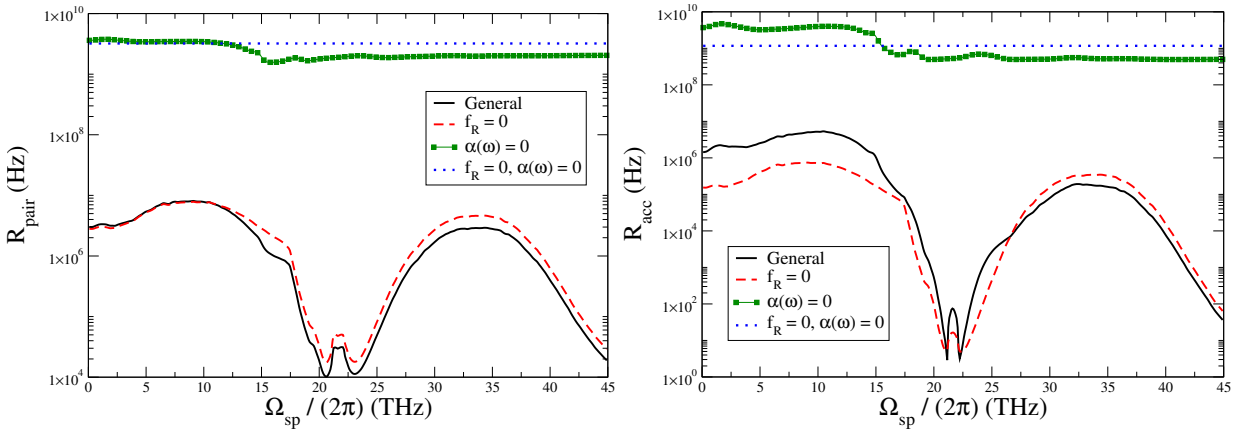

(a) (b)

Figure 7.5: Evolution of true, plot (a), and accidental, plot (b), coincidences counting rates given by (7.35a) and (7.35b), respectively, as a function of frequency detuning between pump and signal fields. In both plots we have used $\Delta\nu = 100$ GHz, and $\tau_c = 30$ ps. The fiber parameters used are equal to the ones used in Fig. 7.1.

Figure 7.3 shows the CHSH parameter, $\mathcal{S}(0)$, given by (7.36) as a function of frequency detuning, Fig. 7.3(a), and as a function of fiber input pump power, Fig. 7.3(b). In Fig. 7.3(c) we present the fringe pattern visibility associated to the CHSH parameter, given by (7.37), as a function of the time delay between signal and idler waves, for five different values of frequency detuning between pump and signal fields. Results present in Fig. 7.3(a) show that, in general the fiber loss has a positive impact on the degree of quantum entanglement, since the value of $\mathcal{S}(0)$ parameter increase in the presence of loss. In particularly, in the range 20-45 (THz) $\mathcal{S}(0)$ is close to the maximum value of $2\sqrt{2}$, even considering both fiber loss and Raman scattering. For $\Omega_{sp}/(2\pi) < 20$ (THz) the Raman scattering process reduces the value of $\mathcal{S}(0)$. Results present in Fig 7.3(b) show that an increase on the fiber input pump power completely degrades the degree of quantum entanglement. This is due to an increase on the probability of multiphoton generation, since an increase on the pump power leads to an increase in the stimulated FWM and Raman scattering processes [7]. In that scenario, the individual signal and idler photon-fluxes are dominant over the signal-idler photon pairs. Results present in Fig. 7.3(c) show that $V(\tau)$ is close to 1 for $\Omega_{sp}/(2\pi) \approx 21$ (THz), which correspond to the maximum on the spectrum of the fiber loss presented on Fig. 7.1(c). For $\Omega_{sp}/(2\pi) < 21$ (THz), the visibility decreases due to the presence of uncorrelated Raman scattered photons. Due to that fact, the minimum on the visibility is for $\Omega_{sp}/(2\pi) \approx 13$ (THz), the peak of Raman gain, see Fig. 7.1(d). For $\Omega_{sp}/(2\pi) > 21$ (THz), we obtain again $V(0) \approx 1$, because in that frequency range $\alpha(\omega)L \gg 1$.

Figure 7.4 shows the contour plot for the $\mathcal{S}(0)$ parameter, Fig. 7.4(a), and for the ratio of signal to idler photon-fluxes $I_s(L,0)/I_i(L,0)$, Fig. 7.4(b), as a function of idler, $\alpha_{\bar{i}}$, and signal, $\alpha_{\bar{s}}$, fiber loss coefficients. It can be seen in Fig. 7.4(a) that, a strong violation of the CHSH inequality is obtained for high values of both signal and idler loss coefficients. Results also show that, if the signal loss is almost negligible and the idler loss is very high it is not observed a violation of the CHSH inequality. This is due to the fact that, the ratio of signal to idler photon fluxes, $I_s(L,0)/I_i(L,0)$, is much higher than one, see Fig 7.4(b). Otherwise, when the signal loss coefficient is high and the idler loss is almost null, we observe a violation of the CHSH inequality, according with the result present in Fig. 7.4(a). In that case, $I_s(L,0)/I_i(L,0)$ is less than one, as can be seen in Fig. 7.4(b). From Fig. 7.4(a) and Fig. 7.4(b), we can see that a maximum on $\mathcal{S}(0)$ value happens when $I_s(L,0)/I_i(L,0)$ lies between 0.5 and 0.8, with $\alpha_{\bar{s}} > 45$ dB/km.

Figure 7.5 shows the true, Fig. 7.5(a), and accidental, Fig. 7.5(b), coincidences counting rates given by (7.35a) and (7.35b), respectively, as a function of frequency detuning between pump and signal. It can be seen in Fig. 7.5 that the fiber loss decreases significantly the photon

counting rate. However, that decrease is more pronounced on the rate of accidental coincidence counts, Fig. 7.5(b). Assuming a lossless medium the maximum true-to-accidental ratio (TAR) is around 4 ($R_{\text{pair}} \approx 2$ GHz and $R_{\text{acc}} \approx 0.5$ GHz). When the loss is considered the maximum value for the TAR is approximately 8000 ($R_{\text{pair}} \approx 23$ kHz and $R_{\text{acc}} \approx 3$ Hz), see Fig. 7.5(a) and Fig. 7.5(b), and see also Fig. 7.1(c). In this case most of generated photons are signal-idler pairs generated through spontaneous FWM. For $\Omega_{sp}/(2\pi) < 20$ (THz) the Raman scattering process is the main source of uncorrelated photons, which leads to a higher increase on R_{acc} than on R_{pair}. According with the results present in Fig. 7.5, photon pairs generated through FWM in the regime $\alpha(\omega)L \gg 1$ are suitable to be used in sources of entangled photon pairs for quantum key distribution systems, since the expected TAR value can go up to 8000, which is much higher than the values in waveguides with $\alpha(\omega)L \ll 1$, typical measured values are of the order of 10 [4, 17, 21].

7.4 Experimental Setup and Results

In order to test experimentally the CHSH inequality, we implement in the laboratory a setup capable of measure the coincidence counting rate between signal and idler photon pairs obtained through spontaneous FWM process. The experimental setup was implemented by Á. J. Almeida, L. M. Martins, and S. R. Carneiro [10, 11]. Figure 7.6 shows the experimental setup used in the laboratory.

In order to generate a polarization entangled state, we place a highly nonlinear fiber (HNLF) in a loop configuration with a polarization beam splitter (PBS), as shown in Fig. 7.6. At PBS input a pump pulse with a 45° linear polarization state is divided into horizontal P_H and vertical P_V polarization components with equal power. Each pump polarization component generates signal and idler photon pairs, $|H\rangle_s|H\rangle_i$ in clockwise direction and $|V\rangle_s|V\rangle_i$ in counterclockwise direction. At PBS output, we obtain a superposed state of the two product states $|H\rangle_s|H\rangle_i$ and $|V\rangle_s|V\rangle_i$ [23]. After removing the pump photons at PBS output we obtain the entangled state [23]

$$|\Psi\rangle = \frac{1}{\sqrt{2}}\left(|H\rangle_s|H\rangle_i + |V\rangle_s|V\rangle_i\right), \tag{7.38}$$

In Fig. 7.6 a pump field from a tunable laser source (TLS) centered at 1550.918 nm, with a full width at half maximum of 830 ps and a repetition rate of 2.2 MHz passes through an optical filter, F_p, in order to eliminate the laser sidebands. At filter output the pump field passes through a polarization controller (PC) in order to align the pump photons polarization with the

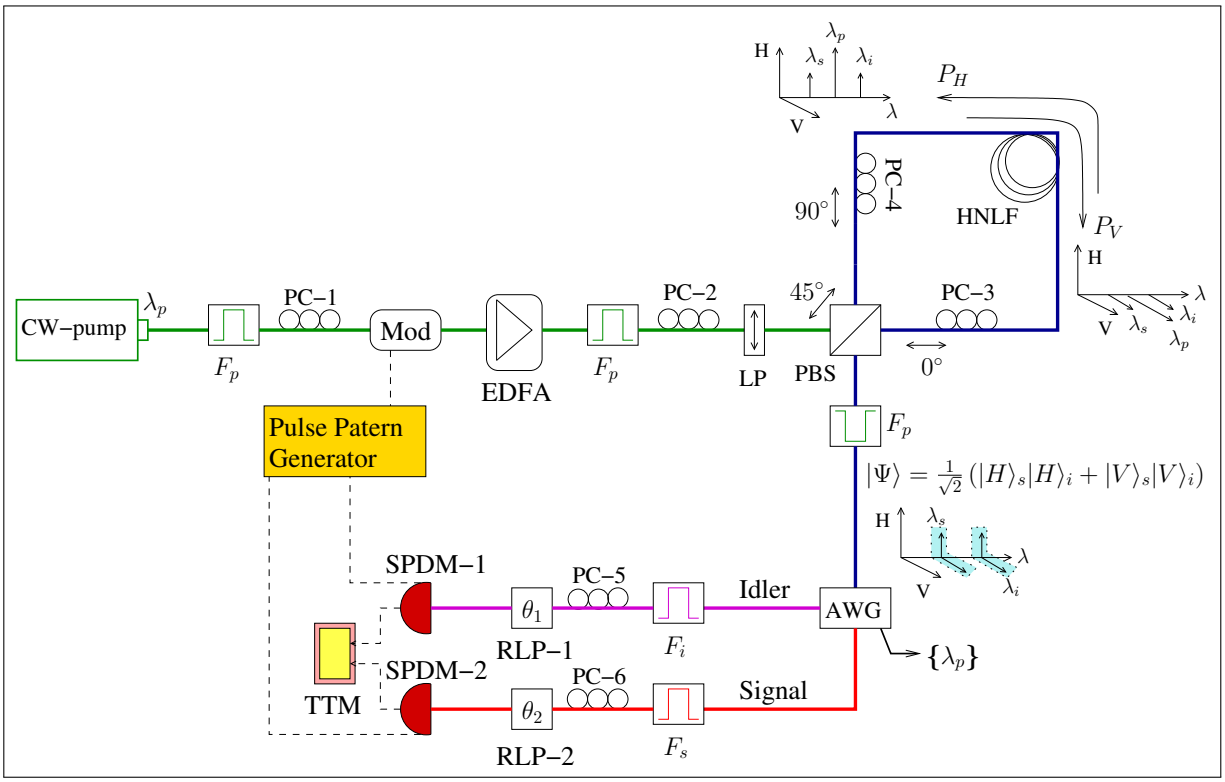

Figure 7.6: Experimental setup used to generate polarization-entangled photon pairs through spontaneous FWM process in a fiber loop, and test the CHSH inequality. The dashed lines represents electrical signals and the solid lines the optical path. Details of the experiment are presented in the text.

$LiNbO_3$ crystal intensity modulator (Mod). At the output of the Mod the pump field is amplified using an erbium doped fiber amplifier (EDFA). The amplified spontaneous emission (ASE) in the EDFA output was eliminated using a 100 GHz flat fixed optical filter, F_p. The state of polarization of the pump pulses was adjusted to 45° linear polarization using a PC and a linear polarizer (LP). Then, the pump pulses are launched into the loop which consists of a PBS, a 150 m long HNLF with a nonlinear coefficient, $\gamma \approx 10.5$ $W^{-1}km^{-1}$, and a zero-dispersion wavelength $\lambda_0 = 1550$ nm, and two PCs. The two PCs inside the loop are used to perfect align the generated signal/idler photon pairs inside the HNLF with the PBS output port. The pump power at the input of each arm of the HNLF was 2.2 mW. At the loop output the pump photons are eliminated, using a band-reject optical filter, F_p. Then, the idler and signal photons go into an arrayed waveguide grating (AWG), with a 100 GHz channel spacing, which separates the signal and idler photons. The AWG channels used in the experimental setup were centered at wavelengths of $\lambda_s = 1547.715$ nm and $\lambda_i = 1554.134$ nm for the signal and idler, respectively.

The output signal and idler photons from the AWG were filtered with a cascade of flat-top fixed optical filters centered at λ_s and λ_i (represented in Fig. 7.6 with F_s and F_i, respectively) to further suppress the pump photons. After, the signal and idler photons passes through a PC (PC-1 for the idler field and PC-2 for the signal wave) in order to adjust the polarization states of the signal and idler photons so that the two optical fields experienced the same polarization change after they were separated by the AWG. Each individual signal and idler waves was lead into a rotatable linear polarizer (RLP) (RLP-1 and RLP-2) and was detected with a single photon detector module (SPDM) from IdQuantique. The SPDMs were operating in a gated Geiger mode [59]. The SPDM-1 (id201) has a dark count probability per time gate, $t_g = 2.5$ ns, of $P_{dc} < 5 \times 10^{-6}$ ns^{-1}, and a quantum detection efficiency, $\eta_D \sim 10\%$ [60]. The SPDM-2 (id200) has a dark count probability per time gate, $t_g = 2.5$ ns, of $P_{dc} < 5 \times 10^{-5}$ ns^{-1}, and a quantum detection efficiency, $\eta_D \sim 10\%$ [61]. In order to avoid after-pulses, a 10 μs dead-time was applied to both detectors. The electric signals from the SPDMs were input into a time tag module (TTM) for coincidence measurements. The TTM worked in a continuous mode, with a time resolution of 82.3 ps. In order to demonstrate polarization entanglement of the generated photon pairs experimentally, we inserted a RLP, before each SPDM, as shown in Fig. 7.6.

We measured the coincidence rate $C(\theta_1, \theta_2)$ for 16 combinations of polarizer settings (θ_1 = -45°, 0°, 45°, 90°; θ_2 = -22.5°, 22.5°, 67.5°, 112.5°) in order to obtain the $\mathcal{S}(0)$ value of the CHSH inequality [55]. Any realistic theory must satisfy the condition $|\mathcal{S}(0)| \leq 2$. In order to

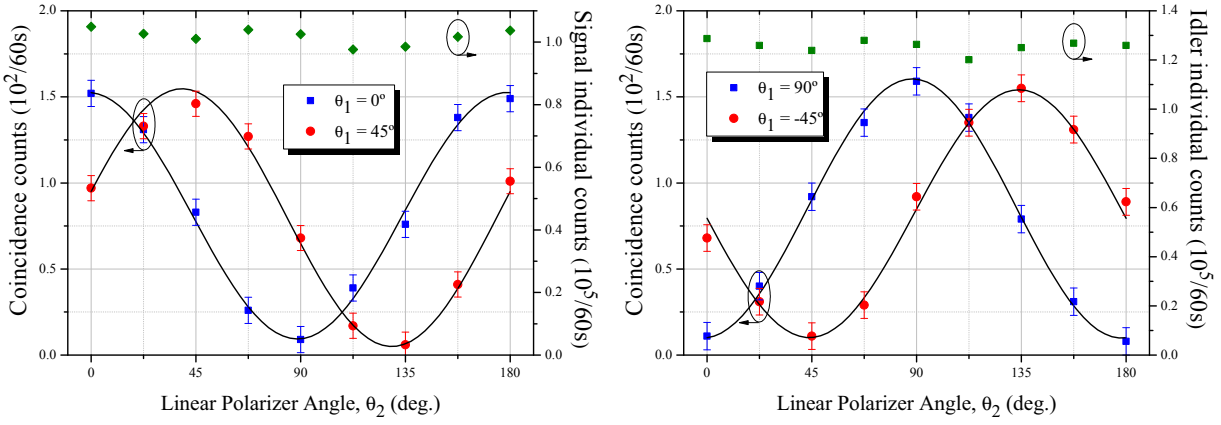

Figure 7.7: Coincidence and single counts as a function of θ_2. In plot (a) we use θ_1 = 0°, 45°, whereas in plot (b) we use θ_1 = 90°, -45°. The solid curve is a sinusoidal fit to the experimental data. Error bars are a 5% deviation in relation to the maximum value, in each case.

Table 7.1: Measured correlation coefficients required for the CHSH inequality.

$E(\theta_1,\theta_2)$	(0°, 22.5°)	(0°, 67.5°)	(45°, 22.5°)	(45°, 67.5°)
Value	0.5460	-0.6545	0.6962	0.5732
Error	0.0396	0.0445	0.0469	0.0418

verify the violation of CHSH inequality, it should be found that $|\mathcal{S}(0)| > 2$ [55]. In the CHSH inequality, the parameter $\mathcal{S}(0)$ is defined as [62]

$$\mathcal{S}(0) = |E(\theta_1,\theta_2) - E(\theta_1,\theta_2') + E(\theta_1',\theta_2) + E(\theta_1',\theta_2')|, \tag{7.39}$$

where $E(\theta_1,\theta_2)$ is the polarization correlation coefficient, and $\theta_1' = \theta_1 + 90°$ and $\theta_2' = \theta_2 + 90°$ [62]. More details about the evaluation of $E(\theta_1,\theta_2)$ can be found in [10].

In Fig. 7.7, we present coincidence and single counts detected over 60 s, varying the RLP-2 (θ_2), while the RLP-1 (θ_1) is fixed for values 0°, 45° and 90°, -45°. Results for coincidence counts show that our source produces entangled photon pairs with a fringe visibility higher than 86%. From the results presented in Fig. 7.7, we can conclude that our method successfully generated polarization entangled photon pairs. In Fig. 7.7(a) we present signal single counts, whereas in Fig. 7.7(b) it is presented the idler single counts. Results show that that single counts are roughly constant means that single photons are unpolarized or randomly polarized. This is a key characteristic of polarization-entangled photons [24].

The correlation coefficients required for the CHSH inequality and the respective errors are presented in Table 7.1. From the measured values we obtained $\mathcal{S}(0) = 2.4699 \pm 0.1729$, when accidental coincidences were subtracted. Thus, we observed a violation of CHSH inequality by 2.7 standard deviations.

7.5 Summary

We investigate the impact of fiber loss on the generation of quantum-correlated photon pairs through the spontaneous FWM process. We show that the presence of fiber loss and an absorption reservoir does not change the statistics of the individual signal and idler fields. The frequency dependence of the fiber loss coefficient completely changes the obtained spectrum of the photon-flux at fiber output, since the signal (idler) photon-flux depends on the idler (signal) loss coefficient. Our analysis also show that, the fiber loss increase the expected signal-idler correlation at fiber output, due to the fact that the accidental coincidences from the individual signal

and idler fields decreases. This impact of the fiber loss is verified through the analysis of the CHSH parameter. In that case, the presence of loss increases the value of $\mathcal{S}(0)$ parameter, when compared with the case $\alpha(\omega) = 0$. However, our results show that the Raman scattering process remains the main source of uncorrelated photon pairs, over the frequency range 0-20 (THz). In that frequency range, the fiber loss have a positive impact on the violation of the CHSH parameter. The fiber loss increases the purity of the photon pair correlation, due to the fact that fiber absorption reduces the rate of uncorrelated photons generated by Raman scattering inside the fiber. Finally, we have shown that to maximize the $\mathcal{S}(0)$ parameter the ratio $I_s(L,0)/I_i(L,0) < 0.8$. In addition, we have shown that waveguides with non-negligible loss, $\alpha(\omega)L \gg 1$ can be used for efficient generation of quantum-correlated photon pairs. In that case, we can use waveguides with length $L \gg 1/\alpha(\omega)$ which allow to use a regime of low pump power, increasing the quality of the photon pairs.

We demonstrated the generation and detection of polarization-entangled photon pairs inside a HNLF in the 1550 nm telecom window, using the spontaneous FWM process. When accidental coincidences were subtracted, we obtained a visibility for the coincidence fringe higher than 86%, and thus observed the violation of CHSH inequality by 2.7 standard deviations.

Appendix 7.A The CHSH Inequality

In this appendix, we derive the CHSH form of the Bell's inequality for polarization entangled states constructed using the single pump FWM process in a fiber loop, given by (7.38). Entangled states of quantum particles highlight the non-separability and nonlocality of quantum mechanics [63]. The Bell inequalities, a set of inequalities which any local hidden variable theory that takes separability into consideration must satisfy in some form. Quantum mechanics does not satisfy these inequalities, and hence the predictions of hidden variable theories and quantum mechanics differ [55, 64]. In its work, Bell show that all deterministic hidden variable theories preserving locality must satisfy the inequality [64]

$$\left| E\left(\vec{a}_1, \vec{a}_2\right) - E\left(\vec{a}_1, \vec{a}_3\right) \right| \leq 1 + E\left(\vec{a}_2, \vec{a}_3\right), \tag{G.40}$$

where E is the correlation coefficient of the measurements on two particles, and $\vec{a}_1$, $\vec{a}_2$, $\vec{a}_3$ are the orientations over which the measurements are performed. Its contradiction with quantum mechanics can be seen when we take $\vec{a}_1$, $\vec{a}_2$ and $\vec{a}_3$ to be coplanar, with $\vec{a}_3$ making an angle of

$2\pi/3$ with $\vec{a}_1$, and $\vec{a}_2$ making an angle of $\pi/3$ with both $\vec{a}_1$ and $\vec{a}_3$ [65]. In that case we obtain

$$\left|E\left(\vec{a}_1,\vec{a}_2\right)-E\left(\vec{a}_1,\vec{a}_3\right)\right| \leq 1+E\left(\vec{a}_2,\vec{a}_3\right) \Leftrightarrow \tag{G.41}$$

$$\Leftrightarrow \left|-\frac{1}{2}-\frac{1}{2}\right| \leq 1-\frac{1}{2} \tag{G.42}$$

This is a clear violation of Bell's inequality, demonstrating the incompatibility between quantum mechanics and local hidden variable theories.

An experiment testing the Bell inequality (G.40) requires the use of perfect analyzers and detectors [65]. Due to that, inequality (G.40) has been converted to a more experiment-friendly form by Clauser, Horne, Shimony, and Holt, known as the CHSH form of Bell's inequality [55, 63]. In they work, Clauser, Horne, Shimony, and Holt show that the Bell's inequality can be written as [55, 65]

$$\left|E(a,b)-E(a,b')\right|+\left|E(a',b)+E(a',b')\right| \leq 2\,, \tag{G.43}$$

where a, b, a', and b' are four possible analyzers settings. A weaker form of the inequality (G.43) is often employed in real experiments [63]

$$|\mathcal{S}(0)| = \left|E(a,b)-E(a,b')+E(a',b)+E(a',b')\right| \leq 2\,. \tag{G.44}$$

This weaker version means that, if some theory satisfies (G.43), then it must have already satisfied (G.44), but the reverse is not necessarily true. On the other hand, if some theory violates (G.44), it must have already violated (G.43) [66].

A generic setup used to test the CHSH form of the Bell's inequality is depicted in Fig. 7.8. In the figure a source, **S**, emits polarization entangled photon pairs for two different receivers. The entangled state at the source output is given by (7.38). Which photon passes through a polarization analyzer and is collected by a set of two detectors. The polarization analyzer is typically

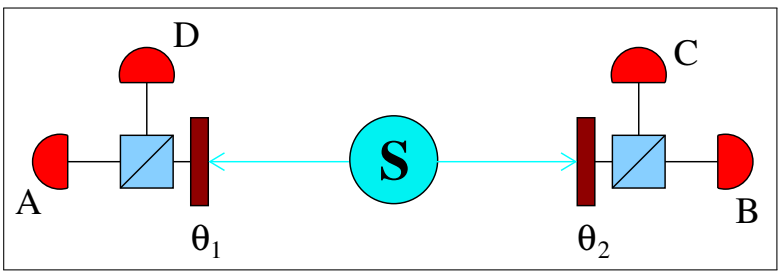

Figure 7.8: A schematic of the experimental setup for testing the CHSH form of the Bell's inequality (G.44).

composed by a half-wave plate and a PBS. From Fig. 7.8 we can see that a coincidence count between detectors C and D at analyzer settings θ_1 and θ_2 is equivalent to a coincidence count between detectors A and B at analyzer at analyzer settings $\theta_1^{\perp}$ and $\theta_2^{\perp}$, where $\theta_u^{\perp} = \theta_u + \pi/2$. This essentially removes the need to use four detectors, only two detectors (for instance A and B in Fig. 7.8) are required to test the CHSH form of the Bell's inequality for polarization entangled photon pairs [63]. Nevertheless, this requires the additional auxiliary assumption that the state from the source is independent of the analyzer settings [63]. For polarization entangled photon pairs, Fig. 7.8, the CHSH form of the Bell's inequality can be written as [7, 63, 67, 68]

$$|\mathcal{S}(\tau)| = \left|E(\tau,\theta_1,\theta_2) - E(\tau,\theta_1,\theta_2') + E(\tau,\theta_1',\theta_2) + E(\tau,\theta_1',\theta_2')\right| \leq 2\,, \tag{G.45}$$

where $\mathcal{S}(\tau)$ is the CHSH parameter, and τ is the time delay between the two-photons that compose the entangled pair. Quantum mechanically, the correlation function in (G.45) can be written as [7, 67, 68]

$$E(\tau,\theta_1,\theta_2) = \frac{\left\langle \mathcal{T} : \hat{I}_2^-(t+\tau)\hat{I}_1^-(t) : \right\rangle}{\left\langle \mathcal{T} : \hat{I}_2^+(t+\tau)\hat{I}_1^+(t) : \right\rangle}\,, \tag{G.46}$$

where $\mathcal{T}$ denotes time ordering, and :: denotes normal ordering. In (G.46), $\hat{I}_u^{\pm}(t)$ is the sum and difference photon-flux operator for two orthogonal polarization angles, given by [7, 67, 68]

$$\hat{I}_u^{\pm}(t) = \hat{A}_u^{\dagger}(t,\theta_u)\hat{A}_u(t,\theta_u) \pm \hat{A}_u^{\dagger}(t,\theta_u^{\perp})\hat{A}_u(t,\theta_u^{\perp})\,. \tag{G.47}$$

Assuming that each polarizer in Fig. 7.8 is aligned at an angle θ_u with respect to the fiber x axis, the optical field $\hat{A}_u(t,\theta_u)$ can be written as [7]

$$\hat{A}_u(t,\theta_u) = \hat{A}_{ux}(L,t)\cos(\theta_u) + \hat{A}_{uy}(L,t)\sin(\theta_u)\,, \tag{G.48}$$

with $\hat{A}_{ux}(L,t)$ and $\hat{A}_{uy}(L,t)$ being the x- and y-polarized optical fields at source output, with L representing the length of the source that gives rise to the entangled photon pair, see for instance Fig. 7.6 and (7.38). Combining (G.48) with (G.47) we obtain [7, 69]

$$\begin{aligned}\left\langle \mathcal{T} : \hat{I}_2^+(t+\tau)\hat{I}_1^+(t) : \right\rangle = (I_{1x}+I_{1,y})(I_{2x}+I_{2y}) + |\mathcal{P}(\tau,\theta_1,\theta_2)|^2 + |\mathcal{P}(\tau,\theta_1^{\perp},\theta_2^{\perp})|^2 \\ + |\mathcal{P}(\tau,\theta_1,\theta_2^{\perp})|^2 + |\mathcal{P}(\tau,\theta_1^{\perp},\theta_2)|^2\,,\end{aligned} \tag{G.49}$$

and

$$\begin{aligned}\left\langle \mathcal{T} : \hat{I}_2^-(t+\tau)\hat{I}_1^-(t) : \right\rangle = (I_{1x}-I_{1,y})(I_{2x}-I_{sy})\cos(2\theta_1)\sin(2\theta_2) + |\mathcal{P}(\tau,\theta_1,\theta_2)|^2 \\ + |\mathcal{P}(\tau,\theta_1^{\perp},\theta_2^{\perp})|^2 - |\mathcal{P}(\tau,\theta_1,\theta_2^{\perp})|^2 - |\mathcal{P}(\tau,\theta_1^{\perp},\theta_2)|^2\,,\end{aligned} \tag{G.50}$$

where $I_{ux} = \langle \hat{A}^{\dagger}_{ux}(L,t)\hat{A}_{ux}(L,t)\rangle$ and $I_{uy} = \langle \hat{A}^{\dagger}_{uy}(L,t)\hat{A}_{uy}(L,t)\rangle$ are the photon-flux for the jth polarization component with $j = x,y$, see for instance Fig. 7.6. In (G.49) and (G.50), $\mathcal{P}(\tau,\theta_1,\theta_2)$ is given by [7, 69]

$$\begin{aligned}\mathcal{P}(\tau,\theta_1,\theta_2) &= \left\langle \hat{A}_2(t+\tau,\theta_2)\hat{A}_1(t,\theta_1)\right\rangle \\ &= \mathcal{P}_x(\tau)\cos(\theta_1)\cos(\theta_2) + \mathcal{P}_y(\tau)\sin(\theta_1)\sin(\theta_2) \end{aligned} \tag{G.51a}$$

$$\begin{aligned}\mathcal{P}(\tau,\theta_1^{\perp},\theta_2^{\perp}) &= \left\langle \hat{A}_2(t+\tau,\theta_2^{\perp})\hat{A}_1(t,\theta_1^{\perp})\right\rangle \\ &= \mathcal{P}_x(\tau)\sin(\theta_1)\sin(\theta_2) + \mathcal{P}_y(\tau)\cos(\theta_1)\cos(\theta_2) \end{aligned} \tag{G.51b}$$

$$\begin{aligned}\mathcal{P}(\tau,\theta_1,\theta_2^{\perp}) &= \left\langle \hat{A}_2(t+\tau,\theta_2^{\perp})\hat{A}_1(t,\theta_1)\right\rangle \\ &= \mathcal{P}_y(\tau)\sin(\theta_1)\cos(\theta_2) - \mathcal{P}_x(\tau)\cos(\theta_1)\sin(\theta_2) \end{aligned} \tag{G.51c}$$

$$\begin{aligned}\mathcal{P}(\tau,\theta_1^{\perp},\theta_2) &= \left\langle \hat{A}_2(t+\tau,\theta_2)\hat{A}_1(t,\theta_1^{\perp})\right\rangle \\ &= \mathcal{P}_y(\tau)\cos(\theta_1)\sin(\theta_2) - \mathcal{P}_x(\tau)\sin(\theta_1)\cos(\theta_2)\,, \end{aligned} \tag{G.51d}$$

where $\mathcal{P}_x(\tau) = \left\langle \hat{A}_{2x}(L,t+\tau)\hat{A}_{1x}(L,t)\right\rangle$, and $\mathcal{P}_y(\tau) = \left\langle \hat{A}_{2y}(L,t+\tau)\hat{A}_{1y}(L,t)\right\rangle$, with $\hat{A}_{ux}(L,t)$ and $\hat{A}_{uy}(L,t)$ being the x- and y-polarized optical fields at source output.

Polarization-entangled states can be obtained using the FWM process in a fiber loop, see Fig. 7.6. In that case, the optical pump field is divided into two parts of equal powers with orthogonal polarizations. Each pump polarization generates co-polarized photon pairs. After combining both polarizations and eliminating time or path information between the orthogonal polarizations, an entangled polarization state is obtained, according with (7.38) [7, 69]. In that configuration, $I_{ux} = I_{uy} = I_u$ and $\mathcal{P}_x(\tau) = \mathcal{P}_y(\tau) = \mathcal{P}(\tau)$. In that case, equation (G.46) is given by

$$E(\tau,\theta_1,\theta_2) = \frac{|\mathcal{P}(\tau)|^2}{2I_1I_2 + |\mathcal{P}(\tau)|^2}\left(\cos^2(\theta_2-\theta_1) - \sin^2(\theta_2-\theta_1)\right). \tag{G.52}$$

Finally, the CHSH parameter can be written as

$$\begin{aligned}\mathcal{S}(\tau) = \frac{|\mathcal{P}(\tau)|^2}{2I_1I_2 + |\mathcal{P}(\tau)|^2}\Big(&\cos^2(\theta_2-\theta_1) - \sin^2(\theta_2-\theta_1) - \cos^2(\theta_2-\theta_1') + \sin^2(\theta_2-\theta_1') \\ &+ \cos^2(\theta_2'-\theta_1) - \sin^2(\theta_2'-\theta_1) + \cos^2(\theta_2'-\theta_1') - \sin^2(\theta_2'-\theta_1')\Big). \end{aligned} \tag{G.53}$$

The CHSH is maximized by setting for example $\theta_2 = \pi/8$, $\theta_2' = -\pi/8$, $\theta_1 = 0$, and $\theta_1' = -\pi/4$. For that angles, equation (G.53) reduces to equation (7.36) and the CHSH parameter is given by [7, 69]

$$\mathcal{S}(\tau) = 2\sqrt{2}\frac{|\mathcal{P}(\tau)|^2}{2I_1I_2 + |\mathcal{P}(\tau)|^2}\,. \tag{G.54}$$

References

[1] N. Gisin, G. Ribordy, W. Tittel, and H. Zbinden, "Quantum cryptography," *Rev. Mod. Phys.*, vol. 74, pp. 145–195, 2002.

[2] D. de Brito and R. Ramos, "Analysis of heralded single-photon source using four-wave mixing in optical fibers via Wigner function and its use in quantum key distribution," *IEEE Journal of Quantum Electronics*, vol. 46, pp. 721 –727, 2010.

[3] C. Liang, K. F. Lee, J. Chen, and P. Kumar, "Distribution of fiber-generated polarization entangled photon-pairs over 100 km of standard fiber in oc-192 wdm environment," in *Optical Fiber Communication Conference and Exposition and The National Fiber Optic Engineers Conference*. Optical Society of America, 2006, p. PDP35.

[4] P. Kumar, "Practical quantum communication and cryptography for wdm optical networks," in *AIP Conference Proceedings*, S. M. Barnett, O. Hirota, P. Ohberg, J. Jeffers, and E. Andersson, Eds., vol. 734. AIP, 2004, pp. 3–11.

[5] P. L. Voss and P. Kumar, "Raman-effect induced noise limits on $\chi^{(3)}$ parametric amplifiers and wavelength converters," *Journal of Optics B: Quantum and Semiclassical Optics*, vol. 6, p. S762, 2004.

[6] Q. Lin, F. Yaman, and G. P. Agrawal, "Photon-pair generation by four-wave mixing in optical fibers," *Opt. Lett.*, vol. 31, pp. 1286–1288, 2006.

[7] Q. Lin, F. Yaman, and G. P. Agrawal, "Photon-pair generation in optical fibers through four-wave mixing: Role of Raman scattering and pump polarization," *Phys. Rev. A*, vol. 75, p. 023803, 2007.

[8] N. A. Silva and A. N. Pinto, "Role of absorption on the generation of quantum-correlated photon pairs through FWM," *IEEE Journal of Quantum Electronics*, vol. 48, pp. 1380 –1388, 2012.

[9] N. A. Silva and A. N. Pinto, "Photon-pair generation in chalcogenide glass: Role of waveguide linear absorption," 2014, accepted for publication in: PHOTOPTICS 2014.

[10] A. J. Almeida, S. R. Carneiro, N. A. Silva, N. J. Muga, and A. N. Pinto, "Polarization-entangled photon pairs using spontaneous four-wave mixing in a fiber loop," in *EUROCON and CONFTELE 2011*, vol. 1, April 2011, pp. 1–4.

[11] A. J. Almeida, L. M. Pinto, N. A. Silva, N. J. Muga, and A. N. Pinto, "Correlated photon-pair generation in a highly nonlinear fiber using spontaneous FWM," in *Symp. on Enabling Optical Networks - SEON*, vol. 1, July 2011, pp. 1–4.

[12] G. Agrawal, *Nonlinear Fiber Optics*, 3rd ed. Academic Press, 2001.

[13] N. A. Silva, N. J. Muga, and A. N. Pinto, "Effective nonlinear parameter measurement using FWM in optical fibers in a low power regime," *IEEE Journal of Quantum Electronics*, vol. 46, pp. 285–291, 2010.

[14] X. Gai, R. P. Wang, C. Xiong, M. J. Steel, B. J. Eggleton, and B. Luther-Davies, "Near-zero anomalous dispersion $Ge_{11.5}As_{24}Se_{64.5}$ glass nanowires for correlated photon pair generation: design and analysis," *Opt. Express*, vol. 20, pp. 776–786, 2012.

[15] NKT Photonics, "NL-PM-750 data sheet," http://www.nktphotonics.com/files/files/NL-PM-750-090612.pdf.

[16] C. Xiong, L. G. Helt, A. C. Judge, G. D. Marshall, M. J. Steel, J. E. Sipe, and B. J. Eggleton, "Quantum-correlated photon pair generation in chalcogenide As_2S_3 waveguides," *Opt. Express*, vol. 18, pp. 16 206–16 216, 2010.

[17] J. Fan, A. Migdall, J. Chen, and E. Goldschmidt, "Microstructure-fiber-based source of photonic entanglement," *IEEE Journal of Selected Topics in Quantum Electronics*, vol. 15, pp. 1724 –1732, 2009.

[18] A. Politi, M. J. Cryan, J. G. Rarity, S. Yu, and J. L. O'Brien, "Silica-on-silicon waveguide quantum circuits," *Science*, vol. 320, pp. 646–649, 2008.

[19] M. Fiorentino, P. Voss, J. Sharping, and P. Kumar, "All-fiber photon-pair source for quantum communications," *IEEE Photonics Technology Letters*, vol. 14, pp. 983 –985, 2002.

[20] J. E. Sharping, M. Fiorentino, and P. Kumar, "Observation of twin-beam-type quantum correlation in optical fiber," *Opt. Lett.*, vol. 26, pp. 367–369, 2001.

[21] J. Fan, A. Dogariu, and L. J. Wang, "Generation of correlated photon pairs in a microstructure fiber," *Opt. Lett.*, vol. 30, pp. 1530–1532, 2005.

[22] J. Chen, K. F. Lee, C. Liang, and P. Kumar, "Fiber-based telecom-band degenerate-frequency source of entangled photon pairs," *Opt. Lett.*, vol. 31, pp. 2798–2800, 2006.

[23] H. Takesue and K. Inoue, "Generation of polarization-entangled photon pairs and violation of Bell's inequality using spontaneous four-wave mixing in a fiber loop," *Phys. Rev. A*, vol. 70, p. 031802, 2004.

[24] X. Li, P. L. Voss, J. E. Sharping, and P. Kumar, "Optical-fiber source of polarization-entangled photons in the 1550 nm telecom band," *Phys. Rev. Lett.*, vol. 94, p. 053601, 2005.

[25] X. Li, C. Liang, K. Fook Lee, J. Chen, P. L. Voss, and P. Kumar, "Integrable optical-fiber source of polarization-entangled photon pairs in the telecom band," *Phys. Rev. A*, vol. 73, p. 052301, 2006.

[26] J. Fan, M. D. Eisaman, and A. Migdall, "Bright phase-stable broadband fiber-based source of polarization-entangled photon pairs," *Phys. Rev. A*, vol. 76, p. 043836, 2007.

[27] H. Takesue and K. Inoue, "Generation of 1.5-μm band time-bin entanglement using spontaneous fiber four-wave mixing and planar light-wave circuit interferometers," *Phys. Rev. A*, vol. 72, p. 041804, 2005.

[28] H. Takesue, "Long-distance distribution of time-bin entanglement generated in a cooled fiber," *Opt. Express*, vol. 14, pp. 3453–3460, 2006.

[29] X. Li, L. Yang, X. Ma, L. Cui, Z. Y. Ou, and D. Yu, "All-fiber source of frequency-entangled photon pairs," *Phys. Rev. A*, vol. 79, p. 033817, 2009.

[30] C. Xiong, G. D. Marshall, A. Peruzzo, M. Lobino, A. S. Clark, D.-Y. Choi, S. J. Madden, C. M. Natarajan, M. G. Tanner, R. H. Hadfield, S. N. Dorenbos, T. Zijlstra, V. Zwiller, M. G. Thompson, J. G. Rarity, M. J. Steel, B. Luther-Davies, B. J. Eggleton, and J. L. O'Brien, "Generation of correlated photon pairs in a chalcogenide As_2S_3 waveguide," *Applied Physics Letters*, vol. 98, p. 051101, 2011.

[31] L. J. Wang, C. K. Hong, and S. R. Friberg, "Generation of correlated photons via four-wave mixing in optical fibres," *Journal of Optics B: Quantum and Semiclassical Optics*, vol. 3, p. 346, 2001.

[32] J. Chen, X. Li, and P. Kumar, "Two-photon-state generation via four-wave mixing in optical fibers," *Phys. Rev. A*, vol. 72, p. 033801, 2005.

[33] O. Alibart, J. Fulconis, G. K. L. Wong, S. G. Murdoch, W. J. Wadsworth, and J. G. Rarity, "Photon pair generation using four-wave mixing in a microstructured fibre: theory versus experiment," *New Journal of Physics*, vol. 8, p. 67, 2006.

[34] P. L. Voss and P. Kumar, "Raman-noise-induced noise-figure limit for $\chi(3)$ parametric amplifiers," *Opt. Lett.*, vol. 29, pp. 445–447, 2004.

[35] P. L. Voss, K. G. Köprülü, and P. Kumar, "Raman-noise-induced quantum limits for $\chi(3)$ nondegenerate phase-sensitive amplification and quadrature squeezing," *J. Opt. Soc. Am. B*, vol. 23, pp. 598–610, 2006.

[36] Q. Lin and G. P. Agrawal, "Silicon waveguides for creating quantum-correlated photon pairs," *Opt. Lett.*, vol. 31, pp. 3140–3142, 2006.

[37] P. D. Drummond and J. F. Corney, "Quantum noise in optical fibers. I. Stochastic equations," *J. Opt. Soc. Am. B*, vol. 18, pp. 139–152, 2001.

[38] P. D. Drummond, *Coherence and Quantum Optics VII*. Springer, 1996, ch. Quantum Theory of Fiber-Optics and Solitons, pp. 323–332.

[39] L. Boivin, F. X. Kärtner, and H. A. Haus, "Analytical solution to the quantum field theory of self-phase modulation with a finite response time," *Phys. Rev. Lett.*, vol. 73, 1994.

[40] F. X. Kärtner, D. J. Dougherty, H. A. Haus, and E. P. Ippen, "Raman noise and soliton squeezing," *J. Opt. Soc. Am. B*, vol. 11, pp. 1267–1276, 1994.

[41] R. W. Boyd, *Nonlinear Optics*, 2nd ed. Academic Press, 2003.

[42] Q. Lin and G. P. Agrawal, "Effects of polarization-mode dispersion on fiber-based parametric amplification and wavelength conversion," *Opt. Lett.*, vol. 29, pp. 1114–1116, 2004.

[43] R. W. Hellwarth, *Third-order optical susceptibilities of liquids and solids*. Pergamon Press, Oxford ; New York, 1977.

[44] N. Silva, N. Muga, and A. Pinto, "Influence of the stimulated Raman scattering on the four-wave mixing process in birefringent fibers," *IEEE/OSA Journal of Lightwave Technology*, vol. 27, pp. 4979–4988, 2009.

[45] N. A. Silva, N. J. Muga, and A. N. Pinto, "Evolution of first-order sidebands from multiple FWM processes in HiBi optical fibers," *Optics Communications*, vol. 284, pp. 3408 – 3415, 2011.

[46] D. Hollenbeck and C. D. Cantrell, "Multiple-vibrational-mode model for fiber-optic raman gain spectrum and response function," *J. Opt. Soc. Am. B*, vol. 19, pp. 2886–2892, 2002.

[47] Q. Lin and G. P. Agrawal, "Raman response function for silica fibers," *Opt. Lett.*, vol. 31, pp. 3086–3088, 2006.

[48] M. Artoni and R. Loudon, "Propagation of nonclassical light through an absorbing and dispersive slab," *Phys. Rev. A*, vol. 59, pp. 2279–2290, 1999.

[49] A. Zonnenberg, "Supercontinuum generation in the picosecond regime," Bachelor's thesis, Leiden Institute of Physics, Faculty of Science, Leiden University, Netherlands, September 2006, http://www.molphys.leidenuniv.nl/qo/thesis/Bachelor-Arthur-Zonnenberg.pdf.

[50] N. A. Silva, A. J. Almeida, and A. N. Pinto, "Interference in a quantum channel due to classical four-wave mixing in optical fibers," *IEEE Journal of Quantum Electronics*, vol. 48, pp. 472 –479, 2012.

[51] R. Loudon, *The Quantum Theory of Light*, 3rd ed. Oxford University Press, USA, 2000.

[52] E. A. Goldschmidt, M. D. Eisaman, J. Fan, S. V. Polyakov, and A. Migdall, "Spectrally bright and broad fiber-based heralded single-photon source," *Phys. Rev. A*, vol. 78, p. 013844, 2008.

[53] P. L. Voss, R. Tang, and P. Kumar, "Measurement of the photon statistics and the noise figure of a fiber-optic parametric amplifier," *Opt. Lett.*, vol. 28, pp. 549–551, 2003.

[54] J. F. Clauser, "Experimental distinction between the quantum and classical field-theoretic predictions for the photoelectric effect," *Phys. Rev. D*, vol. 9, pp. 853–860, 1974.

[55] J. F. Clauser, M. A. Horne, A. Shimony, and R. A. Holt, "Proposed experiment to test local hidden-variable theories," *Phys. Rev. Lett.*, vol. 23, pp. 880–884, 1969.

[56] M. Kozierowski, "Violation of the Cauchy-Schwarz inequality and anticorrelation effect in second-harmonic generation," *Phys. Rev. A*, vol. 36, pp. 2973–2975, 1987.

[57] J. Chen, J. B. Altepeter, and P. Kumar, "Quantum-state engineering using nonlinear optical sagnac loops," *New Journal of Physics*, vol. 10, p. 123019, 2008.

[58] A. Almeida, S. Carneiro, N. Silva, N. Muga, and A. Pinto, "Polarization-entangled photon pairs using spontaneous four-wave mixing in a fiber loop," in *EUROCON - International Conference on Computer as a Tool (EUROCON), 2011 IEEE*, april 2011, pp. 1 –4.

[59] G. Ribordy, N. Gisin, O. Guinnard, D. Stucki, M. Wegmuller, and H. Zbinden, "Photon counting at telecom wavelengths with commercial InGaAs/InP avalanche photodiodes: current performance," *Journal of Modern Optics*, vol. 51, pp. 1381–1398, 2004.

[60] idQuantique, "id 201 Single-Photon Detector Module - Operating Guide, Version 4.0," pp. 1–28, 2008. [Online]. Available: http://www.idquantique.com/products/files/id201-operating-guide.pdf

[61] idQuantique, "id 200 Single-Photon Detector Module - Operating Guide, Version 2.2," pp. 1–26, 2005. [Online]. Available: http://www.idquantique.com/products/files/id200-operating.pdf

[62] A. Aspect, P. Grangier, and G. Roger, "Experimental Realization of Einstein-Podolsky-Rosen-Bohm Gedankenexperiment: A New Violation of Bell's Inequalities," *Physical Review Letters*, vol. 49, pp. 91–94, 1982.

[63] P. G. Kwiat, K. Mattle, H. Weinfurter, A. Zeilinger, A. V. Sergienko, and Y. Shih, "New high-intensity source of polarization-entangled photon pairs," *Phys. Rev. Lett.*, vol. 75, pp. 4337–4341, 1995.

[64] J. S. Bell, "On the Einstein-Podolsky-Rosen paradox," *Physics*, vol. 1, pp. 195–200, 1964.

[65] J. F. Clauser and A. Shimony, "Bell's theorem. experimental tests and implications," *Reports on Progress in Physics*, vol. 41, p. 1881, 1978.

[66] J. Chen, "Development and applications of fiber-based entanglement sources," Ph.D. dissertation, Center for Photonic Communication and Computing, EECS Department - Northwestern University, Evanston, Illinois, 2007.

[67] D. Walls and G. J. Milburn, *Quantum Optics*, 1st ed. Springer, 1994.

[68] M. D. Reid and D. F. Walls, "Violations of classical inequalities in quantum optics," *Phys. Rev. A*, vol. 34, pp. 1260–1276, 1986.

[69] Q. Lin, "Polarization and fiber nonlinearities," Ph.D. dissertation, The Institute of Optics, The College School of Engineering and Applied Sciences - University of Rochester, Rochester, New York, 2006.

Chapter 8

Effects of Losses and Nonlinearities on the Generation of Polarization Entangled Photons

ENTANGLED photon sources at telecom band are important resources for quantum communications, mainly for distribution of polarization qubits in quantum key distribution (QKD) systems [1]. The spontaneous four-wave mixing (FWM) provides a natural solution to obtain sources of polarization entangled photon-pairs already inside optical fibers, through the implementation of fiber loops [2–7]. In this Chapter we present a detailed description of the generation of polarization entangled photon-pairs in waveguides with high values of both loss coefficient and nonlinearities. We extend our previous work in Chapter 7 to include the impact of nonlinearities and fiber length on the generation of polarization entangled photons inside of lossy waveguides. Our goal is to identify appropriates regimes for the coincidence-to-accidental ratio (CAR) and the Clauser, Horne, Shimony, and Holt (CHSH) inequality, for which the trade-off between waveguide losses and nonlinearities maximizes that parameters. The obtained results consider the Raman scattering process that occurs inside the waveguide. The results present in this Chapter are valid for the case where the waveguide loss is distributed by all fiber length. Note that if we concentrate all the loss at the fiber output, by using for instant a coupler, the photon-pair correlation is the same before and after the coupler [8]. This Chapter is based on the reference [9], and is divided as follows: Section 8.1 provides an introduction to the role of waveguide linear absorption and nonlinear parameter on the generation of polarization entangled photons through spontaneous FWM process. In section 8.2, we present the theoretical model that describes the generation of polarization entangled photon-pairs through FWM, in the single and continuous pump configuration. In section 8.3, we apply that formalism to obtain the evo-

lution of the coincidence-to-accidental ratio and the CHSH parameter with both waveguide loss coefficient and nonlinear parameter. We investigate those effects for waveguides with different lengths. We identify appropriate regimes for the loss coefficient and for the nonlinear parameter that maximizes the CHSH inequality. Finally, section 8.4 summarizes the main conclusions of this Chapter.

8.1 Waveguide Linear Absorption and Nonlinear Parameter

The spontaneous FWM provides a natural solution to implement sources of polarization entangled photon-pairs already inside optical fibers [2–7]. Typically, efficient generation of photon-pairs through FWM demands two main conditions, perfect phase-matching and waveguides with high values of nonlinear parameter [10–13]. However, waveguides with high values of nonlinear parameter, such as photonic crystal fibers and chalcogenide glasses, tends to present high values of losses [14–16]. To avoid the impact of photon losses, waveguides with lengths $L \ll 1/\alpha$ are used, which requires high values of pump power, since the length of the waveguide tends to be very small [13, 14, 16]. The generation of quantum-correlated photon-pairs over short distances is essential to implement on-chip quantum technologies [17]. Nevertheless, high values of pump power can damage the waveguide [16], and removing the pump photons tends to be very difficult due to the high power regime [6]. Moreover, high values of both pump power and nonlinear parameter can lead to the generation of multiphotons, which decreases the photon-pair correlation [13]. A complete description of the effects of waveguide loss and nonlinearities on the generation of polarization entangled photon-pairs through FWM, remains an open issue, to the best of our knowledge.

The generation of quantum-correlated photon-pairs through FWM in chalcogenide glass waveguides was already studied, see for instance [14, 16, 18], in the regime $L \ll 1/\alpha$. In optical fibers, the spontaneous FWM process as a source of correlated photons was studied in [19, 20], using only a pump field. Subsequent studies have used the FWM process to obtain mainly entangled photon sources on polarization [3–7] and time-bin [21, 22] degrees of freedom. The spontaneous FWM process was studied theoretically in [23]. Since then, generalized studies about the FWM process have been carried out to account for the spectral shape of pump pulses [24–26]. However, in those works the Raman scattering process that occurs inside the fiber was ignored. In the Heisenberg picture, the combined processes of FWM and Raman scattering were studied in [13, 27–30], in different continuous wave pump configurations. Recently, in [31], we presented a theoretical model capable of describing the evolution of the signal and idler quantum

operators inside a lossy waveguide. In that work, we analyze the impact of frequency dependent loss coefficient on the generation of quantum-correlated photon pairs through FWM.

8.2 Signal and Idler Photon-Fluxes and Coincidence Counting Rates

In this section, we present the theoretical model that describes the generation of single and polarization entangled photon-pairs inside an optical waveguide with non-negligible loss. We use the FWM process in the single pump configuration and we consider that the photons are created in the same polarization mode as the pump field.

In optical waveguides, the linear response represents the dominant contribution to the total polarization induced by an optical field. The linear response function, $\tilde{R}^{(1)}(\omega)$, includes the dispersive and loss properties of the fiber [10, 32]

$$\tilde{R}^{(1)}(\omega) = \beta(\omega) + \frac{i}{2}\alpha(\omega), \tag{8.1}$$

where $\beta(\omega)$ represents the effect of fiber dispersion, and $\alpha(\omega)$ is the fiber loss coefficient, at frequency ω. The lowest-order nonlinear polarization in optical fibers is described by the third-order response function [10]. In third-order nonlinear materials, such as optical fibers or chalcogenide glass waveguides, the nonlinear response of the medium to an applied optical field is governed by [11, 13, 33, 34]

$$\tilde{R}^{(3)}(\Omega) = \gamma(1 - f_R) + \gamma f_R \left(\tilde{R}_a(\Omega) + \tilde{R}_b(\Omega)\right), \tag{8.2}$$

where the first term accounts for the instantaneous response of the nonlinear material, and give rise to nonlinear processes such as FWM. The second term of (8.2) represents the retarded molecular response of the medium, and give rise to the Raman scattering process. In (8.2), Ω is the Stokes ($\Omega < 0$) or anti-Stokes ($\Omega > 0$) frequency shift, γ is the nonlinear coefficient of the fiber, and $f_R = 0.18$ is the fractional contribution of the Raman process to the nonlinear refractive index [10]. $\tilde{R}_a(\Omega)$ and $\tilde{R}_b(\Omega)$ are the isotropic and anisotropic Raman response functions, respectively, and they are related with the Raman gain coefficient $g_R(\Omega) = 2\gamma f_R \mathrm{Im}[\tilde{R}_a(\Omega) + \tilde{R}_b(\Omega)]$[11, 13, 33–35].

In the single pump configuration, the signal (at ω_s) and the idler (at ω_i) photons are created due to the annihilation of two pump photons (at ω_p), such that $2\,\omega_p = \omega_s + \omega_i$. In order to analyze the CHSH inequality, we need to calculate the photon-flux originating from both FWM and Raman scattering in a medium with non-negligible loss. We assume that the pump field is much

more intense than the signal and idler waves, and the fiber length is much shorter than the walk-off length [10]. In a typical experiment the signal and idler fields are spectrally filtered. In that case, the photon-flux for the signal and idler fields generated inside the fiber over a propagation distance L can be given by [13, 36]

$$I_u = \langle \hat{A}_u^\dagger(L,\tau)\hat{A}_u(L,\tau)\rangle \approx \Delta\nu_u \, \mathcal{F}_u(L), \tag{8.3}$$

where $\hat{A}_u(L,\tau)$ is the slowly varying field annihilation operator [31], and

$$\Delta\nu_u = 1/(2\pi)\int d\omega_u |H_u(\omega_u - \bar{\omega}_u)|^2 \tag{8.4}$$

with $H_u(\omega_u - \bar{\omega}_u)$ being a filter function centered at $\bar{\omega}_u$. For the signal field the filter central frequency is $\bar{\omega}_s$, whereas for the idler is $\bar{\omega}_i$, such that $2\omega_p = \bar{\omega}_s + \bar{\omega}_i$. In (8.3), $\mathcal{F}_u(L)$ is the photon-flux spectral density evaluated at $\bar{\omega}_u$, and it is given by [29, 31, 37, 38]

$$\mathcal{F}_u(L) = |\nu_u(L,0)|^2 + \alpha_u \mathcal{N}_u \int_0^L dz |\mu_u(L,z)|^2 + \alpha_v(\mathcal{N}_v+1)\int_0^L dz |\nu_u(L,z)|^2 + (\mathcal{N}_{up}+\Theta_{up})|g_R(\Omega_{up})| \int_0^L dz \left|\bar{A}_p(z)\mu_u(L,z) - \bar{A}_p^*(z)\nu_u(L,z)\right|^2, \tag{8.5}$$

where $u,v = s$ or i with $u \neq v$ represents the signal or idler field, $\Theta(-\Omega_{up})$ is the Heaviside step function, $\Omega_{up} = \bar{\omega}_u - \omega_p$, $\mathcal{N}_u = [\exp\{\hbar\bar{\omega}_u/(k_B T) - 1\}]^{-1}$, and $\mathcal{N}_{up} = [\exp\{\hbar|\Omega_{up}|/(k_B T) - 1\}]^{-1}$. In (8.5), α_s is the fiber loss coefficient at signal frequency, whereas α_i is the fiber loss coefficient at idler frequency, and [29, 31],

$$\mu_s(L,z) = e^{p(L,z\bar{\omega}_s)} \sum_{n=0}^{+\infty} s_n(z) F_{\text{eff}}^n(L,z), \tag{8.6a}$$

with $s_0 = 1$ and $a_0^* = 0$,

$$\nu_i(L,z) = e^{p(L,z,\bar{\omega}_i)} \sum_{n=0}^{+\infty} a_n(z) F_{\text{eff}}^n(L,z), \tag{8.6b}$$

with $s_0 = 1$ and $a_0^* = 0$. The series coefficients $s_n(z)$ and $a_n(z)$ are given by

$$s_1(z) = i\gamma P_p(z)\left(\xi(\Omega_{sp}) - 1\right) s_0 + i\gamma\eta(\Omega_{sp})\bar{A}_p^2(z)a_0^* - \frac{\alpha_s + \alpha_i + 2i\Delta\beta}{4} s_0, \tag{8.7a}$$

$$a_1^*(z) = -i\gamma P_p(z)\left(\xi^*(\Omega_{ip}) - 1\right) a_0^* - i\gamma\eta^*(\Omega_{ip})\bar{A}_p^{2*}(z)s_0 + \frac{\alpha_s + \alpha_i + 2i\Delta\beta}{4} a_0^*, \tag{8.7b}$$

$$s_{n+1}(z) = \frac{n}{n+1}\alpha_p s_n(z) - \frac{\alpha_s+\alpha_i+2i\Delta\beta}{4(n+1)}s_n(z) + i\frac{\gamma P_p(z)}{n+1}\left(\xi(\Omega_{sp})-1\right)\left(s_n(z)-\alpha_p s_{n-1}(z)\right) + i\frac{\gamma\eta(\Omega_{sp})}{n+1}\bar{A}_p^2(z)\left(a_n^*(z)-\alpha_p a_{n-1}^*(z)\right), \quad (8.7c)$$

$$a_{n+1}^*(z) = \frac{n}{n+1}\alpha_p a_n^*(z) + \frac{\alpha_s+\alpha_i+2i\Delta\beta}{4(n+1)}a_n^*(z) - i\frac{\gamma P_p(z)}{n+1}\left(\xi^*(\Omega_{ip})-1\right)\left(a_n^*(z)-\alpha_p a_{n-1}^*(z)\right) - i\frac{\gamma\eta^*(\Omega_{ip})}{n+1}\bar{A}_p^{2*}(z)\left(s_n(z)-\alpha_p s_{n-1}(z)\right), \quad (8.7d)$$

where α_p is the fiber loss coefficient at pump frequency, $\Delta\beta$ is the phase matching condition, $P_p(z)$ is the pump power at a distance z on the fiber, and

$$\xi(\Omega_{up}) = 2 - f_R + f_R\left(\tilde{R}_a(\Omega_{up}) + \tilde{R}_b(\Omega_{up})\right), \quad (8.8a)$$

$$\eta(\Omega_{up}) = 1 - f_R + f_R\left(\tilde{R}_a(\Omega_{up}) + \tilde{R}_b(\Omega_{up})\right). \quad (8.8b)$$

The function ν_s is the same series as μ_s except that the initial condition is $s_0 = 0$ and $a_0^* = 1$, see (8.6a). The function μ_i is the same series as ν_i except that the initial condition is $s_0 = 0$ and $a_0^* = 1$, see (8.6b). In (8.6)

$$F_{\text{eff}}(L,z) = \frac{1-\exp\{-\alpha_p(L-z)\}}{\alpha_p}, \quad (8.9a)$$

$$p(L,z,\bar{\omega}_u) = -\frac{\alpha_s+\alpha_i+2i\Delta\beta}{4}(L-z) + i\left(\beta_u(L-z) + \gamma P_p(0)F_{\text{eff}}(L,z)\right), \quad (8.9b)$$

where β_u is the propagation constant at signal ($u = s$) or idler ($u = i$) frequencies, and $\bar{A}_p(z)$ is the classical pump amplitude, given by

$$\bar{A}_p(z) = \bar{A}_p(0)\exp\left\{i\left(\beta_p z + \gamma P_p(0)L_{\text{eff}}\right) - \frac{\alpha_p}{2}z\right\}, \quad (8.10)$$

where β_p is the propagation constant at pump frequency, and

$$L_{\text{eff}} = \frac{1-\exp\{-\alpha_p L\}}{\alpha_p}, \quad (8.11)$$

is the fiber effective length at pump frequency. Note that in the case of perfect phase matching condition, if we ignore the Raman scattering process and the fiber loss in (8.5), the signal and idler photon fluxes are equal and independent of the frequency detuning between pump and signal. In that ideal regime, the efficiency of the FWM process is independent of the frequency detuning [10].

In optical fibers the FWM process has been used to generate polarization entangled photon-pairs. To achieve that goal, it is usually implemented a fiber loop that give rise to two co-polarized FWM processes, one clockwise (CW) and other counterclockwise (CCW) [2]. The Bell inequality has been used to distinguish between non-local and local theories [39, 40]. The CHSH form of the Bell's inequality states that, for all local theories $|\mathcal{S}| \leq 2$, where $\mathcal{S}$ is the experimentally determinable CHSH parameter [39–41]. A violation of the CHSH inequality is assumed to be an evidence of a violation of the Bell inequality [39–41], despite the loopholes that can affect the experimental measurements [40]. The degree of quantum entanglement can be tested with the CHSH form of the Bell's inequality [41]. In the specific case of polarization entanglement, a polarizer is placed in front of the detectors, and coincidence measurement are performed for different combinations of signal θ_s and idler θ_i polarizer angles [3–7, 42]. Between all the possible combinations for the signal and idler polarizer angles, it can be shown that the CHSH parameter is maximized for $\theta_s = \pi/8$, $\theta_s' = -\pi/8$, $\theta_i = 0$ and $\theta_i' = -\pi/4$ [13, 39, 43]. In that case the CHSH parameter can be written as [13]

$$\mathcal{S}_m = 2\sqrt{2}\,\frac{G^{(2)}_{(si)}(0) - I_i I_s}{G^{(2)}_{(si)}(0) + I_i I_s}, \tag{8.12}$$

where the violation of the inequality happens when $\mathcal{S}_m > 2$. In (8.12) I_u is given by (8.3), and

$$\begin{aligned} G^{(2)}_{(si)}(\tau) &= \langle \hat{A}_i^\dagger(L,t)\hat{A}_s^\dagger(L,t+\tau)\hat{A}_s(L,t+\tau)\hat{A}_i(L,t)\rangle \\ &= \left|\langle \hat{A}_s(L,t+\tau)\hat{A}_i(L,t)\rangle\right|^2 + I_i I_s \approx |\phi_c(\tau)|^2\,|\mathcal{F}^c(L,\bar{\omega}_s,\bar{\omega}_i)|^2 + I_i I_s, \end{aligned} \tag{8.13}$$

where we use the Gaussian moment-factoring theorem. In a low photon-flux regime, $\mathcal{F}_u(L) \ll 1$ with $\mathcal{F}_u(L)$ given by (8.5), the Gaussian field correlation approaches the quantum theory results [44]. In (8.13), $\phi_c(\tau)$ is given by

$$\phi_c(\tau) = \frac{1}{2\pi}\int d\omega H_s(\omega - \bar{\omega}_s)H_i(\bar{\omega}_s - \omega)e^{-i\omega\tau}, \tag{8.14}$$

and $\mathcal{F}^c(L,\bar{\omega}_s,\bar{\omega}_i)$ is the cross-correlation spectral density evaluated at $\bar{\omega}_s$ and $\bar{\omega}_i$, and given by [31]

$$\mathcal{F}^c(L,\bar{\omega}_s,\bar{\omega}_i) = \mu_s(L,0)\nu_i(L,0) + \alpha_s(\mathcal{N}_s+1)\int_0^L dz\mu_s(L,z)\nu_i(L,z)$$
$$+\alpha_i\mathcal{N}_i\int_0^L dz\nu_s(L,z)\mu_i(L,z) - (\mathcal{N}_{ip}+\Theta_{ip})|g_R(\Omega_{ip})|$$
$$\times\int_0^L \left(\bar{A}_p(z)\mu_s(L,z) - \bar{A}_p^*(z)\nu_s(L,z)\right)\left(\bar{A}_p(z)\mu_i(L,z) - \bar{A}_p^*(z)\nu_i(L,z)\right)dz. \quad (8.15)$$

In practice the source of polarization entangled photon-pairs is characterized by both coincidence and accidental counting rates, given respectively by [13, 21, 45]

$$R_{cc}(t_0) = \eta_s\eta_i(\tau_p f_p)\int_{t_0}^{t_0+t_c} G^{(2)}_{(si)}(\tau)d\tau, \quad (8.16)$$

$$R_{ac}(t_0) = \eta_s\eta_i(\tau_p f_p)^2\int_{t_0}^{t_0+t_c} I_i\, I_s\, d\tau, \quad (8.17)$$

where t_c is the coincidence time window, η_u is the signal or idler detector efficiency, and $\tau_p f_p$ is the pump duty cycle, where τ_p is the pump pulses duration, and f_p is the pump repetition rate. We assume that the transmission function of the signal and idler filters is Gaussian shaped

$$H_u(\omega-\bar{\omega}_u) = \exp\left\{-\frac{(\omega-\bar{\omega}_u)^2}{2(\Delta\omega)^2}\right\}, \quad (8.18)$$

where $\Delta\omega$ is the bandwidth of the filters, which we assume to be equal for the signal and idler. In that case, $\Delta\nu_s = \Delta\nu_i = \phi_c(0)$, where

$$\phi_c(\tau) = \sqrt{\pi}\frac{\Delta\omega}{2\pi}\exp\left\{-\left(\frac{\Delta\omega\tau}{2}\right)^2\right\}\exp\{-i\bar{\omega}_u\tau\}. \quad (8.19)$$

With this condition, the coincidence and accidental counting rates are given by

$$R_{cc}(0) = \eta_s\eta_i(\tau_p f_p)\left[\frac{\Delta\omega}{4\sqrt{2\pi}}\mathrm{Erf}\left(\frac{t_c\Delta\omega}{\sqrt{2}}\right)|\mathcal{F}^c(L,\bar{\omega}_s,\bar{\omega}_i)|^2 + \pi\left(\frac{\Delta\omega}{2\pi}\right)^2 t_c\,\mathcal{F}_i(L)\mathcal{F}_s(L)\right], \quad (8.20)$$

and

$$R_{ac}(0) = \eta_s\eta_i(\tau_p f_p)^2\pi\left(\frac{\Delta\omega}{2\pi}\right)^2 t_c\,\mathcal{F}_i(L)\mathcal{F}_s(L), \quad (8.21)$$

respectively, where Erf is the error function. With $R_{cc}(0)$ and $R_{ac}(0)$, we can evaluate the purity of the photon source, through the analysis of the CAR, which is given by [13, 21, 45, 46]

$$\mathrm{CAR} = \frac{R_{cc}(0)}{R_{ac}(0)} = \frac{\sqrt{2\pi}|\mathcal{F}^c(L,\bar{\omega}_s,\bar{\omega}_i)|^2}{2(\tau_p f_p) t_c \Delta\omega \mathcal{F}_i(L)\mathcal{F}_s(L)} + \frac{1}{\tau_p f_p}. \tag{8.22}$$

Moreover, we can estimate the true coincidence counting rate, originated from photon-pairs, given by [13, 21, 45]

$$\begin{aligned} R_{tc}(t_0) &= \eta_s\eta_i(\tau_p f_p) \int_{t_0}^{t_0+t_c} \left(G^{(2)}_{(si)}(\tau) - I_i I_s \right) d\tau \\ &= \eta_s\eta_i(\tau_p f_p) \left[\frac{\Delta\omega}{4\sqrt{2\pi}} \mathrm{Erf}\left(\frac{t_c\Delta\omega}{\sqrt{2}} \right) |\mathcal{F}^c(L,\bar{\omega}_s,\bar{\omega}_i)|^2 \right], \end{aligned} \tag{8.23}$$

where we use $t_0 = 0$. With $R_{tc}(0)$ we can estimate the single (uncorrelated) photon generation rate for the signal and idler fields, [13, 45]

$$R_u(0) = \eta_u(\tau_p f_p) I_u - R_{tc}(0), \tag{8.24}$$

where I_u is given by (8.3) and (8.19), and $R_{tc}(0)$ is given by (8.23).

8.3 Numerical Results

In this section, we show results for the evolution of the signal and idler photon fluxes, and the coincidence and accidental counting rates with both loss coefficient, α, and fiber nonlinear parameter, γ. Moreover, it is also presented the evolution of the CHSH parameter and the CAR coefficient with both α and γ. We also show the evolution of the CHSH parameter with the CAR coefficient and with the ratio $R_s(0)/R_i(0)$. We present those results for two distinct cases. First, we assume that the fiber length is fixed. Second, we admit that the fiber length varies with the value of α.

We assume an equal loss coefficient for all the fields involved in the FWM process $\alpha_p = \alpha_s = \alpha_i = \alpha$, a fixed frequency detuning between the signal and pump waves $\Omega_{sp}/(2\pi) = 3$ THz, and a temperature of $T = 300$ K. The pump, signal and idler wavelengths used are $\lambda_p = 1257.45$ nm, $\lambda_s = 1241.82$ nm, and $\lambda_i = 1273.47$ nm, respectively. Moreover, we assume that the loss coefficient and the fiber nonlinear parameter can go up to α_f and γ_f, respectively, where $\alpha_f = 100$ dB/km and $\gamma_f = 200$ W^{-1}km^{-1}. Furthermore, we also admit an ideal phase matching condition $\Delta\beta = 0$, in order to obtain efficient generation of photons through FWM. The Raman

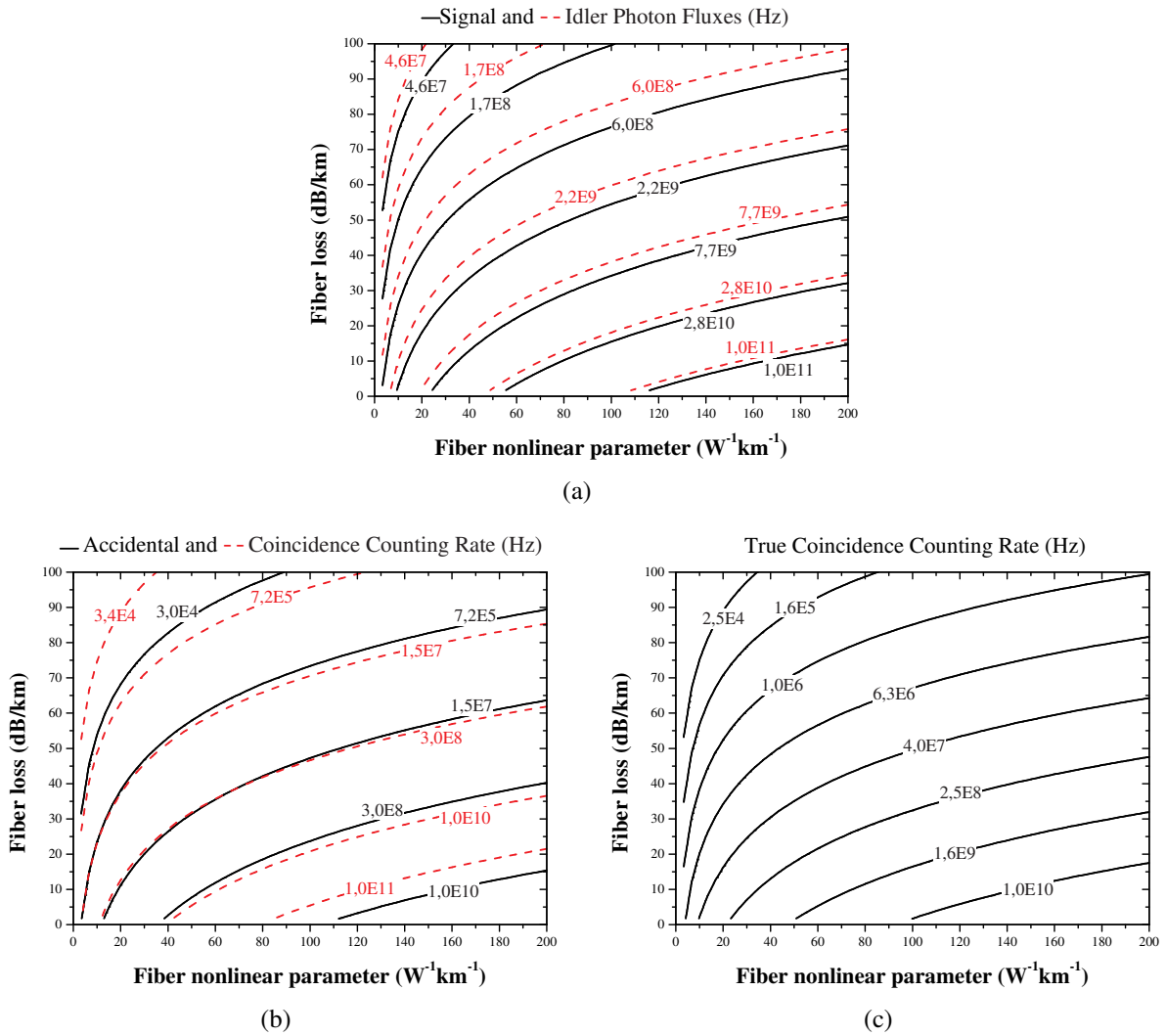

Figure 8.1: Contour plot for: (a) signal and idler photon fluxes given by (8.3); (b) coincidence and accidental counting rates given by (8.20) and (8.21), respectively; (c) true coincidence counting rate given by (8.23), as a function of α and γ.

response functions were taken from [47]. We consider ideal detectors $\eta_s = \eta_i = 1$, a continuous pump field $\tau_p f_p = 1$, signal and idler filters bandwidth of $\Delta\omega/(2\pi)$=100 GHz and a coincidence time window of $t_c = 1$ ps. Finally, we adopt a low pump power regime, $P_p(0) \approx 29$ mW.

8.3.1 Fixed Fiber Length

We first consider an optical fiber with length equal to $L = 5/\alpha_f \approx 217$ m, with $L_{\text{eff}} < 210$ m. In Fig. 8.1(a), we present the contour plots for the signal and idler photon fluxes given by (8.3), as a function of α and γ. Figure 8.1(b) shows the contour plot for the coincidence and accidental

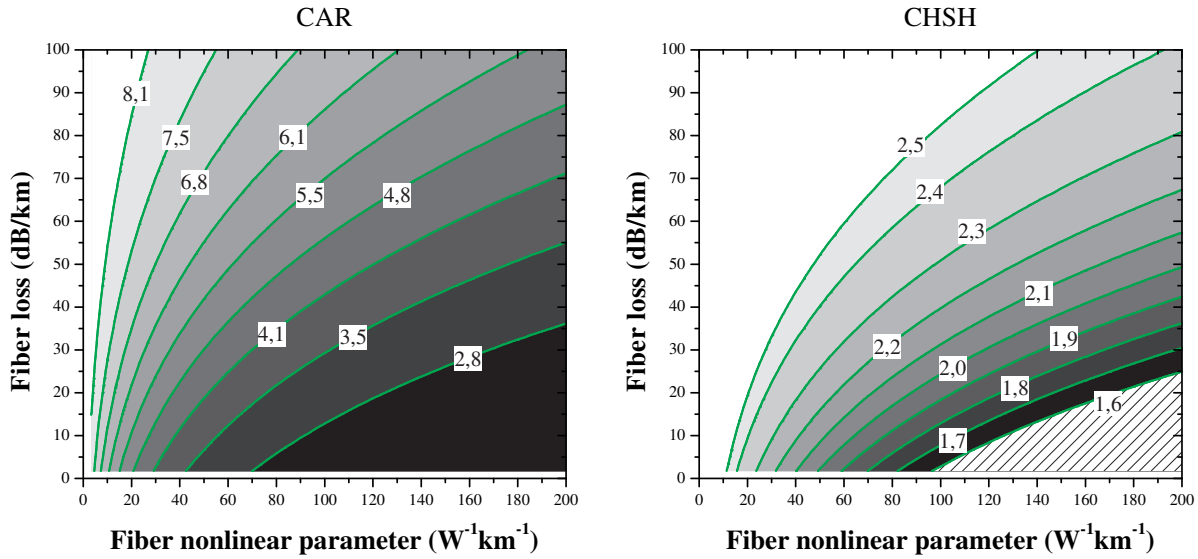

Figure 8.2: Contour plot for the CHSH parameter (a) and for the CAR (b) given by (8.12) and (8.22), respectively, as a function of α and γ.

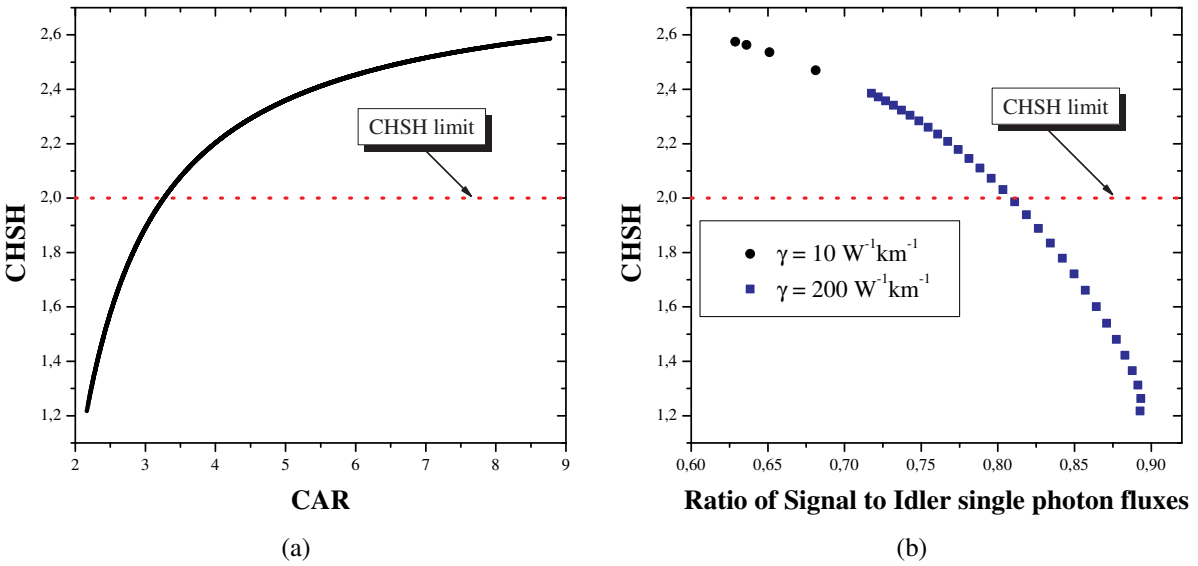

Figure 8.3: CHSH parameter as a function of: (a) CAR given by (8.22); (b) ratio $R_s(0)/R_i(0)$ given by (8.24).

counting rates given by (8.20) and (8.21), respectively. Figure 8.1(c) presents the evolution of the true coincidence counting rate as a function of α and γ.

It can be seen in Fig. 8.1(a) that for high values of waveguide loss are generated more photons on the idler wave than in the signal one. This is due to the Raman noise which generates more photons on the Stokes frequency shift. However, decreasing the value of α the flux of signal and idler photons tends to be equal, mainly for high values of γ. This mean that for low values of α and high values of γ, we tend to operate in a regime where are predominantly generated multiphotons on the signal and idler waves, through the stimulated FWM process [11, 13]. It can be seen in Fig. 8.1(b) that the difference between coincidence and accidental counting rates is higher for high values of α. In that regime the coincidence counting rate is 10 times larger than the accidental counting rate. For low values of α and high values of γ the rate of coincidence and accidental counts is of the same order. Results also show that for a fixed value of γ, an increase on α leads to a decrease on both accidental and coincidence counting rates. However, that decrease tends to be more pronounced on the accidental counting rate. That is due to a decrease on the generation rate of photons through the stimulated FWM and Raman scattering processes. Results present in Fig. 8.1(c) show that for low values of α and high values of γ the true coincidence counting rate is of the order of 10 GHz. Results also show that the coincidence counting rate for high values of α and low values of γ is of the order of 25 kHz. It can also be seen in Fig. 8.1(c) that for a fixed value of α an increase of γ tends to lead to an increase on the true coincidence counting rate. This is due to the fact that an increase on γ leads to a higher efficiency of the FWM process. However, this increase of the true coincidence counting rate tends to be counterbalanced by a further increase on the rate of accidental coincidences, see Fig. 8.1(b). When compared with Fig. 8.1(b), results present in Fig. 8.1(c) show that for high values of α and low values of γ most of the coincidences present in Fig. 8.1(b) are true coincidences.

Figure 8.2 shows the contour plot for the CHSH and for the CAR parameters given by (8.12) and (8.22), respectively, as a function of α and γ. It can be seen in Fig. 8.2(a) that a strong violation of the CHSH parameter happens for high values of α and low values of γ. For high values of γ, we obtain $\mathcal{S}_m > 2$ only for $\alpha > 30$ dB/km. This is due to the fact that, increasing only γ, the signal and idler photon fluxes increases, which leads to a growth on the accidental coincidences, see Fig. 8.1. According with (8.12), an increase on $I_s(L,0)\, I_i(L,0)$ leads to a decrease on the value of $\mathcal{S}_m$. From Fig. 8.2(b), we can see that the CAR parameter is maximum for high values of α and low values of γ, where the accidental counting rate is low, see Fig. 8.1(b). Moreover, from Fig. 8.2, we can see that a strong violation of the CHSH inequality demands high values of CAR. However, from Fig. 8.1(b) and Fig. 8.2(b), we can see that a high rate of coincidence counts does not leads to a high value of CAR (or CHSH) parameter. This can be seen in Fig. 8.3 where we show the evolution of the CHSH parameter with the CAR coefficient, Fig. 8.3(a). It

can also be seen in Fig. 8.3 the ratio of single to idler single photon fluxes, $R_s(0)/R_i(0)$ given by (8.24), for $\gamma = 10$ W^{-1}km^{-1} and $\gamma = 200$ W^{-1}km^{-1}, Fig. 8.3(b). It can be seen in Fig. 8.3 that a high value of $\mathcal{S}_m$ demands high values of CAR coefficient and low values of $R_s(0)/R_i(0)$. In that regime most of the photons are signal-idler pairs generated through spontaneous FWM. Moreover, Fig. 8.3(b) show that for low values of γ we observe always a strong violation of the CHSH inequality, whereas for high values of γ a $\mathcal{S}_m > 2$ demands high values of α. According with the results present in Fig. 2 and Fig. 3, in a medium with non-negligible loss, $\alpha(\omega)L \gg 1$, it is possible to obtain CAR> 8 and $\mathcal{S}_m > 2.5$, which is inline with typically measured values for the CAR and CHSH parameters in waveguides with $\alpha(\omega)L \ll 1$. For instance, measured values of CAR≈ 9 and $\mathcal{S}_m = 2.65$ were recently reported in [4, 48, 49].

8.3.2 Fiber Length Varies With Loss

In this section, we admit that the fiber length is dependent of the loss coefficient, $L = 5/\alpha$, where L is maximum for the lowest considered value of $\alpha \approx 1.7$ dB/km. This allows us to compare short fiber lengths where α is high, with long fiber lengths where α assumes a smaller value.

In Fig. 8.4(a), we present the evolution of the signal and idler photon fluxes, given by (8.3) as a function of α and γ. In Fig. 8.4(b), we show the evolution of both coincidence and accidental counting rates given by (8.20) and (8.21), respectively, as function of α and γ. Finally, Fig. 8.4(c) shows the evolution of the true counting rate, given by (8.23), with α and γ. Unlike the results presented in Fig. 8.1, findings plotted in Fig. 8.4 show that the contour lines for the photon fluxes, rate of accidental and coincidence counts, and true coincidence counts evolves linearly with both α and γ coefficients. This arises from the linear increase of the fiber length with α. Results also show that for low values of α we obtain the same photon flux for both signal and idler field. This arises from the dominance of the photon generation through the stimulated FWM process. It can be seen in Fig. 8.4(b) that for high values of α and low values of γ the coincidence counting rate is of the order of 40 kHz. Decreasing α and increasing γ the coincidence counting rate increase significantly, $R_{cc}(0) \approx 0.3$ GHz. However, in that regime the accidental counting rate reaches its maximum value.

In Fig. 8.5, we plot the evolution of both CHSH parameter given by (8.12), and CAR coefficient given by (8.22), as a function of α and γ. It can be seen in Fig. 8.5(a) that the contour lines of the CHSH parameter evolves linearly with the increase of both α and γ. Results also show that for a given α (or fiber length), increasing γ leads to a decrease on the value of CHSH. This mean that, a strong violation of the CHSH inequality requires a fiber with non-negligible loss (short

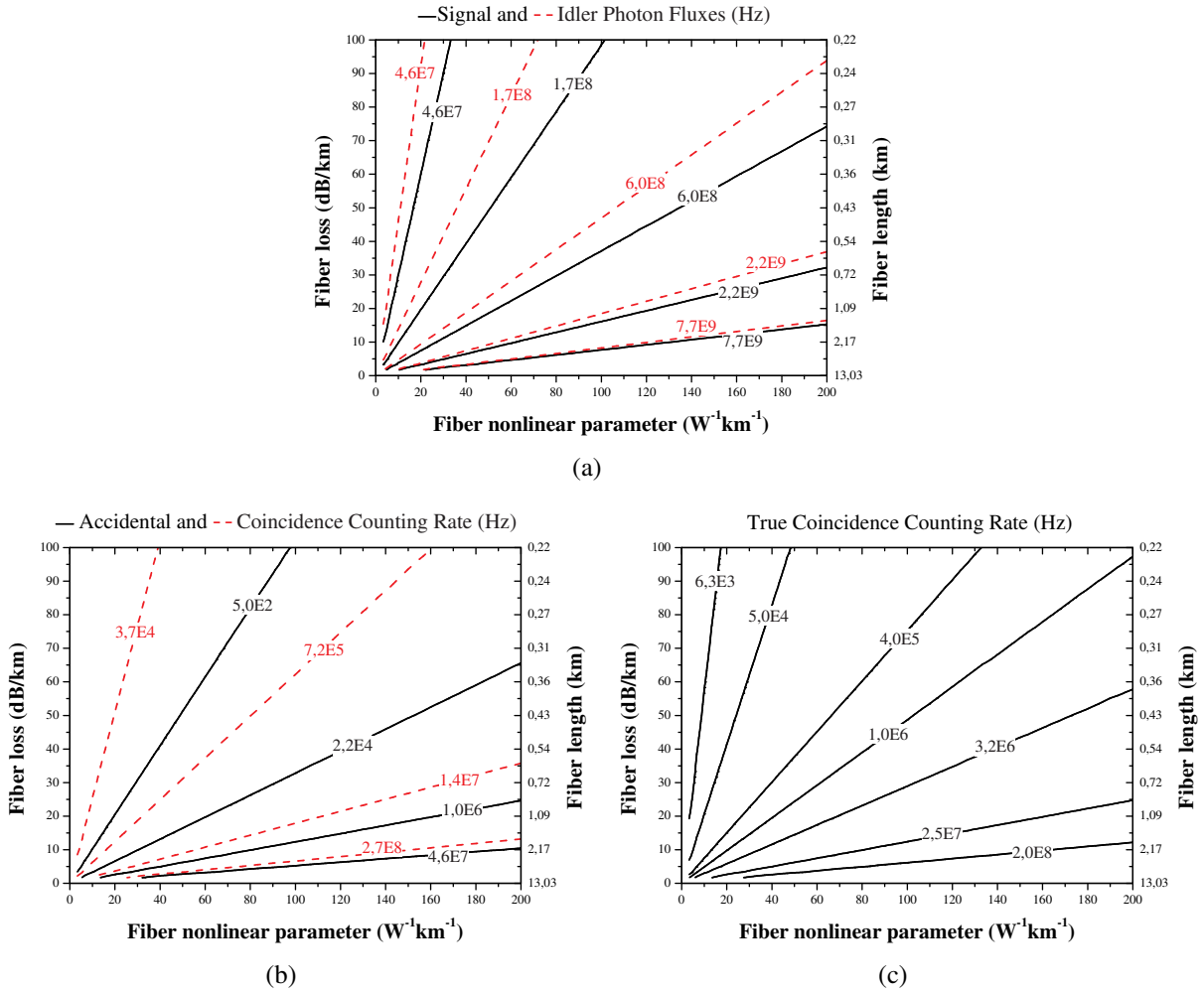

Figure 8.4: Contour plot for: (a) signal and idler photon fluxes given by (8.3); (b) coincidence and accidental counting rates given by (8.20) and (8.21), respectively; (c) true coincidence counting rate given by (8.23), as a function of α and γ.

fiber lengths) with low value of γ, to avoid the generation of multiphotons during the evolution of the signal and idler photons inside the waveguide. This can be seen in Fig. 8.5(b) where we plot the evolution of the CAR coefficient given by (8.22), with the α and γ. From Fig. 8.5(b) we can see that a high value of CAR coefficient is obtained in the same regime where we observe a strong violation of the CHSH parameter, see Fig. 8.5(a).

Figure 8.6 shows the evolution of the CHSH with the CAR, Fig. 8.6(a), and with the ratio $R_s(0)/R_i(0)$, Fig. 8.6(b). Results present in Fig. 8.6 show that a violation of the CHSH inequality is observed for a CAR$>$ 3.5 and a ratio of signal to idler uncorrelated photon fluxes $R_s(0)/R_i(0) < 0.8$. Moreover a strong violation demands high values of CAR coefficient, typi-

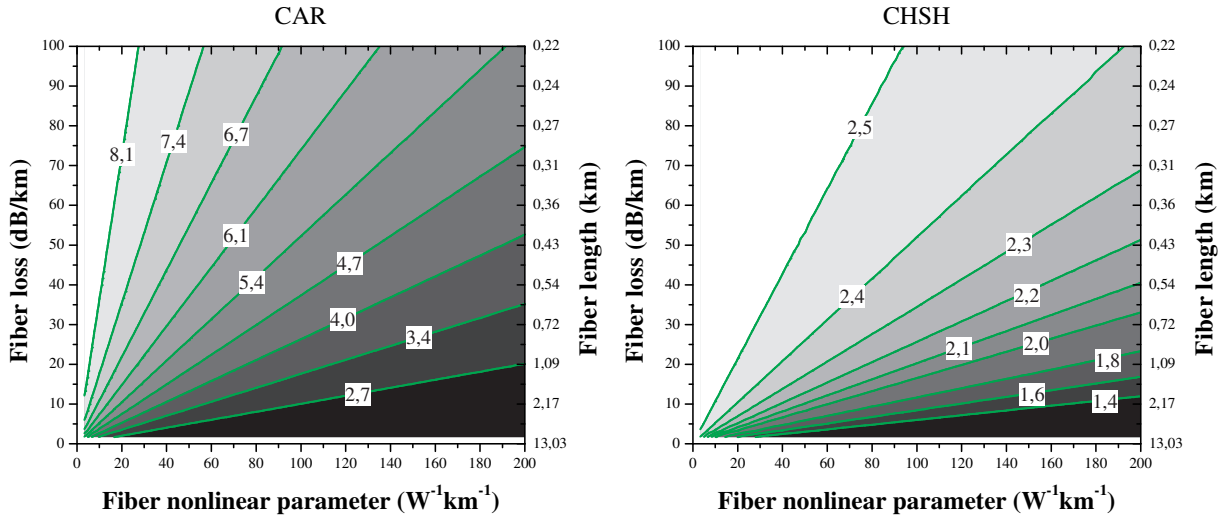

(a) (b)

Figure 8.5: Contour plot for the CHSH parameter (a) and for the CAR (b) given by (8.12) and (8.22), respectively, as a function of α and γ.

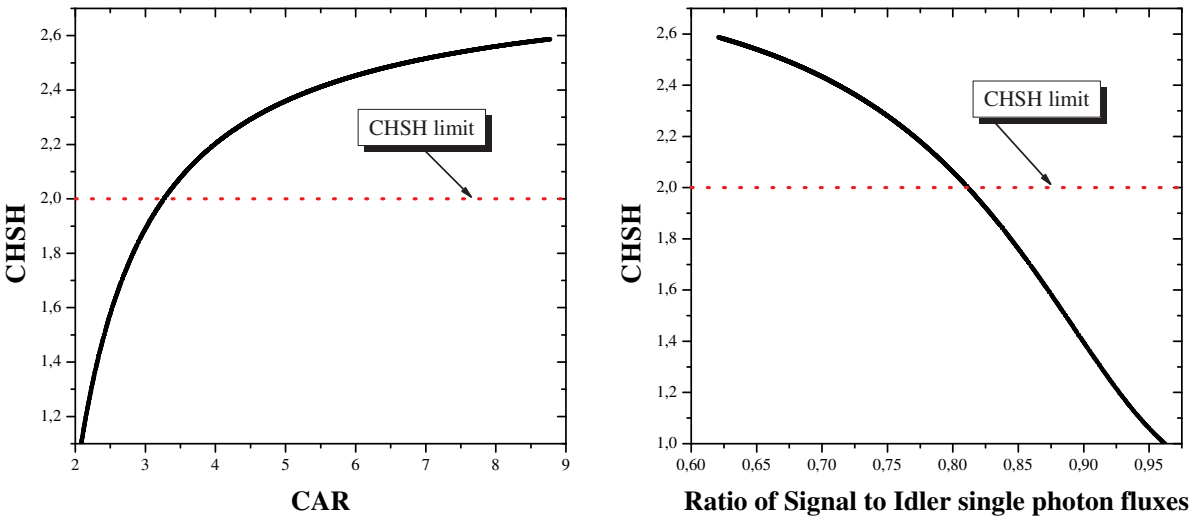

(a) (b)

Figure 8.6: CHSH parameter as a function of: (a) CAR given by (8.22); (b) ratio $R_s(0)/R_i(0)$ given by (8.24).

cally a CAR grater than 8, and low values of ratio of signal to idler uncorrelated photon fluxes, $R_s(0)/R_i(0) < 0.65$. In that regime, the flux of uncorrelated photons is minimum, and most of the rate of coincidences are true coincidences, originated from signal-idler pairs, generated through

spontaneous FWM.

8.4 Summary

We investigate the effects of fiber loss and nonlinear coefficient on the generation of polarization entangled photon pairs. We show first that for a fixed fiber length and for a fixed value of α, increasing γ tends to lead to a worst performance of the polarization entangled source. This is due to the increase generation of multiphotons on the signal and idler fields through stimulated FWM. In a second scenario, we assume that the fiber length is dependent of the loss coefficient, $L = 5/\alpha$. In that case, our results show that the contour lines of CHSH parameter evolves linearly with α and γ. This mean that for a given value of α is always possible to find a γ that leads to a strong violation of the CHSH inequality.

We verify the possibility of efficient generation of quantum correlated photon-pairs through FWM in a medium with non-negligible loss and moderate value of γ. This new regime allow us to obtain results similar to the ones with $\alpha L \ll 1$. However, since in this new regime we can use $L \gg 1/\alpha$ the waveguide output pump power tends to be much lower, which makes easier removing the pump photons. In this new regime, it is also possible to use lower pump powers because the waveguide length can be increased, due to the moderate value of γ and high value of α. We show that a strong violation of the CHSH inequality can be obtained with fibers with high values of $\alpha > 50$ dB/km and moderate values of $\gamma < 60$ $\mathrm{W^{-1}km^{-1}}$. Nevertheless, extreme high values of $\alpha > 90$ dB/km can not be used, since in that case the generation rate of photon-pairs is almost null.

References

[1] N. Gisin, G. Ribordy, W. Tittel, and H. Zbinden, "Quantum cryptography," *Rev. Mod. Phys.*, vol. 74, pp. 145–195, 2002.

[2] J. Chen, J. B. Altepeter, and P. Kumar, "Quantum-state engineering using nonlinear optical sagnac loops," *New Journal of Physics*, vol. 10, p. 123019, 2008.

[3] J. Fan, A. Migdall, J. Chen, and E. Goldschmidt, "Microstructure-fiber-based source of photonic entanglement," *IEEE Journal of Selected Topics in Quantum Electronics*, vol. 15, pp. 1724 –1732, 2009.

[4] H. Takesue and K. Inoue, "Generation of polarization-entangled photon pairs and violation of Bell's inequality using spontaneous four-wave mixing in a fiber loop," *Phys. Rev. A*, vol. 70, p. 031802, 2004.

[5] X. Li, P. L. Voss, J. E. Sharping, and P. Kumar, "Optical-fiber source of polarization-entangled photons in the 1550 nm telecom band," *Phys. Rev. Lett.*, vol. 94, p. 053601, 2005.

[6] X. Li, C. Liang, K. Fook Lee, J. Chen, P. L. Voss, and P. Kumar, "Integrable optical-fiber source of polarization-entangled photon pairs in the telecom band," *Phys. Rev. A*, vol. 73, p. 052301, 2006.

[7] J. Fan, M. D. Eisaman, and A. Migdall, "Bright phase-stable broadband fiber-based source of polarization-entangled photon pairs," *Phys. Rev. A*, vol. 76, p. 043836, 2007.

[8] M. Beck, "Comparing measurements of $g^{(2)}(0)$ performed with different coincidence detection techniques," *J. Opt. Soc. Am. B*, vol. 24, pp. 2972–2978, 2007.

[9] N. A. Silva and A. N. Pinto, "Effects of losses and nonlinearities on the generation of polarization entangled photons," *IEEE/OSA Journal of Lightwave Technology*, vol. 31, pp. 1309–1317, 2013.

[10] G. Agrawal, *Nonlinear Fiber Optics*, 3rd ed. Academic Press, 2001.

[11] N. Silva, N. Muga, and A. Pinto, "Influence of the stimulated Raman scattering on the four-wave mixing process in birefringent fibers," *IEEE/OSA Journal of Lightwave Technology*, vol. 27, pp. 4979–4988, 2009.

[12] N. A. Silva, N. J. Muga, and A. N. Pinto, "Effective nonlinear parameter measurement using FWM in optical fibers in a low power regime," *IEEE Journal of Quantum Electronics*, vol. 46, pp. 285–291, 2010.

[13] Q. Lin, F. Yaman, and G. P. Agrawal, "Photon-pair generation in optical fibers through four-wave mixing: Role of Raman scattering and pump polarization," *Phys. Rev. A*, vol. 75, p. 023803, 2007.

[14] X. Gai, R. P. Wang, C. Xiong, M. J. Steel, B. J. Eggleton, and B. Luther-Davies, "Near-zero anomalous dispersion $Ge_{11.5}As_{24}Se_{64.5}$ glass nanowires for correlated photon pair generation: design and analysis," *Opt. Express*, vol. 20, pp. 776–786, 2012.

[15] NKT Photonics, "NL-PM-750 data sheet," http://www.nktphotonics.com/files/files/NL-PM-750-090612.pdf.

[16] C. Xiong, L. G. Helt, A. C. Judge, G. D. Marshall, M. J. Steel, J. E. Sipe, and B. J. Eggleton, "Quantum-correlated photon pair generation in chalcogenide As_2S_3 waveguides," *Opt. Express*, vol. 18, pp. 16 206–16 216, 2010.

[17] A. Politi, M. J. Cryan, J. G. Rarity, S. Yu, and J. L. O'Brien, "Silica-on-silicon waveguide quantum circuits," *Science*, vol. 320, pp. 646–649, 2008.

[18] C. Xiong, G. D. Marshall, A. Peruzzo, M. Lobino, A. S. Clark, D.-Y. Choi, S. J. Madden, C. M. Natarajan, M. G. Tanner, R. H. Hadfield, S. N. Dorenbos, T. Zijlstra, V. Zwiller, M. G. Thompson, J. G. Rarity, M. J. Steel, B. Luther-Davies, B. J. Eggleton, and J. L. O'Brien, "Generation of correlated photon pairs in a chalcogenide As_2S_3 waveguide," *Applied Physics Letters*, vol. 98, p. 051101, 2011.

[19] M. Fiorentino, P. Voss, J. Sharping, and P. Kumar, "All-fiber photon-pair source for quantum communications," *IEEE Photonics Technology Letters*, vol. 14, pp. 983 –985, 2002.

[20] J. E. Sharping, M. Fiorentino, and P. Kumar, "Observation of twin-beam-type quantum correlation in optical fiber," *Opt. Lett.*, vol. 26, pp. 367–369, 2001.

[21] H. Takesue and K. Inoue, "Generation of 1.5-μm band time-bin entanglement using spontaneous fiber four-wave mixing and planar light-wave circuit interferometers," *Phys. Rev. A*, vol. 72, p. 041804, 2005.

[22] H. Takesue, "Long-distance distribution of time-bin entanglement generated in a cooled fiber," *Opt. Express*, vol. 14, pp. 3453–3460, 2006.

[23] L. J. Wang, C. K. Hong, and S. R. Friberg, "Generation of correlated photons via four-wave mixing in optical fibres," *Journal of Optics B: Quantum and Semiclassical Optics*, vol. 3, p. 346, 2001.

[24] J. Chen, X. Li, and P. Kumar, "Two-photon-state generation via four-wave mixing in optical fibers," *Phys. Rev. A*, vol. 72, p. 033801, 2005.

[25] O. Alibart, J. Fulconis, G. K. L. Wong, S. G. Murdoch, W. J. Wadsworth, and J. G. Rarity, "Photon pair generation using four-wave mixing in a microstructured fibre: theory versus experiment," *New Journal of Physics*, vol. 8, p. 67, 2006.

[26] K. Garay-Palmett, H. J. McGuinness, O. Cohen, J. S. Lundeen, R. Rangel-Rojo, A. B. U'ren, M. G. Raymer, C. J. McKinstrie, S. Radic, and I. A. Walmsley, "Photon pair-state preparation with tailored spectral properties by spontaneous four-wave mixing in photonic-crystal fiber," *Opt. Express*, vol. 15, pp. 14 870–14 886, 2007.

[27] P. L. Voss and P. Kumar, "Raman-effect induced noise limits on $\chi^{(3)}$ parametric amplifiers and wavelength converters," *Journal of Optics B: Quantum and Semiclassical Optics*, vol. 6, p. S762, 2004.

[28] P. L. Voss and P. Kumar, "Raman-noise-induced noise-figure limit for $\chi(3)$ parametric amplifiers," *Opt. Lett.*, vol. 29, pp. 445–447, 2004.

[29] P. L. Voss, K. G. Köprülü, and P. Kumar, "Raman-noise-induced quantum limits for $\chi(3)$ nondegenerate phase-sensitive amplification and quadrature squeezing," *J. Opt. Soc. Am. B*, vol. 23, pp. 598–610, 2006.

[30] Q. Lin, F. Yaman, and G. P. Agrawal, "Photon-pair generation by four-wave mixing in optical fibers," *Opt. Lett.*, vol. 31, pp. 1286–1288, 2006.

[31] N. A. Silva and A. N. Pinto, "Role of absorption on the generation of quantum-correlated photon pairs through FWM," *IEEE Journal of Quantum Electronics*, vol. 48, pp. 1380 –1388, 2012.

[32] R. W. Boyd, *Nonlinear Optics*, 2nd ed. Academic Press, 2003.

[33] R. W. Hellwarth, *Third-order optical susceptibilities of liquids and solids*. Pergamon Press, Oxford ; New York, 1977.

[34] N. A. Silva, N. J. Muga, and A. N. Pinto, "Evolution of first-order sidebands from multiple FWM processes in HiBi optical fibers," *Optics Communications*, vol. 284, pp. 3408 – 3415, 2011.

[35] Q. Lin and G. P. Agrawal, "Raman response function for silica fibers," *Opt. Lett.*, vol. 31, pp. 3086–3088, 2006.

[36] N. A. Silva, A. J. Almeida, and A. N. Pinto, "Interference in a quantum channel due to classical four-wave mixing in optical fibers," *IEEE Journal of Quantum Electronics*, vol. 48, pp. 472 –479, 2012.

[37] P. D. Drummond and J. F. Corney, "Quantum noise in optical fibers. I. Stochastic equations," *J. Opt. Soc. Am. B*, vol. 18, pp. 139–152, 2001.

[38] P. D. Drummond, *Coherence and Quantum Optics VII*. Springer, 1996, ch. Quantum Theory of Fiber-Optics and Solitons, pp. 323–332.

[39] D. F. Walls and G. F. Milburn, *Quantum optics*. Springer Verlag, Berlin, 1994.

[40] R. Chiao and J. Garrison, *Quantum Optics*. Oxford University Press, USA, 2008.

[41] J. F. Clauser, M. A. Horne, A. Shimony, and R. A. Holt, "Proposed experiment to test local hidden-variable theories," *Phys. Rev. Lett.*, vol. 23, pp. 880–884, 1969.

[42] A. Almeida, S. Carneiro, N. Silva, N. Muga, and A. Pinto, "Polarization-entangled photon pairs using spontaneous four-wave mixing in a fiber loop," in *EUROCON - International Conference on Computer as a Tool (EUROCON), 2011 IEEE*, 2011, pp. 1 –4.

[43] P. G. Kwiat, K. Mattle, H. Weinfurter, A. Zeilinger, A. V. Sergienko, and Y. Shih, "New high-intensity source of polarization-entangled photon pairs," *Phys. Rev. Lett.*, vol. 75, pp. 4337–4341, 1995.

[44] J. H. Shapiro and K.-X. Sun, "Semiclassical versus quantum behavior in fourth-order interference," *J. Opt. Soc. Am. B*, vol. 11, pp. 1130–1141, 1994.

[45] J. Fan, A. Migdall, and L. Wang, "A twin photon source based on all-optical fiber," *Opt. Photon. News*, vol. 18, pp. 26–33, 2007.

[46] K. F. Lee, J. Chen, C. Liang, X. Li, P. L. Voss, and P. Kumar, "Generation of high-purity telecom-band entangled photon pairs in dispersion-shifted fiber," *Opt. Lett.*, vol. 31, pp. 1905–1907, 2006.

[47] D. Hollenbeck and C. D. Cantrell, "Multiple-vibrational-mode model for fiber-optic raman gain spectrum and response function," *J. Opt. Soc. Am. B*, vol. 19, pp. 2886–2892, 2002.

[48] H. Takesue and K. Inoue, "1.5-μm band quantum-correlated photon pair generation in dispersion-shifted fiber: suppression of noise photons by cooling fiber," *Opt. Express*, vol. 13, pp. 7832–7839, 2005.

[49] J. Rarity, J. Fulconis, J. Duligall, W. Wadsworth, and P. Russell, "Photonic crystal fiber source of correlated photon pairs," *Opt. Express*, vol. 13, pp. 534–544, 2005.

Chapter 9

Conclusions and Future Directions

In this thesis was analyzed the physical layer of a quantum key distribution (QKD) system, mainly covering the generation and transmission of single and entangled photons in optical fibers. In the framework of this thesis, we have obtained new theoretical and numerical results which some of them have been validated experimentally. In this Chapter, we overview the developed work, and summarize the main conclusions of this thesis. It is also presented in section 9.2 some topics to be considered in future studies.

9.1 Conclusions

The implementation of a few-photon source in optical fibers was analyzed in Chapter 3. The theoretical model developed in that Chapter accurately describes the classical process of four-wave mixing (FWM) that occurs inside of an optical fiber. We observed the possibility of efficient generation of the idler wave considering the pump outside of the zero-dispersion of the fiber and with pump and signal fields far apart. That arises from the inclusion of the nonlinear contribution in the parametric gain. This analytical result was validated experimentally, and a good agreement was observed for several different pump powers. We also observed experimentally the loss of efficiency in the FWM process due to the polarization decorrelation between pump and signal fields. The best efficiency was obtained when pump and signal are co-polarized, whereas the orthogonal scheme leads to the worst efficiency. We show experimentally that exist a transition region over which the pump and signal fields go from an almost co-polarized situation to a decorrelated state of polarization (SOP). In order to describe the influence of the polarization effects on the evolution of the idler power, we introduced the effective nonlinear parameter, $\gamma_{\text{eff}}(\Delta\lambda)$. We found that the $\gamma_{\text{eff}}(\Delta\lambda)$ varies as an hyperbolic secant with the wavelength separation between pump and signal. The few-photon source based on the classical process of FWM was later used

to implement a quantum communication link between two users. We observed a good agreement between the emitted polarization state and the received idler photon state if a polarization controller (PC) scheme is included, since we obtained a fringe visibility higher than 98%. This indicates that the few-photon source based on FWM process can in principle be used for QKD applications.

The impact of the stimulated Raman scattering (SRS) on the classical process of FWM in optical fibers was analyzed in Chapter 4. We have considered the single- and dual-pump configuration in both co-polarized and orthogonal polarization schemes. We verified that in the single- and dual- pump configuration the signal wave is mostly described by the imaginary part of the fiber nonlinear response function. We observed that the generation of the idler wave in the co-polarized scheme is dependent of the real part of the fiber nonlinear response function. For frequency detunings less than 3 THz the approximation $f_R = 0$ is quite good. We verified that the orthogonal scheme leads to an inefficient generation of the idler wave due to the high value of the group birefringence. However, in the dual pump configuration when the signal is launched into the fiber parallel to the right pump the generation of the idler wave is very efficient for small frequency detunings. We also explored the generation of two idler waves inside a high birefringent (HiBi) optical fiber, considering three FWM processes and the SRS. We observed that in the co-polarized scheme the SRS does not change dramatically the optical power evolution of the two idler waves with the wavelength separation between the pumps. We verified that the contribution of several FWM processes to the generation of idler wave can increase the efficiency of the process. We have showed that the orthogonal polarization scheme leads to an inefficient generation of the idler waves, due to the high value of fiber birefringence. We verified that the SRS decreases the optical power of the idler waves when compared with the limit $f_R = 0$. We observe that the evolution from the co-polarized to the orthogonal polarization scheme leads to a continuous loss of efficiency on the generation of the idlers waves. As we assume a nonlinear parameter higher than the one for standard single mode fibers (SSMFs), the results obtained can help to guide the development of optical signal processing devices using photonic crystal fibers (PCFs) and based on FWM and SRS processes.

The photon statistics of the idler wave generated through the classical process of FWM in a low power regime was addressed in Chapter 5. The theoretical model developed in that Chapter accurately describes the evolution of the idler photon statistics with both fiber input power and frequency detuning. We have examined the photon statistics of the idler wave fully generated inside the fiber, and how the idler photons generated through FWM and Raman scattering

processes affects the photon number distribution of an incident coherent quantum channel. The photon number distribution was studied theoretically in terms of the second-order coherence function. We observed that the statistics of the idler wave generated through FWM follows a thermal distribution when the fiber input power is maintained in a low level. However, we have also showed that an increase on the input power rapidly leads to a Poissonian distribution for the idler photons at the fiber output. Our analysis have showed that the in-band noise photons created by FWM and Raman scattering processes can change the statistics of a quantum channel used for QKD. At low power level the statistics of the coherent quantum channel can evolve from Poissonian to thermal. We also observed that when we increase the wavelength detuning between the pump and signal the coherent quantum channel evolves from a Poissonian statistics to a thermal one. The statistics of the idler photons was experimentally validated through the implementation of the FWM process in a low power regime inside of a dispersion-shifted fiber (DSF). The detailed knowledge of the photon statistics is essential to correctly detect the presence of an eavesdropper.

The spontaneous FWM process as a source of heralded single photons was studied in Chapter 6. We have examined the statistics of the heralded single photon source based on spontaneous FWM process in optical fibers through the analysis of the second-order coherence function for the signal field conditioned on observing an idler event. In a back-to-back configuration and for low values of pump power we observed the nonclassical nature of the photon source, even in the presence of Raman noise photons. In the absence of Raman scattering process, we have obtain an almost perfect conditional source of single photons. We have also showed that, to avoid the Raman noise photons we need to operate in a high frequency detuning regime. Nevertheless, a continuous increase of the pump power level leads to a Poissonian and to a multithermal statistics of the photon source. When we include a SSMF between the heralded photon source and the detection stage, we observe that the photon absorption reservoir in the SSMF only changes significantly the statistics of the photon source for high values of SSMF length. For low values of SSMF length, the statistics of the source does not change significantly due to propagation.

The impact of waveguide linear loss on the generation of quantum correlated photon-pairs through the combined processes of FWM and Raman scattering was analyzed in Chapter 7. The theoretical model developed in that Chapter accurately describes the signal and idler photon-fluxes as well the auto- and cross-correlation functions for signal and idler waves. We observed that the presence of fiber loss does not change the statistics of the individual signal and idler fields. Moreover, we have showed that the fiber loss increase the expected signal-idler correla-

tion at fiber output. We also observed that the presence of loss increases the value of Clauser, Horne, Shimony, and Holt (CHSH) parameter, when compared with the case $\alpha(\omega) = 0$. The fiber loss increases the purity of the photon pair correlation, due to the fact that fiber absorption reduces the rate of uncorrelated photons generated by Raman scattering inside the fiber. In addition, we have showed that waveguides with non-negligible losses can be used for efficient generation of quantum correlated photon-pairs. We also experimentally test the CHSH inequality for polarization-entangled photon-pairs obtained through the implementation of the spontaneous FWM process in a highly nonlinear fiber (HNLF). We observed a visibility for the coincidence fringe higher than 86%, and a violation of CHSH inequality by 2.7 standard deviations. The results obtained in that Chapter can help to guide the implementation of on-chip quantum technologies.

The spontaneous FWM provides a natural solution to implement sources of polarization entangled photon-pairs already inside optical fibers. Typically, efficient generation of photon-pairs through FWM demands waveguides with high values of nonlinear parameter. However, waveguides with high values of nonlinear parameter, such as photonic crystal fibers and chalcogenide glasses, tends to present high values of losses. The effects of losses and nonlinearities on the generation of polarization entangled photons was addressed in Chapter 8. We observed that for a fixed value of waveguide loss, increasing the nonlinear parameter tends to lead to a worst performance of the polarization entangled source. We also verified the possibility of efficient generation of quantum correlated photon-pairs through FWM in a medium with non-negligible loss and moderate value of nonlinear parameter. We showed that a strong violation of the CHSH inequality can be obtained with fibers with high values of waveguide loss, $\alpha > 50$ dB/km and moderate values of nonlinear parameter, $\gamma < 60$ $\mathrm{W^{-1}km^{-1}}$. The results obtained in that Chapter can help to guide the implementation of entangled photon sources in waveguides with high values of both loss coefficient and nonlinearities.

9.2 Future Directions

This thesis has addressed several research topics on the physical layer of a QKD system. Related with this work, several topics can be considered in future studies.

- The theoretical model in Chapter 3 for the evolution of the idler wave inside the fiber could be generalized to include the polarization effects that occurs inside the fiber, and leads to a

loss of efficiency in the FWM process due to polarization decorrelation between the optical fields.

- In a typically wavelength-division multiplexing (WDM) lightwave system the quantum channel used in the QKD setup share the same fiber with several other classical optical signals, of the order of 96. Hence, it would be good to expand the theoretical model used for the photon statistics for that WDM configuration.

- In a multiple-access QKD network, where different users are connected together via a WDM router, the theoretical model characterizing the statistics of the heralded single photon source must be generalized for that multi-user configuration, in which each user detects an idler and a signal event.

- In optical fibers the capacity does not growth indefinitely with the increase of the optical power. It will be good to study the fiber channel capacity in a scenario where each symbol used to transmit information contain only few-photons.